On dispersive interactions between a trapped ion and a cavity field

DISSERTATION

zur Erlangung des Grades

DOCTOR OF PHILOSOPHY

an der Fakultät für
Mathematik, Informatik und Physik
der Leopold-Franzens-Universität Innsbruck

vorgelegt von
DIPL.-PHYS. KONSTANTIN FRIEBE

durchgeführt am Institut für Experimentaphysik
unter der Leitung von
o. Univ.-Prof. Dr. Rainer Blatt und Univ.-Prof. Dr. Tracy E. Northup

2018

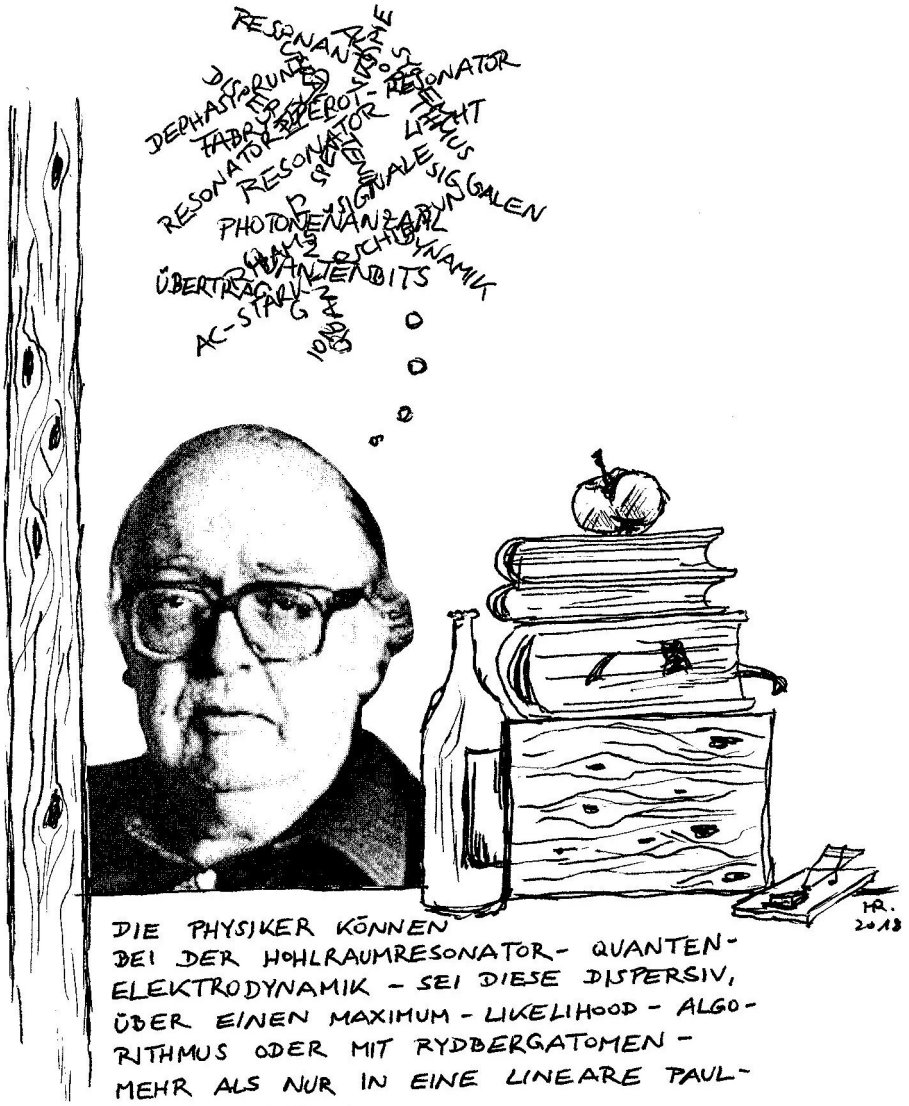

DIE PHYSIKER KÖNNEN BEI DER HOHLRAUMRESONATOR-QUANTEN-ELEKTRODYNAMIK – SEI DIESE DISPERSIV, ÜBER EINEN MAXIMUM-LIKELIHOOD-ALGORITHMUS ODER MIT RYDBERGATOMEN – MEHR ALS NUR IN EINE LINEARE PAUL-FALLE TAPPEN ...

Kurzfassung

Die vorliegende Dissertation beschreibt im ersten Teil die Charakterisierung eines Experimentaufbaus zur Hohlraumresonator-Quantenelektrodynamik, bestehend aus einer linearen Paul-Falle für $^{40}Ca^{+}$-Ionen und einem Fabry-Perot-Resonator. In diesem Aufbau wurde das im zweiten Teil der Arbeit beschriebene Experiment durchgeführt: Ein nicht-resonant (dispersiv) an den Resonator gekoppeltes Ion wurde verwendet, um durch Ramsey-Spektroskopie des Ions Informationen über die Photonenstatistik des elektrischen Felds des gepumpten Resonator zu erhalten ohne die Photonen zu zerstören. Die auf der AC-Stark-Verschiebung beruhende Phasenverschiebung sowie die Dephasierung, die das Ion durch den Einfluss der Photonen im Resonatorfeld erfährt, wurden im Ramseysignal beobachtet. Aus diesem Signal wurde durch Kalibrierung der Photonenanzahl im Resonator einerseits die Kopplungsstärke zwischen Ion und Resonatorfeld bestimmt. Andererseits wurde über einen Maximum-Likelihood-Algorithmus die statistische Verteilung der Photonenzahlen aus den Ramseysignalen rekonstruiert. Diese Rekonstruktion gelang sowohl für kohärentes Pumplicht, als auch für Licht mit gemischt thermisch-kohärenter Statistik. Es handelt sich bei diesem Experiment um die erste Übertragung von Konzepten, die bereits mit Rydbergatomen und supraleitenden Quantenbits in Mikrowellenresonatoren erfolgreich angewendet worden sind, auf ein System mit einem Resonator für optische Photonen.

Abstract

The first part of this dissertation describes the rebuilding and characterisation of an experimental setup on cavity quantum electrodynamics, which consists of a linear Paul trap for $^{40}Ca^{+}$-ions and a Fabry-Perot cavity. This setup was used in the following experiment, which is described in the second part of the thesis: Via non-resonant (dispersive) coupling between the resonator and an ion and a Ramsey sequence, information about the photon statistics of the field of the driven resonator was obtained without destroying the photons. Both the AC Stark shift and dephasing experienced by the ion due to the influence of photons in the resonator field were observed in the Ramsey signal of the ion. From this signal the coupling strength between ion and resonator field was extracted via a calibration of the photon number. On the other hand, the statistical distribution of photon numbers was reconstructed from the Ramsey signals by means of a maximum likelihood algorithm. This reconstruction performed successfully when the cavity was driven with coherent light as well as with light of mixed thermal-coherent statistics. The presented experiment demonstrates the first transfer to the optical domain of successfully tested concepts from experiments with Rydberg atoms and superconducting quantum bits in microwave resonators.

Contents

List of abbreviations

AC:	alternating current, time-varying
AOM:	acousto-optic modulator
APD:	avalanche photodiode
BOT:	branch-on-trigger
CAD:	computer-aided design
CCD:	charge-coupled device
CQED:	cavity quantum electrodynamics
CW:	continuous wave
DC:	direct current, constant in time
DDS:	direct digital synthesiser
EIT:	electromagnetically-induced transparency
EOD:	electro-optic deflector
EOM:	electro-optic modulator
FPGA:	field-programmable gate array
FFT:	fast Fourier transform
FSR:	free spectral range
FWHM:	full width at half maximum
NPBS:	non-polarising beam splitter
PBS:	polarising beam splitter
PID:	proportional-integral-differential controller
PMT:	photomultiplier tube
ppm:	parts per million, 10^{-6}
RF:	radiofrequency
RMS:	root mean square
ROC:	radius of curvature
SWR:	standing wave ratio
TA:	tapered amplifier
TiSub:	titanium sublimation pump
TTL:	transistor-transistor logic
UHV:	ultra-high vacuum
ULE:	ultra-low expansion
UV:	ultra-violet
XPM:	cross-phase modulation

Chapter 1

Introduction

Omnium enim rerum principia parva sunt.

– Cicero, De finibus bonorum et malorum

It is customary to start thesis introductions in the field of quantum physics with an appreciation of the great success of quantum mechanics. And indeed, this theory has proved to be very successful, although its beginnings emerged from a quasi-static scientific environment, in which all the big questions were considered answered: M. Planck's professor P. von Jolly tried to convince Planck not to study physics, as only little bits and pieces would require further examination in an otherwise near complete scientific system [1]. Fortunately, Planck persisted and with his quantised description of electromagnetic radiation inaugurated an era of successful theory building, culminating in the mid-1920s, when N. Bohr, W. Heisenberg, E. Schrödinger and numerous other physicists succeeded in constructing a theoretical model for the microscopic world: quantum mechanics. This theory has indeed not only helped to significantly promote our understanding of atomic systems, but has also led to astounding applications. If the field in its modest beginnings was only of theoretical interest, a few decades later, quantum science had started to conquer the world in many ways: During what is dubbed the first quantum revolution, lasers were developed [2], which found many and diverse applications, and transistors and semi-conductor technology [3] have revolutionised the way information is processed. These achievements, based on effects fundamentally relying on quantum mechanics, have heavily influenced not only science and industry, but also everyday life of the majority of humankind.

At the time of the writing of this thesis, some of the enthusiasm and optimism that accompanied the development of quantum mechanics in the early 20th century seems to have come to life again. In contrast to the quantum effects exploited in the first quantum revolution, this time, the direct creation and manipulation of quantum states in well-controlled systems attracts attention. And in the form of devices using such quantum technology, quantum mechanics is once again on the brink of traversing from a research field of purely academic interest to the industrial world and thus also to everyday life. Efforts to promote quantum technology are mostly supported by public finance, but more strikingly an increasing number of multinational corporations and companies are also investing in their own programmes for developing commercial quantum devices, and some companies already sell complete solutions. The interest in quantum technology is focusing mainly on three topics: quantum sensing promises promises higher measurement sensitivities [4]; quantum communication offers secure cryptography [5]; and in

quantum computers and simulators, the strangeness of the quantum world can be harnessed to reach a computational power which surpasses that of classical computers [6, 7].

In this euphoric atmosphere with its focus on commercialisation of quantum phenomena, other research topics in quantum physics, no less fascinating than the ones listed above, should not be neglected. Many splendid achievements in the field have been made without any thoughts of marketability in mind and impress the observer because of the sheer beauty of the results, the ingenuity of the measurement schemes, or simply because they can attain what had been deemed impossible a hundred years ago. For instance, cavity quantum electrodynamics (CQED) describes the interaction of quantised matter and light in an optical resonator, or cavity. Although the field also has applications in the context of quantum technology, e.g., as a quantum interface, CQED is distinguished by its conceptually simple models of single atoms interacting with single photons.

One of the earliest exemplary systems for CQED experiments consists of Rydberg atoms flying through superconducting cavities and interacting with the cavities' microwave fields [8]. In these experiments, detecting the state of the atoms allowed the experimenters to extract information about the state of the cavity field, which has imprinted some of its properties onto the atom during the interaction. In this way, it was possible to observe for the first time unequivocally the graininess of the quantised cavity light field as a superposition of states with different numbers of photons [9]. Multiple outstanding experiments followed, including further measurements of the cavity field and feedback to the cavity field state [10, 11].

In parallel with experimental progress in atomic systems, solid state quantum electrodynamic systems were developed. These platforms employ superconducting quantum bits based on Josephson junctions and microwave cavities and quickly caught up with the more "traditional" way of quantum optics experiments. For instance, in the early 2000s, such a system was used to measure the energy shift induced by cavity photons [12, 13].

All of these experiments used methods based on the dispersive, i.e., non-resonant interaction between two-level systems and the electric field of microwave resonators. The goal of the project presented in the thesis at hand consisted in transferring these methods to the optical domain, and in using them to analyse photon statistics in our CQED setup, which is based on an optical resonator and and ion trap. This transfer on the one hand allows cross-platform validation of fundamental physical phenomena, i.e., observation of the same effect in different systems. On the other hand, such an analyser can also be useful in future quantum network applications for evaluating the performance of photonic channels between network nodes. Finally, in a modified setup, the use of such techniques will allow the generation of non-classical cavity field states, which can then be transferred between network nodes and thus be investigated in a coupled cavity system (see Section 5.5).

This thesis is structured as follows: Chapter 2 starts with a short history of CQED, including the contributions from Innsbruck, and an outlook on future experiments in Innsbruck in Chapter 2. Chapter 3 follows with the theory foundations necessary for understanding our experimental system. The experimental setup is described in detail in Chapter 4, and the experiment in the dispersive ion-cavity coupling regime is described in Chapter 5. The main part of the thesis closes with Chapter 6, on simulations and proposals for future experiments. Finally, the appendix contains additional information, e.g., on uncertainty calculations and on how the setup was rebuilt.

Chapter 2

CQED: its history and how it shaped our experiment

Von wannen kommt dir diese Wissenschaft?

– F. Schiller, Die Jungfrau von Orleans

This chapter contains a brief historical overview of cavity quantum electrodynamics both in worldwide research groups and in Innsbruck. The purpose of this chapter is to provide the reader with a background in CQED and to show how existing results helped us to plan and execute the experiment described in Chapter 5. For more details on the history of CQED, the reader is referred to review articles such as, e.g., References [14, 8, 15–17].

2.1 Cavity QED: a synopsis

Cavity quantum electrodynamics can be defined as the section of physics that investigates the interaction between quantised matter and the quantised electromagnetic field inside resonators or cavities. Depending on the system, the cavity can for instance consist of two mirrors that are aligned such that electromagnetic waves are reflected back and forth between them, until the light gets absorbed in the mirrors, leaks through the mirrors due to their imperfect reflectivity, or gets scattered out. In other systems using microwaves, it can simply consist of an LC-circuit. The quantised matter system or qubit can consist of atoms, ions, molecules, or solid state systems. Such CQED systems make it possible to investigate the quantised interaction between electromagnetic fields and matter at a very fundamental level.

The beginnings of CQED as a research field can be dated to a short publication by E. M. Purcell in 1946 [18]. In this report, the author noted that the spontaneous emission of a spin in a magnetic resonance setup is modified because the resonator increases the density of modes the spin can couple to. More specifically, a spin that is prepared in a state with higher energy than the ground state was observed to decay faster to the ground state when coupled to the resonator.

In the following decades, many researchers investigated this effect, i.e., the modification of the mode density of the electromagnetic field by surfaces or mirrors. For example, the modification of spontaneous emission was observed in systems such as Rydberg atoms in microwave cavities [19, 20]. Rydberg atoms are atoms whose valence electron is excited to high principal quantum numbers and therefore exhibit large electric dipole moments, leading to a strong

interaction with the cavity field. Both the enhancement and the inhibition of the spontaneous emission were observed, with the specific effect depending on the frequency difference of the cavity and atom resonances. In these experiments, the transition frequency of the Rydberg atoms and consequently also the resonance frequency of the cavity were in the microwave domain. The same effects were however also observed with atoms interacting with cavities in the infrared part of the spectrum [21–23].

The next, important step in CQED, facilitated by the progress in laser cooling, was the observation of collective strong coupling between atoms and light in resonators. In the strong coupling regime, the characteristic rate of energy exchange between cavity field and atoms is larger than dissipation rates like atomic spontaneous emission of energetically higher lying states or the decay of light fields out of the cavity due to imperfect reflectivity of the resonator mirrors. The signature of this strong interaction consists in the observation of a splitting of the frequency spectrum of the resonator: Instead of a single transmission peak, which is observed if the frequency of electromagnetic fields sent through an empty resonator is varied, the transmission spectrum of a strongly coupled qubit-resonator system exhibits two peaks, whose splitting is directly related to the interaction strength. This effect is called vacuum Rabi splitting and was observed in systems with multiple atoms coupled to cavities either in the microwave or the optical domain in the late 1980s and early 1990s [24, 25].

A second effect indicating the collective strong interaction of atoms with resonator fields is the vacuum Rabi oscillation. This complementary effect to the vacuum Rabi splitting in the time domain consists of the periodic energy exchange between the cavity field and the atoms: Atoms which are coupled to a resonator and initially prepared in the excited state will emit energy into the resonator field, but reabsorb the energy after a characteristic time determined by the coupling strength. This process will continue until it is damped out by dissipation. Experiments in the microwave and the optical domain observed these effects [26, 27].

While these experiments showed collective effects, the goal of reaching the fundamental limit of a single atom interacting with the quantised electromagnetic field of a resonator was not reached until the end of the last century. Once again, progress in laser cooling and trapping of atoms finally enabled experimenters to reach this regime [28]: First observations of vacuum Rabi splitting and Rabi oscillations were reported around the turn of the century, including both experiment with single atoms flying through the field of a resonator [29, 9, 30, 31], and experiments with atoms trapped inside the resonator field [32, 33]. Note that there had been experiments with single trapped electrons and ions before, but none with single trapped two-level systems coupled to a cavity. Further progress with single atoms followed: Researchers investigated, e.g., the statistics of photons emitted by atoms into the resonator [34, 35], or the generation of single photons on demand by controlling the state of an atom coupled to a resonator with a laser [36–40].

These experiments had been done with neutral atoms. However, around the same time, electromagnetic traps for ions started to be used in CQED experiments, e.g., in H. Walther's group or in Innsbruck. Ion traps had been around for some time before these experiments [41]. Beside their original use as mass filters for charged particles, they later enabled the first observations of single particles such as electrons or ions with implications for, e.g., spectroscopy: Instead of averaging over multiple particles, using these traps, the properties of single particle can be measured precisely, and the individual states of ions can be controlled. Such trapped-ion systems are nowadays, e.g., used as optical clocks [42]. Because the quantum state of ions

in electromagnetic traps can be controlled very well and different ions can be coupled via the Coulomb force, such systems are also employed very successfully for quantum computing and simulation.

In the first ion-trap–cavity experiments, researchers investigated for instance the use of ions for probing the electromagnetic field of the cavity [43], or for the generation of single photons with arbitrary temporal shape [44]. The field of ion-trap–CQED has progressed significantly in the last two decades, with experiments covering such different topics as, e.g., using the cavity for cooling the ion [45], for photon collection [46], or for investigating the interaction between large Coulomb crystals of ions with the cavity mode [47]. Other experiments focused on the integration of cavities based on optical fibres with ion traps [48]. Due to the stronger confinement of the electromagnetic field in a smaller volume, the coupling strength of the light field with matter can be enhanced in such systems. Results in this sub-field include, e.g., the coupling of single and multiple ions to fibre cavities [49–51]

Besides neutral atoms and trapped ions, other systems have become available for CQED experiments within the last decades, based on solid-state devices: Quantum dots positioned in cavities are mainly designed for the use as single-photon sources. On the other hand, there are systems with superconducting qubits, coupled to microwave resonators [52, 53]. Superconducting qubits are based on the quantisation of charges, currents, or fluxes in Josephson junctions, i.e., the transition between normal conducting and superconducting materials. Using such systems, a wide range of experiments has been conducted, reaching from fundamental topics such as the vacuum Rabi splitting [54] to the engineering of complicated cavity field states [55].

While many experiments in CQED to date have investigated physics questions at the fundamental level of the interaction between single quanta of light and matter, researchers are nowadays also using more application-driven approach to CQED: Cavities and qubits can be used as a quantum interface for linking stationary matter qubits and travelling photons [56, 16, 17]. Such systems can be used in a quantum network, i.e., a set of matter qubits, linked by photon channels. Applications of quantum networks are found in quantum communication or larger-scale quantum computation. The challenges of this field lie in connecting several such systems to build larger networks and to demonstrate the advantage of quantum networks in quantum communication and computation.

Still, fundamental physics questions remain important: Researchers are, e.g., investigating collective quantum phenomena such as the use of CQED systems as sources of quantum states of the electromagnetic field with a specific number of n photons, or the use of a single atom for generating coupling between different light fields in a cavity [57, 58]. In Innsbruck, research in CQED was mainly focused on quantum networking applications, as described in the following section. However, the work described in this thesis is concerned with a more fundamental topic.

2.2 CQED in Innsbruck

The first efforts of building a CQED experiment in Innsbruck go back to the time of C. Roos' PhD work [59]. In his thesis, C. Roos described a first CQED setup, which combined a cavity at 729 nm with an ion trap for $^{40}Ca^{+}$ ions. However, due to several technical problems the experiment was not successful: The voltages applied to the cavity mirror piezos for controlling the cavity resonance frequency via the cavity length negatively influenced the trapping potential

for the ions, and in addition, ion lifetimes were too short. A second version was then built during A. Mundt's thesis work [60]. With this setup, the excitation of the ion on its quadrupole transition via the cavity field was investigated as a function of the cavity frequency and of the position of the ion in the standing wave [61]. Furthermore, the dependence of the coupling to the ion's motional sidebands was investigated as a function of the position of the ion in the cavity mode. During the thesis work of the following PhD student A. Kreuter [62], the modulation of the lifetime of the $3^2D_{5/2}$ states in $^{40}Ca^+$-ions was measured as a function of the position of the ion in the cavity standing wave [63]. This work can be seen as an analogy of the early CQED experiments concerned with the enhancement and inhibition of spontaneous emission.

The setup used during that time had a rather low coupling of the ion to the cavity field and it was difficult to control the relative positioning of ion and cavity. Therefore, a new setup[1] based on a linear Paul trap was built during C. Russo's PhD research [64]. This setup was designed for the dipole transition at 854 nm in $^{40}Ca^+$ and with some modifications was also used for the experiment described in this thesis. The first results of experiments in the new machine, obtained during C. Russo's and H. Barros' PhD work, include the demonstration of a deterministic single-photon source [65, 66], similar to experiments using neutral atoms in cavities. The statistics of the photon stream generated depend on the drive laser parameters, exhibiting a threshold behaviour similar to a laser [67, 68].

In the following years, during A. Stute's [69, 70] and B. Casabone's PhD work [71], we further optimised the setup and used it for two schemes in the context of quantum networking: Entanglement between the electronic state of a single trapped ion and the polarisation of a single photon, tunable in amplitude and phase, was generated with high fidelity [72], and the quantum state of a single trapped ion was mapped onto the polarisation state of a cavity photon with high fidelity [73] via cavity-mediated Raman transitions. Further experiments include the generation of entanglement between two ions in the same trap, heralded by photon detection [74], and the use of a two-ion entangled state for an improved quantum interface [75]. During most of these experiments I was already part of the CQED team in Innsbruck. Future experiments topically connected to quantum networking are outlined in Chapter 6 of my thesis. In addition to these proposals, the mid-term goal of experimental CQED in Innsbruck consists in connecting the three existing setups in a small quantum network.

However, in the following years, during my PhD research, the setup was rebuilt (see Appendix B) and characterised in preparation for the experiment described in Chapter 5 of this thesis. This experiment is thematically closer to fundamental quantum optics than to quantum networking. It was planned to a large part by postdoc M. Lee, inspired by experiments in the microwave domain of CQED: We investigated the interaction between the ion qubit and the cavity field in a dispersive regime, i.e., in a regime, where the quanta of the light field cannot be absorbed by the qubit because of a frequency mismatch between the two. Instead, the qubit introduced into the cavity field can be seen as a modification of the refractive index experienced by the light field, or in a complementary picture, the cavity field introduces a phase shift of the qubit's quantum state. Such experiments have been executed before with either highly excited Rydberg atoms or superconducting quantum bits as qubits and resonators at microwave frequencies.

In these previous experiments, the phase shift that the qubit experienced due to the cavity

[1] Note, that two more CQED setups exist in Innsbruck, one based on a fibre cavity, and one optimised as a quantum interface in B. Lanyon's group.

field was measured, making it possible to infer the number of photons, i.e., excitation of the cavity fields [76, 77]. This technique made it possible to investigate the photon statistics of the quantised cavity field states by using the qubit as a probe [78, 13, 79, 10, 80]. We transferred the measurement method employed in these experiments for the first time to a CQED system with an optical cavity.

Chapter 3

How to model ions in cavities: a theoretical description

Die Theorie an und für sich ist nichts nütze, als insofern sie uns an den Zusammenhang der Erscheinungen glauben macht.

– J. W. von Goethe, Wilhelm Meisters Wanderjahre

This chapter gives an overview of the relevant theory background for the setup described in Chapter 4 and the experiment described in Chapter 5. After an introduction on ion trapping in Paul traps, the basics of quantum information are explained. A description of light-matter interaction follows with special focus on cavities and cavity quantum electrodynamics.

3.1 Trapping ions in radiofrequency traps

This section gives a summary of the working principle of Paul traps. More extensive treatment of the matter can be found, e.g., in References [41, 81–85] or in doctoral theses published previously in the field, e.g., in References [86–88]. Paul traps were initially developed for mass spectrometry. They employ quadrupole electromagnetic fields for dynamic confinement of charged particles. The field is generated by hyperbolic electrodes, which are however usually approximated by electrodes with circular cross section for reasons of easier machinability.

In our experiment, a linear Paul trap is used, shown in Figure 3.1. The trap consists of four blades at angles of $90°$ between neighbouring ones and two endcaps at the ends of the trap axis. By applying a voltage $V_{\mathrm{RF}} \cos(\Omega_{\mathrm{RF}} t)$, oscillating at radiofrequency ω_{RF}, to one pair of opposite blades and grounding the other, and a DC voltage U_{DC} to the endcaps, it is possible to generate a quadrupole potential at the trap centre of the form

$$\Phi(\mathbf{r}, t) = \frac{V_{\mathrm{RF}}}{2} \cos(\Omega_{\mathrm{RF}} t) \left(\alpha_1 x^2 + \alpha_2 y^2 + \alpha_3 z^2\right) + \frac{U_{\mathrm{DC}}}{2} \left(\alpha_1' x^2 + \alpha_2' y^2 + \alpha_3' z^2\right). \tag{3.1}$$

The geometric factors α_i and α_i' describe how well the potential matches the ideal quadrupole and therefore depend on the shape of the ion trap electrodes and the trap geometry in general [85].

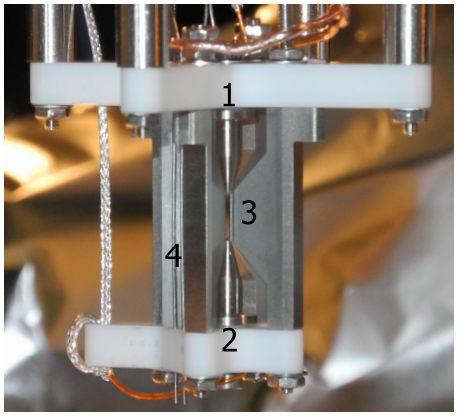

Figure 3.1: Linear Paul trap used in our experiment, consisting of two endcaps (1 and 2) on the trap axis, blades (3) for confinement in the plane perpendicular to the trap axis, and compensation electrodes (4). For trapping, a DC potential is applied to the endcaps, and radiofrequency voltages are applied to one pair of opposite blades, while the second pair is grounded. The compensation electrodes are used for compensating the influence of electric stray fields.

Since the Laplace equation $\Delta\Phi = 0$ has to be fulfilled for every time t, the geometric factors have to satisfy the following conditions:

$$\sum_i \alpha_i = 0, \quad \sum_i \alpha'_i = 0$$

For linear Paul traps, one chooses $\alpha := \alpha_1 = -\alpha_2 = 1/r_0^2, \quad \alpha_3 = 0$ and $-(\alpha'_1 + \alpha'_2) = \alpha'_3 = 1/z_0^2$, where $2r_0$ is the distance between the opposite RF electrodes and $2z_0$ that between the two endcaps [83]. In this case, the trapped particles are confined along the trap axis via the DC potential and in the plane perpendicular to the trap axis (the radial plane) via the radiofrequency potential.

Starting from the general potential of Equation 3.1, the equations of motion $m\ddot{\mathbf{r}} = Q\mathbf{E}$ for a trapped particle of mass m and charge Q in the electric field $\mathbf{E} = -\boldsymbol{\nabla}\Phi$ can be written as:

$$\begin{aligned} m\ddot{\mathbf{r}} &= Q\mathbf{E} = -Q\boldsymbol{\nabla}\Phi\left(\mathbf{r}, t\right) \\ \ddot{r}_i &= \frac{Q}{m}\left[V_{\text{RF}}\,\alpha_i \cos\left(\Omega_{\text{RF}} t\right) + U_{\text{DC}}\,\alpha'_i\right] r_i, \quad i = 1, 2, 3. \end{aligned}$$

Using the substitutions

$$\begin{aligned} \tau &= \frac{1}{2}\Omega_{\text{RF}} t \\ a_i &= \frac{4Q\,U_{\text{DC}}\,\alpha'_i}{m\Omega_{\text{RF}}^2} \\ q_i &= -\frac{2Q\,V_{\text{RF}}\,\alpha_i}{m\Omega_{\text{RF}}^2}, \end{aligned}$$

the equations of motion can be cast in the form of the canonical Mathieu equations [89]

$$\frac{\mathrm{d}^2 r_i}{\mathrm{d}\tau^2} + \left[a_i - 2q_i \cos(2\tau)\right] r_i = 0, \quad i = 1, 2, 3.$$

Note, that in the parameters a_i and q_i the length unit in the denominator is hidden in the geometric factors α_i and α_i'. The Mathieu equations can be solved using Floquet theory and yield recursive relations for a_i and q_i for which the particle trajectories are stable. In the lowest approximation – and considering only x since the coordinates are decoupled – the trajectory of the trapped particle is given by

$$x(t) \propto \cos\left(\beta_1 \frac{\Omega_{\text{RF}}}{2} t\right) \left[1 - \frac{q_1}{2} \cos\left(\Omega_{\text{RF}} t\right)\right],$$

where $\beta_1 \approx \sqrt{a_1 + q_1^2/2}$. The particle oscillates with the so-called secular frequency

$$\omega_1 = \beta_1 \Omega_{\text{RF}}/2, \tag{3.2}$$

but its motion is modulated at the original RF frequency. Note, that this frequency grows linearly with the RF voltage but as the square root of the DC voltage.

The residual modulation at the RF frequency is called micromotion. Minimising the amplitude of this motion is necessary for several reasons: Micromotion can modify the line shape of atomic transitions or shift atomic transitions via the AC-Stark effect which is detrimental to both cooling and precision spectroscopy [90], and – in the case of a CQED experiment – it increases the ion's spatial extent such that the coupling to the cavity is reduced by averaging over the standing wave of the cavity mode (see also Section 4.5). In our setup, the effect of micromotion is minimised by pushing the ion into the RF null at the trap centre by applying voltages to compensation electrodes. If micromotion is compensated, the trap can be approximated by a harmonic potential. The same result can be derived from a pseudopotential approximation [91].

3.2 How to manipulate quantised matter with light

3.2.1 Qubits and their manipulation

In quantum computation[1], the smallest unit of information is a quantum bit, or qubit. A qubit is encoded in two states $|0\rangle$ and $|1\rangle$ of a quantum system, e.g., in two electronic states of an atom, ion or solid-state system; in the polarisation or time bin of a single photon; or in the charge or phase of superconducting devices. An arbitrary state of the qubit can be written in a two-dimensional complex Hilbert space $\mathcal{H}_2$ as

$$|\psi\rangle = \cos(\theta)\,|0\rangle + e^{i\phi}\sin(\theta)\,|1\rangle$$

with two parameters $\theta, \phi \in \mathbb{R}$. The state $|\psi\rangle$ is normalised, i.e., the inner product with itself is one,

$$\langle\psi|\,\psi\rangle = 1,$$

and the orthonormal basis states are defined as

$$|0\rangle = \begin{pmatrix} 1 \\ 0 \end{pmatrix}, \quad |1\rangle = \begin{pmatrix} 0 \\ 1 \end{pmatrix}.$$

[1] See, e.g., Reference [6] for a more complete description of quantum information.

Section 4.2 describes how $^{40}Ca^{+}$-ions can be used as quantum bits.

Unitary operations on the qubit can be parametrised in terms of the Hermitian Pauli operators

$$\sigma_x = \begin{pmatrix} 0 & 1 \\ 1 & 0 \end{pmatrix}, \quad \sigma_y = \begin{pmatrix} 0 & -i \\ i & 0 \end{pmatrix}, \quad \sigma_z = \begin{pmatrix} 1 & 0 \\ 0 & -1 \end{pmatrix}.$$

Any unitary manipulation of the qubit can then be described by concatenating at most three of the following unitary operators and applying them to the qubit state:

$$U_z(\theta) = \exp\left(-i\frac{\theta}{2}\sigma_z\right), \quad U_\phi(\theta) = \exp\left(-i\frac{\theta}{2}\sigma_\phi\right),$$

where $\sigma_\phi = \cos(\phi)\,\sigma_x + \sin(\phi)\,\sigma_y$, and ϕ parameterises the angle of the rotation axis in the x-y plane. In the experiment, these rotations are implemented via laser pulses with a certain intensity, duration, and phase.

A typical rotation consists, e.g., in a simple rotation of the qubit from state $|0\rangle$ into state $|1\rangle$. The corresponding rotation operator is given by $U_{\phi=0}(\theta = \pi)$, i.e., a rotation with Pauli matrix σ_x. Such a rotation can be used in spectroscopy for probing the qubit transition: By measuring how well the qubit is transferred into state $|1\rangle$ as a function of the frequency of the light pulse, th experimenter can tune the light frequency on resonance with the qubit transition.

In a more complicated experiment, the rotation of the qubit from $|0\rangle$ to $|1\rangle$ is split into two rotations in what is known as a Ramsey experiment [92, 93][2]: The first rotation is given by $U_{\phi=0}(\theta = \pi/2)$, and the second by $U_\phi(\theta = \pi/2)$ with variable phase ϕ. These rotations are separated by a time delay T, and due to the time-energy uncertainty relation [95] this measurement scheme allows the experimenter to measure the frequency of the qubit transition with higher precision. Any interaction of the qubit with fields that happens during the time delay T will influence the result of such a measurement. We therefore use such a Ramsey-type measurement for investigating the interaction of a qubit with the electromagnetic field of an optical cavity, as described in Chapter 5

The state $|\psi\rangle$ considered so far is a pure state, which is a valid description only if the system under investigation only undergoes unitary evolution. For describing the more realistic case of an open system[3], the density operator ρ is defined. The density operator in fact describes a statistical mixture of quantum states which are in pure states $|\psi_i\rangle$ with probabilities $0 \leq p_i \leq 1$ and normalisation $\sum_i p_i = 1$:

$$\rho = \sum_i p_i\, |\psi_i\rangle\langle\psi_i|$$

This operator can be interpreted as a description of either an ensemble of identical quantum systems which are not all prepared in the same state but in a mixture of states, or as a way to include the imperfect knowledge about the state of a single quantum system in its description.

Normalisation in the case of the density matrix translates into the condition $\mathrm{Tr}[\rho] = 1$ with the trace operation $\mathrm{Tr}[\cdot]$. The density matrix is Hermitian, i.e., its eigenvalues are real: The diagonal elements ρ_{ii} are the probabilities p_i to find the system in the basis state $|\psi_i\rangle$ while the off-diagonal elements ρ_{ij} $(i \neq j)$ describe the quantum coherences, i.e., phase relations between the basis states.

[2] See also, e.g., chapters 19 and 20 in Reference [94], or chapter 3.3.3 in Reference [8].

[3] See Reference [96] on open system dynamics.

Using the Bloch model, the density matrix of a qubit can also be written in terms of the Pauli operators as

$$\rho = (\mathbb{1} + \mathbf{B} \cdot \boldsymbol{\sigma})/2, \tag{3.3}$$

where $\mathbf{B}$ is the Bloch vector and $\boldsymbol{\sigma} = \sum_{i=1}^{3} \sigma_i \hat{e}_i$ is a vector of the Pauli matrices. The Bloch vector thus contains the full information about the quantum state and can be written in polar coordinates as $\mathbf{B} = \mathbf{B}(|\mathbf{B}|, \theta, \phi)$. Single qubits can then, e.g., be drawn as vectors on the so-called Bloch sphere, which has unity radius. Pure states have a Bloch vector extending to the surface of the sphere, while the Bloch vector of mixed states ends inside the volume of the sphere. Unitary operations on the qubit correspond to rotations of the Bloch vector on the Bloch sphere.

If a quantum system consists of multiple subsystems (qubits), the total density matrix $\rho_{\text{tot}} = \otimes_i \rho_i$ lies in the product space $\mathcal{H}_{\text{tot}} = \otimes_i \mathcal{H}_{2,i}$ of the individual subspaces $\mathcal{H}_{2,i}$. For such systems, the total state $|\Psi\rangle$ can either be written as the product of independent states of the N subsystems, $|\Psi\rangle = |\psi_1\rangle \otimes ... \otimes |\psi_N\rangle$, or the state is entangled, i.e., not separable. For instance, the two-particle entangled state $|\Psi\rangle = (|0\rangle \otimes |1\rangle + |1\rangle \otimes |0\rangle)$ cannot be written as the tensor product of two superposition states of qubit 1 and qubit 2. Entangled states exhibit quantum correlations in more than one basis. In ion traps, entangled states between can be generated, e.g., via the Mølmer-Sørensen gate [97–99], which makes use of the common motion of ions in the trapping potential due to their coupling via Coulomb forces. The entanglement of two qubits can, e.g., be quantified via the concurrence [100, 101], which is a monotonic measure of entanglement, with a concurrence of 0 corresponding to a separable state and a concurrence of 1 to a maximally entangled state.

The unitary time evolution of the system is described by its Hamilton operator (or Hamiltonian) H, which describes the energy in the system. The system evolution in the Schrödinger picture is determined by the von Neumann equation for the density operator, which is equivalent to the Schrödinger equation for a pure state:

$$\frac{\mathrm{d}\rho}{\mathrm{d}t} = -\frac{i}{\hbar}[H, \rho],$$

where $[\cdot, \cdot]$ stands for the commutator. If the system undergoes non-unitary evolution, the Lindblad equation[4] is used, which is a quantum master equation in Markov approximation [96]:

$$\frac{\mathrm{d}\rho}{\mathrm{d}t} = -\frac{i}{\hbar}[H, \rho] + \sum_i \gamma_i \left(L_i \rho L_i^\dagger - \frac{1}{2} L_i^\dagger L_i \rho - \frac{1}{2} \rho L_i^\dagger L_i \right).$$

Here, interaction with the environment is described by jump operators L_i, which describe the non-unitary interaction between the system described by ρ and the environment. Examples for jump operators are atomic decay operators or photon annihilation operators, which act on the system with rates γ_i (e.g., spontaneous emission rates or photon loss rates of a cavity). This equation can be integrated numerically in order to calculate the time evolution of the density operator. The Lindblad equation is used for reconstructing the photon number distribution of the cavity field in the experiment described in Chapter 5.

[4] This equation is also termed Gorini-Kossakowski-Sudarshan-Lindblad equation.

3.2.2 Light-matter interaction

This section contains a description of light-matter interaction in a semi-classical model and the interaction between a two-level system with a harmonic oscillator. A good overview of the topic is provided by, e.g., References [94, 83].

Minimal coupling and Rabi oscillations

The Hamiltonian describing the energy of a quantum system is given by

$$H_0 = \frac{\boldsymbol{p}^2}{2m} + V(\boldsymbol{r}),$$

where $\boldsymbol{p} = -i\hbar\boldsymbol{\nabla}$ is the quantum mechanical momentum operator and $V(\boldsymbol{r})$ is a potential. The interaction of this system with an electromagnetic field corresponding to a vector potential $\boldsymbol{A}(\boldsymbol{r},t)$ and a scalar potential $\Phi(\boldsymbol{r},t)$ is then given via minimal coupling[5] as

$$H = \frac{1}{2m}\left[\boldsymbol{p} - q\boldsymbol{A}(\boldsymbol{r},t)\right]^2 - q\Phi(\boldsymbol{r},t) + V(\boldsymbol{r}),$$

where q is the charge of the quantum system. The electric and magnetic fields follow as $\boldsymbol{E}(\boldsymbol{r},t) = -\boldsymbol{\nabla}\Phi(\boldsymbol{r},t) - \frac{\partial A(\boldsymbol{r},t)}{\partial t}$ and $\boldsymbol{B}(\boldsymbol{r},t) = -\boldsymbol{\nabla}\times\boldsymbol{A}(\boldsymbol{r},t)$. In the dipole approximation, the spatial extent of the quantum system is small with respect to the wavelength λ of the electromagnetic radiation:

$$\boldsymbol{k}\cdot\boldsymbol{r} \ll 1,$$

with the wave vector $\boldsymbol{k}$. Using the Coulomb (or radiation) gauge

$$\boldsymbol{\nabla}\cdot\boldsymbol{A}(\boldsymbol{r},t) = 0, \quad \Phi(\boldsymbol{r},t) = 0,$$

we now choose a gauge transformation of $\chi(\boldsymbol{r},t) = -\boldsymbol{A}(\boldsymbol{r},t)\cdot\boldsymbol{r}$, which leaves $\boldsymbol{E}$ and $\boldsymbol{B}$ invariant. The transformed vector and scalar potentials now read

$$\begin{aligned}\boldsymbol{A'}(\boldsymbol{r},t) &= \boldsymbol{A}(\boldsymbol{r},t) + \boldsymbol{\nabla}\chi(\boldsymbol{r},t) = 0,\\ \boldsymbol{\Phi'}(\boldsymbol{r},t) &= \boldsymbol{\Phi}(\boldsymbol{r},t) - \frac{\partial\chi(\boldsymbol{r},t)}{\partial t} = -\boldsymbol{r}\cdot\boldsymbol{E}(\boldsymbol{r},t).\end{aligned}$$

Accordingly, the Hamiltonian becomes

$$H = \frac{\boldsymbol{p}^2}{2m} + V(\boldsymbol{r}) - \boldsymbol{d}\cdot\boldsymbol{E},$$

with the dipole operator $\boldsymbol{d} = q\boldsymbol{r}$. We assume the electric field has the form

$$\boldsymbol{E} = E_0\cos\left(\omega_{\mathrm{L}}t + \phi\right)\boldsymbol{e},$$

with amplitude E_0, angular frequency ω_{L}, phase ϕ, and direction $\boldsymbol{e}$, where the spatial dependence has been neglected due to the dipole approximation. Because the dipole operator only

[5] See, e.g., chapter 5 of Reference [94].

has off-diagonal components due to a parity argument, we can then write the interaction part of the Hamiltonian as

$$H_1 = -\Omega\hbar\cos\left(\omega_L t + \phi\right)\sigma_x,$$

with the Rabi frequency $\Omega = E_0\langle 0|\,\boldsymbol{d}\cdot\boldsymbol{e}\,|1\rangle$.

By transforming the total Hamiltonian $H_0 + H_1$ into an interaction picture with respect to H_0, applying a rotating wave approximation at the light frequency ω_{L}, and using raising and lowering operators $\sigma_\pm = (\sigma_x \pm i\sigma_y)$, one finds the interaction Hamiltonian

$$H_{\mathrm{int}} = \frac{1}{2}\hbar\Omega\Big[\exp\big(-i\left(\Delta t+\phi\right)\big)\sigma_+ + \exp\big(i\left(\Delta t+\phi\right)\big)\sigma_-\Big]. \tag{3.4}$$

Here, $\Delta = \omega_{\mathrm{L}} - \omega_0$ is the detuning of the laser from the qubit transition frequency ω_0. On resonance, this Hamiltonian corresponds to a unitary operation on the two-level system of

$$\mathcal{U}(\phi,t) = \begin{pmatrix} \cos(\Omega t) & -ie^{-i\phi}\sin(\Omega t) \\ -ie^{i\phi}\sin(\Omega t) & \cos(\Omega t)\end{pmatrix}.$$

The rotation angle is determined by the Rabi frequency Ω and the pulse duration T, while the axis around which the qubit is rotated on the Bloch sphere is set by the angle ϕ.

Calculating the system evolution under continuous driving with the laser, one finds that the two-level system's state periodically changes between the two states in so-called Rabi oscillations. If the system was initially prepared in the energetically lower state, the probability to find the system in the excited state at time t is given by

$$p_{\mathrm{exc}}(t) = \frac{\Omega^2}{\Omega^2+\Delta^2}\,\sin\left(\frac{1}{2}\sqrt{\Omega^2+\Delta^2}\,t\right).$$

If the laser is detuned from resonance ($\Delta \neq 0$), the oscillations are faster, but their amplitude is reduced.

In the case of $\Delta \gg \Omega$, the probability for exciting the system from the energetically lower state to the higher state approaches zero, but the levels experience a shift in energy: the so-called AC-Stark shift. The upper level and the lower level will each be shifted by an amount

$$\Delta E = \frac{\hbar\Omega^2}{4\Delta},$$

such that the transition frequency is changed by $\Omega^2/(2\Delta)$. If the laser is red-detuned from the transition ($\Delta < 0$), the upper level will be shifted to a higher energy and the lower level to a lower energy. In the experiment described in Chapter 5, the AC-Stark shift experienced by an ion and caused by the photons in the cavity field is used to extract information about the cavity field itself.

Interaction of a two-level system and a harmonic oscillator

In this subsection, we consider the interaction between a two-level system and a quantum harmonic oscillator. This is relevant for, e.g., the description of quantised motion of ions in harmonic trapping potentials or the interaction between a qubit and the quantised field of an optical

resonator. The classical Hamiltonian for a one-dimensional harmonic oscillator with mass m and frequency ω is given by

$$H_{\text{class}} = \frac{p^2}{2m} + \frac{1}{2}m\omega^2 x^2,$$

where p is the momentum of the oscillator and x its displacement. The quantum mechanical Hamiltonian is obtained via the canonical quantisation $x \mapsto \hat{x}$, $p \mapsto \hat{p} = -i\hbar\boldsymbol{\nabla}$. By introducing the ladder operators $\hat{a}$ and $\hat{a}^\dagger$ as

$$\hat{a} = \frac{1}{2x_0}\left(\hat{x} + \frac{i}{m\omega}\hat{p}\right), \qquad \hat{a}^\dagger = \frac{1}{2x_0}\left(\hat{x} - \frac{i}{m\omega}\hat{p}\right),$$

with $[a, a^\dagger] = 1$ and the ground state extent $x_0 = \sqrt{\hbar/(2m\omega)}$, the position and momentum operators take the form

$$\hat{x} = x_0\left(\hat{a} + \hat{a}^\dagger\right), \qquad \hat{p} = \frac{i\hbar}{2x_0}\left(\hat{a}^\dagger - \hat{a}\right).$$

The Hamiltonian follows as[6]

$$H = \hbar\omega\left(a^\dagger a + \frac{1}{2}\right).$$

Here, the number operator $a^\dagger a$ counts the number of excitations in the system.

It is convenient to define the states of the system in the number (or Fock state) basis $\{|n\rangle, n \in \mathbb{N}\}$. The lowest state $|0\rangle$ has the zero-point energy $\hbar\omega/2$, and the energy levels are separated by $\hbar\omega$. By applying the annihilation and creation operators a and $a^\dagger$, the states can be changed as

$$a^\dagger|n\rangle = \sqrt{n+1}\,|n+1\rangle, \quad a|n\rangle = \sqrt{n}\,|n-1\rangle, \quad a|0\rangle = 0.$$

A similar argument can be made in quantising the electromagnetic field[7]. In that case, a state $|n\rangle$ corresponds to n excitations of the vacuum state $|0\rangle$, or n photons. Light emitted by lasers can be described as coherent states $|\alpha\rangle$ [102], defined as

$$|\alpha\rangle = e^{-|\alpha|^2/2}\sum_{n=0}^{\infty}\frac{\alpha^n}{\sqrt{n!}}|n\rangle.$$

Coherent states are eigenstates of the annihilation operator: $a|\alpha\rangle = \alpha|\alpha\rangle$ and can be interpreted as superpositions of Fock states, with the probability of finding Fock state $|n\rangle$ given by the Poisson distribution

$$p(n) = |\langle n|a\rangle|^2 = e^{-\bar{n}}\frac{\bar{n}^n}{n!},$$

with mean photon number $\bar{n} = |\alpha|^2$. In the experiment described in Chapter 5, coherent states in the electromagnetic field of a cavity are interacting with a single trapped ion.

Returning once more to ions in harmonic traps, the concept of quantised motion can be used to find a description of the interaction between a two-level system coupled to a harmonic

[6] Circumflexes as markers of quantum mechanical operators are dropped from now on for convenience.

[7] Cf. chapter 1 of Reference [94].

oscillator and a coherent monochromatic light field, i.e., a laser beam, which is treated semi-classically. This interaction is relevant for laser cooling of ions, since the ions as two-level systems are trapped in a harmonic potential and their internal state can therefore couple to the quantised motion in the trap. The interaction Hamiltonian changes from Equation 3.4 to [83]

$$H_{\text{int}} = \frac{\hbar\Omega}{2}\Big[\exp\left(-i\left(\Delta t+\phi\right)\right)\,\sigma_+\exp\left[i\eta\left(ae^{-i\omega_{\text{L}}t}+a^\dagger e^{i\omega_{\text{L}}t}\right)\right]+\text{h.c.}\Big], \tag{3.5}$$

where h.c. stands for Hermitian conjugate. In this equation, η is the Lamb-Dicke parameter $\eta = k\,x_0\cos(\varphi)$, which describes the ratio between the ground-state extent of the oscillator x_0 and the wavelength of the driving light $2\pi/k$, and the laser beam propagates along a direction with angle φ with respect to the direction of oscillation. If the condition

$$\eta^2\left(2\bar{n}+1\right)\ll 1$$

is satisfied, the system is said to be in the Lamb-Dicke regime[8], and the Hamiltonian can be simplified by a Taylor expansion of the exponential, keeping only terms up to first order in η:

$$H_{\text{int}} \approx \frac{\hbar\Omega}{2}\Big[\exp\left(-i\left(\Delta t-\phi\right)\right)\,\sigma_+\left[\mathbb{1}+i\eta\left(ae^{-i\omega_{\text{L}}t}+a^\dagger e^{i\omega_{\text{L}}t}\right)\right]+\text{h.c.}\Big]$$

Spectroscopically, the qubit transition now exhibits three peaks: one so-called carrier transition on resonance, and two so-called sideband transitions at frequencies detuned by ω from the carrier transition (for $\Omega \ll \omega$). Driving the two-level system on resonance, i.e., on the carrier transition, one finds that the Rabi oscillations decay because the light is coupled to the different states of the harmonic oscillator and the effective coupling strength is now given by

$$\Omega_{n,n} = \Omega\left(1-\eta^2 n\right).$$

If the transition is driven on a sideband, the number of quanta in the harmonic oscillator is increased or decreased by one. For the red sideband, i.e., $\Delta = -\omega$, the Hamiltonian includes terms like

$$\eta\Omega_{n,n-1}a\sigma_+$$

and

$$\eta\Omega_{n,n-1}a^\dagger\sigma_-,$$

which correspond to the annihilation and creation of one quantum while the two-level system is excited and de-excited, respectively. This process happens at a modified Rabi frequency $\Omega_{n,n-1} = \eta\sqrt{n}\Omega$. For $\Delta = +\omega$, i.e., on the blue sideband, the opposite process happens with rate $\Omega_{n,n+1} = \eta\sqrt{n+1}\Omega$ and operators in the Hamiltonian of the form

$$\eta\Omega_{n,n+1}a^\dagger\sigma_+$$

and

$$\eta\Omega_{n,n+1}a\sigma_-.$$

The red sideband can be used for cooling of trapped ions close to the motional ground state (see Section 4.2.1). Note also, that the terms of the red sideband correspond to the Jaynes-Cummings Hamiltonian of cavity quantum electrodynamics (see Section 3.3), while the blue

[8] See also Appendix A.3 for Lamb-Dicke parameters in our setup.

sideband Hamiltonian or anti-Jaynes-Cummings Hamiltonian has no correspondence in cavity QED [103].

If the system is not in the Lamb-Dicke regime, higher-order terms in the Lamb-Dicke parameter become relevant. For example, the term in η^2 in Equation 3.5 (neglecting the phase terms) is given by

$$-\frac{\eta^2}{2}\left(a^\dagger + a\right)^2 = -\frac{\eta^2}{2}\left[aa + aa^\dagger + a^\dagger a + a^\dagger a^\dagger\right].$$

This term therefore corresponds to processes in which two phonons can be created or annihilated or in which one phonon is created and one annihilated. Accordingly, a prerequisite to reach the ground state via laser cooling is that the system has to be in the Lamb-Dicke regime, since otherwise the population of the motional quanta cannot be well controlled.

3.3 Cavity quantum electrodynamics

By coupling a quantum emitter to the light field of a resonator or cavity, the strength of the light-matter interaction introduced in Section 3.2 can be increased. Thus, it becomes easier to observe the influence that single quanta of light exert on the matter qubit. Such quantised cavity-mediated interactions are described by cavity quantum electrodynamics[9]. In this section, the properties of cavities are discussed, followed by a description of the paradigmatic Jaynes-Cummings model in the resonant and dispersive case. Please note that in the convention of Innsbruck cavity QED, which is used in this thesis, all rates are specified as half widths, i.e., the full spectral width of the cavity modes is 2κ, the full width of the atomic state is 2γ, etc.

3.3.1 Cavities: definition and properties

Optical cavities of the Fabry-Perot type [106, 107] consist of two planar or convex mirrors with field transmission, reflection, and loss coefficients t, r, l per mirror. The corresponding coefficients for the intensity are given by $\mathcal{T} = |t|^2, \mathcal{R} = |r|^2, \mathcal{L} = |l|^2$. The losses can be caused by absorption or scattering into free-space modes both in the medium between the mirrors or in the mirrors themselves. Because of energy conservation, the following equation has to hold for each mirror:

$$\mathcal{T} + \mathcal{R} + \mathcal{L} = 1 \tag{3.6}$$

Given mirrors with a radius of curvature R_i $(i = 1, 2)$ separated by a length L, stable modes exist between the mirrors only if the stability parameter

$$g_{\mathrm{st,i}} = 1 - \frac{L}{R_i}$$

fulfils[10]

$$0 \leq g_{\mathrm{st,1}} \cdot g_{\mathrm{st,2}} \leq 1,$$

[9] See References [8, 104, 105] for in-depth treatment of the matter covered in this section.

[10] Cf., e.g., chapter 9 of Reference [105].

During the rest of this section, we assume $R_1 = R_2 = R$, such that the $g_{\text{st},1} = g_{\text{st},2} = g_{\text{st}}$, and $0 \leq g_{\text{st}}^2 \leq 1$. In other words, the cavity length has to be finite but less than twice the radius of curvature. Special cases include the confocal cavity with $g_{\text{st}} = 0$, i.e., $R = L$; the planar cavity for $g_{\text{st}} = 1$; and the concentric cavity with $g_{\text{st}} = -1$, i.e., $2R = L$. The cavity in our setup operates in a near-concentric regime, i.e., $2R \lesssim L$ (cf. Section 4.4). This has the advantage of minimising the mode cross-section in the centre and hence maximising the coupling to the matter qubit (see Equation 3.9 below). The disadvantage of near-concentric cavities is that they are much harder to align, as they are operating very close to an instable regime.

The value of g_{st} also influences the spectrum of the cavity. Using Hermite-Gauss polynomials to solve the Helmholtz equation, the frequencies of transverse electromagnetic modes (TEM_{klm}) modes are given by[11]

$$\omega_{klm} = 2\pi\,\nu_{\text{FSR}}\left[k + 1 + \frac{l+m+1}{\pi}\arccos\left(g_{\text{st}}\right)\right]. \tag{3.7}$$

Here, the parameter k labels the longitudinal modes, l and m the transverse modes, and ν_{FSR} is the free spectral range (FSR), i.e., the separation between two adjacent longitudinal modes. In vacuum, the free spectral range only depends on the speed of light c and the cavity length L:

$$\nu_{\text{FSR}} = \frac{c}{2L},$$

which follows from the resonance condition that the light of wavelength λ build up a standing wave between the two resonator mirrors:

$$k\,L = n\pi \quad \text{or} \quad L = n\lambda/2,$$

with the wavenumber $k = 2\pi/\lambda$.

The intensity profile along the cavity axis (z-axis) is given by[12]

$$I(x) = I_0 \frac{\mathcal{T}}{(1-\mathcal{R})^2}\,\frac{1}{1 + \left(\mathcal{F}/\pi\right)^2 \sin^2(kL)}\cos^2(kz),$$

where I_0 is the intensity at the cavity input, and $\mathcal{F}$ is the finesse of the resonator. The finesse is related to the FSR and to the linewidth (full width at half maximum, FWHM) of the longitudinal modes, as well as to the quality factor Q:

$$\mathcal{F} = \frac{\nu_{\text{FSR}}}{\text{FWHM}} = \frac{\nu_0}{\nu_{\text{FSR}}}Q \approx \frac{\pi\sqrt{\mathcal{R}}}{1-\mathcal{R}}, \tag{3.8}$$

with the resonance frequency of the cavity ν_0. The quality factor describes the ratio of the energy stored in the resonator to the power loss of the resonator. The finesse is higher for lower resonator losses, and it describes the number of round trips a photon takes between the mirrors before it is lost from the resonator mode. For very high reflectivity $\sqrt{\mathcal{R}} \approx 1$, and using Equation 3.6, Equation 3.8 can be simplified to

$$\mathcal{F} \approx \frac{\pi}{\mathcal{T} + \mathcal{L}}.$$

[11] Cf. chapter 19.3 in Reference [104]

[12] Cf. chapter 9.1 of Reference [105].

The $1/e$-lifetime of light inside the cavity is also determined by the finesse:

$$\tau_\mathrm{c} = \frac{\mathcal{F}\, L}{\pi\, c},$$

i.e., cavities with high finesse store light longer since a high finesse means a high mirror reflectivity. The photon lifetime is directly related to the cavity decay rate[13] κ:

$$\kappa = \frac{1}{2\tau_\mathrm{c}}$$

Another important parameter for cavity QED is the coupling strength g between a dipolar emitter and the cavity field mode. For an atomic dipole transition with dipole moment $\boldsymbol{d}$ and the atom located at an antinode of the cavity the coupling strength is given by[14]

$$g = (\boldsymbol{d}\cdot\boldsymbol{E})/\hbar = \sqrt{\frac{3c\,\gamma\,\lambda^2}{L\,w_0^2\,\pi^2}}, \tag{3.9}$$

where $\Gamma = 2\gamma$ is the FWHM of the upper coupled atomic level (spontaneous emission rate), $\mathbf{E}$ the electric field at the antinode and w_0 the waist of the cavity mode. The waist is determined by the condition that the radii of curvature of the mode wavefront and the mirror have to be equal at the mirror, and is given by[15]

$$w_0^2 = \frac{\lambda\, L}{2\pi}\sqrt{\frac{1+g_\mathrm{st}}{1-g_\mathrm{st}}} = \frac{\lambda}{2\pi}\sqrt{L(2R-L)}. \tag{3.10}$$

At any given position along the cavity axis (z-axis), the beam radius can be calculated via Gaussian optics as

$$w(z) = w_0\sqrt{1+\left(\frac{z}{z_\mathrm{R}}\right)^2}$$

with the Rayleigh range

$$z_\mathrm{R} = \frac{\pi w_0^2}{\lambda} = \frac{1}{2}\sqrt{L(2R-L)}.$$

Both the cavity length L and the waist w_0 determine the mode volume V_{mn} of the cavity for a given TEM$_{mn}$-mode:

$$V_{mn} = V_0\cdot m!\,n!\cdot 2^{m+n}, \quad V_0 = \frac{L\,\pi\,w_0^2}{4} \tag{3.11}$$

The coupling strength thus is proportional to the inverse square root of the mode volume, which makes cavities with small mode volumes more desirable in order to achieve higher coupling strengths in cavity QED experiments. This advantage of smaller cavities is also the reason for the ongoing efforts to integrate a Fabry-Perot cavity based on mirrors on the tips of optical

[13] Note, that we are using half widths. For the full width of the cavity transmission $\kappa' = 2\kappa$, the photon lifetime would read $\tau = 1/\kappa'$.

[14] See Appendix A.2 for a derivation.

[15] Cf., e.g., chapter 17.1 of Reference [104].

fibres with an ion trap in our research group [108, 109]. The cavity in our setup operates in a near-concentric configuration ($L \lessapprox 2R$), which minimises the waist w_0 and therefore minimises the mode volume for a given radius of curvature. Additionally, we use the fundamental TEM_{00} mode, which has the smallest mode volume of all TEM modes. All parameters of our cavity can be found in Section 4.4.

Cavity QED experiments are characterised by the three parameters coupling strength g, cavity decay rate κ, and atomic decay rate γ. If $g \gg (\kappa, \gamma)$, the system is said to operate in the strong coupling regime, resulting in a vacuum Rabi splitting of the cavity transmission spectrum[16]. Another figure of merit is the cooperativity

$$C = \frac{g^2}{2\kappa\gamma},$$

which quantifies the ratio of the coherent rate g to the incoherent rates of cavity and atomic decay. Even if a system is not operating in the strong-coupling regime, depending on the specific experiment, coherent interactions are still possible, if the cooperativity is larger than one. For example, high-fidelity entanglement between the cavity field and the quantum emitter can be generated for a cooperativity of 1.7 [72]. It is interesting to note that in the case of a two-level atom, the cooperativity for a given wavelength λ only depends on properties of the resonator, i.e., on the finesse and the beam waist:

$$C = \frac{3\lambda^2\mathcal{F}}{2\pi^3 w_0^2} \tag{3.12}$$

3.3.2 Resonant and dispersive light-matter interactions in cavities

The paradigmatic model of CQED is given by the Jaynes-Cummings Hamiltonian [110]. It describes the interaction of a two-level system with a single quantised mode of an optical cavity in the rotating wave approximation and the dipole approximation. In contrast to the light-matter interaction described in Section 3.2.2, in the Jaynes-Cummings model the light field is quantised. The Hamiltonian is given by

$$H_{\mathrm{JC}}/\hbar \approx \frac{1}{2}\omega_0\sigma_z + \omega_{\mathrm{C}} a^\dagger a + g\left(\sigma_+ a + \sigma_- a^\dagger\right).$$

Here, $\hbar\omega_0$ is the energy difference between the two qubit states $|0\rangle$ and $|1\rangle$ in the two-level system, ω_{C} is the cavity resonance frequency, g is the coupling strength as defined in the previous section, σ_+ is the atomic raising and σ_- the lowering operator, and a is the annihilation operator of the electric field.

After transforming the Hamiltonian into an interaction picture[17], the eigenstates of this Hamiltonian are found to be dressed states, i.e., linear combinations of the so-called bare states $|1, n\rangle = |1\rangle \otimes |n\rangle$ and $|0, n+1\rangle = |0\rangle \otimes |n+1\rangle$, where $|n\rangle$ is the Fock state with n photons in the cavity mode:

$$\begin{aligned} |n, +\rangle &= \quad \cos(\theta_n/2)\ |1, n\rangle + \sin(\theta_n/2)\ |0, n+1\rangle \\ |n, -\rangle &= -\sin(\theta_n/2)\ |1, n\rangle + \cos(\theta_n/2)\ |0, n+1\rangle, \end{aligned} \tag{3.13}$$

[16] Cf., e.g., chapter 5.1.6 in Reference [8].
[17] Cf., e.g., chapter 6.2 in Reference [94].

with the mixing angle given by

$$\theta_n = \arctan\left(\frac{2g\sqrt{n+1}}{\Delta}\right), \tag{3.14}$$

where $\Delta = \omega_C - \omega_0$ is the detuning between cavity and atomic transition.

The energies of the dressed states are given by

$$E_\pm(n)/\hbar = \left(n + \frac{1}{2}\right)\omega_C \pm \frac{1}{2}\Omega_n(\Delta),$$

with the energy splitting

$$\hbar\Omega_n(\Delta) = \sqrt{4g^2(n+1) + \Delta^2}$$

given by the detuning-dependent Rabi frequency $\Omega_n(\Delta)$. In the strong coupling regime, the energy splitting can be observed as a splitting of the cavity transmission into two peaks with separation $\Omega_n(\Delta)$. For $n = 0$, this is referred to as vacuum Rabi splitting. Due to the energy splitting, the state of the qubit prepared initially in the excited state will oscillate with frequency $\Omega_n(\Delta)$ between $|1, n\rangle$ and $|0, n+1\rangle$, if n photons are populating the cavity mode. If the cavity mode is empty, the oscillation will still happen with the vacuum Rabi frequency $\Omega_0 = 2g$.

In the most recent experiments executed in our setup [72–75], the coupling between trapped ions and the cavity mode was achieved via a Raman transition. It relies on coupling the ground state of the ion $|0\rangle$ with a laser field detuned from excited state $|1\rangle$ by an amount Δ to the third state $|2\rangle$, which is coupled to the excited state $|1\rangle$ via the cavity mode in a Λ-like scheme of atomic states. If the cavity resonance frequency is detuned by the same amount Δ from the excited state as the Raman laser field, the population can be transferred between states $|0\rangle$ and $|2\rangle$, and the system is reduced to an effective two-level system. If $\Omega < \Delta$, where Ω is the Rabi frequency of the Raman laser, the spontaneous emission from the excited state with rate γ is reduced to a value of $\gamma' = \gamma\left(\Omega/(2\Delta)\right)^2$ and the effective coupling strength between the effective two-level system and the cavity is given by $g_{\text{eff}} = \Omega g/(2\Delta)$. By coupling the ion to the cavity mode, preparing the ion in the ground state, and illuminating it with the laser, the ion's population can be transferred to the final state $|2\rangle$, while a single photon is generated in the cavity mode during this process. Changing the position of the ion in the cavity standing wave and maximising the flux of generated photons, are used in our setup for carefully maximising the coupling between ion and cavity. More details on the Raman transition and its implementation in our setup can be found in References [64, 67, 69, 71].

Dispersive regime

For the case of large detuning $\Delta \gg 2g\sqrt{n+1}$, the system reaches the dispersive regime and the energies can be Taylor expanded in Ω_n/Δ. In first order, one finds for $\Delta > 0$ that the energies of dressed the states are shifted from those of the bare states by an amount

$$\Delta E_\pm = \pm\hbar(n+1)\chi,$$

where $\chi = \Omega_0^2/(4\Delta) = g^2/\Delta$ is the dispersive shift per photon. In this regime, the dressed states are approximately equal to the bare states because the mixing angle given in Equation 3.14 is

very small: the eigenstates are either "atom-like", containing mainly the contribution of the excited atom, or "photon-like", containing mainly the contribution of the photonic excitation. Such states can be used for weak measurements, i.e., for measurements which only minimally disturb the state of the measured quantum system, but still allow the experimenter to extract some information about the system [111, 112].

Note that even in the case of $n = 0$, the energies of the states are shifted by $\hbar\chi$ due to the vacuum, in analogy to the Lamb shift in atomic systems. In an alternative view, the atomic states are considered fixed but the resonance frequency of the cavity is shifted by χ. In this picture, the atom acts as a dielectric whose index of refraction depends on the state of the atom.

The interaction part of the approximate Hamiltonian in the dispersive regime is given by

$$H_{\text{int}}/\hbar = \chi\sigma_z a^\dagger a.$$

This term describes how the energy of the atomic state is shifted by the $\bar{n} = \langle a^\dagger a\rangle$ photons in the cavity mode. This term leads to a phase evolution of the atomic state in time, which can be measured in a Ramsey experiment. During my thesis research, we implemented such a measurement, using a single ion coupled to a cavity. The details on how the system was modelled are given in Section 5.2.3.

While the dispersive approximation holds for $\Delta \gg 2g\sqrt{n+1}$, References [13, 79] additionally distinguish between different dispersive regimes: For $\chi > \gamma, \kappa$, the system is in the strong dispersive regime (or strong-pull regime), indicating that the shift of the cavity resonance is larger than the cavity linewidth. If $\chi > \kappa$, the qubit spectrum is split into distinct lines, each corresponding to a different photon number, thus directly exhibiting a signature of the quantised nature of the cavity field. Conversely, if $\chi > \gamma$, each photon shifts the qubit transition by more than one linewidth. Our system, however, is operating in the weak dispersive limit with $\chi < \gamma, \kappa$. In this regime, the effect of a single photon is not sufficient to shift the cavity transmission by one linewidth as in the strong dispersive limit. However, it is still possible to extract information about the cavity field via the qubit or vice versa, even though the dispersive coupling is weak.

Chapter 4

Bringing ions and photons close: the experimental setup

Frisch also! Mutig ans Werk!

– F. Schiller, Die Räuber

This chapter contains a description of the experimental setup, in which a linear ion trap is combined with a Fabry-Perot cavity. In particular, the chapter will contain descriptions of the properties of the ion trap and how to load ions; of the lasers used for manipulating the ion; of the cavity and its properties; how $^{40}Ca^{+}$-ions can be used as qubits and how they can be coupled to the cavity; and how photons emitted from the ion into the cavity are detected.

The setup was built about ten years ago during the PhD research of Carlos Russo [64]. During my thesis work, the setup was to a large part rebuilt and re-characterised. The reason for this overhaul was a sudden vacuum leak, during which a plasma was created in the trap. The plasma caused the glue in the cavity assembly to change its properties and the cavity lost alignment. As a consequence, the vacuum chamber had to be opened, the cavity was removed from the chamber and rebuilt, and a new calcium oven was inserted. This process also involved reinstalling a large part of the optics around the vacuum chamber. Overall, this repair and overhaul of the setup was a significant part of my thesis work. The accident itself happened on the 1st of April 2015 and it took about two years to fully rebuild and recover the setup. A description of the rebuilding can be found in Appendix B.

Throughout this chapter, the different parts of the setup and the lasers beams are described according to the convention that has been used in this setup for the last years: via cardinal directions defined as shown in Figure 4.1. When looking towards the setup from the end of the optical table that is closest to the control desk, the left side is referred to as "west", the right side as "east", while the upper side of the setup is "top" or "north" and the lower side of the setup is "bottom" or "south". The side facing the spectator is denominated "front", the far side, which is closest to the LinTrap experiment, is called "back". Note that no distinction is made between, e.g., north-east and east-north.

Any data sets reported in this and the following chapters are referenced with unique identifiers of the form [DataXXy], where "XX" stands for the year of the data acquisition and "y" for an additional letter for distinguishing between different data sets acquired in the same year. Detailed information on these data sets is found in Appendix C, including the date and time

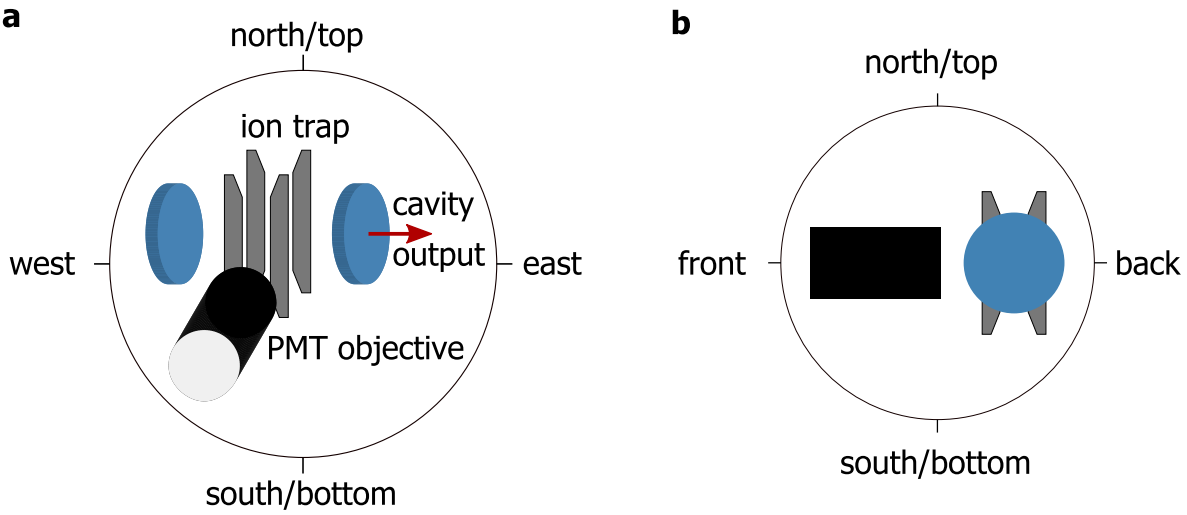

Figure 4.1: Explanation of how directions are defined in the experimental setup. **a** Setup as seen from the side of the control desk. **b** Setup as seen from the cavity output side. Note that north/south and top/bottom are used equivalently.

of acquisition, the kind of measurement, and references to the laboratory notebook. Figure 4.2 shows a legend of the symbols used for drawings of optical setups in this chapter.

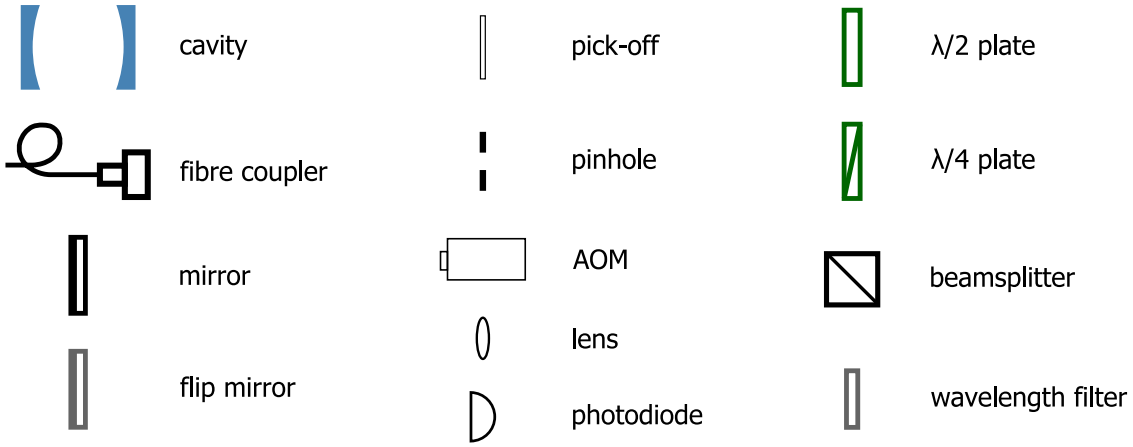

Figure 4.2: Legend of symbols used for optical elements in drawings of optical setups.

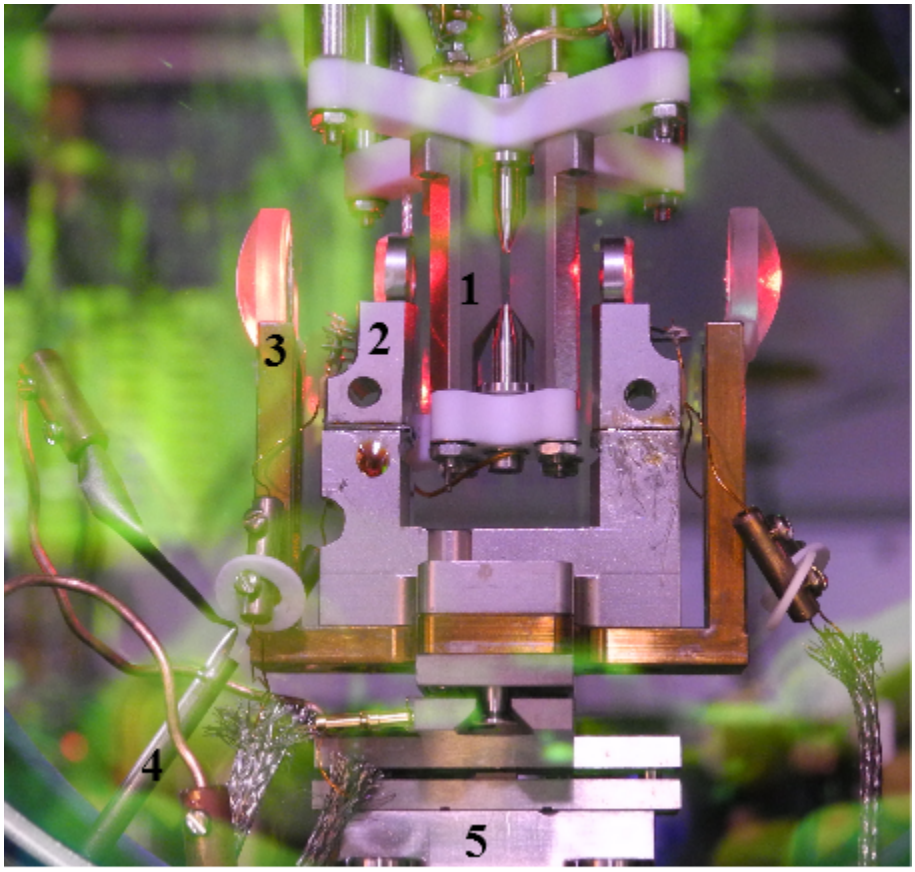

Figure 4.3: Image of the ion trap and the cavity. 1: ion trap; 2: cavity on U-shaped mount; 3: collimating lens; 4: calcium oven; 5: baseplate with piezo translation stages.

4.1 Ion trap

The ion trap used in this setup was built following the Innsbruck-style linear trap design first reported by S. Gulde [113]. It consists of two conical endcap electrodes for DC voltages and four blade-shaped radiofrequency (RF) electrodes for confinement in the radial plane. All electrodes are machined from stainless steel and mounted in glass-ceramic[1] insulators. The assembled trap is suspended from the top of the vacuum chamber, such that the trap axis is vertical. It should be noted, however, that there are several differences between our trap and the trap described in Reference [113]: our trap has a different angle of the RF blades of 22° (in contrast to 30° in the Gulde trap)[2], and its micromotion compensation electrodes have a different geometry. A photograph of the ion trap and the cavity is shown in Figure 4.3.

In more recent designs, the trap blade material has been replaced with gold-plated titanium and the insulator by sapphire [114]. These new materials have more closely matched thermal expansion coefficients, and in addition, sapphire has a lower RF loss tangent than the glass-ceramics employed in the older trap designs. The advantage of these new materials consists of reduced dissipation of electrical power in the trap, and consequently a reduced trap temperature.

[1] Corning, MACOR.

[2] Cf. p.39 in Reference [64] and p.51 in Reference [113]. The angle determines the radius of curvature of the RF electrodes.

Lower temperatures are beneficial especially for high-precision measurements, e.g., in optical clocks, as the systematic uncertainty due to black-body radiation emanating from the trap can be reduced.

Trap geometry

The trap has an endcap-endcap separation of 4 mm and a diagonal blade-to-blade distance of 1.6 mm. Therefore, for a single trapped ion at the trap centre the ion-to-endcap distance is 2 mm and the ion-to-blade distance 0.8 mm. These trap dimensions also determined the feasible length of the cavity and also the coupling strength between trapped ions and the cavity field (see Section 4.4). There are two additional pairs of electrodes in the back and west of the trap. These electrodes consist of thin wires running in parallel to the RF electrodes and are used for compensating micromotion in the trap (see Section 3.1). They are built as pairs so as not to obscure the beam access through the blades.

Electrical connections

The DC voltages for the trap are supplied by a stable voltage source[3]. This voltage source has eight channels, two of which are used for the two endcaps, while the other two supply the voltage for the micromotion compensation electrode pairs. For the experiments reported in this thesis, voltages of 770 V are applied to the endcaps for trapping a single $^{40}Ca^{+}$-ion. This voltage determines the secular frequency of the ion in the axial direction according to Equation 3.2. The corresponding motional frequency of the ion along the trap axis of (cf. Section 3.1) was measured to be [Data17i][4]

$$\omega_{\mathrm{ax}}/(2\pi) = 1.010(5)\ \mathrm{MHz}.$$

The voltages applied to the micromotion compensation electrodes are in the range of a few hundreds of volts.

The radiofrequency voltages are applied to two opposite blades of the trap, while the other two blades are grounded. The RF signal is supplied by a frequency generator[5] at a frequency of 23.3 MHz and amplified by an RF amplifier[6] and a helical resonator [115, 116], which is directly connected to the vacuum feedthrough for the trap electrodes, and whose Q-factor was measured to be about 200 at the time of Carlos Russo's thesis[7]. The Q-factor has not been remeasured since. A frequency generator output of -18.0 dBm corresponds to 2.0 W of forward power going to the trap ($50\ \Omega$ load; measured by a standing wave ratio and power meter[8]), while the reflected power is kept below 0.1 W by fine adjustments to the frequency.

At 2.0 W RF power, the two motional frequencies for the two radial modes of a single ion in the trap have been measured to be [Data17i]

$$\omega_{\mathrm{r1}}/(2\pi) = 1.723(1)\ \mathrm{MHz} \qquad \text{and} \qquad \omega_{\mathrm{r1}}/(2\pi) = 1.778(1)\ \mathrm{MHz}.$$

[3] ISEG, EH-8-020-X.
[4] Measured with 2 W radiofrequency power applied to the RF electrodes.
[5] Marconi, model 2024.
[6] Mini-Circuits, ZHL-20W-13+.
[7] Cf. p.38 of Reference [64].
[8] Daiwa, CN-410M.

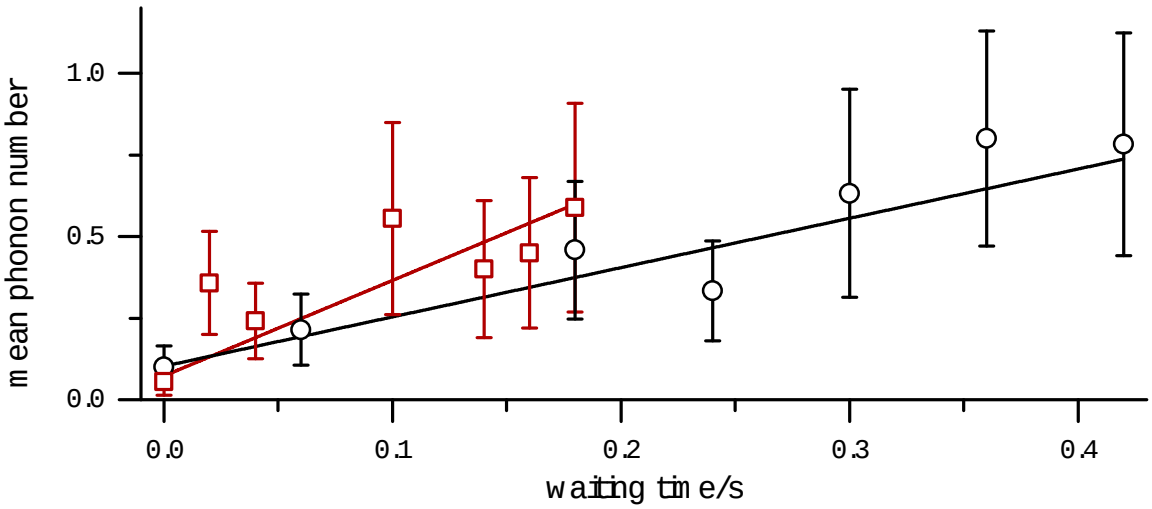

Figure 4.4: Measurement of the heating rate of the axial mode of motion for a single trapped ion. Two data sets (black circles and red squares) were measured, yielding results of $\dot{n}_{\text{ax.}} = 2.9(7)$ quanta/s and $\dot{n}_{\text{ax.}} = 1.5(2)$ quanta/s. Data are [Data15d].

For 3.0 W RF power (-16.2 dBm output of the frequency generator), the corresponding frequencies are [Data17h][9]

$$\omega_{\text{r1}}/(2\pi) = 2.177(5)\ \text{MHz} \qquad \text{and} \qquad \omega_{\text{r1}}/(2\pi) = 2.224(5)\ \text{MHz},$$

as expected from the scaling of the radial frequencies with the square root of the applied power. The nondegeneracy of the radial modes is most likely caused by imperfections of the alignment in the trap. This nondegeneracy is actually desirable since it allows one to cool both radial modes [86].

Heating rate

Ion traps exhibit heating of the trapped ion, i.e., the motional state of the ion changes in time. Different potential causes of this heating mechanism are discussed in the literature (see, e.g., Section IV of Reference [117], or the appendix of Reference [87]). In our setup, the measured heating rates are comparatively low, and do not cause any limitation on the time scale of the executed experiments.

The heating rate for the axial mode of our trap of a single ion was measured to be $1.9(2)$ quanta/s before my time in the group [69][10]. After the overhaul, this heating rate was remeasured twice on the same day, with results of [Data15d]

$$\dot{n}_{\text{ax.}} = 2.9(7)\ \text{quanta/s} \qquad \text{and} \qquad \dot{n}_{\text{ax.}} = 1.5(2)\ \text{quanta/s};$$

see Figure 4.4. However, because of the long waiting times during the measurement, there were issues with the control software which caused the measurement to be rather noisy. In

[9] The axial frequency was remeasured at this RF power to be $\omega_{\text{ax}}/(2\pi) = 996(6)$ kHz.
[10] The data were acquired on the 9th April 2010.

any case, the measured values are close to the previously measured values and sufficiently low, considering that the duration of a single run of an experiment is always below one second. It may thus be concluded that the plasma generated during the vacuum accident and the following repair did not influence the trap characteristics.

The radial heating rates have not been measured to date. However, since the heating rate Γ_{h} for well-compensated micromotion is given by [117]

$$\Gamma_{\mathrm{h}} \simeq \frac{e^2}{4m\hbar\omega} S_{\mathrm{E}}(\omega),$$

with the spectral density of the noise S_{E}, the mode frequency ω, and the ion mass m, the heating rates for the radial modes are expected to be lower as the frequencies for these modes are higher and S_{E} typically falls off with increasing frequency.

Oven and loading

$^{40}Ca^{+}$-ions are loaded into the trap by driving a current through an oven containing neutral calcium. The neutral calcium atoms are then photoionised with two lasers at wavelengths of 423 nm and 375 nm at the trap centre (see also Section 4.3.2). Before the setup was rebuilt, the oven consisted of a stainless steel tube, spot-welded to two long connectors, fixed to the bottom feedthrough[11]. During the rebuild, this oven had to be replaced for two reasons: First, the oven was mounted between the cavity's west collimating lens mount and the mount of the west cavity mirror, so that removing the cavity was not possible without removing the oven from the bottom feedthrough. Since we tried to keep the intervention inside the chamber to a minimum, we wanted to avoid removing the bottom flange. Instead, the connections of the old oven were cut close to the tube containing the calcium. The connections going to the bottom feedthrough were then reused as mount and electrical connection for the new oven. Second, in spite of our flushing the chamber with dry nitrogen while it was open, the old oven was exposed to air during the operation. The resulting oxidation of the top calcium layer in the oven can make loading impossible, making a replacement advisable.

For that reason, a new commercial calcium oven[12] was installed. The option of rebuilding a homemade oven was discarded because it would have taken longer. The new oven consists of a stainless steel tube with an aperture at one end and two metal strips, one at each end of the tube, that serve as connections to the current source (see Figure 4.5). These electrodes are connected to the remaining connectors of the old oven (and thus to the bottom feedthrough) via barrel connectors. In addition, the oven tube is closed by an indium seal to protect the calcium from oxidation. This seal is removed via melting when current is sent through the oven for the first time.

The oven is heated via a current supply[13] at currents typically between 3 A and 5 A, while during melting of the indium seal currents and the first observation of atomic fluorescence

[11] Cf. p.55 of Reference [64].

[12] Alvatec AS-3-Ca-90-V; diameter 3 mm and containing 90 mg of calcium. The company was taken over by AlfaVakuo e.U. The activation temperature for melting the protective indium seal is stated as 450 K, and the minimum evaporation temperature at a pressure of 10^{-8} mbar of 555 K. The 3 mm diameter version is specified to reach a temperature of approximately 570 K with a current of 3 A.

[13] Wayne Kerr Electronics (also sold under the Farnell brand), LS30-10.

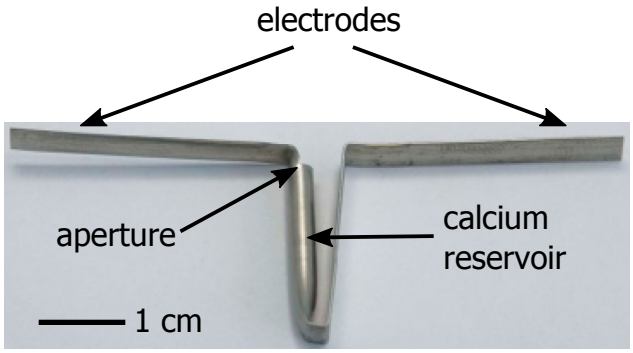

Figure 4.5: Image of the type of calcium oven installed in our setup. Image adapted from the Alvatec data sheet.

currents up to 10 A had been used. With photoionisation, cooling, and repumping lasers well aligned, loading is typically possible within $3 - 5$ minutes, but depends also on the scanned wavelength range of the photoionisation laser at 423 nm.

The oven was aligned pointing towards the trap centre via the cut-out in the west lens mount and the hole in the west cavity mirror mount, the latter of which had also been used for the old oven. This alignment relied on the rigidity of the old oven's connectors to the bottom feedthrough and that of the new oven's connectors. Unfortunately, though, the positioning of the new oven proved not to be stable enough and we found that the alignment of the oven had shifted during baking. As a consequence, for loading ions, the cavity, which is mounted on piezo translation stages, needs to be moved from the position in which its mode is coupled to the ion towards the back. The position is monitored and compared to reference pictures via two USB microscopes[14], one from the front-north, the other from the east-back direction. However, the cavity only has to be translated along one axis (front-back), while the east-west direction can be left untouched. This is a slight improvement over the situation before the vacuum leak, when it was necessary to change the cavity position along both horizontal directions each time an ion was loaded.

In an improved version of our setup, B. Lanyon's team members at IQOQI Innsbruck have addressed the oven alignment problem by mounting the oven in an additional alignment structure that also serves as a collimator and shields the trap electrodes from the calcium flux as well as from the heat radiation. This shielding avoids another issue in our setup: The cavity assembly gets heated by thermal contact to the hot oven via the bottom flange as well as through heat radiation. In our case, such heating of the cavity makes experiments impossible for the first one to two hours after loading, since the cavity resonance drifts out of the range of the cavity piezos directly after loading and keeps drifting due to the contraction of the cavity mount while it cools down (see also Section 4.4). For a future setup, a solution similar to the one used in the new setup at IQOQI Innsbruck should be considered. However, even in that setup it was not possible to completely eliminate the thermal influence of loading onto the cavity resonance. Another option for loading would consist of the implementation of ablation loading [118–120] in a new setup with the advantage that the thermal influence of loading on the cavity would be negligible. However, for ablation loading a target containing calcium would need to be mounted

[14] Jiusion, DigiMicro Scale; 20- to 230-fold magnification.

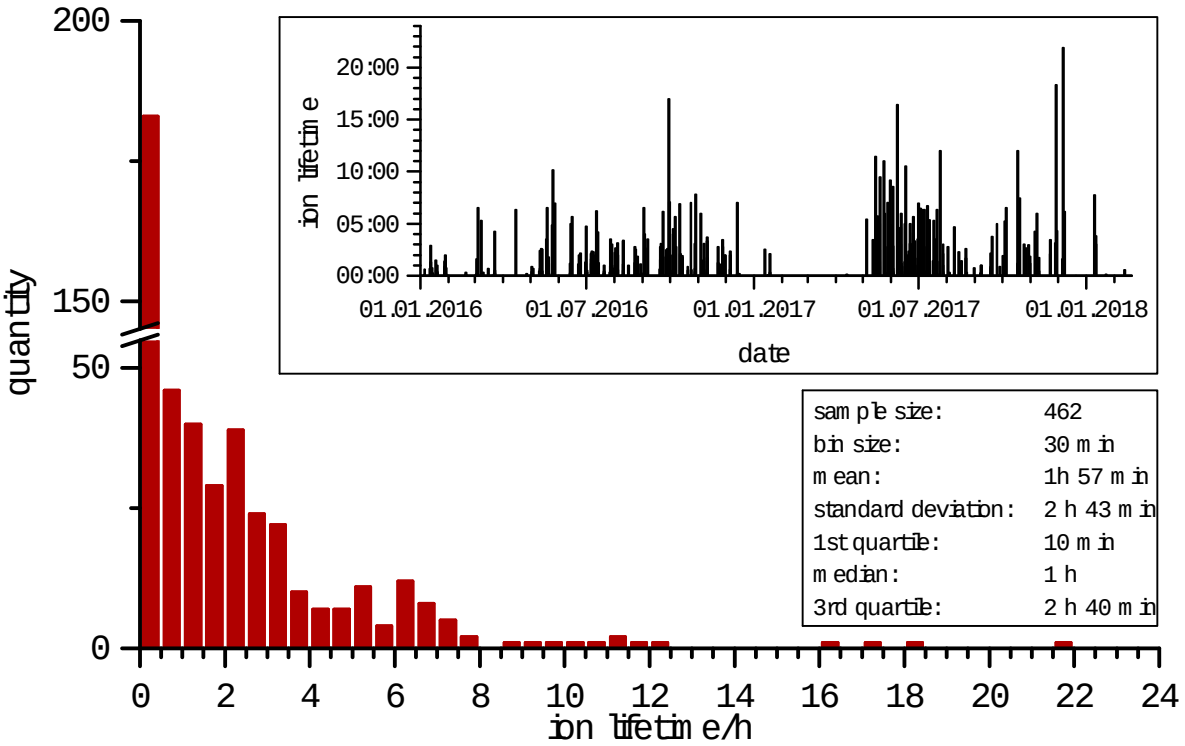

Figure 4.6: Histogram of all recorded single-ion trapping times from January 2016 to mid-February 2018, binned in 30 min intervals [Data18]. The majority of ions did not stay trapped for longer than 2 hours. The maximum recorded trapping time was 21 h 54 min. The insets show the time trace of recorded single-ion trapping times and the statistics of the sample.

close to the trap and a pulsed laser would be required.

Vacuum system

Ion trap experiments require ultra-high vacuum (UHV) in order to reduce the likelihood of collisions between the ions and gas particles. Otherwise, the energy transfer from such collisions would disturb the motional state of the ions or even prevent trapping altogether. Typical pressures for ion trap setups in our group lie in the low 10^{-11} mbar range. In our setup, the ion trap was initially assembled and the vacuum chamber pumped out with a scroll and a turbo pump, during which time the assembly was also baked. Afterwards, the required low pressure in our vacuum chamber was reached and is maintained via an ion getter pump[15] and a titanium sublimation pump[16] (TiSub). The latter pump is switched on only when the pressure has increased above the desired level and was the only pump that was replaced after the accident. The chamber pressure is monitored regularly, using an ion gauge[17] with typical values around $3 \cdot 10^{-11}$ mbar. It should be noted, however, that this gauge has to be switched off during measurements involving the cavity, since its electrical signals interfere with the cavity locking

[15] Varian, VacIon Plus 20 Starcell, 20 l/s; controlled by Agilent, MiniVac.
[16] Agilent, TSP Filament Cartridge.
[17] Varian, UHV-24; controlled by Varian, XGS-600.

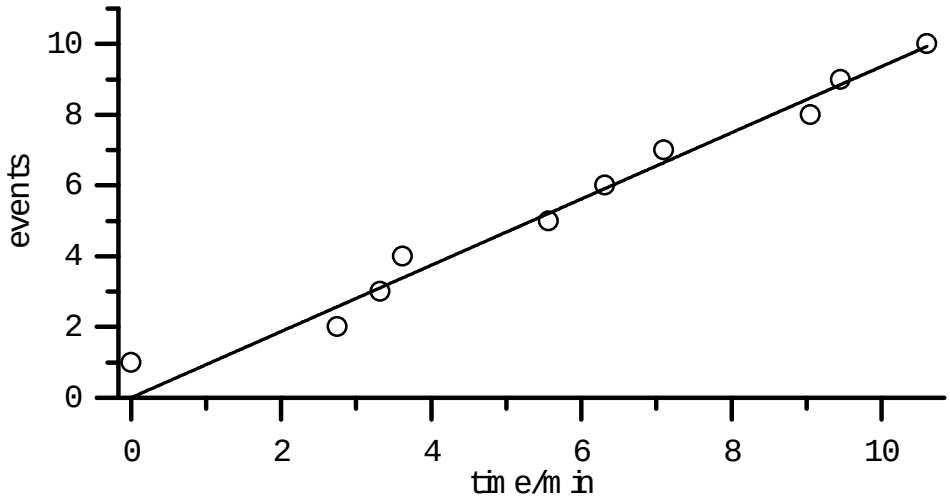

Figure 4.7: Measurement of the rate of background gas collisions. A linear fit to the data yields a slope of $0.94(2)$ events/min, corresponding to one event every 1 min $04(2)$ s. Note that there are no uncertainties, as the plotted quantity is the counted number of events. Data are [Data16b].

setup. More details on the vacuum considerations during the rebuild of the setup can be found in Appendix B.

Ion stability and trapping times

Before rebuilding the setup, ion trapping times ranged from two hours to 20 hours [71]. After we repaired the setup, the trapping times were shorter, usually not exceeding two hours, even though the pressure in the vacuum chamber as measured at the ion gauge was below $3 \cdot 10^{-11}$ mbar, with pressures rising up to $5 \cdot 10^{-10}$ mbar during loading. Such short trapping times are problematic since the cavity needs at least one hour after loading to cool down before is is possible to work with ion and cavity without fast drifts of the cavity resonance. A summary of the trapping time statistics after the setup was rebuilt is shown in Figure 4.6 [Data18]. Note, that these statistics are not completely representative, as not all trapping times have been recorded.

In addition, the ions were observed to chemically react with residual gas particles in the vacuum chamber[18]. This reaction can be observed when more than one ion is residing in the trap. If one ion has reacted with a gas particle and thus formed a charged molecule, it may still be trapped, but it will no longer react to the cooling and detection lasers and hence not emit fluorescence light at the wavelength of $^{40}Ca^{+}$. Whenever the $^{40}Ca^{+}$-ions change position due to collisions with residual gas atms or molecules disturbing the ion crystal, this position change can be observed since the molecular ion is dark and can be tracked in the ion crystal. This hopping can be used to estimate the rate of background gas collisions (see, e.g., p.148 in reference [86]). From such a measurement, shown in Figure 4.7, we extract a collision rate of one event every 1 min $04(2)$ s [Data16b].

[18] See Reference [121] for similar observations in another trap of our group and considerations on the likely chemical reactions.

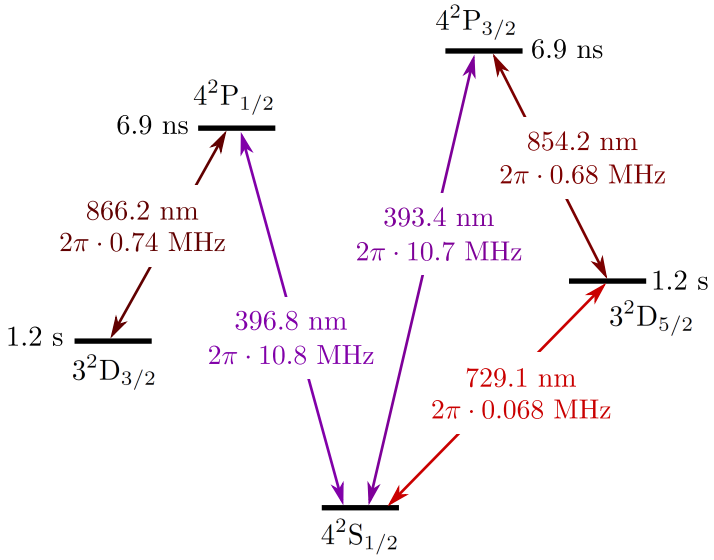

Figure 4.8: Level structure of a $^{40}Ca^+$-ion together with the transition wavelengths [122], lifetimes and decay rates; see also Table 4.1. Specified rates are half widths. The transitions $3^2D_{3/2} - 4^2S_{1/2}$ at 732.4 nm and $4^2P_{3/2} - 3^2D_{3/2}$ at 849.8 nm are not shown, because these transitions are not used in our setup.

Based on these observations, we suspected the oven as a source of contamination. However, degassing the oven several times by heating it to loading temperatures for longer times than for loading (over night) did not bring any improvement in the ion trapping times. We also investigated the correlation between ion trapping time and oven current during loading but could not find any strong correlation. Neither firing the titanium sublimation pump nor focusing the UV laser beams more tightly to avoid creating photoelectrons on the trap blades helped to solve the problem.

Although we were not able to determine the cause for the shorter ion trapping times, by the end of 2016, the trapping times started getting better. Since then, trapping times of two hours and longer are usual, with an observed maximum of 21 h 54 min. One hypothesis for the improvement could be that the oven needed longer to be completely degassed if, e.g., a layer of contaminants on or in the oven tube had to be completely evaporated and pumped off. A second hypothesis relies on the fact that towards the end of 2016 we started using a more careful procedure for setting Doppler cooling, which might have increased the trapping times.

4.2 Using calcium ions as qubits

Figure 4.8 shows the energy levels of a $^{40}Ca^+$-ion relevant for the experiment described in Chapter 5. While the fast dipole transition between the $4^2S_{1/2}$ and the $4^2P_{1/2}$ manifolds is well-suited for Doppler cooling, the long lifetimes of the states in the $3^2D_{5/2}$ manifold suggest using these states together with the ground states in the $4^2S_{1/2}$ manifold for storing and processing quantum information. In such a configuration, the qubit state is detected via electron shelving and detection of fluorescence on the transition $4^2S_{1/2} - 4^2P_{3/2}$ with repumping light on the

Table 4.1: Electronic state lifetimes τ, branching ratios, and decay widths in the $4^2P_{1/2}$, $4^2P_{3/2}$, $3^2D_{3/2}$, and $3^2D_{5/2}$ manifolds of $^{40}Ca^+$. Full widths are denominated Γ.

manifold	τ	$\Gamma/(2\pi$ MHz)	branching ratio	reference
$4^2P_{1/2}$	6.904(26) ns	23.05(9)	0.93572(25) [$4^2P_{1/2} - 4^2S_{1/2}$], 0.06428(25) [$4^2P_{1/2} - 3^2D_{3/2}$]	[123]
$4^2P_{3/2}$	6.924(19) ns	22.99(4)	0.9347(3) [$4^2P_{3/2} - 4^2S_{1/2}$], 0.00661(4) [$4^2P_{3/2} - 3^2D_{3/2}$], 0.0587(2) [$4^2P_{3/2} - 3^2D_{5/2}$]	[124, 125]
$3^2D_{3/2}$	1.168(9) s	0.136(1)	-	[126]
$3^2D_{5/2}$	1.176(11) s	0.135(1)	-	[126]

transition $3^2D_{3/2} - 4^2P_{1/2}$. Table 4.1 gives the lifetimes, branching ratios and decay widths of the states in the $4^2P_{1/2}$, $4^2P_{3/2}$, $3^2D_{3/2}$, and $3^2D_{5/2}$ manifolds.

The qubit is initialised and manipulated using the laser on the $4^2S_{1/2} - 3^2D_{5/2}$ quadrupole transition. The transitions at 854 nm and 866 nm are used for repumping populations from the long-lived states during Doppler cooling at the end of experiments. In our setup, we additionally use the $4^2S_{1/2} - 4^2P_{3/2}$ transition for driving cavity-mediated Raman transitions for generating photons in the cavity, which is coupled to the $4^2P_{3/2} - 3^2D_{5/2}$ transition (cf. Section 3.3.2).

The qubit can be defined in different ways, for example in two Zeeman states in the $3^2D_{5/2}$ manifold, or in one Zeeman state in the $3^2D_{5/2}$ manifold and one Zeeman state in the $4^2S_{1/2}$ manifold. The choice of the Zeeman states in which the qubit is encoded depends on several parameters. While the ion-cavity coupling strength (cf. Section 3.3.1) increases for states with large magnetic quantum number $|m_j|$ since the Clebsch-Gordan coefficients are largest for these states[19], the sensitivity to magnetic fields also increases, leading to lower coherence times (see Section 4.2.3). Additionally, the orientation of the quantisation axis, defined by an externally applied magnetic field, and the possible polarisations of photons in the cavity modes have to be considered for the choice of the qubit states. This is especially the case for experiments where coupling strengths of two Raman transitions need to be carefully matched in order to be able to control both polarisation of the photon generated in one of the cavity modes during the Raman transition. For instance, in the experiment described in Reference [72], a quantisation axis orthogonal to the cavity axis and collinear with the Raman laser beam was used, while the different scheme of the experiment described in Reference [73] required a quantisation axis orthogonal to both the cavity axis and the Raman beam direction[20]. In the experiment described in Chapter 5, the qubit is defined between the states $|4^2S_{1/2}, m_J = 1/2\rangle$ and $|3^2D_{5/2}, m_J = 1/2\rangle$, or between the states $|4^2S_{1/2}, m_J = 1/2\rangle$ and $|3^2D_{5/2}, m_J = 3/2\rangle$.

4.2.1 Laser cooling

For coupling an ion to a cavity mode, it is desirable to have the ion as close as possible to its motional ground state of the motional mode that has largest overlap with the cavity axis. In this way, it can be avoided that the ion experiences a reduced coupling strength to the cavity mode

[19] The Clebsch-Gordan coefficients for the transitions between $4^2S_{1/2}$, $4^2P_{3/2}$, and $3^2D_{5/2}$ are given in the Appendix A.1.

[20] More details can be found in Reference [70].

because of its motion along the standing wave [70]. High-precision measurements and some implementations of high-fidelity quantum operations on multiple ions also require cooling to the ground state of the motional mode used for the gate operations. In other applications, the manipulation of the motional state requires good control over the phonon states, which is typically achieved by first bringing the system into the motional ground state before preparing the desired state.

Several methods are available for cooling [127, 83]. The most common method is Doppler cooling, for which the minimum temperature is limited by the recoil energy of the cooling-lasers photons scattered by the ion. To reach temperatures below the Doppler limit, sideband cooling can be used if the system is in the resolved sideband regime, i.e., if the linewidth of the cooling transition is smaller than the motional frequency [83]. Sideband cooling allows one to reach the motional ground state but has the disadvantage that it is time-consuming if several modes need to be cooled, especially for multi-ion systems, since each motional mode has to be cooled individually. Cooling several modes can be necessary if several modes are used, e.g., when coupling to several modes for implementing long-range interactions [128].

In contrast to sideband cooling, a third method, electromagnetically-induced-transparency (EIT) cooling allows one to cool several modes at the same time [129–131]. This method has been tested recently in the quantum simulation project in our group, but discontinued due to heating of the axial modes while cooling radial modes (cf. References [131, 132] and chapter 4.6.3 in Reference [128]). Another technique, polarisation gradient cooling (or Sisyphus cooling) [133–136], has the advantage of high cooling rates, and is currently being tested in the quantum simulation project. In cavity systems, cavity cooling [137, 45] can be another way to reduce the temperature of the system, however, our system parameters are not favourable for this method. In our setup, we routinely only use Doppler cooling and sideband cooling, since we only use one or two ions such that the number of modes can be handled with Doppler cooling and sideband cooling.

Doppler cooling

When atoms are moving, the frequency at which they absorb light is shifted as compared to a stationary atom due to the Doppler effect. This effect can be used to cool the atoms by illuminating them with a laser beam with frequency red-detuned from the atomic resonance [138, 139, 127]. The atoms of the matching velocity class will absorb the photons from the laser beam but emit photons isotropically. As a consequence, the average momentum of the ion will be reduced after absorbing and re-emitting many photons: the ion will be cooled in the direction along the laser beam and reach a steady-state temperature.

At the optimum detuning of the light frequency of half the atomic linewidth, i.e., at $-\Gamma/2$, the minimum achievable temperature in one dimension is given by

$$T_{\text{Doppler,1D}} = \frac{\hbar\Gamma}{2k_{\text{B}}},$$

where Γ is the full width of the transition, $\hbar$ the reduced Bohr constant, and k_{B} the Boltzmann constant[21]. In three dimensions, and taking into account that cooling happens on a dipole transition but neglecting micromotion in the trap and correlations between absorption and emission

[21] For a trapped ion, to reach this limit the condition $\Gamma \gg \omega$ needs to be fulfilled, where ω is the mode fre-

events, the minimum temperature is [83]

$$T_{\text{Doppler}} \approx \frac{7}{20}\frac{\hbar\Gamma}{k_{\text{B}}} \tag{4.1}$$

if $\Omega \ll \Gamma$ holds for the on-resonance Rabi frequency Ω and the decay rate Γ. For the $4^2\text{S}_{1/2} - 4^2\text{P}_{1/2}$ transition in $^{40}\text{Ca}^+$, the minimum temperature is approximately 0.5 mK (neglecting the decay to $3^2\text{D}_{3/2}$). The corresponding phonon number is given by

$$\bar{n}_{\text{Doppler}} = \frac{k_{\text{B}} T_{\text{Doppler}}}{\hbar\omega},$$

where ω is the trap frequency. For our typical axial trap frequency of $2\pi \cdot 1$ MHz, the minimum temperature of 0.5 mK corresponds to a phonon occupation of $\bar{n}_{\text{Doppler, ax}} \approx 11$, while for the radial frequency of $2\pi \cdot 1.7$ MHz, $\bar{n}_{\text{Doppler, rad}} \approx 6$ (cf. Section 4.1).

Due to the decay of the $4^2\text{P}_{1/2}$ states to the $3^2\text{D}_{3/2}$ manifold, it is necessary to additionally use the repumping laser at 866 nm during Doppler cooling. The power of this laser should be low enough so as not to broaden the cooling transition, which would lead to a higher Doppler temperature. Additionally, the system of the three manifolds involved in Doppler cooling has dark states (cf., e.g., chapter 5.1 in Reference [67]). By slightly blue-detuning the repumping laser from resonance, populating these dark states can be avoided.

Sideband cooling

For sideband cooling, the system needs to be in the Lamb-Dicke regime (cf. Section 3.2.2) and the transition linewidth needs to be less than the motional frequency of the mode that is to be cooled to be able to resolve the sidebands. By tuning the laser frequency to the red motional sideband of the mode to be cooled, the ion's electronic and motional state can be changed simultaneously: The ion is brought from the electronic ground state to the electronic excited state in the $3^2\text{D}_{5/2}$ manifold, while the number of motional excitations is reduced by one. Quenching the ion from the electronic excited state with light at 854 nm via the $4^2\text{P}_{3/2}$ manifold and subsequent spontaneous emission, the ion is brought back into the ground state. This cycle is repeated until the ion population has been pumped to the dark state of the system, which is the motional ground state. The minimum temperature achievable for a given motional mode and transition via sideband cooling is limited by spontaneous emission during the quenching (cf. section IV.B of Reference [83]).

Characterising cooling

The Doppler cooling process can be characterised for a single ion by driving Rabi oscillations on a carrier transition at 729 nm, measuring the probability to excite the ion to a state in the $3^2\text{D}_{5/2}$ manifold as a function of time, and fitting a model to the data of the ion excitation [59]. The model takes into account that the Rabi frequency $\Omega_n \approx \Omega\,(1 - \eta^2 n)$ depends on the phonon number n, where Ω is the Rabi frequency and η is the Lamb-Dicke parameter (see Section 3.2.2 and Appendix A.3). The fit function is given as the superposition of oscillations at the Rabi

quency [138]. This condition corresponds to the ion being weakly confined such that during each oscillation period in the trap it becomes resonant with the Doppler-shifted cooling light.

frequencies Ω_n, weighted by the thermal occupation probability p_n of the corresponding phonon number n:

$$p_{\mathrm{D}} = \frac{1}{2}\left[1 - \sum_{n=0}^{\infty} p_n \cos\left(2\Omega_n t\right)\right],$$
$$p_n = \frac{1}{\bar{n}+1}\left[\frac{\bar{n}}{\bar{n}+1}\right]^n$$

Expanding this equation and extending it to three modes, one finds

$$p_{\mathrm{D}} \approx \frac{1}{2}\left[1 - \frac{\cos\left(2\Omega t\right) + 2\Omega t\, n_{\mathrm{eff}} \sin\left(2\Omega t\right)}{1 + \left(2\Omega t\, n_{\mathrm{eff}}\right)^2}\right],$$

where the effective mean phonon number is given as $\bar{n}_{\mathrm{eff}} = \sum_{k=1}^{3} \eta_k^2 \bar{n}_k$ with η_k the Lamb-Dicke parameters and $\bar{n}_k$ the mean phonon numbers of the three modes (cf. appendix A1 of Reference [59]).

When the ion is close to its motional ground state, the phonon number can also be determined via sideband spectroscopy: Measuring the excitation probability both on the red and blue sidebands of the mode under investigation, the mean phonon number is given by

$$\bar{n} = \frac{R}{1-R},$$

where R is the ratio of the excitation probability to the red sideband to that of the blue sideband for a given pulse duration (cf. equation 115 in Reference [83]).

The spatial extent of the wave packet for a thermal state can then be estimated as the uncertainty of the spatial coordinate [140]:

$$\Delta x = x_0 \sqrt{2\bar{n}+1},$$

where $x_0 = \sqrt{\hbar/(2m\omega)}$ is the ground state extent for a given mass m and trap frequency ω (cf. Section 3.2.2). For trap frequencies $\omega_{\mathrm{ax}} = 2\pi \cdot 1.0$ MHz and $\omega_{\mathrm{rad}} = 2\pi \cdot 1.7$ MHz, the ground state extents are $x_{0,\mathrm{ax}} = 11.2$ nm for the axial mode and $x_{0,\mathrm{rad}} = 8.6$ nm for the radial mode. Using the Doppler limits $\bar{n}_{\mathrm{Doppler,ax}} \approx 11$ and $\bar{n}_{\mathrm{Doppler,rad}} \approx 6$ for the axial and radial modes, we can estimate the spatial extent of the Doppler-cooled ion wave packet as $\Delta x_{\mathrm{ax}} = 46$ nm and $\Delta x_{\mathrm{rad}} = 28$ nm.

With sideband cooling, the individual contributions of the three modes can be investigated more carefully. Applying sideband cooling only to the axial mode, a mean phonon number in that mode of $\bar{n}_{\mathrm{ax}} = 0.017(3)$ is found [Data17p], corresponding to a ground-state population of $98.3(3)\%$ and a spatial extent of $\Delta x_{\mathrm{ax}} = 11.42(4)$ nm. Cooling the axial mode and both radial modes at 2 W RF power[22] , that is, for $\omega_{\mathrm{r1}}/(2\pi) = 1.723(1)$ MHz [Data17q] and $\omega_{\mathrm{r2}}/(2\pi) = 1.778(1)$ MHz [Data17r], we find mean phonon numbers $\bar{n}_{\mathrm{r1}} = 1.9(3)$ and $\bar{n}_{\mathrm{r2}} = 3.3(9)$, corresponding to ground-state populations of 35(3)% and 23(6)% and corresponding spatial extents of $\Delta x_{\mathrm{r1}} = 19(4)$ nm and $\Delta x_{\mathrm{r1}} = 24(3)$ nm.

[22] For this experiment, all three modes were first Doppler-cooled. Each mode was then sideband cooled, and the sideband cooling step was repeated three times. The cooling times were 2 ms of Doppler cooling, 6 ms of axial sideband cooling, and 8 ms for each radial sideband.

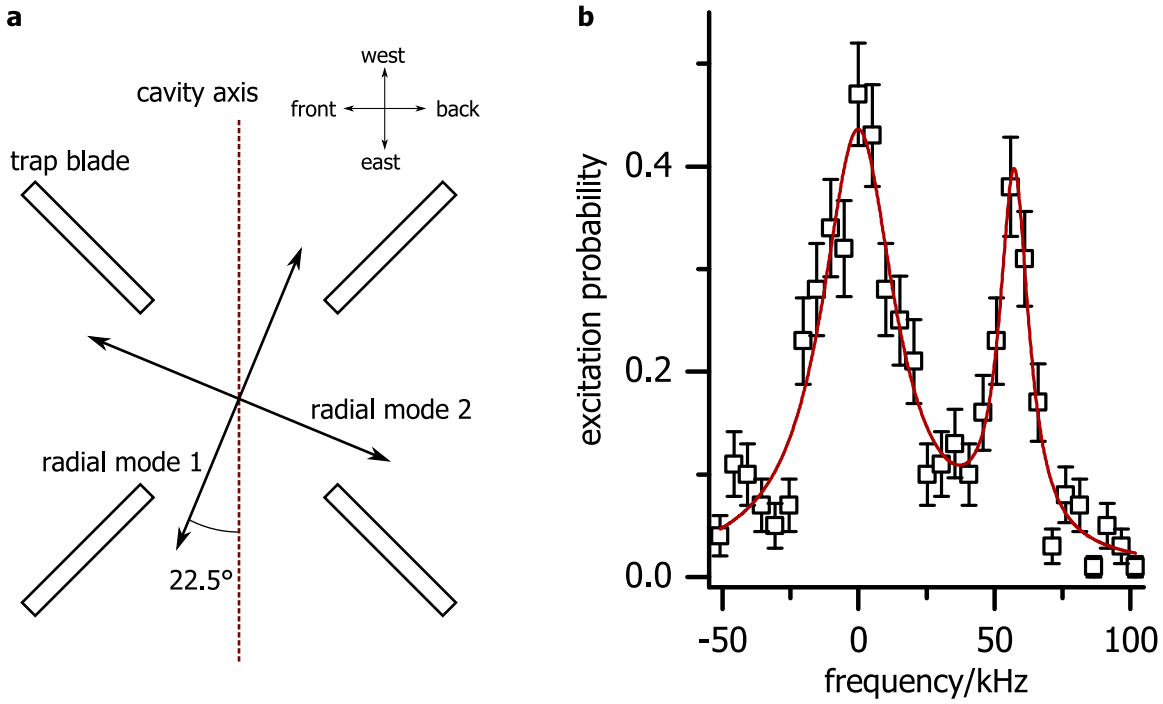

Figure 4.9: Orientation of the radial modes in the trap and spectral structure. **a** The radial modes have an angle between $20°$ and $25°$ with respect to the trap electrodes [69]. Note that it is not clear which way the modes are rotated; the version mirrored on the cavity axis is also possible. **b** The radial modes are split by $57.3(7)$ kHz with 2 W RF power. Their different widths ($33(4)$ kHz and $13(2)$ kHz, respectively) correspond to the different coupling strengths to the two modes. Lines are Lorentzian fits to the data [Data17t].

Note that when cooling both radial modes simultaneously, we have not been able to reach higher ground state populations for both modes: This may be related either to coupling between the modes or to the fact that the north-east beam at 729 nm used for cooling does not have equal overlap with both modes. The second hypothesis is supported by the fact that in the excitation spectrum of the two modes, one mode has larger excitation probability and larger width than the other. Figure 4.9 shows the excitation spectrum of both radial modes as well as a sketch of the assumed mode position, which is based on a characterisation of the radial mode angles reported in Reference [69]. In fact, cooling only the mode of the two radial modes to which the beam is more strongly coupled [Data17s], a mean phonon number of $0.17(2)$ can be reached in that mode, with a ground state population of $85.3(8)\%$ and spatial extent of $10.0(7)$ nm.

Since sideband cooling of all three modes takes several milliseconds, only Doppler cooling was used in the experiment described in Chapter 5, as otherwise measurements would have taken too long with respect to other experimental drifts such as the frequency drift of the laser used for driving the cavity or the thermal drift of the cavity resonance. The effect of the residual phonon populations on the ion-cavity coupling strength is discussed in Section 4.5.

4.2.2 Qubit preparation and detection

The qubit, defined on the $4^2S_{1/2} - 3^2D_{5/2}$ quadrupole transition, is manipulated with the laser at 729 nm. Following initial cooling, experiments consist of the following steps: state preparation is followed by manipulation of the qubit or its interaction with the cavity mode. At the end of the experiment, the qubit state is detected.

State preparation

In order to start the experiment in a well-defined state, optical pumping is employed. The ion is prepared in the ground state manifold, e.g., in $|4^2S_{1/2}, m_J = 1/2\rangle$, by driving the $|4^2S_{1/2}, m_J = -1/2\rangle$ to $|3^2D_{5/2}, m_J = 3/2\rangle$ transition and repumping the excitation with light at 854 nm via the $4^2P_{3/2}$ manifold. Since only a small fraction can decay back to $|4^2S_{1/2}, m_J = -1/2\rangle$[23], by repeating this process, the ion's population will be pumped to $|4^2S_{1/2}, m_J = 1/2\rangle$. Alternatively, the ion can be prepared in the state $|4^2S_{1/2}, m_J = -1/2\rangle$ by driving the carrier transition $|4^2S_{1/2}, m_J = 1/2\rangle - |3^2D_{5/2}, m_J = -3/2\rangle$.

Qubit state detection

At the end of the experimental sequence, the state of the qubit is detected, using electron shelving [83] and detection of the ion fluorescence with a photomultiplier tube[24] (PMT) or an electron-multiplying charge-coupled device camera[25] (EM-CCD). An objective[26] on the front side of the vacuum chamber with aperture 50 mm, working distance 55 mm, and magnification around 7 collects at maximum 6.6% of the light scattered by the ion [69]. In order to avoid light at 729 nm from the new addressing beam (Section 4.3.3) along the front-back axis hitting the PMT, the filter[27] in front of the PMT has been replaced with two filters[28] that transmit 96.1% of the light at 397 nm, but only $7 \cdot 10^{-6}$ at 375 nm, $2.2 \cdot 10^{-7}$ at 423 nm, and $1 \cdot 10^{-7}$ at 729 nm. Note that in order to observe fluorescence at 423 nm from atomic calcium, these filters need to be removed from the PMT assembly. The PMT is further protected from stray light with two slits, one vertical and one horizontal, whose widths can be manually adjusted. When the $4^2S_{1/2}$ to $4^2P_{1/2}$ transition is saturated for a single ion in the trap, a count rate of maximally $60,000$ counts per second is measured at 397 nm with the PMT.

Individual detection of multiple ions is done via an objective on the back side of the chamber and the EM-CCD camera. The objective[29] has an aperture of 38 mm, a working distance of 58 mm and a magnification of 23 [141]. The same objective is also used for focusing the addressing beam at 729 nm, which is overlapped with the path to the camera on a dichroic mirror [142].

[23] See the Clebsch-Gordan coefficients in Appendix A.1.
[24] Hamamatsu, H7360-02.
[25] Andor, iXon DV860AC-BV.
[26] Nikon, model unknown.
[27] Semrock, FF01-377/50.
[28] Both filters Semrock, FF01-392/23-25; replaced on 20160411.
[29] Sill Optics, custom.

4.2.3 Magnetic field and quantisation axis

This section describes the setup for generating the magnetic field as well as the setup for cancelling external magnetic field noise.

Magnetic field coils

The magnetic field applied to the ion in order to lift the degeneracy of the Zeeman sublevels is generated by three pairs of coils around the vacuum chamber along the north-south, east-west, and front-back axes. For the experiment described in Chapter 5, currents of 804 mA, 312 mA, and 362 mA, respectively, were driven through these coil pairs using stable current drivers built by our electronics workshop. These currents resulted in a magnetic field of 4.06 G at the position of the ion. This value was chosen in order to avoid overlap of carrier transitions and motional sidebands in the qubit spectrum. The east-west coil pair makes the smallest contribution magnetic field and mainly serves to compensate the earth's magnetic field. The magnetic field axis itself lies along the north-front to south-back direction at $45°$ with respect to the trap axis and orthogonal to the cavity axis. It is parallel to the laser beam at 393 nm.

Note that the exact orientation of the quantisation axis is important in our experiment: In addition to defining which transitions in the ion can be driven for a given laser polarisation, the magnetic field axis in our setup also determines the polarisation of photons generated in the cavity via Raman transitions. Accordingly, the magnetic field axis has to be chosen carefully, depending on the experiment to be done in the setup.

Magnetic field stabilisation

The coherence times of trapped ions is limited in our setup by magnetic field noise, mainly at 50 Hz, presumably stemming from power supplies of electrical devices in the lab and ultimately from the mains. In order to compensate for these stray fields, a new magnetic field cancellation system[30] was installed around the setup, designed by D. A. Fioretto together with technicians of the company. It consists of two sensors placed on opposite sides of the vacuum chamber, three pairs of compensation coils around the setup, and one control box containing a PID circuit for cancellation of stray fields. The sensors detect magnetic fields from DC to 5 kHz and a mixer on the controller allows the user to select the weights of each of the sensors, such that the field can be compensated at the position of the ion, which lies on the line connecting the two sensors. This system replaced an older system from the same company. The new system employs sensors that are less sensitive to temperature changes and also provides better cancelling. In addition, the compensation coils were rebuilt with smaller diameters so as to minimise their influence on a second setup on the same optical table.

Optimisation of the mixer parameters is best done by comparing the coherence time of a trapped ion for different settings. In order to measure the coherence time, a Ramsey experiment with variable waiting time between the two $\pi/2$ pulses is carried out (cf. Section 3.2). For a given waiting time, the relative phase between the two pulses is scanned, yielding a Ramsey fringe with a contrast that can be extracted from a sinusoidal fit to the ion excitation data. The contrast of the Ramsey fringes as a function of the waiting time decays with a Gaussian shape

[30] Spicer Consulting, SC24.

with the decay constant given by the coherence time [143]. We achieve coherence times of about 900 µs on the $|4^2\mathrm{S}_{1/2}, m_J = 1/2\rangle - |3^2\mathrm{D}_{5/2}, m_J = 1/2\rangle$ transition.

Although this coherence time is large enough for current experiments, in the future, the noise from the magnetic field will likely prove a limiting factor in quantum networking experiments. Such experiments can require longer experimental sequences than have been used to date. Accordingly, the following steps are recommended: the stability of the current drivers for the applied magnetic fields should be checked, and the currently used modules should be replaced by more recent ones, which include thermal stabilisation. Additionally, there might be still room for improvement in the noise cancellation system (see Section 4.2.3), by adjusting the sensor positions. If the experiment at some point in the future will be limited by the coherence time, the installation of a µ-metallic shield around the setup could be considered. Such more cost-intensive solutions have been implemented successfully in two setups of our group but would require a redesign of the optical setup of the experiment.

Table 4.2: List of the optical beams available in the setup for illuminating the trapped ions or driving the cavity. The listed direction is the direction from which the beam comes.

#	wavelength	direction	purpose	label	note
1	375 nm	south-front	loading	PI	overlapped with 397 SF
2	423 nm	south-front	loading	PI	overlapped with 397 SF
3	393 nm	north-front	driving Raman transitions	393	overlapped with 397 σ
4	397 nm	south-front	Doppler cooling	397 SF	used together with 397 NE
			and detection		for cooling; overlapped with PI
5	397 nm	north-east	Doppler cooling	397 NE	overlapped with 729 NE
6	397 nm	north-front	magnetic field alignment	397 σ	overlapped with 393
7	729 nm	north-east	qubit manipulation	729 NE	overlapped with 397 NE
8	729 nm	back	addressed qubit	729 addressing	overlapped with path
			manipulation		to CCD camera
9	729 nm	north-west	qubit manipulation	729 NW	formerly used as addressing beam
10	783 nm	west	cavity lock	783	overlapped with cavity 854
11	854 nm	north-back	repumping	854 NB	overlapped with 866 NB
12	854 nm	west	cavity driving	cavity 854	overlapped with 783
13	866 nm	north-back	repumping	866 NB	overlapped with 854 NB

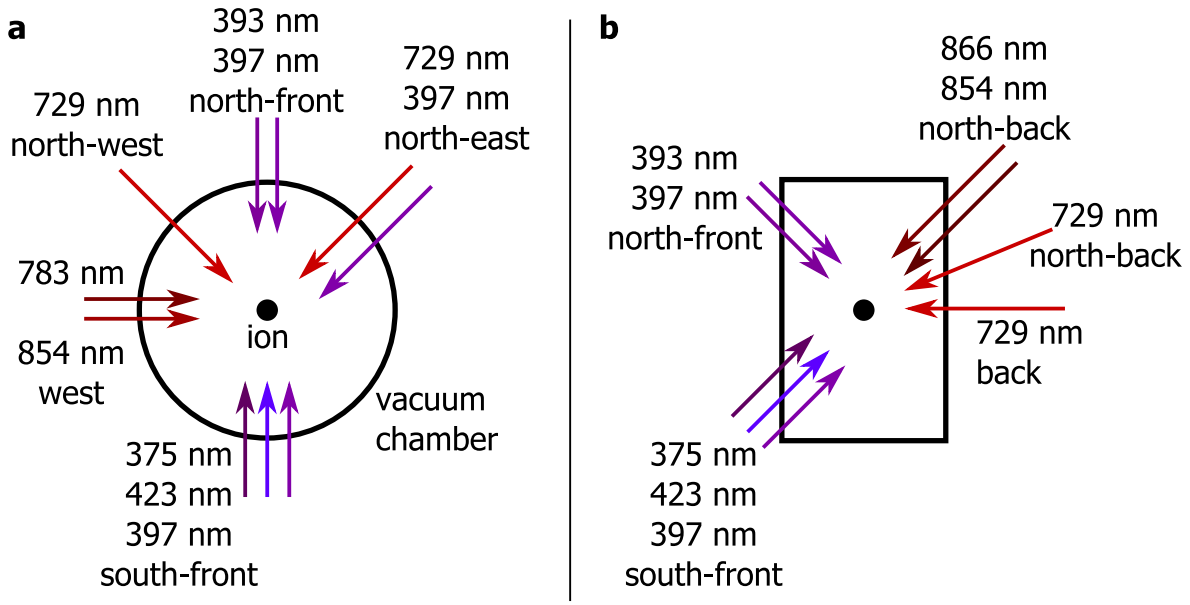

Figure 4.10: Existing optical beams in the setup. **a** View from the front. **b** View the east side. All angles are $45°$ or $22.5°$ (north-back at 729 nm).

4.3 Laser systems

The following section gives an overview of the laser systems employed in the experiment described in Chapter 5 of this thesis. As most of the lasers are used by other projects in the same lab[31], I will only present the portions of the paths that are used for our setup. All laser wavelengths are measured on a wavelength meter[32], which is specified to an absolute accuracy of 30 MHz. The target wavelengths for transitions for which this precision is insufficient are then obtained by stabilising the lasers to a stable reference cavity or even to the ion transition itself.

4.3.1 Laser beam geometry

The purpose of this subsection is to provide the reader with an overview of all laser beams available in the setup and explains the changes in the setup since it was last described in References [69, 71]. All existing beams for illuminating the ion or driving the cavity are shown in Figure 4.10. Additionally, Table 4.2 lists the beams with their purpose and the direction from which they are coming.

Since the new oven shifted in the vacuum chamber and became slightly misaligned (cf. Section 4.1) and due to the wide angular spread of the emitted calcium it, the oven has coated the lower parts of the front and back windows of the vacuum chamber with calcium (see also Appendix B.2.3). Therefore, the repumping beams at 866 nm and 854 nm had to be moved from the south-back to the north-back direction, because their transmission through the coated back window was not sufficient for repumping. There is also some calcium on the lower part of the front viewport, but less than in the back, such that sending the south-front beams along

[31] More specifically, by the quantum information project, the fibre cavity project, and us.
[32] HighFinesse, WS7.

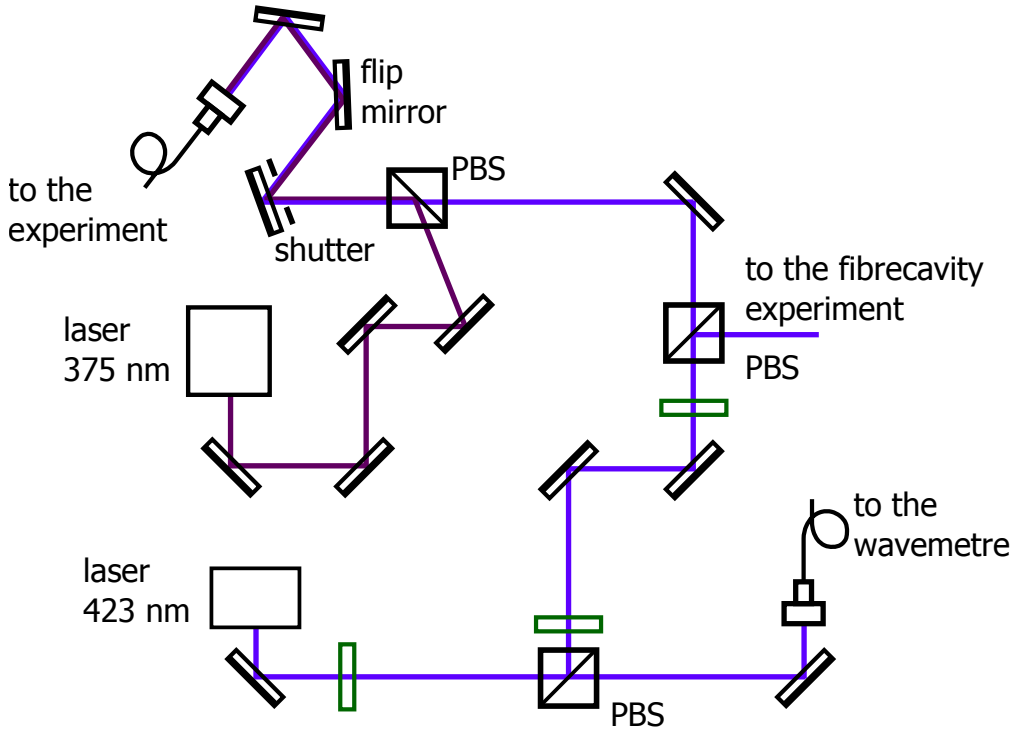

Figure 4.11: Setup of the photoionisation lasers. Light at 423 nm and 375 nm is combined on a polarising beam splitter. A remotely controlled shutter allows the experimenter to switch off the light once the desired number of ions has been loaded. The light is sent to a fibre that leads to our setup via a flip mirror. See Figure 4.2 for a definition of the symbols in the drawing.

this direction is possible with reasonable efficiency. The latest measurement of the transmission of the south-front beam at 397 nm through the whole vacuum chamber gave a transmission of 67% [Data17v], while for the north-front beam at 393 nm a transmission of only 3% was measured [Data16f]. The second beam at 397 nm, which previously had been sent to the ion from the south-east direction, was moved to the north-east because the cavity mount is blocking access to the trap centre for the south-east beam when the cavity is in the position for ion loading.

Additionally, the 729 nm north-west beam that had previously been used for addressing single ions was replaced by a new addressing beam from the back direction [142]. For the 729 north-west beam, a new fibre collimator with non-unity aspect ratio was installed, which allows the beam to be focused more tightly in the radial direction of the ion trap. With this new focusing, more homogeneous addressing on multiple ions will be possible in the future. The following sections describe the lasers used for the beams in more detail.

4.3.2 Photoionisation and Doppler cooling lasers

Photoionisation lasers at 423 nm and 375 nm

Two diode lasers[33] at 423 nm and 375 nm are used to photoionise the neutral calcium atoms coming from the oven. The first laser resonantly excites the valence electron on the $4s^2\,{}^1S_0 - 4s4p\,{}^1P_1$ transition of ^{40}Ca, which has a natural abundance $96.941(156)\%$ [144, 145]. The second laser provides the energy to excite the electron to the continuum.

Both lasers are sent from the laser table to the experimental setup in one fibre and are combined into the south-front beam path with one of the two Doppler cooling lasers in our setup. The first laser has to be resonant with the calcium transition, but the exact transition frequency depends on the angle between the laser beam and the atomic beam due to Doppler shifts since the atoms emanate from the oven with thermal velocities. The oven data sheet specifies a temperature around 600 K for the current of $3-4$ A used in our setup for loading. This temperature corresponds to a mean thermal velocity of $\sqrt{k_\mathrm{B}T/m} \approx 350$ m/s, leading to Doppler shifts up to one gigahertz with respect to atoms at rest. The correct frequency is determined by finding the atomic resonance first. For loading an ion into the trap, the wavelength of the laser at 423 nm is then scanned by approximately 200 MHz around the frequency at which atomic fluorescence has been observed. The exact wavelength of the laser at 375 nm does not matter. Figure 4.11 shows the setup of the photoionisation lasers. Both lasers are shared between our setup and two other projects in the same lab.

The light flux to the setup can be blocked via a homebuilt shutter, remotely controlled from the experiment control desk. This allows one to quickly switch off the photoionisation beams such that no further ion is loaded into the trap beyond the desired number. A homebuilt switch selector controls which of the three setups can use the shutter. Because of this switch and because of the different Doppler shifts in the different setups, it is currently not possible that all three projects load at the same time. In the future, it might be desirable to rebuild the laser setup in such a way that all three projects can couple both wavelengths to their respective optical fibre independently from the other setups as well as to control the frequency of the laser at 423 nm.

Doppler cooling laser at 397 nm

The laser employed for Doppler cooling on the $4^2S_{1/2} - 4^2P_{1/2}$ transition at 397 nm used to be a Ti:sapphire laser[34] at 794 nm, pumped by a diode-pumped, frequency-doubled solid-state laser[35] at 532 nm. The output of the Ti:sapphire laser was then frequency-doubled[36]. This setup was replaced in November 2017 by a fully integrated diode laser and frequency doubling system[37] consisting of a laser head, a tapered amplifier (TA), and a frequency doubler. The output of this system is shared between three setups. Figure 4.12 shows the setup.

On the laser table, the light is split into three paths for the three setups. The light frequency in each path is then upshifted by 160 MHz via a double-pass acousto-optic modulator (AOM). The light is brought from the laser table to the experiment table via an optical fibre. On the

[33] Toptica, DL 100.
[34] Coherent, CR-899-21.
[35] Coherent, Verdi V10.
[36] Spectra Physics, LAS. See, e.g., Reference [67] for a detailed description of this old setup.
[37] Toptica, TA SHG Pro. The system was taken over from the SQIP/EQuAL project in our group.

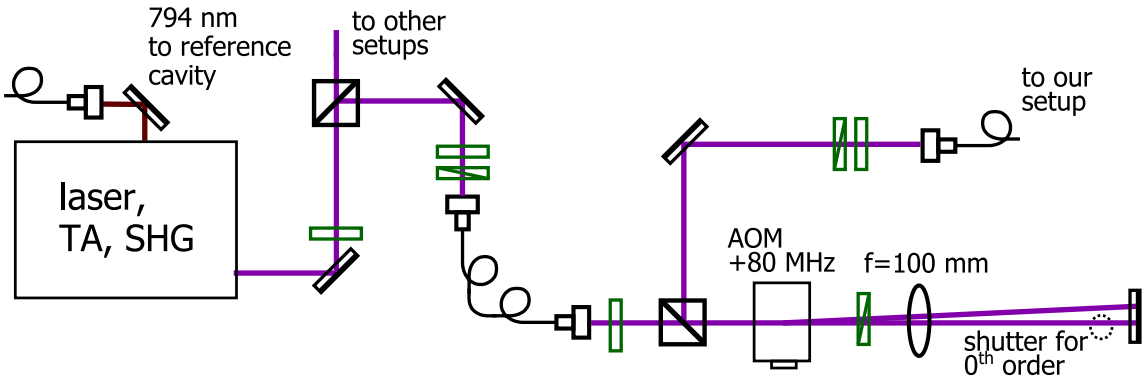

Figure 4.12: Setup of the laser for Doppler cooling at 397 nm. Light from the laser is sent through a short fibre for decoupling the alignment of the laser from the rest of the beam path. Following optional frequency shifting via an AOM, the light is sent to the setup.

experiment table, the light is split into two paths, the frequency of which is upshifted again by one single-pass AOM in each path by 80 MHz. The $+1$ order diffraction beams of each of these AOMs are then sent to the ion, one from the south-front direction, the other from the north-east direction. The south-front beam is overlapped with the photo-ionisation lasers on a polarising beam-splitter (PBS): The beam at 397 nm is transmitted through the PBS, while the photoionisation beams are reflected. The reflection of the beam at 397 nm at this beam splitter can be used for other purposes, if, e.g., another beam is required for trouble-shooting or tests.

Additionally, the zeroth order diffraction beam of the AOM for the south-front beam is sent to another independent single-pass AOM, and after upshifting by 80 MHz, this light is sent to the ion from the north-front direction, overlapped with the laser beam at 393 nm on the $S_{1/2} - P_{3/2}$ transition (see Section 4.3.4). This beam is referred to as the "σ beam" since for the magnetic field configuration used most often in the past experiments (see Section 4.2.3), this beam propagates along the quantisation axis. With the correct polarisation setting, this beam can thus be used to drive σ transitions on the $S_{1/2} - P_{1/2}$ transition, which may be used to optically pump the ion to either the $|j = 1/2, m_j = -1/2\rangle$ or the $|j = 1/2, m_j = +1/2\rangle$ state in the $S_{1/2}$-manifold. This beam is an important tool for checking the direction of the magnetic field, but in standard experiments, in contrast to the south-front and the north-east beams, it is not used regularly.

Both the south-front and the north-east beams are used for Doppler cooling, but only the south-front beam is used for detecting the state of the ion. The reason for using two beams for Doppler cooling is explained in detail in Section 5.2 in Reference [69]. In short, the axes of the two radial modes of our trap oriented such that neither of the two beams would have sufficient overlap individually with both modes to be able to cool both of them sufficiently. For this reason, a second beam was installed. With these two beams, however, interference between the two beams due to their polarisations not being perfectly orthogonal was observed as a modulation of the ion's fluorescence signal (see section 5.4 in Reference [71]). In order to solve this issue, only the south-front beam is used during detection, and additionally, the 80 MHz frequency for the AOM of the north-east beam is mixed with a sinusoidal signal of 1.5 MHz at an amplitude

of 1.10 V (peak-to-peak) from a frequency generator[38]. This modulation leads to sidebands at 78.5 and 81.5 MHz in the north-east beam. These frequency shifts are sufficiently far away from the 80 MHz of the south-front beam to suppress the interference effects during Doppler cooling but close enough to be able to cool the ion, as the full width at half maximum (FWHM) of the transition is 21.4 MHz (cf. Section 4.2). Doppler cooling is explained below in Section 4.2.1.

The laser at the fundamental wavelength of 794 nm, i.e., before frequency-doubling, is locked to a stable reference cavity [146], using a Pound-Drever-Hall (PDH) scheme [147, 148]. The reference cavity contains four separate mirror pairs on the same spacer: one mirror pair is used for the 794 nm laser, two pairs are used for the repumping lasers (see below), and one mirror pair is unused. Locking the laser to this cavity narrows the linewidth of the laser to around 10 kHz, but the linewidth is not crucial for this laser as the atomic line is much broader. The length of the reference cavity is controlled via a piezo on which one of the mirrors is mounted, while the voltage applied to this piezo is controlled either remotely via a programme[39] on the control computer of the Linear Trap project or via the offset on the homebuilt high-voltage amplifier over the laser table. Please note that changing this voltage affects all of the three projects in the lab. Any changes should therefore be agreed on first by all lab workers concerned.

Repumping lasers at 854 nm and 866 nm

Since the ion's states in the $4^2P_{1/2}$ manifold have a branching ratio of about 6.4% for decay to the $3^2D_{3/2}$ manifold (cf. Section 4.2), another laser at 866 nm is necessary for Doppler cooling to repump population from the $3^2D_{3/2}$ manifold to the $P_{1/2}$ manifold and thus close the cooling cycle. When using a qubit, i.e., when bringing population to the $3^2D_{5/2}$ manifold either via the laser at 729 nm or via a Raman transition involving the laser at 393 nm and the cavity mode, it is also necessary to repump this population with a laser at 854 nm to the fast-decaying $P_{3/2}$ manifold at the end of each experimental cycle, since the lifetimes of these qubit states are on the order of one second. For these two purposes, two diode lasers at 866 nm[40] and 854 nm[41] are used. The laser at 866 nm includes a laser head as well as a tapered amplifier. Both of these lasers are shared between three projects. The setup is shown in Figure 4.13.

Each of these lasers is locked to a mirror pair in the same reference cavity setup that is also used for the Doppler cooling laser (see above). The linewidths of the laser at 854 nm is thus narrowed to around 10 kHz on a timescale of seconds [Data15a]. The linewidth of the laser at 866 nm has not been measured. Unfortunately, the reference cavity setup has no temperature stabilisation inside its vacuum chamber, which limits the frequency stability of these lasers to time scales of hours. A comparison between the cavities of the repump lasers and the temperature-stabilised cavity of the laser at 786 nm yielded a relative drift rate of about 20 kHz/min, measured over ten minutes [Data15c]. Both beams are sent to the ion from the north-back direction. They are linearly polarised, such that they drive σ^+- and σ^--transitions to avoid population trapping in dark states of the $3^2D_{5/2}$ and $3^2D_{3/2}$ manifolds.

[38] Grundig, FG 100.
[39] "Laser scan_LIN.vi", based on LabView.
[40] Toptica, TA pro.
[41] Toptica, DL 100.

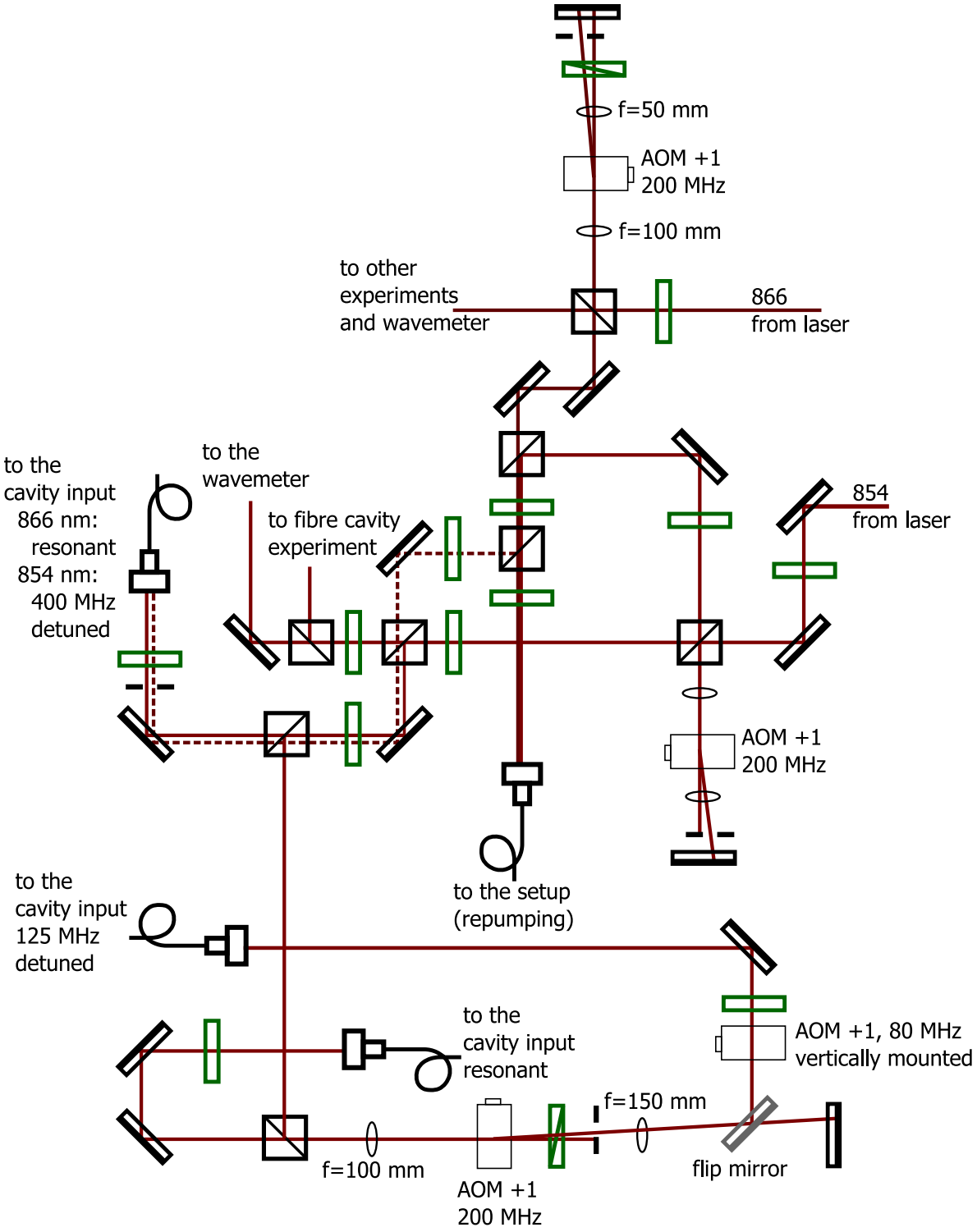

Figure 4.13: Setup of the lasers at 866 nm and 854 nm for repumping. Resonant light at 866 nm and 854 nm can be sent to the ion via the fibre labelled "to the setup (repumping)". Resonant light at 866 nm and light of different detunings at 854 nm can be sent to the cavity input. The beam paths for sending light at 854 nm resonant or 125 MHz detuned to the cavity input are new.

4.3.3 Laser at 729 nm for manipulating ion qubits

The Ti:sapphire laser setup at 729 nm for driving the qubit transitions between the $4^2S_{1/2}$ and $3^2D_{5/2}$ manifolds has changed since its most recent description in B. Casabone's thesis from 2015 [71] and is described in great detail in R. Stricker's master's thesis [149]. It[42] is pumped by a diode-pumped solid state laser[43], and the output of the Ti:sapphire laser is split into four paths: one going to the wavelength meter, one to the high-finesse reference cavity, one to the setup of the quantum information project and our setup, and one to the fibre-cavity experiment. Since the quadrupole qubit transition has a width of ~ 1 Hz (cf. Section 4.2), the laser linewidth needs to be stabilised to a similar width. This is achieved by a three-stage locking scheme: The error signal from a Pound-Drever-Hall-scheme to the high-finesse cavity is fed back to the fast-response piezo of one intra-laser cavity mirror as well as to a slow-response piezo for drift compensation. Additionally, an AOM is used for fast feedback. With this setup, an in-lock linewidth of $3.6(4)$ Hz was achieved (averaged over 4 s) [149]. The laser setup and the ultra-stable reference cavity are each set up in an acoustically insulated box on a vibration isolation platform, so as to suppress acoustic noise. In addition, the temperature in the insulated boxes is stabilised, and the acoustic noise generated in the fibres that bring the light to the setups is cancelled, following Reference [150].

Once the laser light is on the experiment table, our path is split off from the light going to the quantum information setup. This light is amplified in a fibre-coupled tapered amplifier[44]. With an input power of typically 20 mW, we get an output power of the TA of around 120 mW. After the TA, the intensity of the light is stabilised with an 80 MHz AOM in zeroth order[45]. Next, the light frequency is upshifted in a double-pass AOM by 270 MHz. This AOM is used for spectroscopy of the quadrupole transitions. Behind the double-pass AOM, the light is split into three paths for the three laser beams in our setup: The beam coming from the double-pass AOM is either shifted or not shifted by a single-pass 80 MHz AOM. If it is not shifted, it will be coupled to the fibre for the addressing beam. If it is shifted, it is sent to the north-west beam if a flip mirror is flipped up or to the north-east beam if not. In each of these beams, the frequency is shifted by an 80 MHz AOM so that all three beam paths bring light of the same frequency to the vacuum chamber. The setup is shown in Figure 4.14.

The three beams propagate towards the ion from the north-east direction, the north-west, and the back. The north-east beam and the north-west beam are both global beams, i.e., the beam waist of each beam at its focus is on the order of tens of micrometres, so that several ions can be illuminated since the typical separation between two trapped ions is only 5 µm. These beams can therefore be used for global rotations of several qubits. The beam from the back was installed in the course of M. Teller's master's thesis [142]. It is focused to a waist of about 3.5 µm with a custom objective [146, 141], which allows the experimenter to address only one of several ions. Such a beam can be used for addressed operations on only one qubit at a time. An electro-optic deflector (EOD)[46] can be used to select which of several trapped ions is addressed. This feature has not yet been used, but will be required for future experiments.

[42] M Squared, SOLSTIS-PSX.
[43] Lighthouse Photonics, Sprout G.
[44] Toptica, BoosTA Pro.
[45] See electronic lab blog entry of 20161128 for details.
[46] Leysop Ltd., ED2-25-AR729.

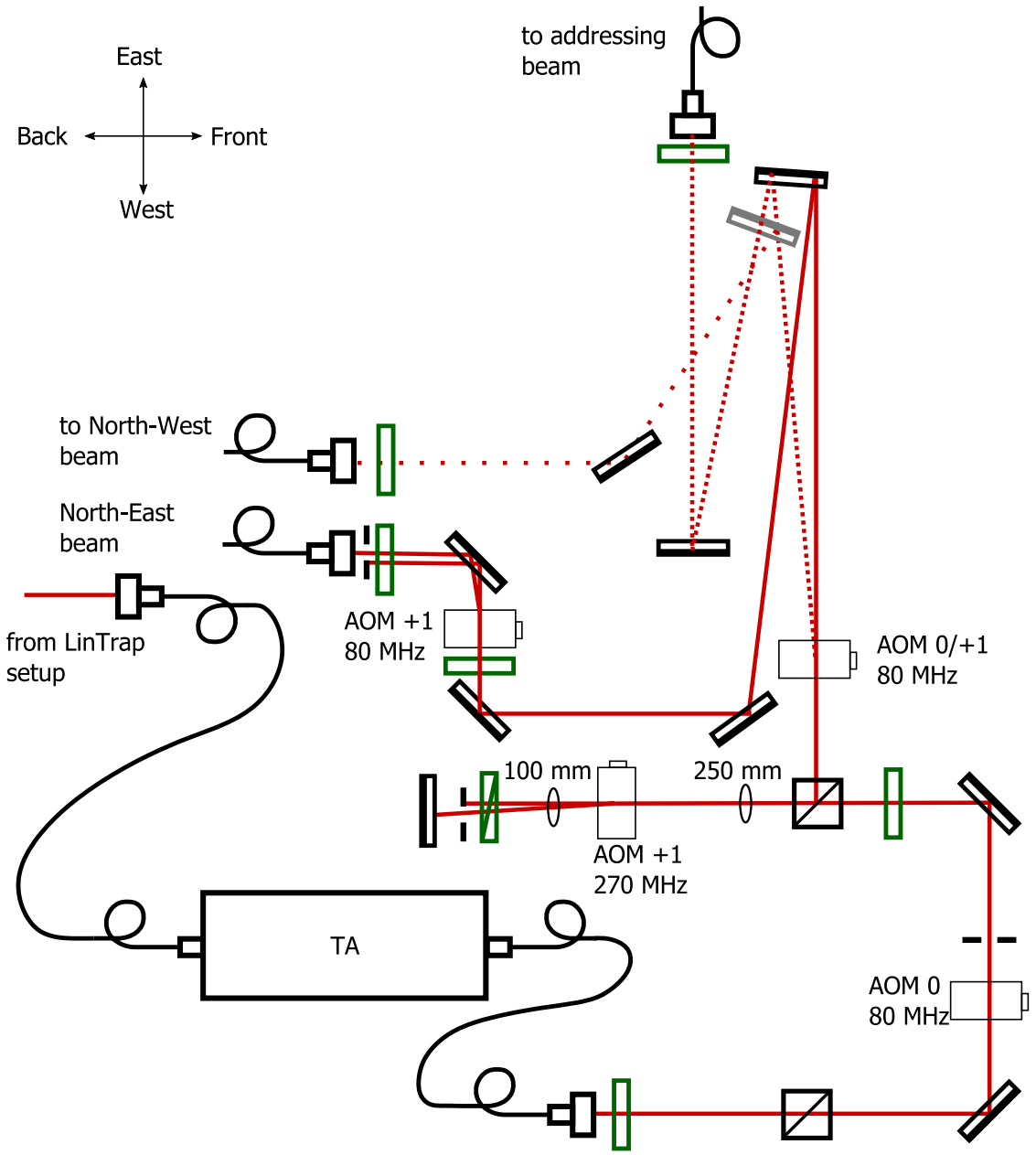

Figure 4.14: Setup of the laser path at 729 nm. The light can be sent to three different beams via the first single-pass AOM at +80 MHz and a flip mirror. Note that the AOM for the north-east beam is positioned very close to the fibre collimator: In this way, bichromatic light can be coupled efficiently into the fibre, i.e., two orders of diffracted light when the AOM is fed two RF signals with different frequencies. Such bichromatic light is required for driving entangling gates on multiple ions (see, e.g., chapter 5.8 of Reference [71] for an implementation).

4.3.4 Raman laser at 393 m and cavity lock laser at 783 nm

Setup

Another Ti:sapphire laser[47] is used for driving Raman transitions between the ground state of the ion and states in the $3^2D_{5/2}$ manifold. The wavelength of 786 nm of this laser is frequency-doubled[48] to 393 nm, the wavelength of the $4^2S_{1/2} - 4^2P_{3/2}$ transition. The frequency of the Ti:sapphire laser is stabilised to a stable reference cavity, while the doubler cavity is locked to the fundamental wavelength. The output of the laser is split into four paths: path one ends in a photodiode and provides a signal that is required for the lock of the laser (see below); path two is the input of the frequency doubler; the light in path three is sent to the wavelength meter; and path four goes to the reference cavity.

The output of the frequency doubler is again split into two paths: in one path ("Raman path"), the light frequency is shifted such that the light arriving at the ion is 400 MHz red-detuned from the $4^2S_{1/2} - 4^2P_{3/2}$ transition, while in the other path ("resonant path"), the light is resonant with the transition. In the Raman path, the light is first frequency-shifted by a double-pass AOM by -160 MHz (two -1 order shifts) and then again by -80 MHz by a single-pass AOM. The input to this AOM is either a single frequency or two frequencies for, e.g., generating entanglement between ions and photons [72] or mapping the quantum state from an ion onto a photon [73]. In total, the shift of the light in this path therefore is -240 MHz. In the resonant path, the light is shifted by $+160$ MHz in a double-pass AOM. Thus, the difference between the two paths adds up to 400 MHz, with the light in the Raman path red-detuned relative to the light in the resonant path. Light from the resonant path is used for aligning the 393 nm laser beam to the ion.

Both paths are then recombined on a polarising beam splitter and coupled to an optical fibre, which brings the light to the experiment table. On this table, the polarisation of the light is adjusted with a half- and a quarter-waveplate, and the light is focused onto the ion.

The same table also hosts a diode laser[49] at 783 nm. This laser is locked to the same reference cavity as the Raman laser and via a transfer lock scheme the length of the cavity in the setup is stabilised to this laser (see 4.4.2). For historical reasons, this laser is sometimes still referred to as the "785 laser", although it is now used at a wavelength of 783 nm.

Note that a second Ti:sapphire laser with frequency doubler[50] belonging to the fibre cavity project was successfully tested in our setup for driving Raman transitions. This laser is stabilised to a temperature stabilised reference cavity[51]. Due to its superior long-term stability relative to the diode repumping lasers (see below), this laser was used in the experiment described in Chapter 5 with its fundamental wavelength tuned to 854 nm.

Frequency stabilisation

In order to be able to efficiently drive Raman transitions, the frequency of the laser should be stabilised to much less than the full cavity linewidth, i.e., to less than 100 kHz (cf. Section 4.4).

[47] Coherent, 899-21, pumped by a Verdi V10.
[48] Coherent, MBD-200.
[49] Toptica, DL Pro.
[50] Msquared, SolsTiS, with doubler ECD-X.
[51] Stable Laser Systems, VH6010-4 and ATF-6010-4.

The setup for this stabilisation is explained in detail in References [67, 69]. In short, there are three branches: a Pound-Drever-Hall signal, derived from the reflection of the laser off a reference cavity, is fed back via a proportional-integral-differential controller (PID) into the laser, where it is used to control the position of a piezo-mounted mirror, a glass plate (Brewster plate) and an intra-cavity EOM. The two poles of the EOM are connected on the one hand to the error signal from a PID controller and on the other hand to the error signal directly for fast feedback.

The reference cavity sits on the same table as the two lasers and is housed in a box for temperature stabilisation. The two lasers enter the cavity from the two opposite sides and with orthogonal polarisations. Locking both lasers to the same cavity suppresses frequency drifts between the Raman laser and the resonance of the experiment cavity via the transfer lock laser. According to Reference [64], the cavity was taken over from a setup by H. Rohde [151]. It is mounted inside a vacuum chamber, which is continuously pumped with an ion getter pump[52] to high vacuum. The cavity mirrors, which have radii of curvature (ROCs) of 50 cm, are optically contacted to a horizontally mounted spacer of length 20 cm, of an unknown material. This cavity length determines the free spectral range (FSR) of 1.5 GHz. The cavity has a full width at half maximum (FWHM) linewidth of 130 kHz at 783 nm [Data14].

The temperature stabilisation box has been replaced recently since the old box had unsatisfactory temperature stability. While the old box consisted of simple aluminium walls a few millimetres thick with styrofoam taped on the outside, the new box consists of 2 cm of wood on the outside, an insulating layer of polystyrol (3 cm) and the old aluminium walls (1.5 mm) on the inside. Reusing the old walls allowed us also to recycle the old heating resistors, which are glued to the aluminium panels. The box is shown in Fig 4.15.

There is an additional stabilisation circuit with heating resistors glued to the vacuum chamber which contains the reference cavity. Each temperature regulation circuit is controlled by a PID controller[53], which takes the signal of a temperature sensor[54] as input and provides the current for the heating resistors. Since there are no cooling elements, the temperature has to be stabilised to a setpoint above room temperature. The outer circuit, i.e., the one for the box, is set to a temperature of 22°C, while the temperature of the vacuum chamber itself is stabilised to 21°C. A temperature stability of about 50 mK can be achieved for time scales of several hours to days, which is sufficient for our purposes. If the cavity spacer were made out of ultra-low expansion (ULE) material, it would be important to stabilise the setup to the zero-crossing temperature of that material (cf., e.g., Chapter 3.3.3 of Reference [86]). However the spacer material is unknown in our case [152], such that the absolute temperature setpoint is not important. Overall, this setup guarantees sufficient stability for the experiment, i.e., working with the Raman and transfer lock lasers over several hours is possible without the need to compensate for frequency drifts.

When locked, the linewidths of these lasers are stabilised to about 30 kHz over time scales of seconds, as estimated from the lock error signal [Data12, Data14]. The locking setup is described in detail in References [67, 69] but is currently being overhauled and simplified by D. A. Fioretto and M. Teller.

[52] Varian, StarCell.
[53] Thorlabs, TED200C 12W.
[54] AD590 temperature transducer.

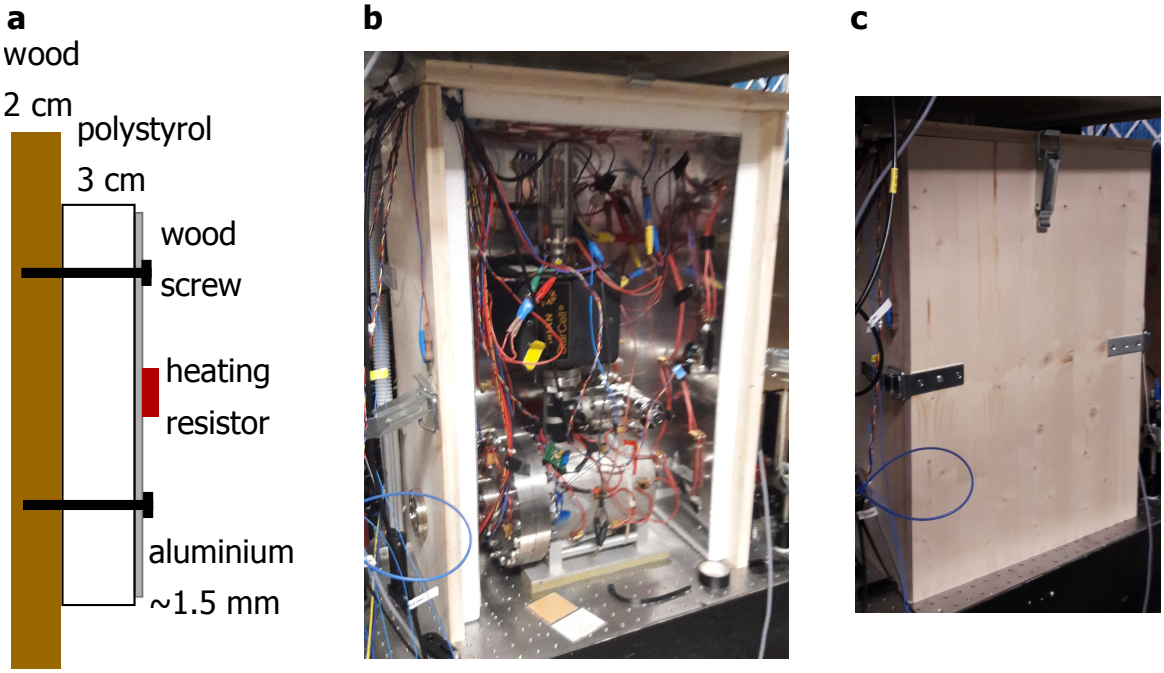

Figure 4.15: The temperature stabilisation box for the reference cavity for the Raman and transfer lock lasers. **a** Cut through the box walls. **b** Picture of the open box from the front side, showing the vacuum vessel and ion pump inside as well as the cabling for the heating resistors and the temperature sensors. **c** Image of the box with the front closed.

4.4 Cavity setup

This subsection contains a description of the cavity in our setup and its properties. The cavity, assembled for the first time during C. Russo's thesis work [64], was rebuilt in 2015, as it had been damaged due to a vacuum leak. In order to maximise the coupling strength between ion and cavity mode, the cavity has been designed to work in the near-concentric regime. A more detailed description of the construction of the cavity can be found in Appendix B.

The cavity consists of two macroscopic superpolished convex substrates[55] with radii of curvature (ROC) specified to 10 mm. The substrates are coated with dielectric coatings[56] for high reflectivity at 866 nm and 854 nm. Each mirror substrate is glued[57] into a stainless steel ring in order to distribute the gluing stress evenly around the mirror to minimise birefringence [153][58]. The rings are glued onto piezo stacks, which in turn are glued into piezo holders (see Appendix B for details on the glue used). Both of these holders sit on a U-shaped mount. The mount provides a collimating hole for the calcium beam from the oven and in turn sits on slip-stick piezo translation stages[59] for movement in the front-back and the east-west directions. Figure 4.16 shows an image of the setup.

Alignment along the third dimension, in the north-south direction, is achieved either via

[55] REO Inc.
[56] REO Inc.
[57] Epotek 353 ND.
[58] See References [154, 155] and references therein on birefringence in dielectric mirrors.
[59] Omicron, MS5; controller: Omicron, MSCU.

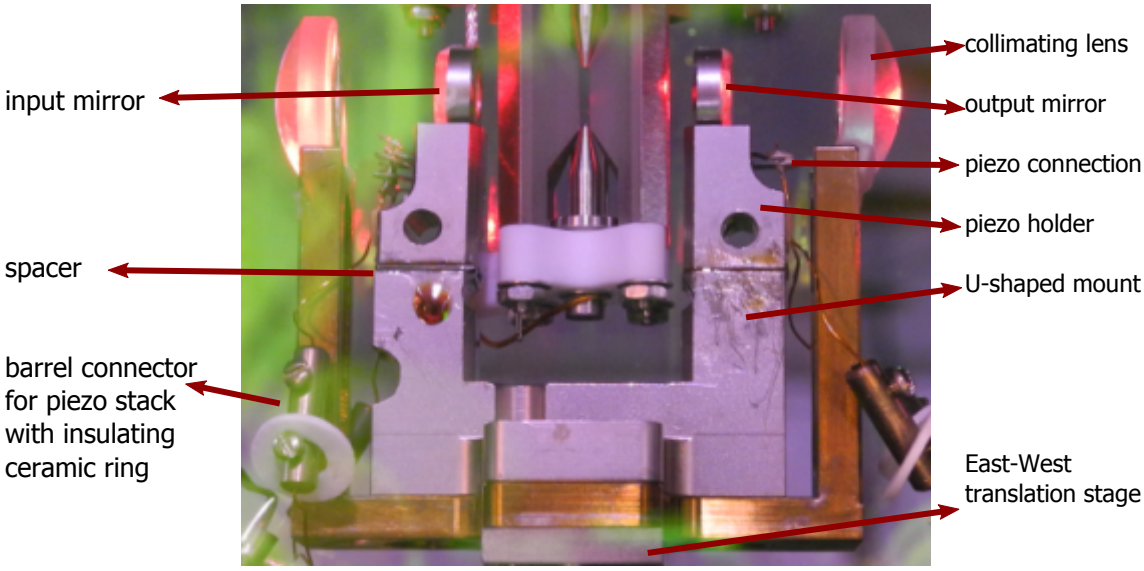

Figure 4.16: Image of the cavity with explanation of the different parts. Cf. also Figure 4.3.

three micrometre screws on the bottom flange of the chamber, by which the cavity mount is translated or tilted, or by moving the ion along the trap axis via the voltages applied to the endcaps. More details on how the cavity mode is aligned to the ion is provided in Section 4.5.

The piezo stacks are used for controlling the cavity length and thereby for tuning the cavity's resonance frequency (see Section 4.4.2), while the translation stages are used for aligning the cavity mode to the ion. The maximum voltage that can be applied to the stacks is ± 250 V [64]. The piezo stack of the west mirror ("slow piezo") consists of six individual layers, which results in a stroke of about 1.6 µm for a voltage difference of 400 V. This stack is used for tuning the cavity into resonance and compensating slow temperature-related drifts of the cavity length. The east piezo stack ("fast piezo") consists of only two layers, which results in a higher bandwidth but a reduced stroke of about 0.5 µm for a voltage difference of 400 V. This stack is used for active feedback on the cavity length.

Light from several sources is sent into the cavity input:

- Light at 783 nm for length/frequency stabilisation.
- Light at 854 nm, red-detuned from the ion's transition by 400 MHz, derived from the repumping laser. This light is used for finding the correct cavity resonance for driving Raman transitions in the ion.
- Light at 854 nm, resonant with the ion's transition, derived from the repumping laser. This light is used to find the cavity modes resonant with the ion transition.
- Light at 854 nm, with red detuning from the ion's transition tunable around 160 MHz, derived from the repumping laser. This light was used for preliminary measurements for the experiment described in Chapter 5, but not used in the final measurement due to the relative drift of the repump lasers's reference cavity with respect to the reference cavity to which the experiment cavity is locked.

- Light at 854 nm, variable detuning, derived from the Ti:sapphire laser of the fibre cavity project. This light was used for the experiment described in Chapter 5. In contrast to the previous light source, this light has lower drifts (due to a more stable reference cavity and a lower intrinsic linewidth.
- Light at 866 nm for repumping the ion during alignment of the cavity (see Section 4.5). This light is used for finding the cavity position in which the ion is coupled to the cavity's TEM_{00} mode (see Section 4.5).

The input path of the cavity is shown in Figure 4.17.

4.4.1 Properties of the cavity

Cavity mode finesse

Before the vacuum leak, the cavity had a finesse of $77,000$ at a wavelength of 854 nm [69]. After the vacuum accident and the repair of the cavity, it was found that adjacent TEM_{00} modes have different finesse values [Data17n]. For the usual laboratory temperature of 21°C, three such modes are accessible within the range of the piezos. Their properties are displayed in Table 4.3.

Table 4.3: List of properties of the cavity modes accessible in our setup.

#	finesse[60] $\mathcal{F}/10^3$	$\kappa/(2\pi$ kHz)	FWHM/$(2\pi$ kHz)	quality factor $Q/10^9$
1	32.2(2)	116(1)	233(2)	1.51(1)
2	54.8(4)	68.4(6)	137(1)	2.57(2)
3	70.2(3)	53.4(4)	106.8(7)	3.29(2)

The finesse of these modes increases with decreasing cavity length (increasing voltage applied to the piezo). Accordingly, there are more losses for modes with larger cavity length. This behaviour can have several causes:

- The mirrors might be damaged or contaminated away from the cavity axis. A mode with larger cavity length will have a larger spot size on the mirror. Therefore, if a defect exists at the periphery of the mirror, only modes with sufficiently large spot size on the mirror will be affected by such a defect or contamination. Since testing this hypothesis would require opening the chamber and inspecting the mirrors optically with a microscope, we have not tried to solve this issue. Should the setup have to be opened in the future, cleaning the mirrors and inspecting their surfaces is recommended.
- The higher losses at larger cavity lengths might be caused by coupling of the TEM_{00} mode to higher order modes due to deviations of the mirror surface from the perfect spherical shape. A comparison between the TEM_{00} mode frequencies with higher order mode frequencies might provide more insight into this hypothesis. F. Kranzl investigated this effect in his master's thesis in fibre cavities [156].

[60] Data are [Data17n]. Uncertainties calculated as $\sqrt{\sum_{n=1}^{N} (\Delta\mathcal{F}_n)^2}/N$, where $\Delta\mathcal{F}_n$ is the uncertainty of the finesse of the nth measurement, extracted from an exponential fit to the ring-down signal, and N is the number of measurements.

- The effect might be caused by a misalignment between the cavity axis and the axis of movement of the cavity mirrors on the piezo stacks. If the piezo stacks have a lateral component of movement, increasing the length of the cavity will cause a misalignment of the cavity mirrors with corresponding clipping losses. This effect might be investigated by observing the position of the mode on one of the mirrors via the transmitted beam. A similar effect has been observed in the second macroscopic CQED setup, recently set up at IQOQI Innsbruck in B. Lanyon's team [157].

A dependence of the finesse on the polarisation of the cavity input field was observed in an initial measurement [Data15b], but could not be reproduced in a second measurement [Data17n]. In addition, we have not observed any indication of birefringence in our cavity (cf. also Chapter 4.3 in Reference [69]). Modes with higher finesse values cannot be accessed in our setup, since the voltage applied to the piezos should not exceed 250 V. Modes with lower finesse are accessible, but not useful in experiments.

For our cavity, the transmission values were measured by C. Russo as $1.3(3)$ ppm for the west mirror and $13(1)$ ppm for the east mirror, with total losses of $68(2)$ ppm [64]. They were not remeasured during the rebuild due to lack of time. However, the high apparent precision, i.e., low uncertainty of the west (input) mirror led in the past to doubts about these values [69]. In fact, the measured photon detection efficiency at the cavity output was shown to be incompatible with these numbers (cf. chapter 4.2 of Reference [71]). Accordingly, we estimate that the transmission values are actually $1.3(30)$ ppm and $13(3)$ ppm. Here, the uncertainties were estimated such that the observed efficiency can be explained by the value and its uncertainty (see also Section 4.6.1).

FSR, mode waist, and coupling strength

The free spectral range of the cavity was remeasured after the rebuild by scanning a laser at 854 nm over several free spectral ranges and noting the frequencies of the laser on the cavity resonances as measured with the wavelength meter as [Data16d][61]

$$\mathrm{FSR} = 7.50(3)\ \mathrm{GHz}.$$

The imprecision of this result is caused by two facts: On the one hand, the diode laser employed in the measurement (also used for repumping) could not be scanned very far, so only eight cavity resonance frequencies were measured. On the other hand, the precision of the wavelength meter used for measuring the frequency difference between adjacent laser-cavity resonances is limited to 30 MHz. A more precise measurement could be done in the future with a wide-range tunable Ti:sapphire laser and/or a more precise wavelength meter. From the measurement of the FSR, the length of the cavity can be calculated, resulting in a value of

$$L = 19.98(7)\ \mathrm{mm}.$$

Compared to the cavity before the rebuild, the cavity length is unchanged within the uncertainty.

By scanning the cavity around the TEM_{00} mode at frequency ν_{00} and measuring the resonance frequencies ν_{01} and ν_{10} of the TEM_{01} and the TEM_{10} modes, we obtained values of

[61] Cf. Reference [70] for the measurement method.

Table 4.4: Cooperativities and photon lifetimes for the three accessible modes. The atomic decay is given by $\gamma = 2\pi \cdot 10.7$ MHz.

#	finesse $\mathcal{F}/10^3$	cooperativity $g_0^2/(2\kappa\gamma)$	photon lifetime τ_c/µs
1	32.2(2)	0.943(8)	0.686(6)
2	54.8(4)	1.60(1)	1.16(1)
3	70.2(3)	2.05(2)	1.49(1)

$\nu_{01} - \nu_{00} = 275.0(6)$ MHz and $\nu_{10} - \nu_{00} = 255.3(5)$ MHz [Data16c]. The splitting of the two modes is interpreted as coming from an ellipticity of the mirror surface. These values can be used to check the specified value for the radius of curvature by numerically solving Equation 3.7 for the radius of curvature. The obtained value (the average of the values obtained from the two frequencies) is

$$R = 10.02(5) \text{ mm}.$$

This value agrees with the specified value and with the one reported in Reference [70].

Next, using the length and the radius of curvature, it is possible to calculate the waist of the TEM_{00}-mode according to Equation 3.10 as

$$w_0 = 12.4(5)\ \mu\text{m}.$$

This value is overlapping with the corresponding number of the cavity before the rebuild within the uncertainties [70]. From the length and the radius of curvature, the minimum mode volume (cf. Equation 3.11) can be calculated as $V_0 = 2.4(2)\cdot 10^{-12}$ m^3 $= 3.9(3)\cdot 10^6 \cdot \lambda^3$ for $\lambda = 854$ nm.

Given the length and the radius of curvature and the coupled $4^2P_{3/2} - 3^2D_{5/2}$ transition in calcium, using Equations 3.9 and 3.10, we calculate the maximum possible value of the coupling strength g_0:

$$g_0 = 1.53(30) \text{ MHz}$$

This value is overlapping within the uncertainties with the corresponding value before the accident [70]. The uncertainty in the coupling strength is determined by the uncertainty in the length measurement via the free spectral range. The cooperativities $g_0^2/(2\kappa\gamma)$ for the three accessible modes, calculated with this maximum coupling constant, are given in Table 4.4 together with the corresponding photon life times.

Temperature sensitivity

As already mentioned in Section 4.1, the cavity is sensitive to the temperature of the calcium oven. In addition, the seasonal changes of the outside temperature are mitigated but not completely eliminated by the air conditioning system. These fluctuations also influence, e.g., which modes of the cavity are within range of the piezo voltage. However, the influence of the oven is largest.

During ion loading, which typically takes two to ten minutes, the cavity expands to such an extent that even the mode #1 is not within range of the piezo voltages. It takes around two hours for the cavity to cool down such that the drift of the cavity resonance is slow enough and coupling an ion to the cavity is possible. Although this proved an issue while the ion lifetimes were shorter, with current lifetimes it is no longer a limitation for single-ion experiments.

4.4.2 Cavity length control and lock

Cavity length control

In order to control the cavity-ion detuning, the length of the cavity needs to be precisely controlled. For this purpose, voltages are applied to the piezo stacks of the two cavity mirrors. These voltages are derived from batteries and controlled by a circuit ("battery box") described in Appendix A.10. This box has been modified since it was last described in Reference [69].

In the past, 300 V batteries[62] were used, but this product has become obsolete and a company[63] producing a replacement and located in the United States of America was not willing to ship to Europe. We therefore currently use two packs of 30 block batteries at 9 V each, one block for the slow piezo stack and one for the fast piezo stack. Since working with many 9 V batteries for controlling the cavity piezos is not very convenient, a quiet amplifier is currently developed to replace the battery box, following Reference [158].

The actual voltage applied to the piezo stacks can be adjusted via potentiometers. It is possible either just to change the length of the cavity (e.g., for finding the resonance with the laser at 854 nm) by applying a voltage to the slow piezo stack, or to move both piezo stacks by the same amount. The second option can be, e.g., used for testing the localisation of the ion in the standing wave of the cavity (see Section 4.5). The battery box can also be used to apply a time-varying voltage, derived from a function generator[64], to the fast piezo stack for scanning the cavity length.

Cavity locking setup

The cavity is locked to the stable reference cavity described in Section 4.3.4 via a transfer lock. A schematic of the setup is shown in Figure 4.17. A Pound-Drever-Hall-scheme is used for locking the cavity length to the frequency of the transfer lock laser at 783 nm. A function generator[65] provides a local oscillator for the lock at 16.34 MHz [Data16e]. Its output is split[66] and sent to the electro-optic modulator[67] in the transfer lock laser beam before the cavity input and to the mixer for deriving the error signal. The light reflected from the input cavity mirror is detected with a fast photodiode[68], whose signal is mixed down[69] with the local oscillator signal to generate the error signal.

The error signal is next fed into a PID controller[70], the output of which is filtered in several stages[71]. This filtering setup was found to be necessary for suppression of acoustic resonances of the cavity and its mount. The digital filter used here is based on the code described in

[62] Eveready Battery Company Inc.
[63] Exell Battery.
[64] Black Star, Jupiter 2000.
[65] SRS, DS345.
[66] Minicircuits, ZSC-2-1+.
[67] Qubig, EO-13L3-NIR.
[68] NewFocus, 1801-FS; bandwidth 125 MHz.
[69] Minicircuits, ZAY-1+.
[70] SRS, SIM960.
[71] RedPitaya, digital notch filters (centred at 6.6 kHz and 12.0 kHz with widths 3.2 kHz, and 4.0 kHz, respectively) and low-pass filter (cut-off frequency 4.8 kHz); Thorlabs, 10 kHz low-pass filter; variable gain amplifier, homebuilt, maximum gain $\sim$ 20.

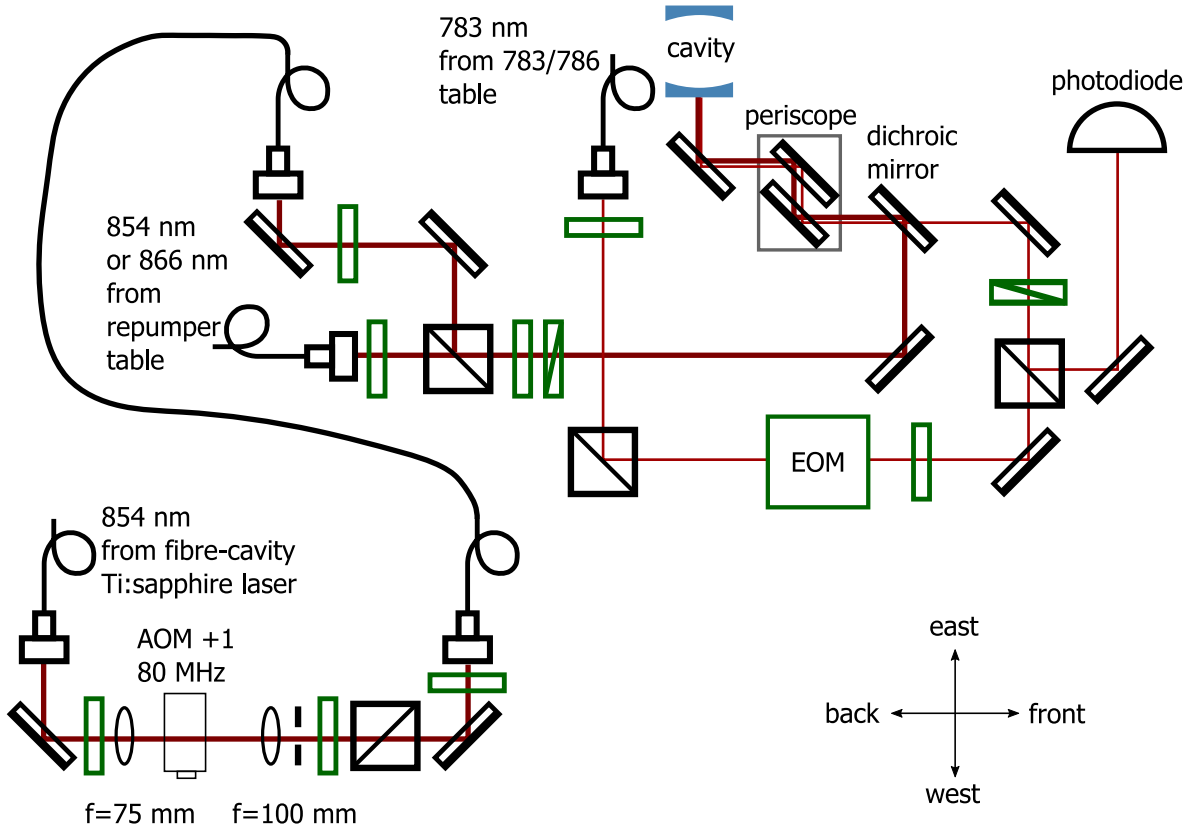

Figure 4.17: Schematic of the setup for locking the cavity to the transfer lock laser at 783 nm. Light at 854 nm from the repump laser or from the Ti:sapphire laser of the fibre cavity project can be sent to the cavity. The light at 783 nm for the transfer lock is overlapped with the light at 854 nm on a dichroic mirror and sent to the vacuum chamber via a periscope.

Reference [159], with the code used in our setup given in Appendix A.9. To close the feedback loop, the filtered error signal is fed back to the fast piezo stack of the east cavity mirror. Note that the cavity is locked to a TEM_{01} mode of the laser at 783 nm in order to minimise the AC-Stark shift induced by this laser at the ion.

Cavity lock performance

Estimates of the lock performance can be derived by comparing the error signal and transmission curve of the scanned cavity to the respective values in-loop. Such a measurement is presented in Figure 4.18 [Data17o]. Figure 4.18a shows a typical time trace of the error signal when the cavity is locked, while figure 4.18b shows the error signal and the transmission photodiode signals of the TEM_{01}-mode at 785 nm and the TEM_{00}-mode at 854 nm when scanning the cavity. From a Lorentzian fit to the transmission signal, the linewidth of the 785 mode is extracted as $\Delta\nu_{785} = 381(6)$ kHz, corresponding to a finesse of $19.7(3) \cdot 10^3$. From $\Delta\nu_{785}$, the peak-to-peak value U_{pp} of the fit to the scanned error signal, and the standard deviation of the

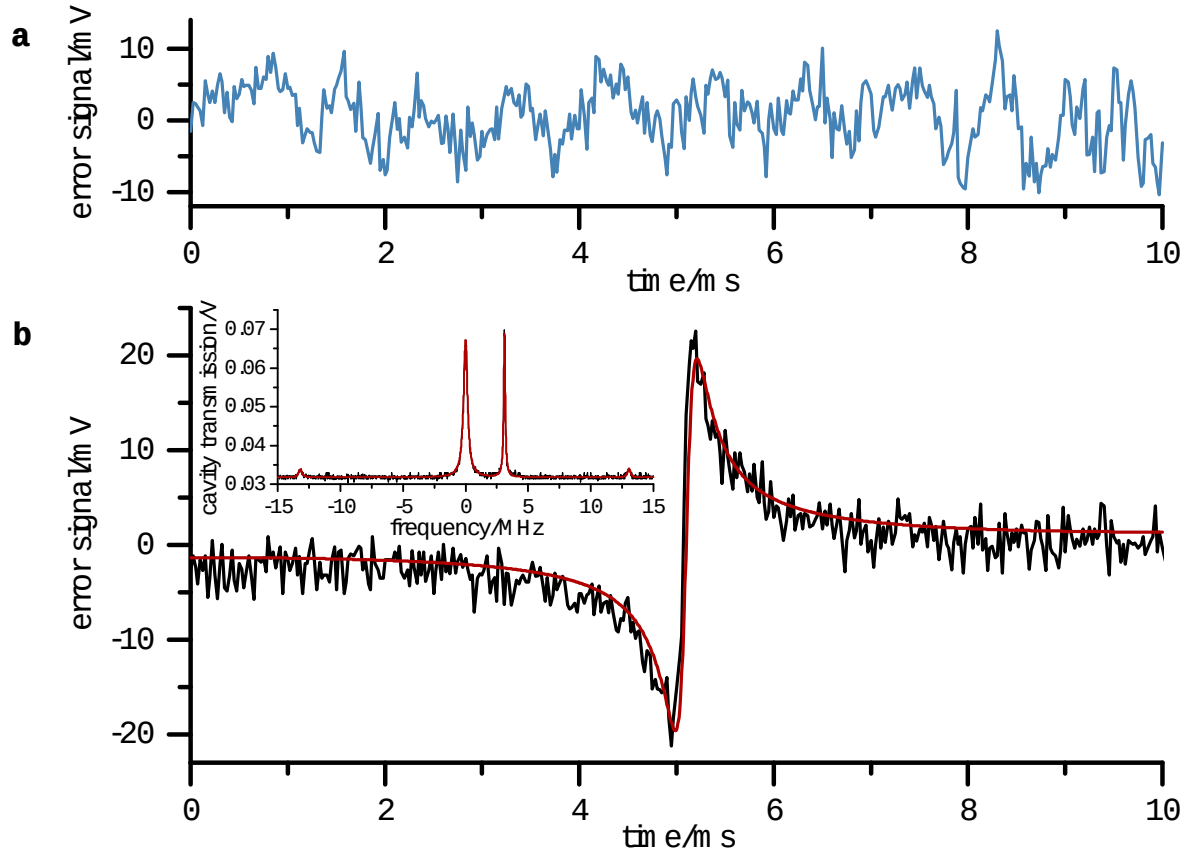

Figure 4.18: Measurement of the in-lock frequency stability. **a** Error signal of the 785 nm laser in lock. **b** Slope of the error signal when the cavity length is scanned. The inset shows the transmission signal of the laser at 785 nm and at 854 nm (narrow peak, $\mathcal{F} = 58.4(4) \cdot 10^3$) together with sidebands used for frequency calibration. From a fit to the scanned error signal, the cavity linewidth of 381(6) kHz at 785 nm, and the root mean square (RMS) excursions of the in-lock error signal (**a**), a value of the frequency excursions of 45(3) kHz is extracted.

locked error signal ΔU_{locked}, the frequency excursions of the lock can be estimated as

$$\delta\nu_{\text{lock}} = \frac{\Delta U_{\text{locked}}}{U_{\text{pp}}} \cdot \Delta\nu = 45(3)\ \text{kHz}.$$

Note that this quantity corresponds to a RMS value, i.e., one standard deviation. Accordingly, comparing $\delta\nu_{\text{lock}}$ to the half linewidth $\Delta\nu_{785}/2$, we find that we can lock the cavity at 785 nm to about 24% of its linewidth. The lock performance is still limited by the dominant resonance of the cavity assembly at 1.45 kHz (see below), which could not be completely eliminated with the digital filter.

Currently, slow drifts of the cavity length are compensated by hand by adjusting the voltage applied to the slow piezo stack, which compensates the cavity length change. However, in the future an implementation with a fast and a slow PID controller might be desirable, thus eliminating the need for manual feedback.

During the analysis of the acoustic excitation of mechanical resonances of the cavity setup (see below), it was observed that the piezo cables pick up RF signal from the trap inside vacuum.

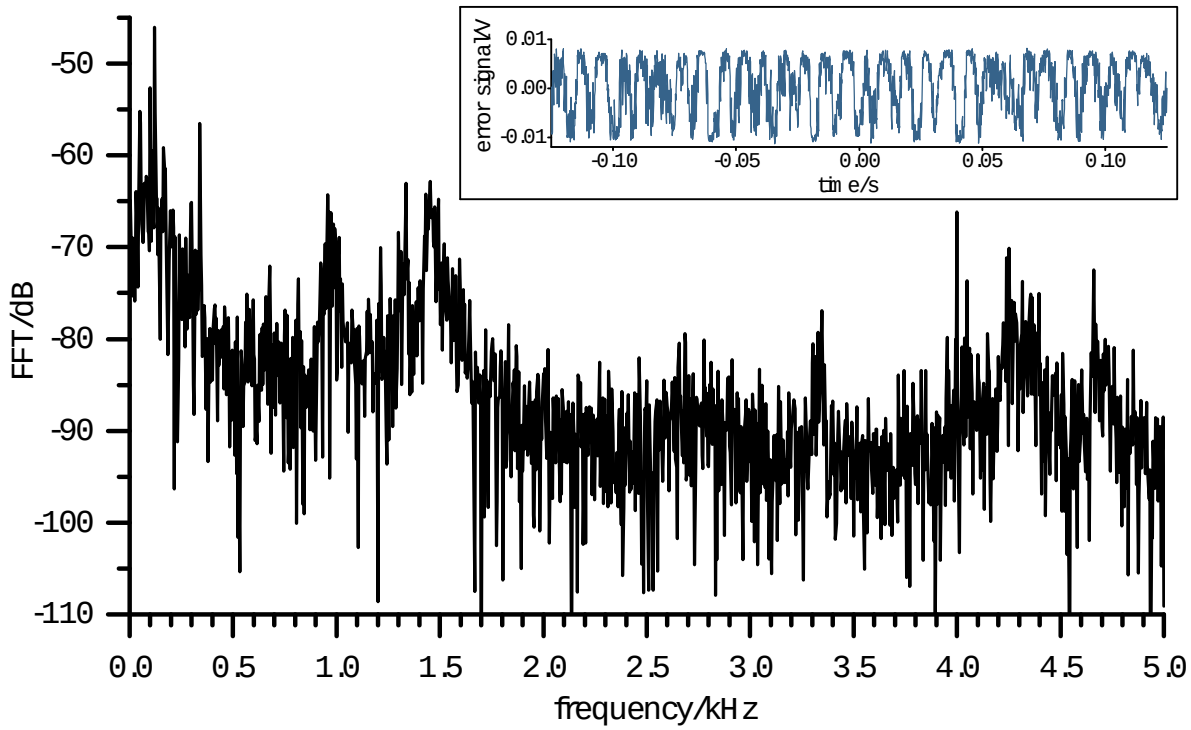

Figure 4.19: Fast Fourier transform of the error signal of the cavity lock [Data17a]. The signal shows resonances at 50 Hz and harmonics of that frequency as well as at 950 Hz, 1.3 kHz, 1.45 kHz, 3.3 kHz, 4.0 kHz, $4.2-4.4$ kHz, 4.7 kHz. The inset shows the corresponding time trace of the error signal. The baseline is at 0 V and the low-frequency oscillation occurs at 1.45 kHz.

If the vacuum chamber has to be re-opened at some point, improving the insulation of the piezo cables might reduce pickup of trap RF on these cables. However, since this noise is in the megahertz range, it does not directly affect the lock performance.

Mechanical resonances

The spectrum of mechanical resonances of the cavity and its mount was measured in the course of the optimisation of the cavity lock. The main reason for these measurements was a deteriorated lock performance, apparent in unusually high frequency excursions in the error signal: Instead of the usual frequency jitter of the cavity of around 50 kHz in-lock, a value of around 170 kHz was measured. In order to understand and fix this issue, several measurements were done, which are described in the following paragraphs.

Measurement 1 – FFT of the error signal in lock: A fast Fourier transform (FFT) of the error signal while locked was done to understand which frequency components are impairing the locking performance [Data17a]. Figure 4.19 shows the FFT of the error signal. Several resonances appear [Data17a]: apart from 50 Hz noise (and higher harmonics of that frequency) from the mains, the error signal shows peaks at 950 Hz, 1.3 kHz, 1.45 kHz, 3.3 kHz, 4.0 kHz, $4.2-4.4$ kHz, and 4.7 kHz. The resonance at 1.45 kHz proved most pernicious to the lock, with the largest contribution in the spectrum of the error signal. A second measurement (not shown) with the cavity unlocked gave similar results. Switching off several sources of acoustic noise

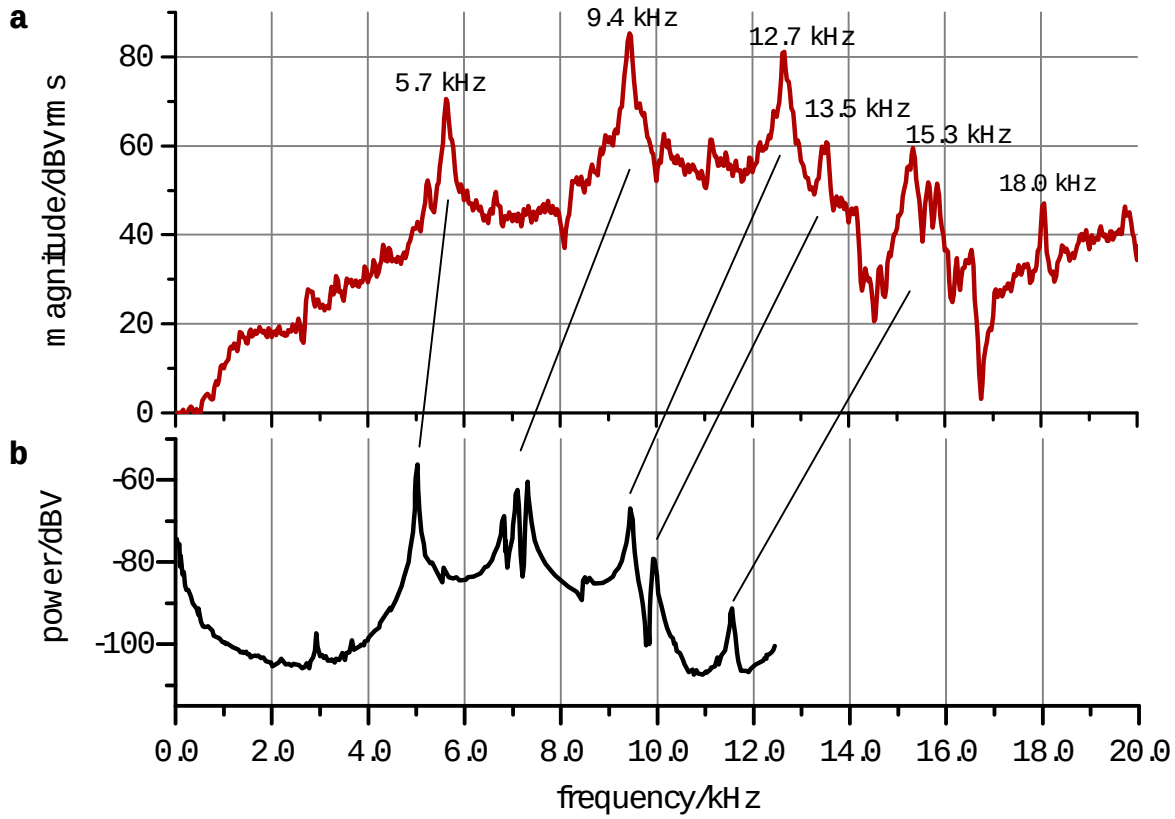

Figure 4.20: Resonances of the cavity and its mount [Data17d]. The spectrum was measured by electrically exciting the slow piezo stack, while analysing the signal picked up by the fast piezo stack with an audio analyser. **a**: Measurement of the current cavity. The most prominent resonances are labelled. **b**: Measurement in C. Russo's thesis (cf. Figure 4.17 in Reference [64]), exciting the slow piezo and analysing the pick-up on the fast piezo. The data were only measured up to a frequency of 12.5 kHz and were digitised by hand from Reference [64], since the original data file is untraceable. Note that these data are probably not background-subtracted. Straight lines show the presumed correspondence of the peaks.

(power supplies) around the setup did not eliminate the noise at 1.45 kHz. The measurements described below were done to diagnose the source of the frequency components in the spectrum of the error signal.

Measurement 2 – mechanical resonances excited via the piezo: One of the piezo stacks was electrically excited with a function generator[72] with the cavity unlocked, while the electrical signal picked up by the other stack was analysed with an audio analyser[73] [Data17d]. This measurement was done in order to understand (1) which parts of the noise on the error signal were caused by mechanical resonances of the cavity and (2) how the frequencies of these resonances compared to those of the previous cavity setup. The result of the measurement is shown in Figure 4.20a.The most prominent resonances occur at frequencies of 5.6 kHz, 9.4 kHz, 12.7 kHz, 13.5 kHz, 15.3 kHz, and 18.0 kHz, but nothing significant was observed at the frequencies

[72] SRS, DS345.
[73] SRS, SR1.

Table 4.5: Frequencies of observed resonances and presumed corresponding mechanical modes of the cavity- and lens assembly.

frequency/kHz (present)	frequency/kHz (C. Russo)	presumed mode
5.6	5.0	centre-of-mass mode (COM) of both cavity mirror mounts along the cavity axis
9.4?	6.8	COM mode of both cavity mirrors orthogonal to cavity axis
9.4?	7.1	out-of-phase (stretch) mode of both cavity mirror mounts orthogonal to the cavity axis
9.4?	7.3	out-of-phase (stretch) mode of both cavity mirror mounts parallel to the cavity axis
12.7	9.5	torsional mode of one of the collimating lens mounts
13.5	9.9	torsional mode of the second collimating lens mount
15.3	11.6	combined mode of lens mounts and mirrors

found in the FFT of the error signal.

A comparison with a measurement of the previous cavity reveals that the resonances in the current setup are more spread and occur at higher frequencies (Figure. 4.20b). Additionally, it seems that the three-fold resonance in C. Russo's measurement around 7 kHz has reduced to a single one, which has shifted to 9.3 kHz. J. Schupp, who is currently working on building an improved version of our setup, has simulated the mechanical modes of our setup[74], based on the CAD drawings by C. Russo[75]. Comparing the simulation result to the spectrum presented in C. Russo's PhD thesis, made it possible to assign specific modes to the resonances and to identify the mechanical modes in our cavity by comparison. Table 4.5 gives the presumed correspondence between modes and frequencies.

In conclusion, this measurement provided insight into how the mechanical properties of the cavity have changed after being rebuild, but did not answer the question of what caused the noise on the locking error signal. Accordingly, another measurement was done to further investigate this issue.

Measurement 3 – mechanical resonances excited acoustically: In this measurement the mechanical resonances were excited acoustically from outside the vacuum chamber from two directions, east and front-east, using a speaker, while the electrical pick up signal of the piezo stacks was recorded with the audio-analyser. The purpose of this measurement was to find an explanation for resonances visible in the error signal FFT but not in measurement 2. Figure 4.21 shows the results of the measurement for frequencies up to 5 kHz [Data17c]. The measurement shows that some resonances can be excited from both directions, while some are only excited from one of the directions. Both spectra show the resonance at 1.45 kHz, implying that this resonance can be excited acoustically.

Additional cavity resonance measurements: In addition to the measurements above, the

[74] Using the stress analysis module of the AUTODESK design software.

[75] Unpublished, but available on the electronic lab notebook of the Quantum Frequency Conversion team with date 18 January 2016.

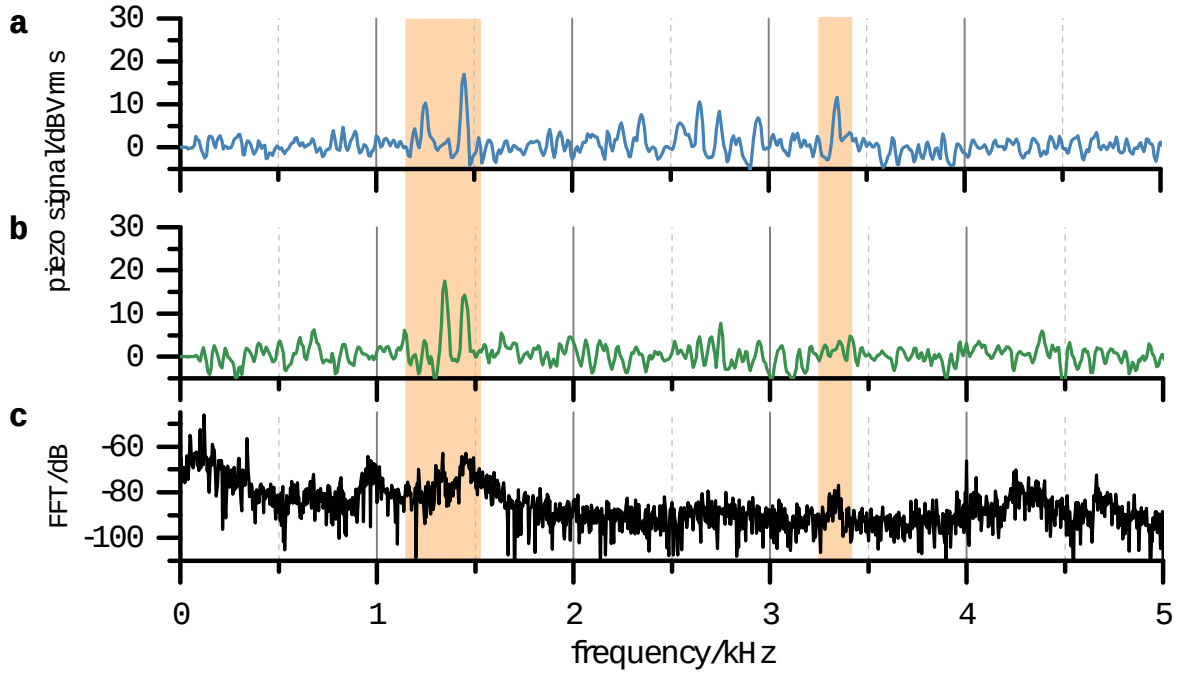

Figure 4.21: Measurement of the slow piezo response of the cavity when **a** excited acoustically from the front-east direction and **b** from the east direction with a speaker from outside the vacuum chamber. Data are [Data17c]. **c** For comparison, the FFT of the error signal is shown. Orange regions indicate correspondences between resonances in the different spectra.

transfer function of the cavity was measured in the following way. The idea for this measurement was to use the inverted transfer function as a digital filter for the cavity lock error signal to flatten the frequency response of that feedback. The measurement itself was done in the following way: Light at a wavelength of 729 nm was sent through the unlocked cavity, which was tuned to the slope of the resonance by hand. For this wavelength, the finesse of the cavity is lower than at 854 nm such that the slope of the resonance is wider. The fast piezo was then excited by a vectorial network analyser, and the transmitted light, detected with a photodiode, was analysed with the same device. The result is shown in Figure 4.22 [Data17u]. Inverting the transfer function for the digital filter did not work well, since the implementation of the digital filter adds some frequency offset. This offset was compensated, but still the locking performance was not satisfactory. Instead, a combination of low-pass and notch filters was eventually used to improve the locking performance (see Section 4.4.2 and Appendix A.9.

Additionally, Figure 4.23 shows a comparison of the spectra obtained with the different methods in the range up to 20 kHz. The comparison shows that most of the acoustically excited resonances in this frequency range have a correspondence in the electrically excited spectrum and vice versa. There are a few exceptions, though, e.g. at 11 kHz or 14.5 kHz, which can only be excited acoustically. With these measurements, the relevant resonance frequencies of the current cavity setup were identified. By using the extracted frequencies up to 12 kHz in a digital filter, the cavity frequency stabilisation was improved. In the future, better acoustic shielding of the cavity setup should be considered, e.g., by replacing the acoustic foam mounted around our setup with better acoustic shielding plates.

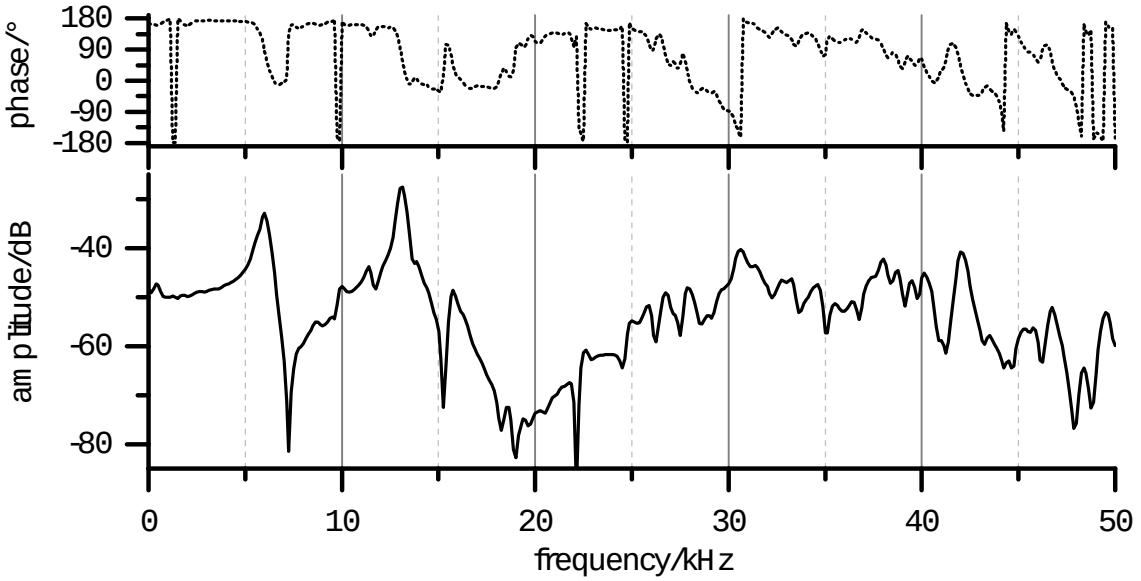

Figure 4.22: Measured transfer function of the cavity with phase and amplitude, as measured by a vectorial network analyser. See main text for details. The data are [Data17u].

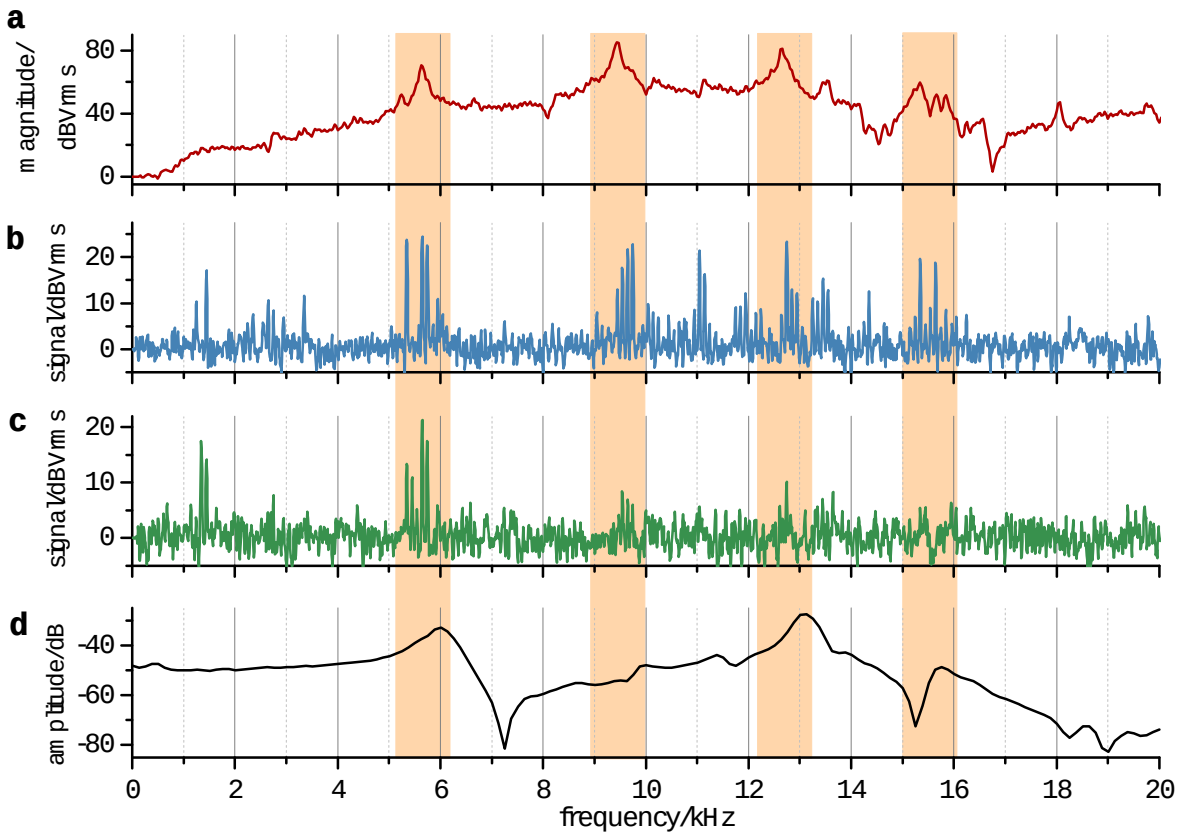

Figure 4.23: Comparison of cavity resonances with different excitation methods. **a** Response of the fast piezo during excitation of the slow piezo. **b**, **c** Response of the fast piezo, during acoustic excitation of the mechanical resonances from the front-east and the east directions. **d** Transfer function of the cavity. Orange regions indicate correspondences between the different spectra. The data are: **a** [Data17d]; **b** and **c** [Data17c]; **d** [Data17u].

4.5 Coupling ions and cavity

This section describes the procedure for coupling a trapped ion to the cavity mode. It also includes an estimation of the localisation of the ion in the cavity standing wave and the influence of the nonzero spatial extent of the ion wave packet on the coupling strength.

Optimising the coupling transverse to the cavity axis

The cavity assembly has to be moved towards the back direction for loading (see Section 4.1). Therefore, in order to couple the ion to the cavity mode, the cavity has to be moved from the loading position towards the front again into the coupled position. The cavity position is determined via two microscopes, which image the trap and cavity from the front-top and the east-back directions. Comparing the live image to reference images taken in the well-coupled position allows the experimenter to position the cavity close to the final coupled position using the slip-stick piezo translation stages[76]. Since the step size of these translation stages is on the order of micrometres, this alignment method is not precise enough for finding the maximal coupling of the ion to the cavity standing wave, which requires sub-wavelength precision.

Whenever an ion needs to be coupled to the cavity, and the cavity has been moved close to the coupled position, light at 866 nm is sent into the cavity (cf. Figure 4.17) to repump the ion via the cavity standing wave. The cavity position is then optimised in the following way: Light at 397 nm illuminates the ion, and the fluorescence signal of the ion, which is repumped via the cavity mode, is maximised by adjusting the cavity position via the translation stage and the cavity mirror piezos. Another way of optimising the coupling consists of driving a cavity-mediated Raman transition and maximising the rate of photons generated in the cavity, which can be monitored via the avalanche photodiode (APD) count rate at the cavity output (cf. Section 3.3.2). Usually, the repumping method is used first for rough alignment, while the Raman method is used for fine alignment, since the coupling can be probed more sensitively this way. Note that with this alignment method only the east-west and front-back directions are covered. The front-back direction is the direction along which the cavity has to be moved most often due to loading.

In order to align ion and cavity along the vertical north-south direction, the ion position can be moved along the trap axis by adjusting the DC potentials on the trap endcaps. This method has the disadvantage, however, that a different ion position may affect the ion's micromotion. It is therefore preferable instead to adjust the vertical cavity position by using the three micrometre screws at the bottom flange of the vacuum chamber for moving the cavity mount along the vertical direction. These screws connect to the bellows on which the cavity assembly is mounted. Rotating all three screws by the same amount will change the vertical position of the cavity. Rotating only one of the screws, or several screws by different amounts, will change the tilt of the cavity.

In recent years, the piezo translation stage for movement along the front-back direction has sometimes stopped working. Usually, this dysfunction could be resolved by changing the frequency (typically between 3 and 4 kHz) of the saw-tooth voltage applied to the stage, but although the stage was still moving, it was moving a smaller distance for a given voltage amplitude as compared to before. The company Omicron suggested also changing the voltage

[76] Controlled via a LabView interface "CQEDGameboy.vi" on the experiment control computer.

amplitude as well as moving the stage over the full travel range to clean the sliding surface of any possible contamination. In June 2017, the stage stopped moving completely. By changing the frequency, we were able to get it moving again. However, while moving over the full travel range to clean the sliding surface as suggested by the company, the stage suddenly tilted around the front-back axis, such that the east side of the stage is now about half a millimetre lower than the west side. This did not influence the movement along front-east but required careful compensation of the tilt with the micrometre screws on the bottom flange. The tilt of the translation stage and the corresponding angle at which photons exiting the cavity are transmitted through the vacuum window might also have contributed to a slight ellipticity measured in photons that leave the vacuum chamber and were expected to be linearly polarised. The ellipticity was compensated for by a tilted waveplate in the cavity output path. At some future point in time, the slip-stick piezo translation stages should be replaced.

Optimising the coupling along the cavity axis and estimating the localisation of the ion

The localisation of the ion coupled to the cavity standing wave can be determined by locking the cavity and translating the locked cavity along its axis [65, 70]. During such a measurement, photons are generated in the cavity mode via a Raman transition in the ion (cf. Section 3.3.2). The visibility V of the cavity standing wave as experienced by the ion can then be measured via the APD counts as a function of the position of the cavity with respect to the ion. For a spatial extent of the ion σ and a Gaussian-shaped probability density of the ion, the visibility is given by [160]

$$V = \exp\left(-2k^2\sigma^2\right)$$

with the wave number $k = 2\pi/\lambda$. We can therefore extract an upper limit for the spatial extent of the Doppler-cooled ion from the measured visibility. From the maximum and minimum recorded photon counts, we extract a visibility of $V = 0.993(8)$ [Data16g], which corresponds to a localisation of the ion in the standing wave of $\Delta x = 2\sigma = 16(10)$ nm. This number, extracted directly from the interaction with the cavity field, is comparable to the spatial extent of the ion wave packet expected from the Doppler limit of the radial mode of $\Delta x_{\text{rad}} = 28$ nm within the uncertainty (cf. Section 4.2.1).

We next calculate the overlap ε of an ion with Gaussian probability density and the cosine-shaped standing wave of the cavity over one wavelength for a given spatial extent $\Delta x = 2\sigma$ of the ion:

$$\varepsilon = \int_{-\lambda/2}^{\lambda/2} \frac{1}{\sqrt{2\pi\sigma^2}} \exp\left(-\frac{x^2}{2\sigma^2}\right) \cdot \cos\left(kx\right) \mathrm{d}x$$

A value of $\varepsilon = 1$ correspond to a maximally coupled ion. In this way, we can extract by how much the ion-cavity coupling strength is reduced for an ion with finite wave-packet size as compared to a point-like ion. The curve is shown in Figure 4.24. For the value of $\Delta x = 16(10)$ nm extracted from the visibility, we find a relative coupling strength of $\varepsilon = 0.998\%$, very close to the maximum coupling strength.

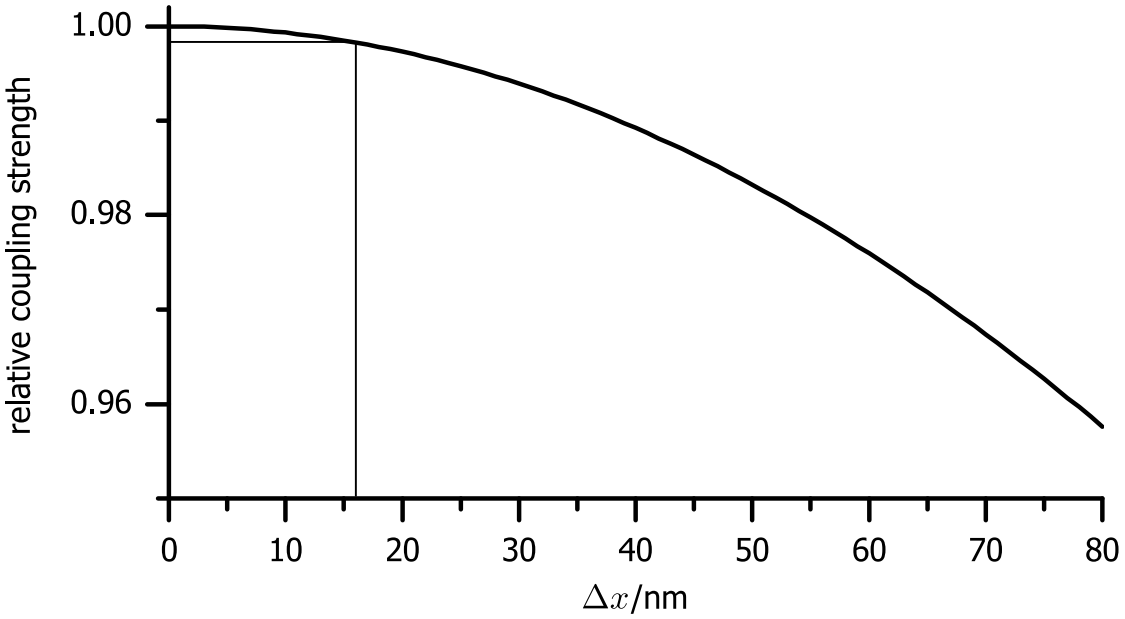

Figure 4.24: Relative coupling strength as a function of the spatial extent Δx of the ion. For the measured value of $\Delta x = 16(10)$ nm indicated by the straight lines, we find a relative coupling strength of 99.8%.

4.6 Photon detection

This section contains information on how photons generated in our CQED setup are analysed and detected. In our setup, the cavity mode is populated either by driving the cavity through one of its mirrors or by generating photons from an ion coupled to the cavity via a Raman transition (cf. Section 3.3.2). The Raman transition has been the workhorse for past experiments [72–75], but in the experiment presented in this thesis, it is only used as a means to align the ion and cavity precisely with respect to each other.

4.6.1 Cavity output path

Photons leave the cavity preferentially through the east mirror, which has higher transmission than the west mirror. The probability for leaving through that mirror depends on the finesse of the mode used. The corresponding probabilities are calculated as

$$p_{\text{out}} = \frac{\mathcal{T}_2}{\mathcal{T}_1 + \mathcal{T}_2 + \mathcal{L}_{\text{tot}}},$$

where $\mathcal{L}_{\text{tot}} \approx \frac{2\pi}{\mathcal{F}} - (\mathcal{T}_1 + \mathcal{T}_2)$ has been used for the overall scattering and absorption losses in the cavity, with $\mathcal{T}_1$ and $\mathcal{T}_2$ the transmission values of the west and east mirrors, and $\mathcal{F}$ the finesse. The values for the three accessible modes are listed in Table 4.6.

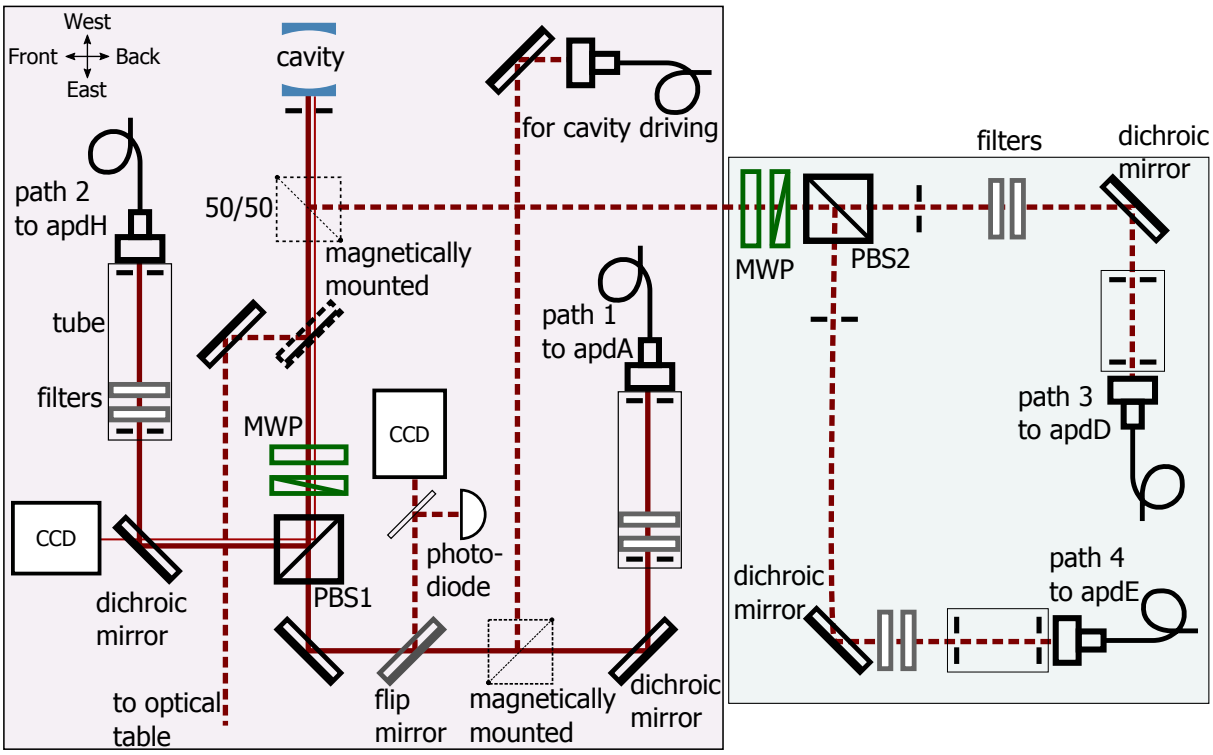

Figure 4.25: Optical path at the cavity output. The setup is mounted on two breadboards on a higher level than the optical table. Light coming from the cavity can be sent to either two or four APDs for detection. Additionally, light can be sent to the level of the optical table via two periscopic mirrors (not shown) or the cavity can be driven from the east side. Waveplates allow for polarisation control, while frequency filters and pinholes and tubes are used for spectral and spatial filtering of the output light. MWP stands for motorised waveplates, each consisting of a $\lambda/2$-$\lambda/4$ pair. The dashed elements and laser paths are optional.

Table 4.6: Probability p_{out} for photons to leave the cavity through the east mirror for the three modes within the range of the piezos that are used in our setup. See p.59 for the transmission values.

#	finesse $\mathcal{F}/10^3$	p_{out}
1	32.2(2)	7(1)%
2	54.8(4)	11(2)%
3	70.2(3)	15(3)%

Cavity output path and APDs

The optical path at the cavity output is shown in Figure 4.25. It has been changed significantly since its last description in Reference [71] and now offers more possibilities for future experiments. The following paragraphs describe the capabilities of the setup.

Photons leaving the cavity first pass through a pin-hole. Next, an optional 50/50-beam splitter can be inserted into the path if four APDs are to be used for detecting the photons. The corresponding paths are labelled path 1 to path 4, while the APDs have unique identifiers apdA,

apdD, apdE, apdH[77].

The photons in each path next pass through a pair ($\lambda/2$ and $\lambda/4$) of motorised waveplates, the angles of which are controlled from a computer[78]. These waveplates are used for analysing the polarisation of cavity photons, which is necessary for analysing qubits encoded in the photon polarisation. Orthogonal polarisations are then split by a polarising beam splitter and sent through frequency filters[79] to filter out the cavity locking light at 783 nm. Stray light is spatially filtered via two more pinholes and a tube. Finally, the photons are coupled to a multimode fibre and sent to the fibre-coupled APDs. The APDs are housed in a black box under the optical table, and the fibres to the APDs are encased in thick plastic hoses to further reduce stray light. The optics for path 3 and path 4 are mounted on a second breadboard due to space constraints.

A dichroic mirror reflecting light at 854 nm and transmitting light at 783 nm and a CCD camera in the reflected output of the first PBS (PBS1 in Figure 4.25) allow the experimenters to check the spatial mode of the locking laser. In a similar way, the spatial mode and transmission intensity of light at 854 nm sent through the cavity can be checked in the transmitted output of PBS1 by flipping up a mirror with a CCD camera and a photodiode at the outputs of a beam splitter.

All these optics are mounted on a breadboard elevated to the height of the vacuum chamber output window. The cavity output light can be routed to the lower level of the optical table by inserting a magnetically mounted mirror behind the optional 50/50 beam splitter. This option can be used for experiments requiring different detection setups for which there is no space on the breadboard. For instance, an interferometric setup, such as required for the experiment proposed in Chapter 6.2, could be mounted on the optical table. By including a magnetically mounted PBS or unbalanced beam splitter in path 1 before the last mirror, light can also be injected into the cavity through the east mirror. This will be relevant for photon absorption experiments in the context of quantum networking (see Chapter 6.3). The beam splitter can be chosen with, e.g., a 90/10 ratio, such that monitoring photons generated in the cavity is still possible via path 1.

Note that to date only path 1 and path 2 have been used. The four-detector setup will, however, become important in experiments in which two photons are generated, that are meant to be sent to two different nodes in a quantum network. For characterising such photon pairs, we will need to analyse their polarisations independently from each other, for which two pairs of waveplates are necessary. The efficiencies of all four paths are given in Table 4.7.

4.6.2 Data processing

The APDs that detect cavity photons send electrical TTL signals to a time-tagging device[80]. The electronics used for this photon detection process are shown schematically in Figure 4.26. First,

[77] apdA: LaserComponents, COUNT-10C-FC, serial number 9683, dark count rate 10(2)/s [Data17j]; apdH: LaserComponents, COUNT-10C-FC, serial number V6134, dark count rate 8(3)/s [Data17k]; apdD: Excelitas, dark count rate 44(5)/s [Data17j]; apdE: Perkin Elmer, dark count rate 45(6)/s [Data17j]. Two more APDs have been purchased recently for the fibre cavity experiment: apdG: LaserComponents, COUNT-10C-FC, serial number 9683, dark count rate 6(2)/s [Data17k]; apdI: LaserComponents, COUNT-10C, serial number V6134, dark count rate 2(2)/s [Data17k].

[78] Controller: OWIS, PS10.

[79] Band-pass filters Semrock, ET850/30M236768; edge filters Semrock, EdgeBasic BLP01-785R-25.

[80] PicoQuant, PicoHarp 300.

Table 4.7: Photon detection efficiencies for the different paths at the cavity output (cf. Figure 4.25). The rightmost column lists the overall photon detection efficiency for a given path and cavity mode. Note that the efficiencies of paths 1 and 2 are given here for the case without the 50/50 beam splitter. If the beam splitter is used, the optical path efficiencies of path 1 and 2 are $0.40(3)$ and $0.38(2)$, respectively, with total efficiencies given in the last column in square brackets.

path	optical path efficiency	fibre efficiency	APD efficiency	finesse $\mathcal{F}/10^3$	p_{out}	total efficiency η_{total}
1	$0.78(5)$	$0.82(6)$	$0.53(4)$	$32.2(2)$	$7(1)\%$	$0.026(6)$ [$0.013(3)$]
			(apdA)	$54.8(4)$	$11(2)\%$	$0.04(1)$ [$0.023(5)$]
				$70.2(3)$	$15(3)\%$	$0.06(1)$ [$0.030(7)$]
2	$0.74(5)$	$0.77(5)$	$0.71(6)$	$32.2(2)$	$7(1)\%$	$0.035(8)$ [$0.018(4)$]
			(apdH)	$54.8(4)$	$11(2)\%$	$0.06(1)$ [$0.031(7)$]
				$70.2(3)$	$15(3)\%$	$0.08(2)$ [$0.040(9)$]
3	$0.41(3)$	$0.88(7)$	$0.55(5)$	$32.2(2)$	$7(1)\%$	$0.015(4)$
			(apdD)	$54.8(4)$	$11(2)\%$	$0.026(6)$
				$70.2(3)$	$15(3)\%$	$0.034(8)$
4	$0.41(3)$	$0.87(5)$	$0.48(4)$	$32.2(2)$	$7(1)\%$	$0.013(3)$
			(apdE)	$54.8(4)$	$11(2)\%$	$0.022(5)$
				$70.2(3)$	$15(3)\%$	$0.029(7)$

the signal coming from each APD is split: one part is sent to the time tagger, while the second part is used as input to a "branch-on-trigger" (BOT) box[81]. This box returns a trigger signal to the experiment control electronics such that the next branch of the experimental sequence is chosen conditioned on the detection of one or two photons[82]. Its logic is programmed via a graphical interface.

The box has three gate inputs, each of which is connected to the experiment control electronics [161, 162], so that the BOT only waits for photon events during a certain part of the experimental sequence[83]. This system has replaced a previous home-built version and provides more flexible capabilities for photon logic. For example, it can be used to restart the photon generation if no photon has been detected without having to restart the complete experimental

[81] Based on Cypress, Cy8CKIT-050 PSoC 5 LP.

[82] The logic depends on whether input "1 photon trigger" or "2 photon trigger" is connected to the digital output channel 2 or the experiment control electronics.

[83] The inputs are: (1) a TTL pulse that switches on the direct digital synthesiser (DDS) of the control electronics to produce a pulse of the Raman laser at 393 nm ("729/393 switch"), (2) a TTL pulse that selects whether resonant or detuned light is produced at 393 nm ("Raman TTL", (3) a TTL pulse that selects whether the ion is cooled (off-resonant light at 397 nm) or detected (resonant light).

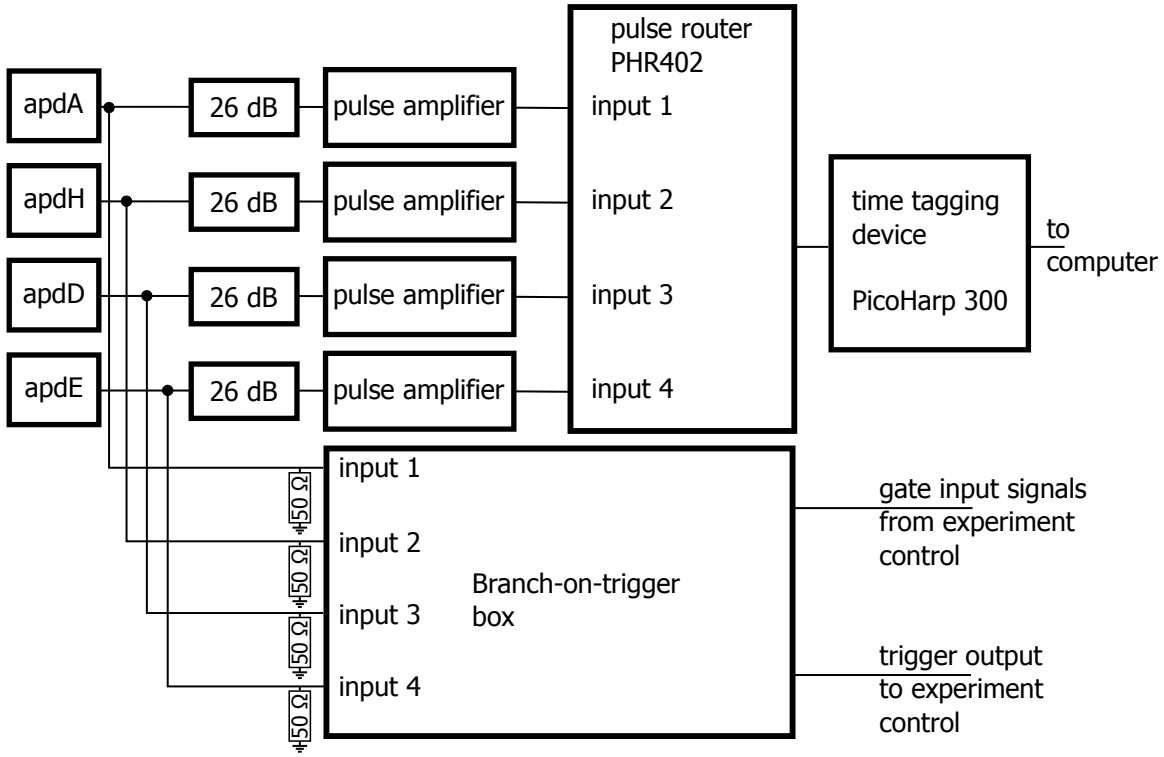

Figure 4.26: Electronics for processing photon detection events. The output of each APD is split between a "branch-on-trigger" box for conditional logic in the experimental sequence and a pulse router and time tagger. Since the pulse router requires different voltage input levels than those supplied by the APDs, the APD signals are attenuated and amplified for the correct input voltage level.

sequence including the time-consuming Doppler cooling step. In two-photon experiments, the system is used to allow the sequence to proceed to the time-consuming ion detection step only if two photons have been detected and otherwise to restart the sequence. Note that the APD signals at the BOT input are terminated with $50\ \Omega$ in order to avoid reflections.

The second part of each APD signal is sent through a combination of attenuation and pulse amplification[84] such that the pulses reach the correct input voltage level for the next element, a pulse router. Care has been taken to choose the attenuation and amplification elements such that distortion of the photon pulses is minimised. The pulse router[85] multiplexes four APD inputs for transfer to the time-tagging device[86], which on its own only provides two inputs. Finally, the time tagger sends the time tags to the experiment-control computer, where the APD data are stored together with the remaining data. Both router and time tagger also receive trigger signals from the experiment control electronics[87], which gate the photon detection.

The raw data can then be parsed with code written in C[88] and processed in the Python-based

[84] MiniCircuits, ZPUL-30P.
[85] PicoQuant, PHR402.
[86] The pulse router is connected to input channel 1 of the time-tagging device.
[87] The gate signals are called "marker0" (digital output 7) and "marker1" (digital output 12).
[88] The programme is called `photons_time_branch.c`.

data analysis tool[89]. This new photon detection setup with four detectors has been successfully tested, but for the measurements presented in Chapter 5, only two detectors were used.

[89]Module `photons_tools_module_4APD.py` is used for processing.

Chapter 5

Probing the cavity field with a single ion

In nature's infinite book of secrecy
A little I can read.

– W. Shakespeare, Antony and Cleopatra

This chapter contains the central result of my thesis work: an experiment, which employs a single trapped ion as probe for the intracavity field. The chapter is structured as follows: First, the general idea of the experiment, the setup, experimental sequence and calibration measurements are described. Next, I explain the measured effects and present a method for extracting the coupling strength from the measurements, which is followed by a comparison between measurements on different ion transitions and with cavity modes of different finesse. An explanation follows of how the measurements can be used to reconstruct the distribution of photon numbers in the cavity field for coherent drive fields and drive fields with mixed coherent and thermal statistics. Finally, an outlook on possible extensions of the project and a summary are given. Calculations of uncertainties are found in Appendix A.8.

5.1 Introduction

The goal of this experiment consists of directly accessing information about the electromagnetic field in an optical resonator without having to rely on the detection of cavity output light and without destroying the cavity photons. This goal can be achieved by dispersively coupling a trapped ion to the field. The ion experiences an AC-Stark shift of its energy levels due to its interaction with cavity photons, which depends on photon number statistics. It is possible to measure this effect of the cavity photons on the state of the ion via Ramsey spectroscopy. The influence of the cavity field strength, viz., the mean photon number, is manifested in a phase shift of the Ramsey fringe and in a contrast reduction of the Ramsey fringe; the latter effect being caused by fluctuations of the cavity photon number. Combining the observations of phase shift and contrast reduction, it is possible to infer the statistics of the intra-cavity field in the following way: By modelling the system and comparing the simulated Ramsey fringe for a given cavity drive strength to the observed fringe, one can find the cavity field that best explains the observed data, using a maximum likelihood method.

The concept of the experiment goes back to proposals from the beginning of the 1990s [163, 164], which were followed by implementations with Rydberg atoms [76, 165, 77, 10, 166] and

superconducting qubits [78, 12, 13, 80] in microwave cavities. Measurements based on this principle eventually also enabled the generation of non-classical cavity field states as well as feedback to and stabilisation of cavity states [166, 11, 167–170]. Other methods for a mapping between the cavity field state and the atomic coherence have been proposed [171, 172], but these methods rely on adiabatic passages in contrast to the dispersive interaction of Reference [164].

In ion traps, similar effects to those caused by dispersive interaction with quantised fields have been observed: Experimenters have used the similarity of the Jaynes-Cummings interaction in CQED and in trapped ions interacting with light [103] to generate nonclassical states of motion of trapped ions [173–175] as well as to implement quantum gates between multiple ions [176]. In another experiment, analogous to the observation of quantised AC-Stark shifts due to cavity photons with Rydberg atoms [76], the quantised AC-Stark shift due to the different motional states of a trapped ion was measured, and the effect was used for constructing a phase gate between two trapped ions [177].

Note that in contrast to References [178, 179], our experiment does not aim at the detection of travelling photons using a CQED setup, but instead allows one to investigate the cavity field itself. In contrast to experiments with Rydberg atoms [76, 165, 77, 10, 166, 11] or superconducting qubits [78, 12, 13, 80, 167–170], though, we are operating in the weak dispersive regime, i.e., the dispersive energy shift per single photon experienced by the ion is smaller than both the cavity linewidth and the atomic linewidth (cf. Section 3.3.2).

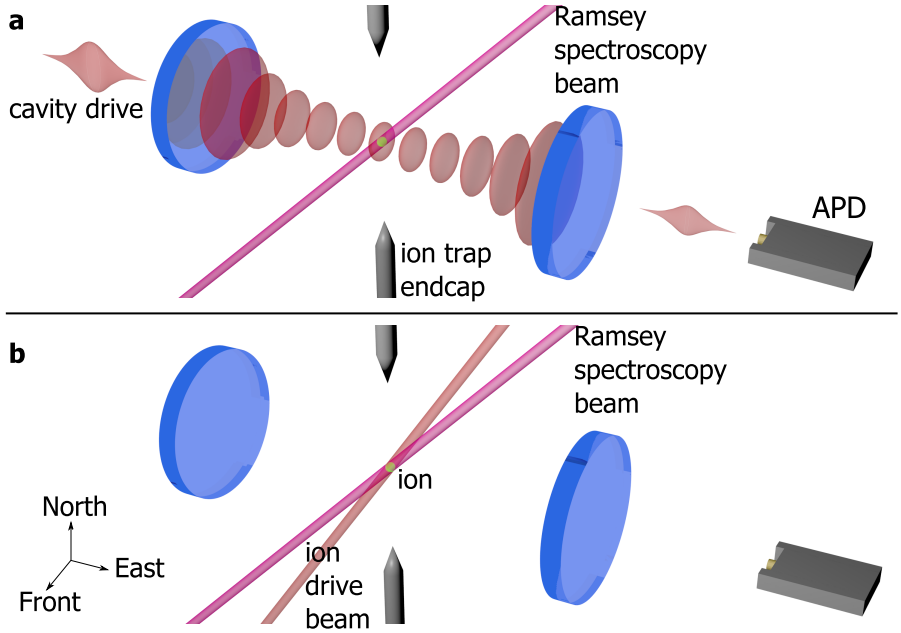

Figure 5.1: Experimental setup for the experiment. Subfigure **a** shows the "cavity drive" configuration. The cavity is driven with weak coherent laser pulses at 854 nm ("cavity drive"), whose linear polarisation is parallel to the quantisation axis along the North-Front direction. The ion (green spot in the centre) in the trap (RF blades not shown) is probed in a Ramsey sequence, using a beam at 729 nm from the North-East direction (not shown). Light transmitted through the cavity is detected with an APD. In the "ion drive" configuration (subfigure **b**), the cavity is not driven by a laser, and instead the ion's levels are Stark-shifted by a laser beam from the North-Back direction at 854 nm.

5.2 Experimental setup, sequence, and theory

The experiment is executed in two different drive configurations. In the so-called "cavity drive" configuration, a single ion is coupled to a TEM_{00} mode of the cavity. The cavity is driven with weak coherent laser pulses at 854 nm with mean photon numbers between $\bar{n} = 0$ and $\bar{n} = 2$. The waveplates at the cavity output are set such that all transmitted light arrives at only one APD. Figure 5.1a shows a sketch of the setup. This configuration is used for probing the cavity field with a single ion.

In a second configuration, shown in Figure 5.1b, the cavity is not driven by a laser, but the ion is driven with light of the same wavelength and detuning as in the cavity drive case but from the side of the cavity. This configuration is used in a reference measurement for estimating the influence of spontaneous emission (see Section 5.3.1).

5.2.1 Levels used in the experiment

The energy levels of the ion used in the experiment are displayed in Figure 5.2a. The ion is prepared in a superposition of the ground state $|S\rangle = |4^2\mathrm{S}_{1/2}, m_J = +1/2\rangle$ and either $|D\rangle = |3^2\mathrm{D}_{5/2}, m_J = +1/2\rangle$ or $|D'\rangle = |3^2\mathrm{D}_{5/2}, m_J = +3/2\rangle$. Interaction with the cavity field or the "ion-drive" laser happens on the transition $|D\rangle - |P\rangle = |4^2\mathrm{P}_{3/2}, m_J = +1/2\rangle$ or $|D'\rangle - |P'\rangle = |4^2\mathrm{P}_{3/2}, m_J = +3/2\rangle$. The state $|P\rangle$ decays to the states in the $4^2\mathrm{S}_{1/2}$ manifold with rate $\Gamma_{\mathrm{P}\to\mathrm{S}} = 2\pi\cdot 21.4$ MHz, to the states in the $3^2\mathrm{D}_{5/2}$ manifold with rate $\Gamma_{\mathrm{P}\to\mathrm{D}} = 2\pi \cdot 1.34$ MHz, and to the states in the $3^2\mathrm{D}_{3/2}$ manifold with rate $\Gamma_{\mathrm{P}\to 3^2\mathrm{D}_{3/2}} = 2\pi \cdot 0.152$ MHz (cf. Section 4.2).

For the simulation of the process on the first transition, four levels are used: $|S\rangle$, $|P\rangle$, $|D\rangle$, and an artificial level $|S'\rangle$, which corresponds to the second ground state but additionally collects the decay from $|P\rangle$ to $3^2\mathrm{D}_{3/2}$ and other states in the $3^2\mathrm{D}_{5/2}$ manifold. Taking into account the corresponding Clebsch-Gordan coefficients (see Appendix A.1), the decay of $|P\rangle$ to $|S'\rangle$ happens at a rate $\Gamma_{|P\rangle\to|S'\rangle} = 1/3\Gamma_{\mathrm{P}\to\mathrm{S}} + 3/5\Gamma_{\mathrm{P}\to\mathrm{D}} + \Gamma_{\mathrm{P}\to 3^2\mathrm{D}_{3/2}} = 2\pi \cdot 8.1$ MHz. The decay rates for $|P\rangle$ to $|S\rangle$ and $|P\rangle$ to $|D\rangle$ are $\Gamma_{|P\rangle\to|S\rangle} = 2/3\Gamma_{\mathrm{P}\to\mathrm{S}} = 2\pi \cdot 14.3$ MHz and $\Gamma_{|P\rangle\to|D\rangle} = 2/5\Gamma_{\mathrm{P}\to\mathrm{D}} = 2\pi \cdot 0.54$ MHz, respectively.

For the second transition $|P'\rangle - |D'\rangle$, the following decay channels exist: $\Gamma_{|P'\rangle\to|S'\rangle} = 11/15\Gamma_{\mathrm{P}\to\mathrm{D}} = 2\pi \cdot 0.983$ MHz, $\Gamma_{|P'\rangle\to|S\rangle} = \Gamma_{\mathrm{P}\to\mathrm{S}}$, $\Gamma_{|P'\rangle\to|D'\rangle} = 4/15\Gamma_{\mathrm{P}\to\mathrm{D}} = 2\pi \cdot 0.357$ MHz. The four levels in the simulation in this case are $|S\rangle$, $|D'\rangle$, $|P'\rangle$, and $|S'\rangle$. Note that in this case, $|S'\rangle$ is different from the simulation of the first transition because decay to the second ground state is forbidden and $|S'\rangle$ only collects the decay from $|P'\rangle$ to $3^2\mathrm{D}_{3/2}$ and other states in the $3^2\mathrm{D}_{5/2}$ manifold.

5.2.2 Experimental sequence

In the experiment described in this chapter, two different transitions of the ion are used with coupling strengths $g = 2\pi \cdot 0.97(19)$ MHz and $g' = 2\pi \cdot 0.79(16)$ MHz (taking into account the Clebsch-Gordan coefficients; cf. Section 4.4.1). The experimental sequence starts with Doppler cooling of the ion for 1 ms. In the next step, the ion is prepared in $|S\rangle$ via optical pumping. During the following Ramsey spectroscopy part of the sequence, the ion is prepared in a superposition of $|S\rangle$ and $|D\rangle$ or $|S\rangle$ and $|D'\rangle$ with a π/2-pulse at 729 nm. The cavity is

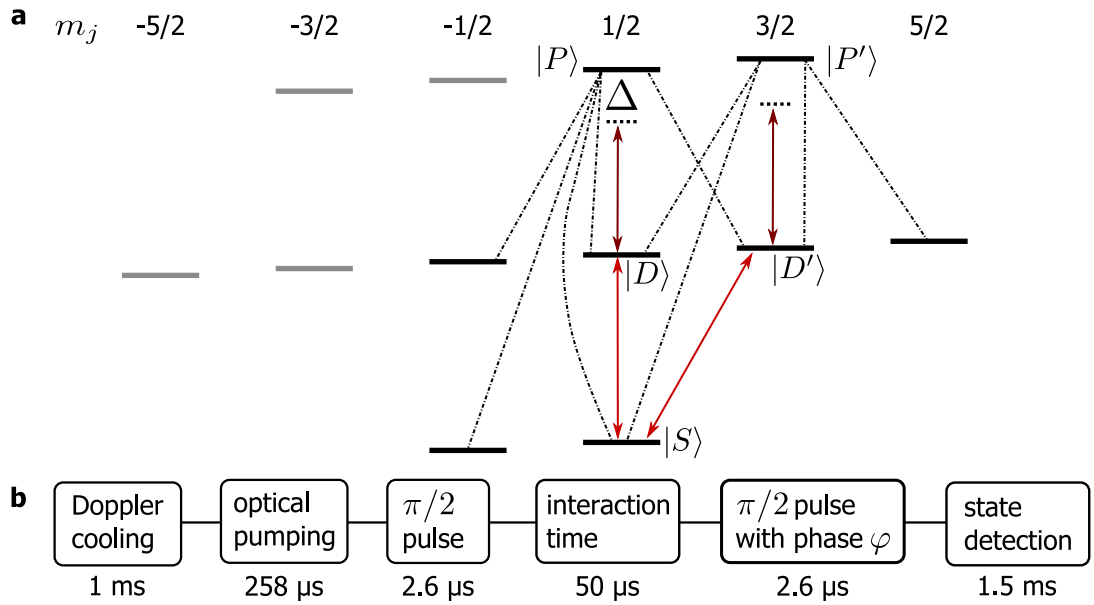

Figure 5.2: Level scheme and experimental sequence. **a** Electronic levels used in the experiment. The ground state $|S\rangle = |4^2\mathrm{S}_{1/2}, m_J = +1/2\rangle$ and states in the manifolds $4^2\mathrm{P}_{1/2}$ and $3^2\mathrm{D}_{3/2}$ (not shown for clarity) are used for cooling and state detection. The Ramsey sequence uses a superposition of $|S\rangle$ and $|D\rangle = |3^2\mathrm{D}_{5/2}, m_J = +1/2\rangle$ (bright red arrow) or $|S\rangle$ and $|D'\rangle = |3^2\mathrm{D}_{5/2}, m_J = +3/2\rangle$, while the cavity (dark red arrow) is coupled on the $|D\rangle - |P\rangle = |4^2\mathrm{P}_{3/2}, m_J = +1/2\rangle$ transition or on the $|D'\rangle - |P'\rangle = |4^2\mathrm{P}_{3/2}, m_J = +3/2\rangle$ transition with detuning $\Delta = 125(1)$ MHz. The decay channels from states $|P\rangle$ and $|P'\rangle$ are shown as dash-dotted lines. Decay from these states to the $3^2\mathrm{D}_{3/2}$-manifold is also possible (not shown). **b** Experimental sequence. Following cooling and state preparation, the ion interacts with light in a Ramsey experiment. The phase of the second Ramsey pulse is scanned. At the end of the sequence, the state of the ion is detected. The sequence is repeated 250 times for each phase of the second Ramsey pulse.

coupled either to the ion's transition between $|D\rangle$ and $|P\rangle$ or between $|D'\rangle$ and $|P'\rangle$. During an interaction time of 50 µs, a laser pulse then drives the cavity. The laser is resonant with the cavity, which in turn is red-detuned by $\Delta = 2\pi\cdot 125(1)$ MHz from the ion's $|P\rangle - |D\rangle$ transition. Due to the difference of the Clebsch-Gordan coefficients on the $|D\rangle - |P\rangle$ and $|D'\rangle - |P'\rangle$ transitions, the ion-cavity coupling strength is different, and as a consequence the dispersive interaction changes. After the interaction time, a second Ramsey pulse with variable phase φ with respect to the first Ramsey pulse is applied to the ion. In the final step of the sequence, the electronic state of the ion is detected. Figure 5.2b shows a schematic of the sequence. Note that the Ti:Sa laser of the fibre cavity experiment was used for driving the cavity or the ion at 854 nm (cf. Section 4.3.4).

In the Bloch-sphere picture (cf. Section 3.2), the first $\pi/2$-pulse transfers the Bloch vector of the ion qubit from the ground state into the equatorial plane. The interaction with the cavity field then leads to a rotation, i.e., a phase shift, of the Bloch vector, and dephasing. These effects are translated into the basis of the ion populations of the ground and excited states by the second $\pi/2$-pulse.

5.2.3 Theoretical model

This section contains the theoretical model for understanding and simulating the experiment, using the sequence and energy levels defined in the previous sections. In the case of dispersive interaction, i.e. for $\Delta \gg g$, the energies of the states in the Jaynes-Cummings model can be expanded in lowest order of g/Δ and are shifted by a frequency of[1]

$$\chi = \frac{g^2}{\Delta}$$

per photon with respect to the bare states[2]. In our experiment, the detuning $\Delta = 2\pi \cdot 125(1)$ MHz corresponds to values of $\chi = 7.5$ kHz for the $|D\rangle - |P\rangle$ transition and $\chi' = 5.0$ kHz for $|D'\rangle - |P'\rangle$. The corresponding interaction Hamiltonian has the form

$$H_{\text{int}} \propto \left(\omega_{\text{C}} + \chi a^\dagger a\right) \sigma_z,$$

with ω_{C} the cavity's bare resonance frequency, $a^\dagger a$ the intracavity photon number operator, and σ_z the inversion operator of the qubit. The effect of the dispersive coupling can be interpreted as a shift of the qubit frequency which depends on the number of photons. Here, χ corresponds to the phase shift per photon. In a complementary picture, the frequency of the cavity is shifted ("pulled") by an amount χ. This can be seen by considering the energy difference between the bare states $|1, n\rangle$ and $|0, n+1\rangle$ (cf. Section 3.3.2), which is independent of n and given by $\hbar(\omega_{\text{C}} - \chi)$.

Since the frequency shift occurs during an interaction time τ, the ion accumulates a total phase shift

$$\phi = \chi \bar{n} \tau, \tag{5.1}$$

where $\bar{n} = \langle a^\dagger a \rangle$ is the mean photon number in the cavity field. This dispersive approximation breaks down for photon numbers larger than the critical photon number $n_{\text{crit}} = \Delta^2/4g^2$ [111]. Note that although the critical photon number is on the order of $4,000$ for the transition $|P\rangle - |D\rangle$ and $6,000$ for $|P'\rangle - |D'\rangle$, we use the full Jaynes-Cummings model in our simulation.

The coupling strengths for the two transitions $|D\rangle - |P\rangle$ and $|D'\rangle - |P'\rangle$ are $g = 2\pi \cdot 0.97(19)$ MHz and $g' = 2\pi \cdot 0.79(16)$ MHz with corresponding phase shifts $\phi_{\text{ph}} = \chi\tau_{\text{c}} = 0.017(3)\pi$ induced by each photon for the transition $|D\rangle - |P\rangle$ and $\phi'_{\text{ph}} = 0.012(2)\pi$ for the transition $|D'\rangle - |P'\rangle$. However, due to the interaction time $\tau = 50$ µs being much longer than the cavity photon lifetime of $\tau_{\text{c}} = 1.16(1)$ µs, multiple photons interact with the ion during this time and the effect accumulates according to Equation 5.1, as multiple photons enter the cavity, interact with the ion, and leave the cavity again.

In our simulations of the process, the system is modelled as a four-level system, with state $|S'\rangle$ as dark state. For the transition $|D\rangle - |P\rangle$, the Hamiltonian is

$$\begin{aligned} H_S/\hbar =& \omega_D \sigma_D + (\omega_D + \omega_P)\, \sigma_P + \Delta_{SS'} \sigma_{S'} \\ &+ \omega_{\text{C}} a^\dagger a + g\left(\sigma_{PD} a + \text{h.c.}\right) \\ &+ \left(\eta a^\dagger e^{-i\omega_{\text{L}} t} + \text{h.c.}\right) + \left(\Omega \sigma_{SD} e^{-i\omega_{\text{s}} t} + \text{h.c.}\right), \end{aligned}$$

[1] Cf. chapter 3.4.4 in Reference [8] or chapter 19.3 in Reference [94].
[2] Cf. Section 3.3.2.

where $\hbar\omega_D$ corresponds to the energy of state $|D\rangle$, $\hbar\omega_P$ to the energy difference between $|D\rangle$ and $|P\rangle$, $\sigma_{D(P)}$ is the projection operator onto $|D\rangle$ ($|P\rangle$), $\Delta_{SS'}$ is the detuning between state $|S\rangle$ and the dark state $|S'\rangle$, and $\sigma_{S'}$ is the projection operator onto $|S'\rangle$. The energy reference is given by state $|S\rangle$. Furthermore, a denotes the annihilation operator of the cavity mode, $\sigma_{PD} = \sigma_{DP}^\dagger$ is the transition operator from state $|D\rangle$ to $|P\rangle$, $\eta = \kappa\sqrt{\bar{n}}$ is the amplitude of the drive laser in the cavity (derived from the Heisenberg equation in steady state [180]), ω_L the frequency of the cavity drive laser, Ω is the Rabi frequency of the Ramsey spectroscopy laser, $\sigma_{SD} = \sigma_{DS}^\dagger$ the transition operator from $|D\rangle$ to $|S\rangle$, and ω_s the frequency of the Ramsey spectroscopy laser. Note that in the simulation, only one of the two driving terms of the Hamiltonian (Ω and η) is used at a given time, dpending on whether the ion-drive or the cavity-drive configuration is simulated.

Using a unitary transformation

$$H_I = i\dot{U}U^\dagger + UH_SU^\dagger$$

with unitary operator

$$U = \exp\left[i\hbar\left(\omega_\mathrm{s}\sigma_D + (\omega_\mathrm{s} + \omega_P)\sigma_P + \omega_P a^\dagger a\right)t\right],$$

the Hamiltonian in the interaction picture then becomes:

$$\begin{aligned} H_I/\hbar =& \Delta_{D\mathrm{s}}\sigma_D + (\Delta_{P\mathrm{L}} + \Delta_{\mathrm{CL}} + \Delta_{D\mathrm{s}})\sigma_P + \Delta_{SS'}\sigma_{S'} \\ &+ \Delta_{\mathrm{CL}}\, a^\dagger a \\ &+ g\left(\sigma_{PD}\, a + \sigma_{DP}\, a^\dagger\right) + \eta(a + a^\dagger) \\ &+ \Omega\left(\sigma_{SD} + \sigma_{DS}\right). \end{aligned}$$

Here, $\Delta_{D\mathrm{s}} = \omega_D - \omega_\mathrm{s}$, $\Delta_{P\mathrm{L}} = \omega_P - \omega_\mathrm{L}$, and $\Delta_{\mathrm{CL}} = \omega_\mathrm{C} - \omega_\mathrm{L}$.

The time evolution of the system can then be calculated by numerically integrating the master equation

$$\begin{aligned} \frac{\mathrm{d}\rho}{\mathrm{d}t} =& -\frac{i}{\hbar}\left[\rho, H_I\right] \\ &+ \sum_{i=D,S,S'} \frac{\Gamma_i}{2}\left(2\sigma_i^-\rho\sigma_i^+ - \rho\sigma_i^+\sigma_i^- - \sigma_i^+\sigma_i^-\rho\right) \\ &+ \frac{\kappa}{2}\left(2a\rho a^\dagger - \rho a^\dagger a - a^\dagger a\rho\right) \\ &+ \delta n\left(\left[\left[a,\rho\right],a^\dagger\right] + \left[\left[a^\dagger,\rho\right],a\right]\right), \end{aligned} \tag{5.2}$$

where σ_i^- is the decay operator from state $|P\rangle$ to state $|i\rangle$, and Γ_i is the corresponding decay rate. The four terms of this equation describe unitary evolution, the atomic decay channels, cavity decay, and incoherent driving, i.e. amplitude noise on the drive laser. The latter term can be derived from a stochastic drive term [181, 96]. Amplitude noise is included in the model to be able to simulate the experiment including artificial noise on the drive laser (see Section 5.4.3). When expanded, the last two terms of the master equation Equation 5.2 are given by

$$\frac{\kappa + \delta n}{2}\left(2a\rho a^\dagger - \rho a^\dagger a - aa^\dagger\rho\right) + \frac{\delta n}{2}\left(2a^\dagger\rho a - \rho aa^\dagger - aa^\dagger\rho\right),$$

which is equivalent to driving the cavity with a field described by thermal statistics [182] with thermal mean photon number $\bar{n}_{\text{th}} = \delta n/\kappa$, where δn is the amplitude of the incoherent drive. Since the incoherent and the coherent parts of the driving field do not interfere, the total mean photon number is simply the sum of the coherent and thermal contributions: $\bar{n} = \bar{n}_{\text{coh}} + \bar{n}_{\text{th}}$. D. Plankensteiner and V. Torggler from Professor H. Ritsch's group (Institut für Theoretische Physik, Leopold-Franzens-Universität Innsbruck) provided support for deriving the theoretical description of amplitude noise on the laser that was used to drive the cavity.

For simulating the second transition, g needs to be replaced with g', D with D', and P with P' in the Hamiltonian and in the master equation. Note that the polarisation of the cavity field is the same in both cases since both transitions are π-transitions, as the light at the cavity input is polarised parallel to the quantisation axis. The simulation is executed in Python using QuTiP [183, 184]. The photon state is described in the Fock state basis up to a photon number of nine. This cut-off is valid, since we work with coherent states with mean photon numbers below two, and a coherent state with $\bar{n} = 2$ would correspond to a population of the first Fock state beyond the cut-off $|n = 9\rangle$ of less than $2 \cdot 10^{-4}$. In addition, an increasing dimension of the Hilbert space increases the run time of the simulation code.

Note, that due to the weakness of the dispersive interaction our measurement is not a quantum nondemolition (QND) measurement following the definition of Reference [185]: Although the interaction Hamiltonian is commuting with the operator of the measured observable, i.e., with $a^\dagger a$, the state is not collapsed onto an eigenstate of the measured observable, i.e., a Fock state. The measurement is, however, nondestructive in the following sense: The employed measurement mechanism, based on the dispersive interaction, is fundamentally not annihilating the measured photons. In our case, since the interaction time is longer than the photon lifetime inside the cavity, the measured photons are still destroyed, but only after they have left the cavity. For the case of a longer photon lifetime (cf. Section 5.5), the measurement scheme would be truly nondestructive.

5.3 Experimental results

The results are presented in the following subsections: First, the intracavity photon number is calibrated and the effect of spontaneous emission estimated. Next, the measured Ramsey fringes are analysed for different mean photon numbers in the cavity field. The single-ion coupling strength to the cavity is then extracted on two transitions from the observed phase shift, and the contrast of the fringes is analysed. An estimation of the phase resolution of the measurement follows. The section concludes with a comparison of the result between modes with different finesse values.

5.3.1 Calibration measurements

Calibrating the intra-cavity photon number

An independent calibration of the intra-cavity mean photon number is necessary in order to compare the experimental results to theory. The calibration is set up as follows: Given the cavity mirror properties of transmissions $\mathcal{T}_{1,2}$ and overall scattering and absorption losses $\mathcal{L}_{\text{tot}}$,

the probability for a single photon to leak out of the cavity through the output mirror is given by (see Section 4.6.1)

$$p_{\text{out}} = \frac{\mathcal{T}_2}{\mathcal{T}_2 + \mathcal{T}_1 + \mathcal{L}_{\text{tot}}}.$$

Using the rate 2κ with which photons leave the cavity in all directions, the rate at which photons leave through the output mirror is $2\kappa \cdot p_{\text{out}}$. The expected number of detection events at the APD is accordingly given by

$$R_{\text{APD}} = p_{\text{out}} \cdot 2\kappa \cdot \eta,$$

where η is the path efficiency. For the cavity mode with finesse $54.8(4) \cdot 10^3$ (see Section 4.4.1), we thus expect a photon detection rate of $38(8)$ kHz with a mean photon number of $\bar{n} = 1$ in the cavity mode. This value is calculated for the APD labelled "apdA", the one in the transmission path of the polarising beam splitter at the cavity output. The other APDs are not used in the experiment, as the cavity output waveplates were set such that all photons are transmitted through the PBS and sent to apdA.

With this count rate, it is now possible to calculate the expected number of photon detection events at apdA during the interaction time. However, for a precise estimate, we need to take into account that the cavity field does not build up instantaneously. It takes a few microseconds for the cavity field to build up to its full strength so that although the cavity is driven with a laser power that corresponds to $\bar{n} = 1$ inside the cavity, a smaller average count rate is detected at the APD. This effect is taken into account by simulating the field buildup and the corresponding intracavity mean photon number in the cavity mode and comparing the area under the simulated pulse to that under an ideal square pulse. The ratio of the two areas yields a correction factor of $c' = 0.922$ for the mode with finesse $54.8(4) \cdot 10^3$, and is calculated as the ratio of the integral of the temporal shape of the simulated intracavity photon to a squared pulse of the same duration and amplitude. Within the interaction time $\tau = 50$ µs, we therefore expect

$$C_0 = \frac{250 \cdot R_{\text{APD}} \cdot \tau}{c'} = \frac{475(100)}{0.922} = 515(108)$$

detection events in apdA, with counts being detected during 250 cycles, each 50 µs long. Note that because we only detect for 50 µs, we do not need to take into account the exponential decay of the photons after the cavity drive laser pulse is switched off. If the correction factor were not included, the intra-cavity mean photon number would be underestimated, as the measured number of photons is always less than in steady state because of the build-up time. For the mode with finesse $32.2(2) \cdot 10^3$, which was used in another measurement, we find $R_{\text{APD}} = 42(7)$ kHz, $c' = 0.953$, and $C_0 = 551(92)$ counts. The large relative uncertainties in the expected photon numbers are due to the large uncertainties on the transmission coefficients of the cavity mirrors (cf. Section 4.4.1).

An additional correction factor was used for the data corresponding to driving the $|D\rangle - |P\rangle$ transition, taken in October 2017 [Data17f]. This correction was necessary, as after taking these data, it was found that a cable connection at the time-tagging device for the APD detection had been faulty during the data acquisition. The bad connection led to an overcounting of APD detection events, presumably due to impedance mismatch and signal reflections in the cable. In Figure 5.3, the average number of APD counts is plotted as a function of the laser power at the cavity input, both before the faulty connection was fixed and afterwards. By comparing the

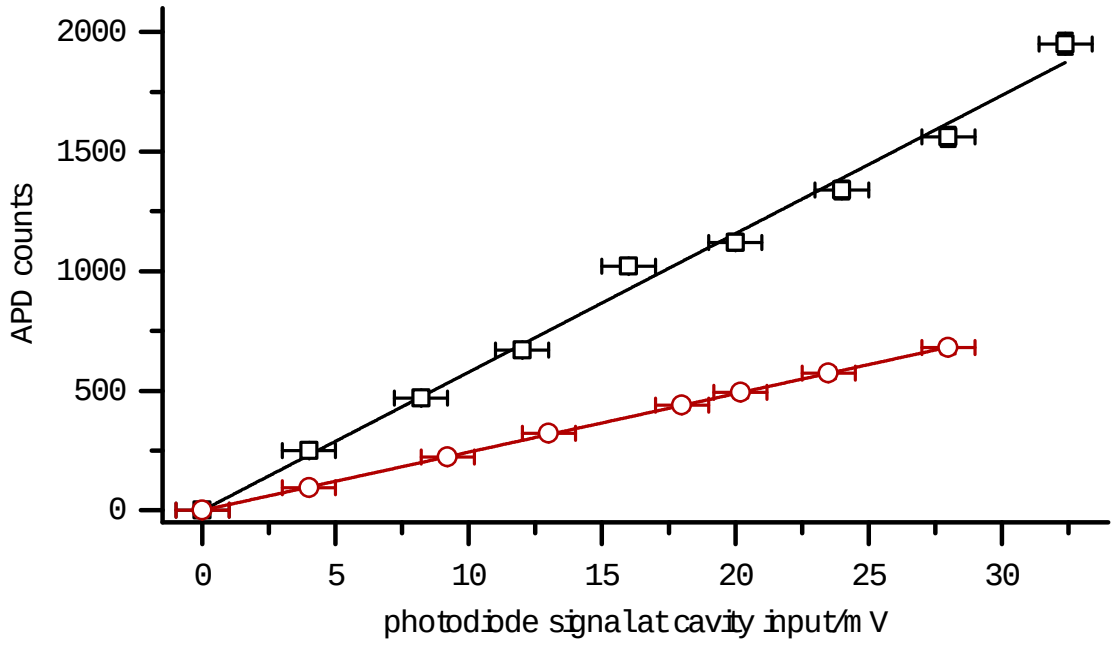

Figure 5.3: In order to compensate for a faulty connection in the APD detection setup, the slope of the APD counts versus laser power at the cavity input are compared before (black squares) and after (red circles) fixing the faulty connection. Each plotted data point is the average of the detected APD counts at each of the 50 points of one Ramsey fringe, with a detection window of $250 \cdot 50\ \mu\text{s} = 12.5$ ms. Lines are linear fits to the data, from which slopes of $58(1)$/mV (black squares) and $24.40(7)$/mV (red circles) are extracted. The ratio of the slopes of $2.38(4)$ is used as a correction factor in the calibration of the mean photon number (see main text). Data are [Data17f] (black squares) and [Data17g] (red circles).

slopes of the two curves, we can extract a correction factor of $\xi = 2.38(4)$ as the ratio of the two slopes, which is used to compensate for the overcounting.

The intracavity mean photon number $\bar{n}$ can thus be calculated from the measured number of detection events C as

$$\bar{n} = \frac{C}{C_0},$$

or

$$\bar{n} = \frac{C}{C_0 \cdot \xi}$$

for the data taken in October 2017 [Data17f].

Setting the detuning and estimating the influence of spontaneous emission

The detuning of the cavity drive beam from the atomic line is set in the following way. In the "ion drive" configuration, the frequency of the laser is shifted with a fibre-coupled EOM such that the contrast of the Ramsey fringe measured with the ion is minimised. This frequency corresponds to the resonance of the ion since the minimum Ramsey contrast corresponds to maximised excitation of the ion from $|D\rangle$ to $|P\rangle$, followed by spontaneous emission which

destroys the coherence necessary for a high Ramsey contrast. Next, the frequency is shifted from this resonance frequency by $125(1)$ MHz to the red of the $|S\rangle - |P\rangle$ transition. The uncertainty of the detuning is an upper limit based on the fact that simulating the experiment for a detuning $\Delta \pm 2\pi \cdot 1$ MHz gives the same result as for a detuning Δ. A value of 125 MHz was chosen since it is about a factor of 10 larger than the half linewidth of the $|P\rangle - |S\rangle$ transition. With this value, spontaneous emission is suppressed while the dispersive shift $\chi = g^2/\Delta$ is kept sufficiently large that the phase shift induced by the cavity photons can be observed for low mean photon numbers. Still, there is a non-negligible amount of spontaneous emission: The ion population in $|D\rangle$ may be off-resonantly excited by the cavity drive light to $|P\rangle$, from which it decays to the ground state $|S\rangle$ or the dark state $|S'\rangle$.

Offresonant excitation and spontaneous emission reduce the contrast of the Ramsey fringes beyond the desired contrast reduction due to the dispersive interaction. In order to estimate the effect stemming from spontaneous emission, a reference measurement was carried out with the same experimental sequence but with the ion addressed directly from the cavity side during the interaction time in the ion-drive configuration, instead of via the cavity. In this ion-drive configuration, the contrast decay of the Ramsey fringes is only due to spontaneous emission, not to the ion-cavity interaction. The Rabi frequency of the ion drive laser is set to the same value as in the cavity drive experiment in order to measure this effect. For setting the same Rabi frequency, the laser intensity is set such that the phase shift of the Ramsey fringe is the same as in the case of cavity drive.

Figure 5.4 shows the result of the reference measurement. In the cavity drive configuration, the contrast is reduced by a factor of 0.6 for a phase shift of $\varphi = \pi$ as compared to the ion drive case because of the additional decoherence introduced by intracavity photon-number fluctuations, in good agreement with theory. It can thus be concluded that the influence of spontaneous emission on the Ramsey measurements is sufficiently small to be able to observe the desired effect due to the cavity photons.

Note that both the spontaneous emission and the dephasing induced by the cavity photon number fluctuations will increase if the detuning Δ is decreased: The rate γ_{sp} of spontaneous emission via off-resonant excitation to the state $|P\rangle$ (or $|P'\rangle$) is proportional to the inverse detuning:

$$\gamma_{\text{sp}} \propto \Gamma \frac{g^2 \bar{n}}{\Delta^2},$$

with Γ the width of state $|P\rangle$ (or $|P'\rangle$). The dephasing rate γ_{deph} induced by the cavity photon number fluctuations is [12]

$$\gamma_{\text{deph}} \propto \kappa \bar{n} \left(\frac{g^2}{\kappa \Delta} \right)^2 = \frac{\bar{n} g^4}{\kappa \Delta^2}.$$

Since the ratio of cavity-induced dephasing to spontaneous emission is proportional to the cooperativity, but independent of the detuning,

$$\frac{\gamma_{\text{deph}}}{\gamma_{\text{sp}}} \propto \frac{g^2}{\kappa \Gamma},$$

changing the detuning cannot increase the relative strength of the effect. Increasing the detuning in order to minimise the spontaneous emission effect is not beneficial either, since the phase shift acquired by the ion during the interaction with the cavity photons is proportional to g^2/Δ.

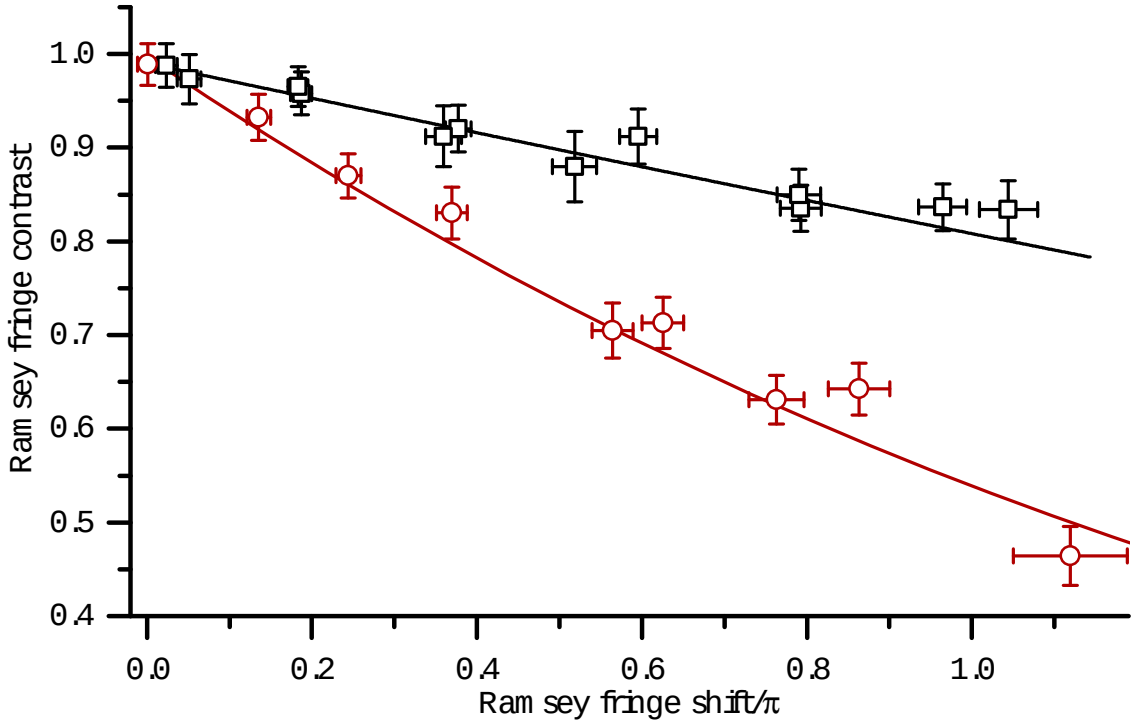

Figure 5.4: Reference measurement for estimating the effect of spontaneous emission. When driving the ion directly (black squares), the contrast of the Ramsey fringes is reduced substantially less as a function of the Ramsey fringe phase shift than when driving the cavity (red circles). The difference is explained by the additional decoherence introduced by the fluctuations of the photon number in the cavity field. Lines are simulations. The data were taken on the transition $|D\rangle - |P\rangle$ [Data17l, Data17m, Data17f].

Only using a higher finesse (smaller value of $\kappa \propto 1/\mathcal{F}$; cf. Section 3.3.1) or a higher coupling strength would change the ratio. For our parameters, the chosen value of 125 MHz is a compromise between a reduced contribution from spontaneous emission and a large enough phase shift per photon for $\bar{n} \sim 1$.

5.3.2 Ramsey fringe shift and contrast reduction

Fig 5.5 shows three Ramsey fringes measured on the $|D\rangle - |P\rangle$ transition, with calibrated mean photon numbers 0, $0.8(2)$, and $1.6(3)$. Note that the uncertainty in the mean photon number, which is on the order of 20%, is dominated by the systematic uncertainty deriving from the photon number calibration. As expected, the phase of each fringe is shifted and its contrast reduced for increasing mean photon number. All Ramsey fringes measured on the transition $|D\rangle - |P\rangle$ are shown in Figure 5.6.

The fit function for the least-squares fit to the Ramsey fringes has the following form and takes into account spontaneous emission via off-resonant excitation of the ion from $|D\rangle$ to $|P\rangle$ or $|D'\rangle$ to $|P'\rangle$:

$$E(\phi) = B + A \cdot \cos(\pi \cdot (\phi - \phi_0)),$$

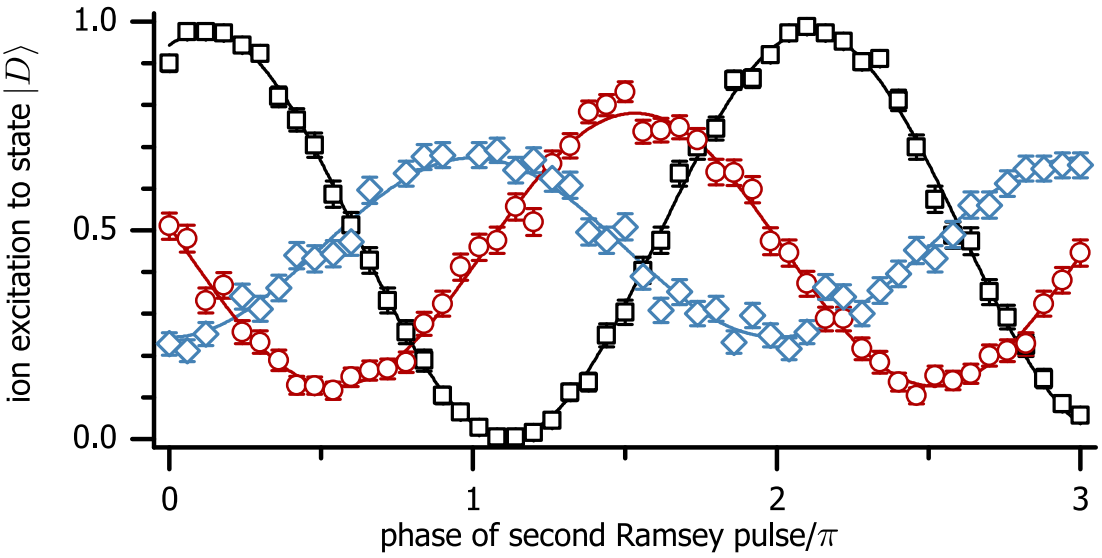

Figure 5.5: Ramsey fringes for values of $\bar{n} = 0$ (black rectangles), $\bar{n} = 0.8(2)$ (red circles), and $\bar{n} = 1.6(3)$ (blue diamonds). For an increasing mean photon number, the Ramsey fringe is shifted in phase, and its contrast is reduced. Lines are sinusoidal fits to the data and uncertainties are quantum projection noise from the 250 repetitions of the measurement for each phase value. Data are [Data17f].

where the offset B is given by

$$B = B_{\bar{n}=0} \cdot \exp\left[-\Gamma_{|S'\rangle} \cdot p_{|P\rangle} \cdot \bar{n} \cdot \tau\right].$$

Here, $B_{\bar{n}=0} = 0.49$ is the measured maximum offset for a Doppler cooled ion when there is no photon in the cavity, $\Gamma_{|S'\rangle}$ is the rate of decay from the excited state to the dark state of the system (cf. Section 5.2.1),

$$p_{|P\rangle} = \frac{2g^2\bar{n}}{\Gamma^2_{|P\rangle\rightarrow|D\rangle} + \Delta^2}$$

is the probability of the ion being off-resonantly excited from $|D\rangle$ to $|P\rangle$, and τ is the interaction time. For the second transition, $|D\rangle$ should be replaced by $|D'\rangle$ and $|P\rangle$ by $|P'\rangle$. The contrast of the Ramsey fringes is calculated as A/B.

From the fits, we find the following values for the contrast C and phase shift ϕ_0:

$$\begin{aligned}
\bar{n} &= 0: && C = 0.99(2), \quad \phi_0 = -0.12(1)\pi \\
\bar{n} &= 0.8(2): && C = 0.72(3), \quad \phi_0 = 0.57(3)\pi \\
\bar{n} &= 1.6(3): && C = 0.47(3), \quad \phi_0 = 1.12(7)\pi
\end{aligned}$$

The phase offset of $-0.12(1)\pi$ for the fringe with $\bar{n} = 0$ is most likely caused by an AC-Stark shift of the ion's levels by the cavity locking laser at 783 nm. Although a TEM_{01} mode of this laser in the cavity is used for stabilising the cavity length, there is still finite spatial overlap between the ion wave packet and this mode. The observed phase shift offset is compatible with an estimation of the effect for our parameters (see Appendix A.5).

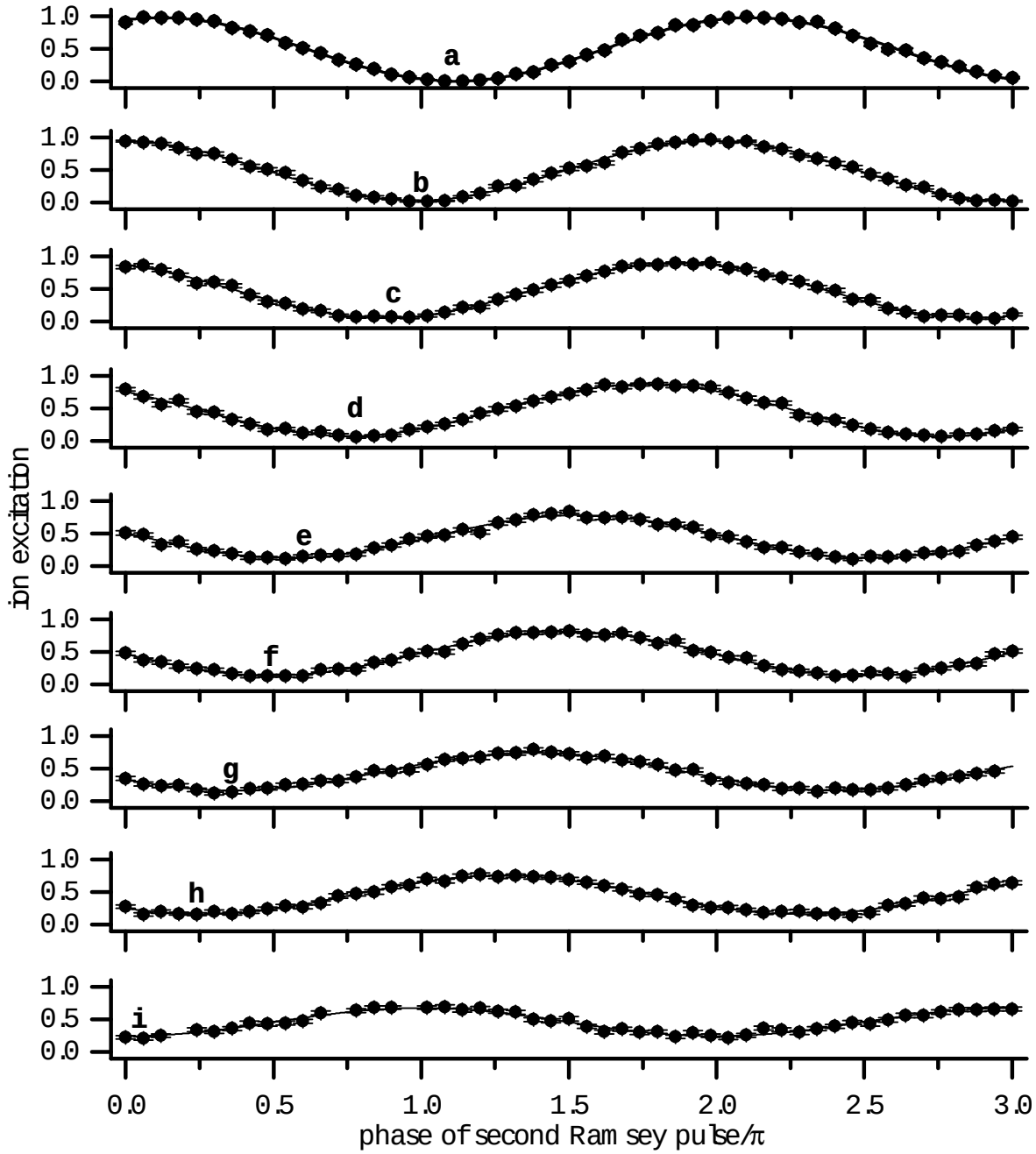

Figure 5.6: All Ramsey fringes measured on the transition $|D\rangle - |P\rangle$ with the mode of finesse $54.8(4) \cdot 10^3$, showing the full range of mean photon numbers measured on this transition. Lines are sinusoidal fits to the data. The calibrated mean photon numbers are (from top to bottom): **a**: $\bar{n} = 0$; **b**: $\bar{n} = 0.20(4)$; **c**: $\bar{n} = 0.38(8)$; **d**: $\bar{n} = 0.5(1)$; **e**: $\bar{n} = 0.8(2)$; **f**: $\bar{n} = 0.9(2)$; **g**: $\bar{n} = 1.1(2)$; **h**: $\bar{n} = 1.3(3)$; **i**: $\bar{n} = 1.6(3)$. The data are [Data17f] and correspond to Figure 5.7 and Figure 5.9 in the main text. Missing data points in **i** were removed because the ion was unstable during the measurement at the corresponding phase. Error bars are smaller than the symbols.

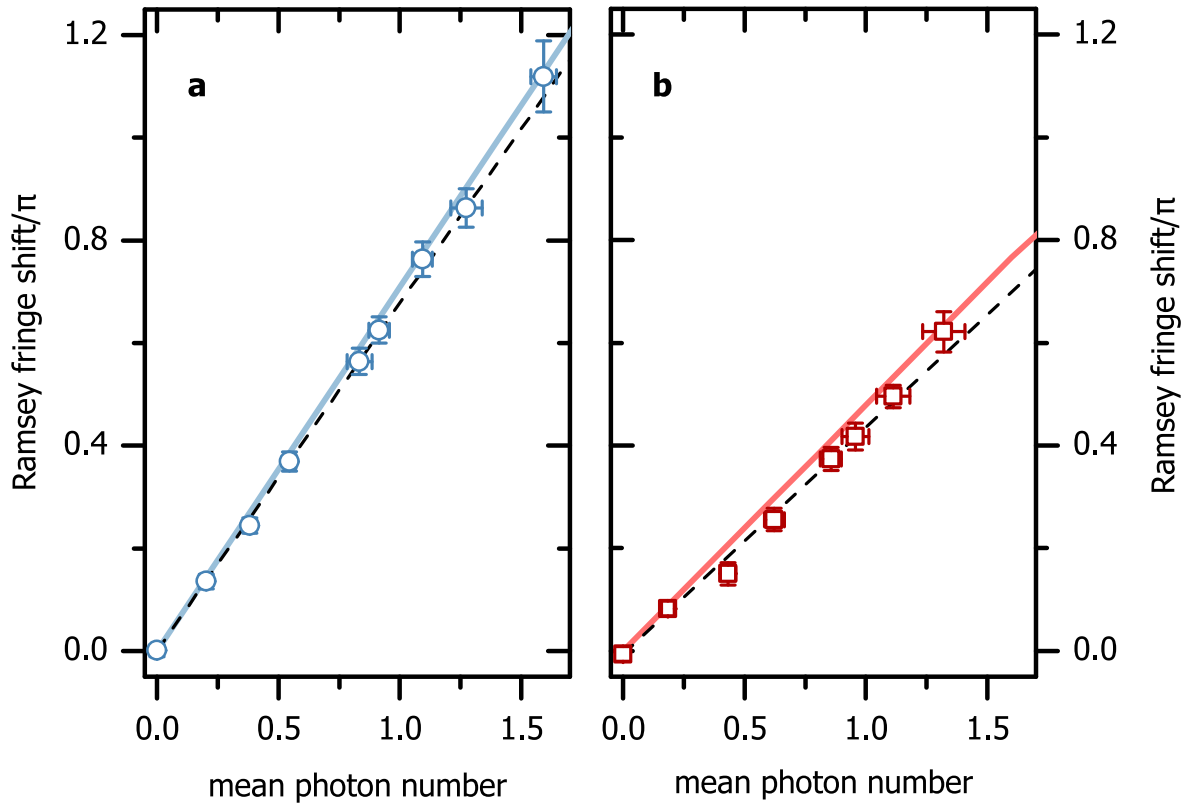

Figure 5.7: Ramsey fringe shift as a function of the mean photon number in the cavity field. **a** For the transition $|D\rangle - |P\rangle$. **b** For the transition $|D'\rangle - |P'\rangle$. Solid lines are theory calculations and dashed black lines linear fits to the data. The displayed uncertainties of the mean photon number are statistical only; systematic uncertainties are on the order of 20%, caused by the large relative uncertainties of the cavity mirror transmission and loss measurements. Data are [Data17f] (left) and [Data17g] (right).

5.3.3 Extracting the coupling strength and understanding the contrast

The Ramsey experiment was executed for nine different values of the mean photon number between 0 and 1.6 on the transition $|D\rangle - |P\rangle$ and for eight different values between 0 and 1.3 on the transition $|D'\rangle - |P'\rangle$. The corresponding phase shifts of the Ramsey fringes are plotted as a function of the mean photon number in Figure 5.7. The phase shift is linear with respect to the mean photon number and is in good agreement with theory. For a given mean photon number, the effect is weaker for the transition $|D'\rangle - |P'\rangle$, as the coupling strength and therefore also the dispersive shift χ are smaller for this transition. Figure 5.8 shows the Ramsey fringes measured on this transition.

Fitting a linear function to the data allows us to extract the ion-cavity coupling strength. This is especially useful since extracting the coupling strength via the vacuum Rabi splitting is not possible as our system is not in the strong-coupling regime. The linear fit is weighted with both the uncertainties of the mean photon number (statistical and systematic) and the uncertainties of the phase shift (standard uncertainty of the fit to the Ramsey fringe) [186]. The coupling

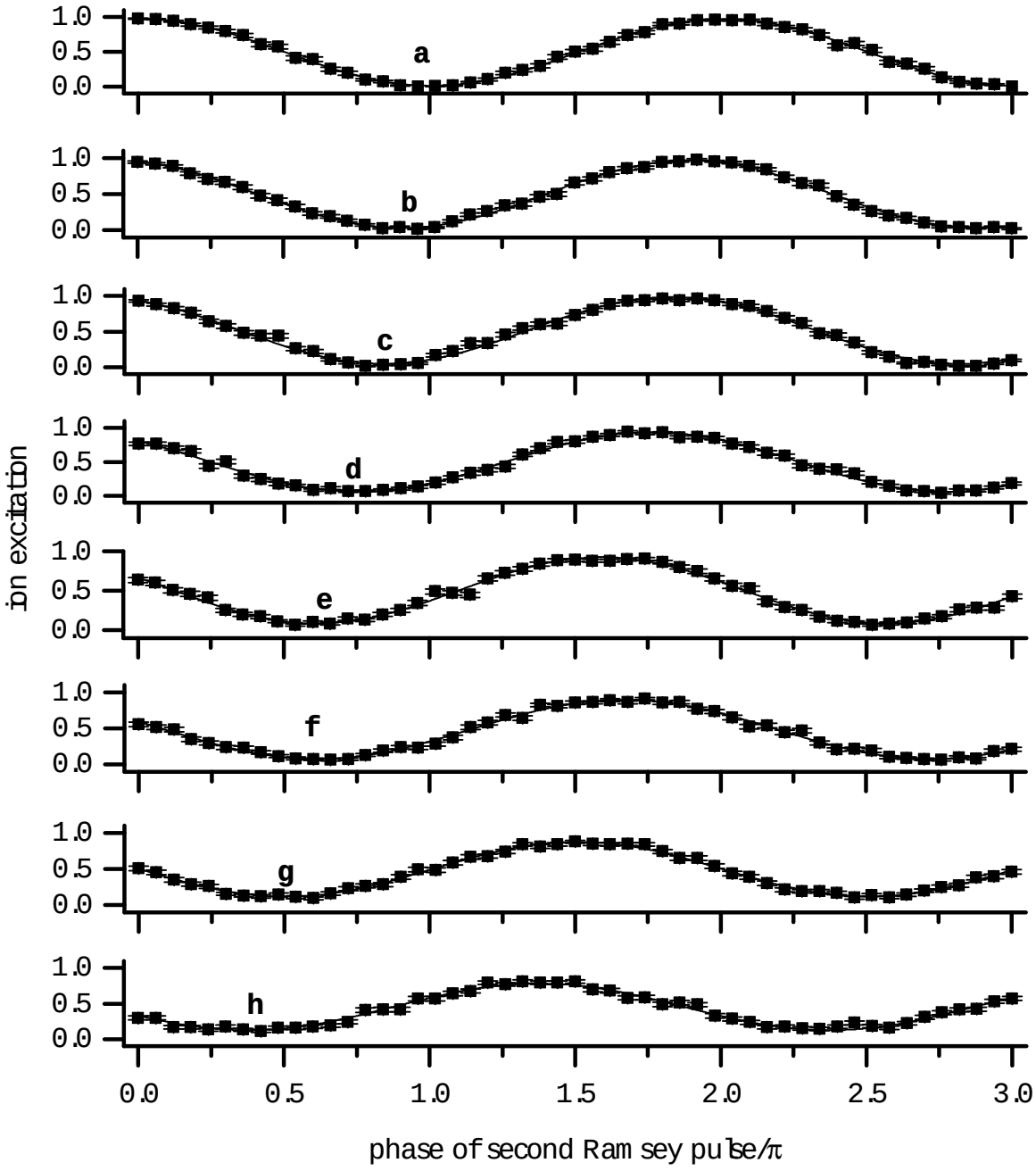

Figure 5.8: All Ramsey fringes measured on the transition $|D'\rangle - |P'\rangle$ with the mode of finesse $54.8(4) \cdot 10^3$. Lines are sinusoidal fits to the data. The calibrated mean photon numbers are (from top to bottom): **a**: $\bar{n} = 0$; **b**: $\bar{n} = 0.18(5)$; **c**: $\bar{n} = 0.4(1)$; **d**: $\bar{n} = 0.6(1)$; **e**: $\bar{n} = 0.9(2)$; **f**: $\bar{n} = 1.0(2)$; **g**: $\bar{n} = 1.1(2)$; **h**: $\bar{n} = 1.3(3)$. The data are [Data17g] and correspond to Figure 5.7 and Figure 5.9 in the main text.

strength is then calculated from the slope s of the linear fit as (cf. Section 5.2.3)

$$s = 2\tau\frac{g^2}{\Delta} \Leftrightarrow g = \sqrt{\frac{s\Delta}{2\tau}}.$$

The factor of 2 takes into account that we measure the phase shift in units of π but specify the coupling strength in terms of terms of 2π.

From the fits, we extract values of

$$g_{\text{exp}} = 2\pi \cdot 0.96(4)\ \text{MHz} \quad \text{and} \quad g'_{\text{exp}} = 2\pi \cdot 0.77(4)\ \text{MHz},$$

in good agreement with the values $g = 2\pi \cdot 0.97(19)$ MHz and $g' = 2\pi \cdot 0.79(16)$ MHz expected from the cavity properties (cf. Section 4.4.1) and the Clebsch-Gordan coefficients. The uncertainty is calculated using both the uncertainty of the slope from the fit (standard error of the fit) as well as the uncertainty of ± 1 MHz in the detuning. The uncertainty of the fit in turn is determined by the quantum projection noise in the Ramsey measurement and the uncertainty of the photon number calibration. Note that the values of the coupling strength extracted in this way have a relative uncertainty of only about 5%, in contrast to the values calculated from the measured cavity properties (see Section 4.4.1), which have uncertainties on the order of 20%. However, the latter measurement was limited in precision by the laser scan over several free spectral ranges, and it is possible to reach a relative precision on the order of 1%, as reported in Reference [72].

Contrast reduction of the Ramsey fringes as a function of the intra-cavity photon number

Figure 5.9 shows the contrast of the measured Ramsey fringes as a function of the mean photon number for the two transitions. For the transition $|D\rangle - |P\rangle$, the contrast decreases from $0.99(2)$ to $0.47(3)$ as the mean photon number increases from 0 to $1.6(3)$, while for the transition $|D'\rangle - |P'\rangle$, an increase of the mean photon number from 0 to $1.3(3)$ corresponds to a decrease of contrast from $0.98(3)$ to $0.73(4)$. The loss in contrast is due to a loss in coherence of the ion during the interaction with cavity photons. Fluctuations of the photon number in the cavity field lead to fluctuations of the ion's transition frequency and hence decoherence.

In an alternative view, the dephasing of the ion qubit can be interpreted as back-action from a weak measurement [78, 12, 187]: When photons exit the cavity after having interacted with the ion, they carry information about the phase of the ion. This information could in principle be detected, e.g., via homodyne detection. Even if the information is not detected, the back-action of this weak measurement by the environment leads to dephasing of the ion qubit. Due to the stronger coupling strength on the transition $|D\rangle - |P\rangle$, the photons extract more information about this transition, and therefore the contrast is reduced more than for the transition $|D'\rangle - |P'\rangle$.

5.3.4 Estimating phase resolution and photon number resolution

The phase resolution of this measurement method for a mean photon number $\bar{n} = 1$ is estimated in the following way. We first simulate a Ramsey fringe by numerically integrating the master

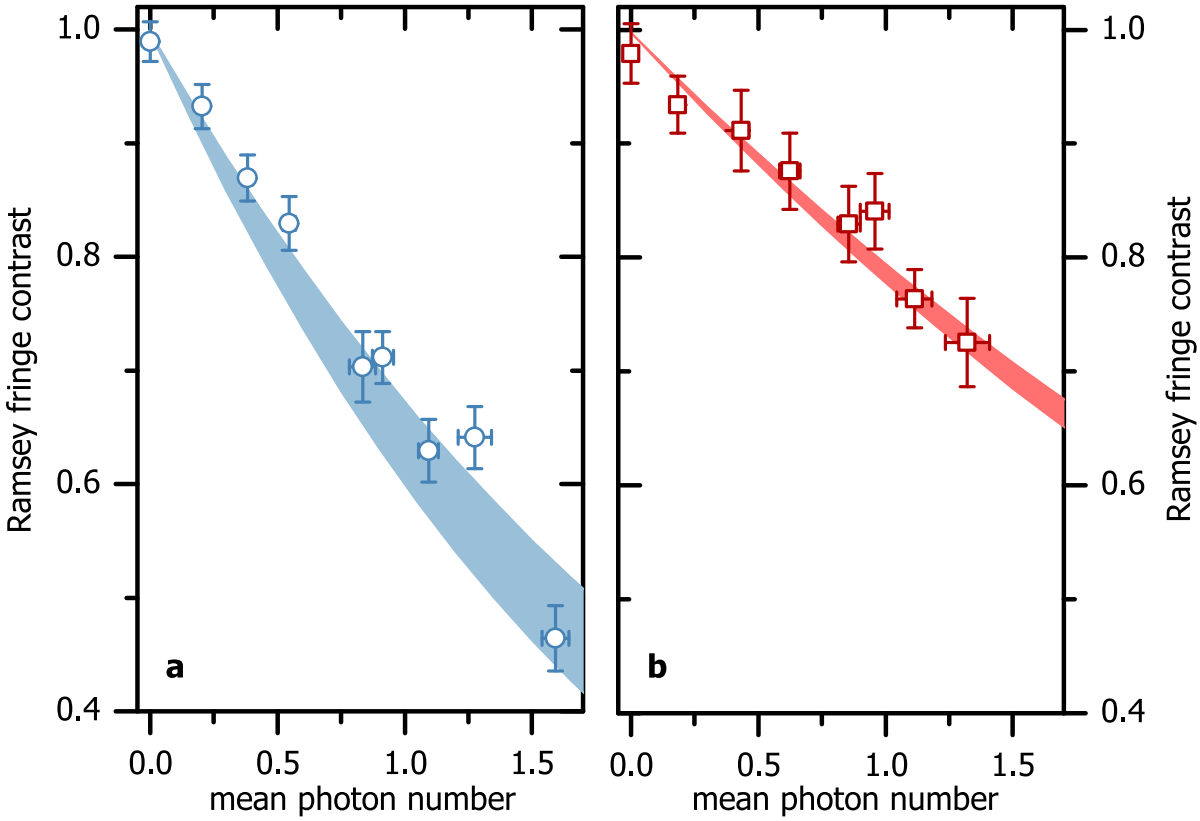

Figure 5.9: Ramsey fringe contrast as a function of the mean photon number in the cavity field. **a** Transition $|D\rangle - |P\rangle$. **b** Transition $|D'\rangle - |P'\rangle$. Shaded areas display the theory region, calculated from g_{exp} (g'_{exp}) and its uncertainties. The displayed uncertainties of the mean photon number are statistical only; systematic uncertainties are on the order of 20%, caused by the large relative uncertainties of the cavity mirror transmission and loss measurements. Data are [Data17f] (left) and [Data17g] (right).

equation (see Section 5.2.3) with $N = 51$ values of the phase. For a given phase ϕ_k, we extract a simulated excitation probability Q_k of the ion. Using the binomial distribution

$$\Pi_k(m_k) = \binom{M}{m_k} Q_k^M \left(1 - Q_k\right)^{M-m_k},$$

with $M = 250$ the number of repetitions in the measurement, we draw random samples m_k with probability Π_k. In other words, for each phase value ϕ_k, we simulate multiple ion excitation values $p_k = m_k/M$, whose distribution $\Pi_k(m_k)$ corresponds to quantum projection noise when repeating the measurement $M = 250$ times. In this way, we generate $50,000$ simulated Ramsey fringes, each with N points at the phases ϕ_k, which correspond to the phases in the measurement. By fitting a sinusoidal function to each fringe and extracting the phase shift, a distribution of $50,000$ phase shift values is built up. The number of $50,000$ has been chosen such that the standard deviation of the distribution converges. In this way, we simulate the way the phase is extracted in the experiment, i.e., by fitting sinusoidal curves to Ramsey fringes which are subject to quantum projection noise.

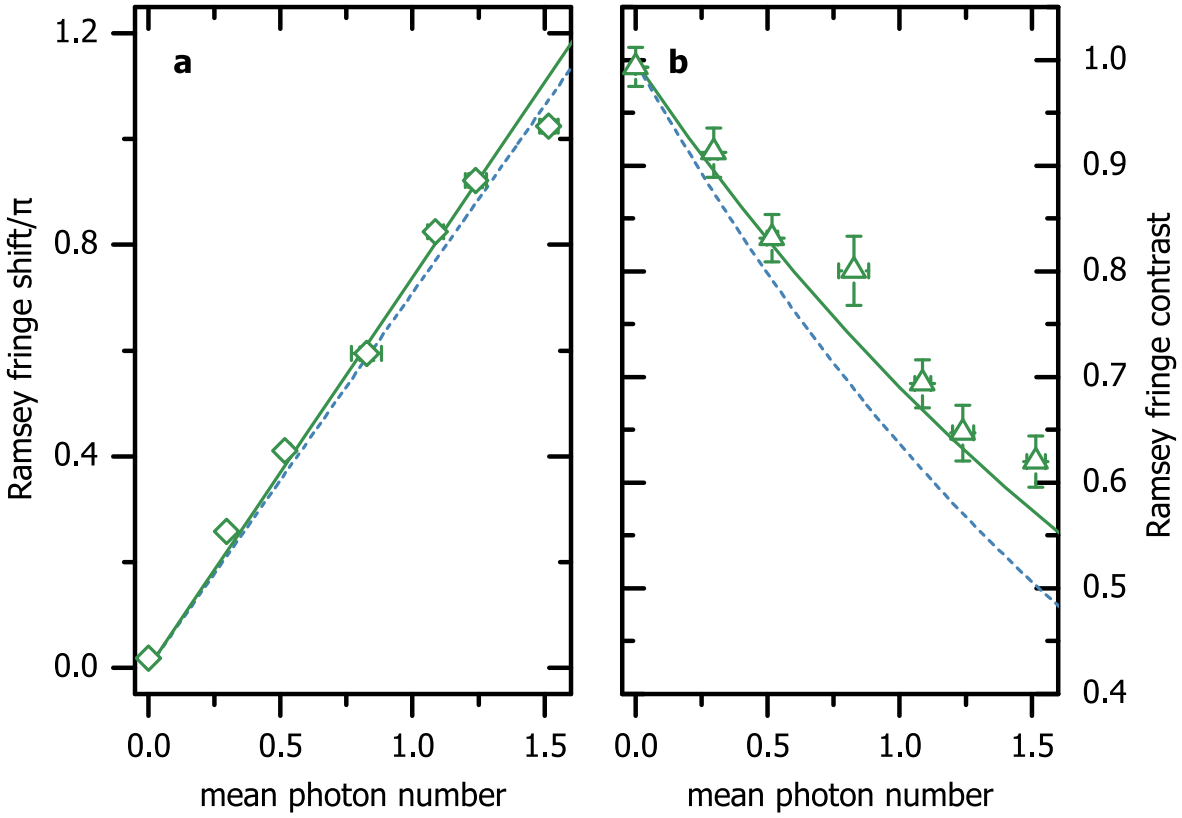

Figure 5.10: Ramsey fringe shift and contrast of the transition $|D\rangle - |P\rangle$ with an ion coupled to the cavity mode with finesse $32.2(2) \cdot 10^3$. Diamonds and triangles are data, while the solid lines are theory calculations for this transition and cavity mode, and the dashed blue lines are the theory for the same transition but for the mode with finesse $54.8(4) \cdot 10^3$. For the lower finesse, the contrast decreases slower than for the higher finesse. Error bars are mostly smaller than the symbols in **a**. The data are [Data17e].

The phase resolution $\delta\phi$ of the measurement can now be defined as twice the standard deviation σ_ϕ of the obtained phase distribution, $\delta\phi := 2\sigma_\phi$, since two such phase distributions can only be distinguished if their difference in phase is $\geq \delta\phi$. We find a value of $\delta\phi = 0.011\pi = 2.0°$. Note that this number has no uncertainty since it is the standard deviation of a distribution. In a worst-case scenario, the phase resolution would be given by the maximum span of the distribution, i.e., the difference between the maximum and minimum phase values in the distribution. This value is $0.0473\pi = 8.5°$ and can be considered an upper bound of the phase resolution.

The phase resolution can be translated into a resolution of the mean photon number via

$$\delta\phi = \frac{g^2}{\Delta}\tau\,\delta\bar{n}. \tag{5.3}$$

Here, $\delta\bar{n}$ is the value of the mean photon number difference for which the Ramsey measurement results taken with $\bar{n}$ and $\bar{n} + \delta\bar{n}$ can still be distinguished in our parameter regime. We find a value of $\delta\bar{n}_{PD} = 0.013(5)$ for the $|D\rangle - |P\rangle$ transition and $\delta\bar{n}_{P'D'} = 0.020(8)$ for the

$|D'\rangle - |P'\rangle$ transition.

5.3.5 Comparing two cavity modes with different finesse

Phase shift and contrast values of Ramsey fringes were also measured with the ion coupled to the cavity mode with finesse $32.2(2) \cdot 10^3$. The result is shown in Figure 5.10, while Figure 5.11 shows all measured Ramsey fringes [Data17e].

Although the phase shift as a function of the mean photon number in the cavity mode is almost the same as for the mode with a higher finesse of $54.8(4) \cdot 10^3$, the contrast is reduced significantly less for the lower finesse mode. Intuitively, this can be explained by the fact that photons in a higher finesse mode accumulate more phase shift due to their interaction with the ion because their lifetime τ_c is larger than for a lower finesse. When a photon in the higher finesse mode exits the cavity, it therefore extracts more information about the ion than it would have for the lower finesse mode, leading to stronger back-action on the ion. In a quantitative analysis, Gambetta et al. found that for $\chi \ll \kappa$ and for an interaction time longer than the photon lifetime, the dephasing rate induced by the cavity photons is inversely proportional to κ (see equation (5.10) of Reference [12]). Hence, for a higher finesse and consequently lower κ, the dephasing is stronger and the reduction in Ramsey contrast is greater.

5.4 Reconstructing the intra-cavity field

In order to reconstruct the photon number distribution from the measured Ramsey fringe, we employ a maximum likelihood algorithm which finds the values of the coherent driving field amplitude η and incoherent driving amplitude δn which best explain the observed data. This method can be used to analyse the statistics of the photons in the cavity field without directly measuring and thereby destroying them. The following section describes this algorithm as well as the reconstruction results. This analysis is only carried out for the data on the $|D\rangle - |P\rangle$ transition measured with the mode of finesse $54.8(4) \cdot 10^3$.

5.4.1 Reconstruction algorithm

In order to quantify how close experimental data and simulation are for a given set $(\eta, \delta n)$, the likelihood function L is defined as

$$\log\left[L\left(\eta, \delta n\right)\right] = \sum_{k=1}^{N} \Big(f_k \log\left[P_k\left(\eta, \delta n\right)\right] + \left(1 - f_k\right) \log\left[1 - P_k\left(\eta, \delta n\right)\right] \Big) + \text{const.} \tag{5.4}$$

Here, $N = 51$ is the number of phase values in each measured Ramsey fringe, f_k is the observed probability of the ion having been detected in state $|D\rangle$ for the k-th phase value in the fringe, and P_k is the calculated ion excitation probability, drawn from the numerical simulation of the master equation for a given set $(\eta, \delta n)$ (see Section 5.2.3).

The algorithm finds the values $(\eta, \delta n)$ which best explain the observed data in the following way: The master equation (Equation 5.2) is integrated for an initial pair of values of η and δn. From the solution of the master equation and the measured data, the likelihood is calculated according to Equation 5.4. In the next iteration, the values of η and δn are changed, and the

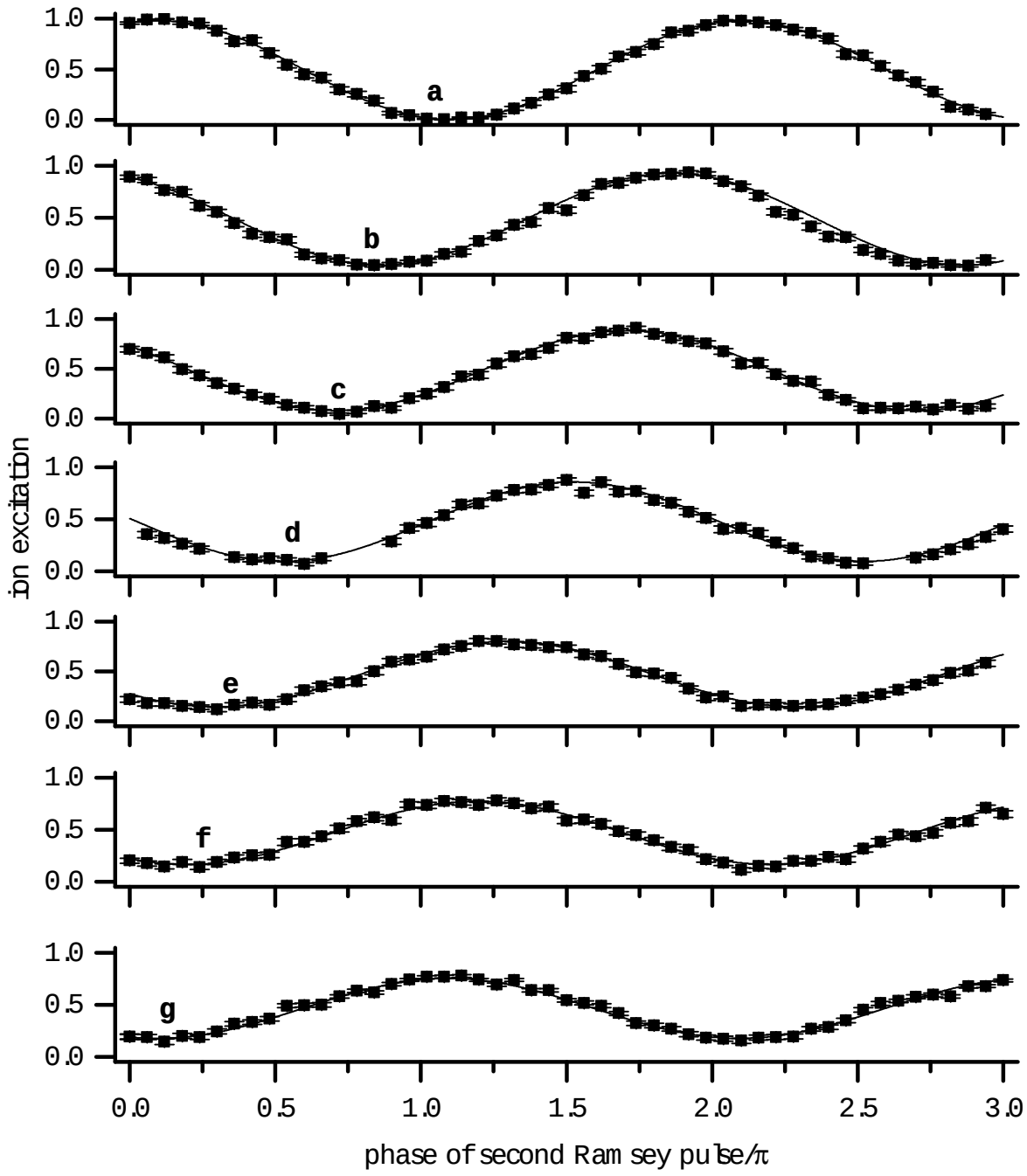

Figure 5.11: All Ramsey fringes measured on the transition $|D\rangle - |P\rangle$ with the mode of finesse $32.2(2) \cdot 10^3$. Lines are sinusoidal fits to the data. The calibrated mean photon numbers are (from top to bottom): **a**: $\bar{n} = 0$; **b**: $\bar{n} = 0.30(6)$; **c**: $\bar{n} = 0.5(1)$; **d**: $\bar{n} = 0.8(2)$; **e**: $\bar{n} = 1.1(2)$; **f**: $\bar{n} = 1.2(3)$; **g**: $\bar{n} = 1.5(3)$. The data are [Data17e] and correspond to Figure 5.10 in the main text. Missing data points (**c**, **d**) were removed because the ion was unstable during the measurement at the corresponding phase. Error bars are smaller than the symbols.

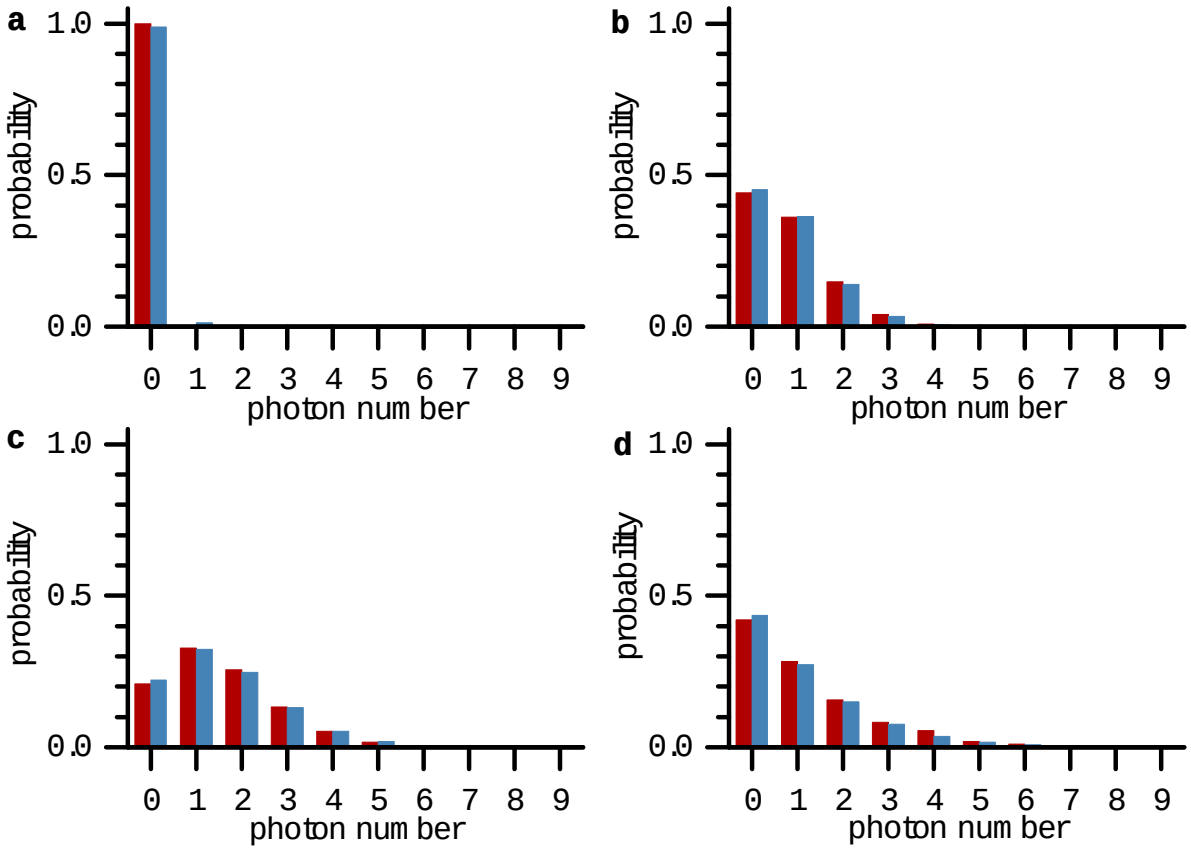

Figure 5.12: Reconstructed photon number distributions. Red bars (left bar of each pair) are the expected distributions based on the calibrated mean photon numbers, while blue bars (right bar of each pair) are the reconstructed distributions. Calibrated and reconstructed mean photon numbers, and the squared statistical overlap between reconstructed and expected distributions, are: **a** $\bar{n} = 0$, $\bar{n}_{\text{rec}} = 0.01^{+0.05}_{-0.02}$, SSO $= 0.99(2)$; **b** $\bar{n} = 0.8(2)$, $\bar{n}_{\text{rec}} = 0.84(8)$, SSO $= 0.99(1)$; **c** $\bar{n} = 1.6(3)$, $\bar{n}_{\text{rec}} = 1.49^{+0.05}_{-0.06}$, SSO $= 0.999(2)$. Subfigure **d** shows the simulated and reconstructed distributions when driving with a thermal state with $\bar{n}_{\text{th}} = 0.44(9)$ and $\bar{n}_{\text{coh}} = 0.6(1)$ (see main text) with squared statistical overlap of $0.997(6)$. The data are [Data17f, Data17b].

master equation is integrated with these new values. The likelihood is calculated again and compared to previous value. This algorithm is iterated until the maximum of the likelihood has been found in a simplex optimisation [188].

The values $(\eta_{\text{opt}}, \delta n_{\text{opt}})$ for which the likelihood is maximised are the ones that best explain the measured data given our model. The reconstructed photon number distribution $p(n)$ is then given by the diagonal elements of the density matrix of the cavity field obtained from the integration of the master equation with input parameters $(\eta_{\text{opt}}, \delta n_{\text{opt}})$.

5.4.2 Reconstruction results

The reconstructed photon number distributions for the calibrated mean photon numbers $\bar{n} = 0$, $\bar{n} = 0.8(2)$, and $\bar{n} = 1.6(3)$ are shown in Figure 5.12a-c. The plot shows both the reconstructed distributions in blue and the expected distributions in red, the latter calculated by integrating the

master equation using the calibrated mean photon number as an input parameter.

In order to quantify the quality of the reconstruction method, the squared statistical overlap (SSO)[3], derived from the statistical overlap [189], is calculated between the reconstructed distribution $p_{\text{rec}}(n)$ and the distribution according to the calibration $p_{\text{cal}}(n)$ as

$$\text{SSO} = \left[\sum_{n=0}^{9} \sqrt{p_{\text{rec}}(n)\, p_{\text{cal}}(n)}\right]^2 .$$

Note that we only consider photon Fock states up to $n = 9$ since for this cutoff the computational effort for the reconstruction algorithm is still maintainable on standard computers and the mean photon numbers in the experiment are far below this number. Typically, the full reconstruction for one state takes on the order of several hours to run. For all three coherent states shown in Figure 5.12a-c, values of SSO > 0.99 are found between the reconstructed distribution and the distribution expected from the photon calibration.

In addition, from the reconstructed distributions, the reconstructed mean photon numbers $\bar{n}_{\text{rec}}$ and the Mandel Q-parameters [190] can be calculated to ascertain that the reconstructed states are close to coherent states as expected. The Mandel Q-parameter is defined as

$$Q = \frac{\langle n^2 \rangle - \bar{n}^2}{\bar{n}} - 1,$$

where $\langle n^2 \rangle$ is the expectation value of n^2. We find values of

$$\begin{aligned} \bar{n}_{\text{rec}} &= 0.01^{+0.05}_{-0.02}, \quad Q = 0.00^{+0.02}_{-0.01}, \\ \bar{n}_{\text{rec}} &= 0.84(8), \quad Q = -0.03(7), \\ \bar{n}_{\text{rec}} &= 1.49^{+0.05}_{-0.06}, \quad Q = 0.04(5). \end{aligned}$$

All values of $\bar{n}$ are consistent with the calibrated values, and the values of the reconstructed Q-parameters indicate that all three states follow Poissonian statistics and are therefore indeed compatible with being coherent states.

5.4.3 Driving with intensity noise

In another measurement, the cavity was driven with light of mixed thermal and coherent photon statistics. For this purpose, intensity noise was added to the RF input of the AOM controlling the cavity drive pulses. The added noise had a bandwidth of 10 MHz, which can be considered white noise since it is much broader than the bandwidth $2\kappa = 2\pi \cdot 136$ kHz of the cavity. The mode with finesse $54.8(4) \cdot 10^3$ was used for this measurement.

In our model, additional fluctuations caused by thermal noise are described by the thermal mean photon number $\bar{n}_{\text{th}}$ (see Section 5.2.3). In order to calibrate this parameter, we detect the cavity drive pulse with a photodiode[4] (see Figure 5.13a). The photodiode is placed at one output of a beam splitter in the laser path to the cavity. The field contributing to the intensity detected

[3] See Appendix A.6 for an analysis of the sensitivity of this measure.

[4] Thorlabs, PDA36A with a bandwidth of 5.5 MHz at 10 dB gain.

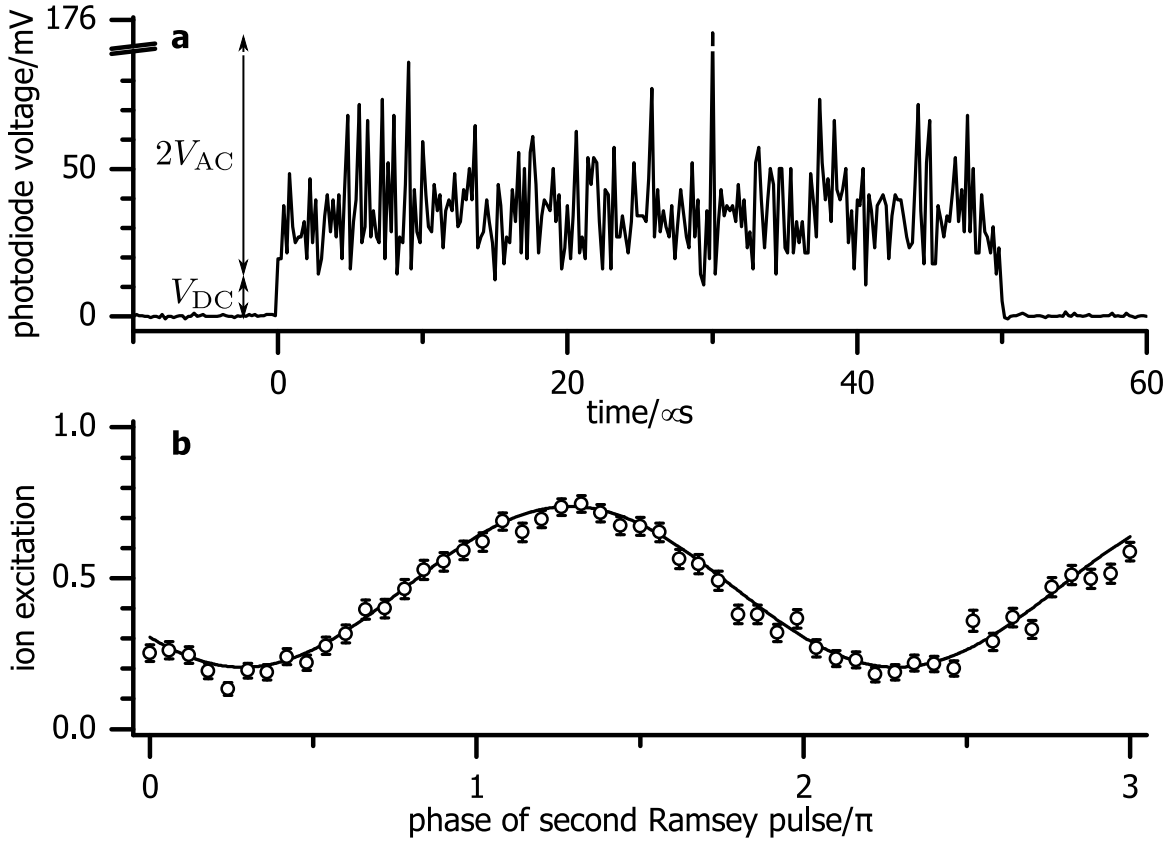

Figure 5.13: Ramsey fringe when driving the cavity with a coherent field with added amplitude noise. **a** Typical pulse of the cavity drive laser with added amplitude noise, as detected on a photodiode before the cavity. For the calibration, the signal is divided into a voltage V_{DC} corresponding to coherent driving and a voltage amplitude V_{AC}, corresponding to incoherent driving. **b** Ramsey fringe for a cavity drive field with calibrated coherent mean photon number $\bar{n}_{\mathrm{coh}} = 0.6(1)$ and thermal mean photon number $\bar{n}_{\mathrm{th}} = 0.44(9)$. The fringe shift is $0.71(2)\pi$, and the contrast is $0.57(3)$. Data are [Data17b].

on the photodiode has a coherent and an incoherent (thermal) contribution. We therefore separate the photodiode voltage into an offset part, corresponding to the coherent contribution, and an oscillating part, corresponding to the thermal contribution (cf. Figure 5.13a).

It thus becomes possible to calibrate the parameter $\delta n = \kappa n_{\mathrm{th}}$ in the master equation by using our calibration of the APD counts with parameters C_1 and ξ (see Section 5.3.1): First, the conversion factor S_{V} between the measured DC photodiode voltage V_{DC} corresponding to coherent drive and the number of counts C detected at the APD is calculated as

$$S_{\mathrm{V}} = C/V_{\mathrm{DC}} = 58(1)/\mathrm{mV}.$$

The incoherent contribution can then be calculated via

$$\bar{n}_{\mathrm{th}} = \frac{S_{\mathrm{V}} V_{\mathrm{AC}}}{C_1 \xi} \Longleftrightarrow \delta n = \kappa \frac{S_{\mathrm{V}} V_{\mathrm{AC}}}{C_1 \xi},$$

where V_{AC} is the amplitude of the oscillations detected on the photodiode. V_{AC} is rescaled in order to account for the bandwidth difference between the photodiode and the cavity (see

Appendix A.7). From this calibration, values of $\bar{n}_{\text{th}} = 0.44(9)$ and $\bar{n}_{\text{coh}} = 0.6(1)$ are found, adding up to a total mean photon number of $\bar{n} = 1.0(1)$. The Mandel Q-parameter of this field is $Q = 0.64^{+0.06}_{-0.07}$, i.e., it consists of super-Poissonian light. The corresponding Ramsey fringe is shown in Figure 5.13b, and the reconstructed distribution in Figure 5.12d. Note that in this case, the expected distribution is determined by solving the master equation with the calibrated values of $\bar{n}_{\text{th}}$ and $\bar{n}_{\text{coh}}$.

From the reconstructed photon distribution, we find a total mean photon number $\bar{n}_{\text{rec}} = 1.05^{+0.07}_{-0.12}$, consisting of $\bar{n}_{\text{coh,rec}} = 0.68(16)$ and $\bar{n}_{\text{th,rec}} = 0.47(15)$. The reconstructed Mandel Q-parameter is $Q_{\text{rec}} = 0.70^{+0.07}_{-0.10}$. All reconstructed values are in agreement with the calibrated values, showing that the reconstruction method also works for light with mixed coherent and thermal statistics and can be used to distinguish between light of such statistics and light with Poissonian statistics[5].

5.5 Outlook on possible extensions of the experiment

Enhancing the sensitivity

The phase sensitivity of the measurement can be enhanced by dispersively coupling more than one ion to the cavity mode. If M ions are in an entangled state, the sensitivity of the Ramsey measurement improves by a factor of $\sqrt{M}$ [4]. In addition, the collective coupling strength grows by $\sqrt{M}$ [75]. This increase in coupling strength will increase the dispersive shift per photon χ by a factor of M and thus increase the sensitivity for the mean photon number (cf. Equation 5.3). The increased coupling strength would also allow for a measurement time reduced by a factor of M, while maintaining the phase resolution.

Note that for reaching higher precision in the reconstruction of the photon number distribution, the quantum projection noise should be reduced by taking more measurement cycles per Ramsey phase. In the measurements presented in this thesis, the number of measurement cycles was limited to 250 due to the technical limitations of the FPGA-based experiment control hardware. On the other hand, with reduced measurement time, the system comes closer to the regime $\tau \approx \tau_{\text{c}}$, in which on average only a single photon with lifetime τ_{c} interacts with the ion during the interaction time τ.

Using more than one ion would also make it possible to observe the effect of true single photons, i.e., Fock states, inside the cavity: One of several ions could be driven in a Raman transition such that a single photon is emitted into the cavity mode. While the first ion generated a photon in the resonant Raman process, the second ion would be initialised in a superposition of $|S\rangle$ and $|D\rangle$ such that the time evolution of the photon generation would be imprinted onto the phase of the second ion.

Extracting the full density matrix

In the measurements presented in this thesis, only the diagonal elements of the cavity-field density matrix were extracted, corresponding to the photon number distribution. Although the reconstruction algorithm returns a full density matrix, the effect of the coherences of the photon

[5] See Reference [191] for an alternative approach in the microwave regime.

field on the ion was not measured directly in the Ramsey fringe. This additional information could be accessed by adding a displacement operation acting on the cavity field, a scheme employed in microwave cavities [166]: The full information about the cavity field can be extracted by letting the unknown cavity field and the known displacement field interfere while changing the amplitude and the phase of the displacement field.

Reversing the measurement scenario and reaching the strong pull regime

Instead of using the ion as a quantum sensor for the cavity field, it would be possible to reverse the scenario and to extract information about the phase of the ion by implementing a homodyne measurement of the cavity output field. Such a measurement of the phase shift induced by the dispersively coupled ion on the cavity field would allow the experimenter to track the phase of the ion.

In the case of microwave cavities with Rydberg atoms or superconducting qubits, such measurements have been used for monitoring quantum trajectories or even feedback and quantum-state stabilisation of qubits [166, 13]. Implementing such a scheme in our setup would allow us to carry out optical quantum feedback experiments with trapped $^{40}Ca^{+}$ ions. In addition, the generation of nonclassical cavity field states would become possible, as measuring the ion in a state corresponding to a specific Fock state in the cavity would project the cavity field onto that state.

However, for such experiments it would be necessary to reach the strong dispersive (or strong-pull) regime with $\chi > \kappa$: If the dispersive shift per photon $\chi = g^2/\Delta$ exceeds the cavity decay rate κ, each photon number component in the cavity field can be measured directly via spectroscopy of the stationary qubit. In order to reach this regime, it would be necessary to replace the cavity mirrors with lower-loss mirrors: The mirrors reported on in Reference [192] have transmission values of $\mathcal{T} = 5 \cdot 10^{-7}$ and scattering and absorption loss of $\mathcal{L} = 1.1 \cdot 10^{-6}$ per mirror for wavelengths near 850 nm, resulting in a finesse of $\mathcal{F} = 2 \cdot 10^6$. If we built a cavity of length 19.98 mm with such mirrors, we would expect a photon lifetime of $\tau_c = 42$ µs, with a one-sided cavity output coupling of $\mathcal{T}/(2\mathcal{T} + 2\mathcal{L}) = 16\%$, comparable to that of our current cavity (cf. Section 4.6.1). Table 5.1 gives a summary of estimated dispersive coupling parameters with such a cavity and $^{40}Ca^{+}$ ions or the D2 line of ^{133}Cs atoms.

Table 5.1: Estimation of dispersive coupling parameters. By using state-of-the-art low-loss mirrors for a cavity, reaching the strong-pull regime ($\chi > \kappa$) in the optical regime would be possible. The cavity parameters are $\mathcal{F} = 2 \cdot 10^6$, $L = 19.98$ mm, and the detuning is assumed as ten times the atomic linewidth γ. Note that γ and κ are half widths.

Species	$^{40}Ca^{+}$	^{133}Cs
Transition	$\lvert 3^2D_{5/2}\rangle - \lvert 4^2P_{3/2}\rangle$	$\lvert 6^2S_{1/2}, F=4\rangle - \lvert 6^2P_{3/2}, F=5\rangle$
Wavelength/nm	854	852
$g/(2\pi$ MHz)	1.53	2.8
$\gamma/(2\pi$ MHz)	11.5	2.6
$\kappa/(2\pi$ kHz)	1.9	1.9
χ/κ	10.7	159

In both cases, the atom-cavity detuning is set as ten times the atomic linewidth. The ratio

χ/κ reaches values of 10.7 for $^{40}Ca^{+}$and 159 for ^{133}Cs, indicating that reaching the strong-pull regime is possible for both atomic species. By employing collective coupling (see above), χ/κ could be increased even further. Note that for $^{40}Ca^{+}$, χ/κ is reduced when the Clebsch-Gordan coefficient for the specific transition is included, e.g., $\chi/\kappa = 4.3 > 1$ for the transition $|3^2D_{5/2}, m_J = 1/2\rangle - |4^2P_{3/2}, m_J = 1/2\rangle$. Using fast ion state readout, which has been demonstrated with 99% fidelity in 10.5 µs $< \tau_c$ [193, 194], it should be possible to collapse the cavity field onto nonclassical states.

Comparing nonclassical states inside and outside the cavity

A nonclassical quantum state generated inside an optical cavity usually has to be transmitted through a cavity mirror before it can be measured. During the process of leaving the cavity, the nonclassical features are washed out because of absorption and scattering in the mirror [195, 196]. One possible solution for measuring the full features of the state could be to observe it directly inside the cavity, using a single quantum emitter as a probe.

A similar argument shows that due to the imperfect mirrors, any photons leaving the cavity will be absorbed or scattered with non-zero probability. Even with detectors with very high quantum efficiency, e.g., using superconducting nanowires with a record efficiency of 98% at 850 nm [197], for experiments with high-efficiency requirements, using an in-cavity sensor might be advantageous.

Exploring non-Markovian systems

The input-output relation $a_{\text{out}} + a_{\text{in}} = \sqrt{2\kappa}\, a_{\text{cavity}}$ [198] describes the relation between the field a_{cavity} inside a cavity and the fields a_{in} and a_{out} at input and output of the cavity. It relies on the assumption that the system is Markovian. This relation can be tested experimentally by directly accessing the intracavity field via an ion as a probe and without having to resort to measuring only input and output fields. To our knowledge, such measurements have not been performed to date. In addition, systems involving coupled cavities [199] or a cavity with feedback are explicitly non-Markovian, and hence cannot be simply described via the input-output formalism (see, e.g., Reference [200]). By directly measuring the cavity field inside, the relation between fields inside and out of the cavity could be probed experimentally in such systems.

5.6 Summary

This chapter reported on an experiment, in which the effect of cavity photons on a trapped ion coupled dispersively to the cavity was investigated. The phase shift and the decoherence caused by the AC-Stark shift induced by the photons were measured in Ramsey experiments using the ion, and the ion-cavity coupling constant was extracted for two transitions from the phase-shift measurement. This dispersive method is a useful tool for extracting coupling strengths since it does not rely on vacuum Rabi splitting and hence also works for systems in intermediate or even weak coupling regimes.

From the measured Ramsey fringes the photon number distribution of the cavity field was reconstructed, with good overlap between expected and reconstructed distributions. In addition

to being able to distinguish between light with coherent and mixed thermal-coherent photon statistics, the method is nondestructive, i.e., the cavity field whose statistics are analysed is not destroyed by the measurement process.

Furthermore, several extensions of the experiment were presented. These included both measurements feasible in our current setup and measurements that would require a cavity with different parameters.

Chapter 6

Proposals for future experiments.

Es ist von einem Experiment zu viel gefordert, wenn es alles leisten soll.
– J. W. von Goethe, Maximen und Reflexionen

This chapter consists of four sections, each containing ideas and considerations for potential future experiments in our setup. The proposals are explained and the feasibility of their implementation is discussed. While the first proposal deals with fundamental quantum optics, the last three sections deal with experiments in the context of quantum networking. The motivation for quantum networking proposals is given by the ongoing project to link the three existing ion-trap–cavity setups in Innsbruck in a three-node quantum network, which can be used to test quantum repeater protocols [201].

6.1 Cavity-mediated entanglement between two ions

This proposed experiment is based on Reference [202], which investigates the case of multiple ions inhomogeneously coupled to the same cavity – a system described by the Tavis-Cummings Hamiltonian [203]. In such a configuration, sub- and superradiant states of N ions exist (cf. also Reference [75]) which radically differ in their coupling to the cavity mode: While the superradiant state exhibits a coupling strength to the cavity that is larger by $\sqrt{N}$ than the single-ion coupling strength, the subradiant state does not couple to the cavity. An initial state of $N = 2$ ions which is a superposition of these states, will eventually evolve into the subradiant state because the superradiant contribution is depopulated via the cavity decay since for $N = 2$ the eigenstates of the multi-ion–cavity system are sub- and superradiant states. In this sense, the interaction with the environment via the cavity decay drives the ions into an entangled state.

There are multiple other proposals for cavity-based entanglement schemes, some of which rely on unitary dynamics [204–208], while others make use of the dissipation via the cavity mode [209–211]. While the infidelity of the entangled state with respect to a maximally entangled state is proportional to $1/\sqrt{C}$, where C is the cooperativity, this scaling changes to $1/C$ for dissipative schemes [211]. We considered the particular concept proposed by Härkönen et al. in Reference [202] for our setup since it explicitly considers $^{40}Ca^{+}$-ions in linear Paul traps. As a side note, the idea of harnessing the dissipation in open systems for the generation of entanglement or for driving the system into desired states has also led to numerous proposals

not involving a cavity [212–216], and the concept has even been extended to dissipation-based quantum error correction schemes [217–221].

6.1.1 Concept of the proposed experiment

For the simplest case of $N = 2$ ions, the system would be prepared initially in a state with one ion excited to a state $|1\rangle$ in the $3^2\mathrm{D}_{5/2}$ manifold and the second ion in $|0\rangle$, one of the ground states. The concrete choice of states could, e.g., be $|0\rangle \equiv |4^2\mathrm{S}_{1/2}, m_J = 1/2\rangle$ and $|1\rangle \equiv |3^2\mathrm{D}_{5/2}, m_J = 5/2\rangle$. The initial state includes only one excitation and can therefore be written as a superposition of the super- and subradiant states $|\psi_+\rangle = r_2^* |1,0\rangle + r_1^* |0,1\rangle$ and $|\psi_-\rangle = r_1 |1,0\rangle - r_2 |0,1\rangle$:

$$|\psi(0)\rangle = \beta_+ |\psi_+\rangle + \beta_- |\psi_-\rangle,$$

where $r_i = g_i/\sqrt{|g_1|^2 + |g_2|^2}$ is the coupling strength of ion i relative to the total coupling strength, $|0,1\rangle$ stands for the state of the first ion being in the ground state and the second in the excited state, and $\beta_\pm$ are coefficients depending on the relative coupling strengths $r_{1,2}$. Note that r_1 and r_2 are not independent but connected via $|r_2| = \sqrt{1 - |r_1|^2}$. Since the superradiant component of the state decays due to its coupling to the cavity and the cavity decay, for times $t \gg 1/\kappa$, only the subradiant component remains.

Reference [202] quantifies the concurrence (cf. Section 3.2) of the generated state in the stationary state as

$$C_{\text{stat}} = 2|r_1 r_2||\beta_-|^2.$$

According to the proposal, a numerical evaluation yields the maximum value of the concurrence of 0.6 because spontaneous emission in the ions prevents the system from reaching a maximally entangled steady state. For a given value of $|\beta_-|^2$, the maximum of the concurrence occurs for asymmetric coupling of the two ions to the cavity, which follows from the specific dependence of the concurrence on the amplitudes of the states $|01\rangle$ and $|10\rangle$ [202]: Starting, e.g., in state $|1,0\rangle$, the concurrence reaches a maximum for $r_1 = 0.5$ and $r_2 = 0.87$ or vice versa.

According to the proposal, the coupling between ion and cavity would be achieved via a Raman transition in an effective two-level system (cf. Section 3.3.2). Hence, the concurrence of the final state depends on the effective coupling strength $g_{\text{eff}} = \Omega g/2\Delta$, where g is the coupling strength between ion and cavity on the $4^2\mathrm{P}_{3/2} - 3^2\mathrm{D}_{5/2}$ transition, Ω the Rabi frequency of the Raman laser connecting $4^2\mathrm{S}_{1/2}$ and $4^2\mathrm{P}_{3/2}$, which includes the Clebsch-Gordan coefficient, and Δ the Raman detuning.

6.1.2 Adapting the proposal to our system

In order to find out which value of the concurrence is achievable with our system, we simulated the three-level model for our parameters with initial state $|0,1\rangle \equiv |4^2\mathrm{S}_{1/2}, m_J = 1/2\rangle \otimes |3^2\mathrm{D}_{5/2}, m_J = 5/2\rangle$, corresponding to the first ion in the ground state and the second ion in a state in the $3^2\mathrm{D}_{5/2}$ manifold. The simulation[1] was written and executed in MATLAB,

[1] Parameters for the simulation: Rabi frequency $\Omega = 2\pi \cdot 50$ MHz, detuning $\Delta = 2\pi \cdot 400$ MHz, coupling strength $g = 2\pi \cdot 1.51$ MHz, and cavity decay $\kappa = 2\pi \cdot 50$ kHz. In the simulation, the magnetic field was aligned along the cavity axis, preventing reduction of the coupling strength due to the non-unity projection of the cavity mode's polarisation onto the atomic dipole aligned with the quantisation axis (see Reference [70]).

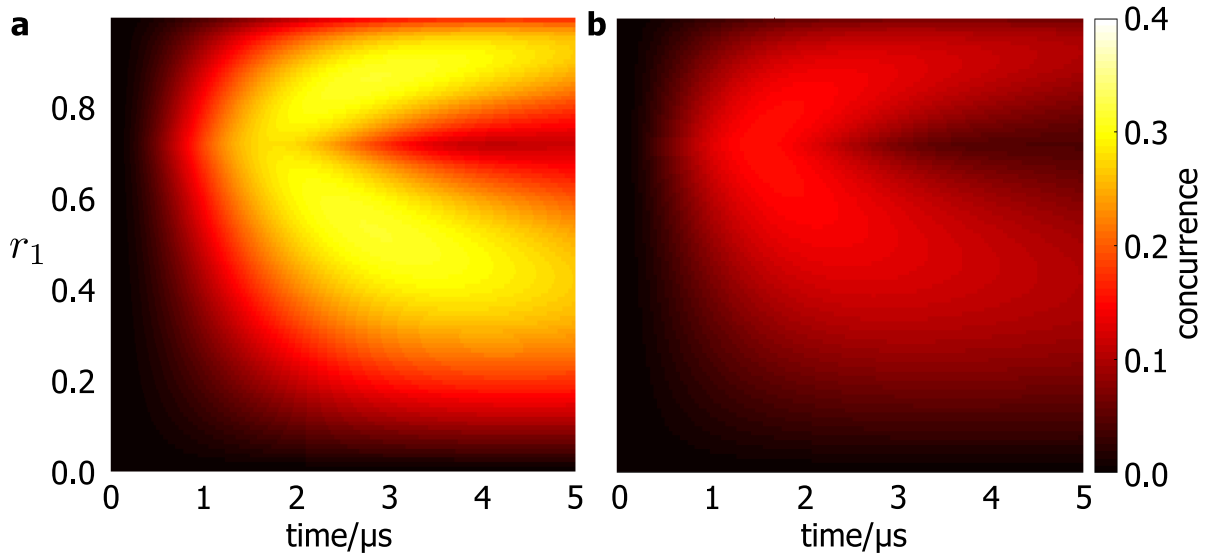

Figure 6.1: Concurrence as a function of the relative coupling r_1 of one of the ions to the cavity mode. **a** If frequency jitter of the cavity lock and the finite linewidth of the Raman laser are neglected, a maximum concurrence of 0.31 is reached after an evolution of 2.8 μs for $r_1 = 0.85$ or $r_1 = 0.54$. **b** Including frequency jitter of the cavity lock and the finite linewidth of the Raman laser, the maximum concurrence is reduced to a value of 0.15. This maximum occurs after an evolution of 1.6 μs for $r_1 = 0.73$. Note, that the asymmetry along r_1 is due to the nonlinear scaling of the relative coupling strength, with equal coupling of both ions occurring at $r_1 = 1/\sqrt{2} \approx 0.707$.

using the quantum optics toolbox written by S. M. Tan [222]. Calculating the concurrence as a function of time and of the relative coupling r_1 yields a result shown in Figure 6.1a. The concurrence reaches a maximum of $C_{\text{max}} = 0.31$ after the system has evolved for 2.8 μs with relative couplings of $r_1 = 0.85$ or $r_1 = 0.54$. These values of r_1 correspond to a factor of 0.63 between the individual coupling strengths of the two ions[2].

The result changes, however, if the nonzero linewidth of the Raman laser and frequency jitter of the cavity lock are taken into account in the simulation. Figure 6.1b shows the result if a linewidth of the laser of 30 kHz and cavity lock frequency jitter with characteristic frequency 50 kHz are included in the simulation. These numbers are conservative values based on the measured ones (cf. Sections 4.3.4 and 4.4.2). The frequency jitter of the cavity lock and the nonzero linewidth of the Raman laser are implemented in the simulation code as a projection of the state coupled to the cavity or laser onto itself with a rate given by the laser linewidth or the frequency jitter. Including the noise sources, the concurrence reaches a maximum of only $C_{\text{max,noise}} = 0.15$ after a time evolution of 1.6 μs. In this case, the relative coupling for maximising the concurrence is $r_1 = 0.73$, corresponding to one ion being maximally coupled and the second ion with strength $0.94g$, which is very close to the case of two maximally coupled ions.

[2] If ion 1 is coupled to the cavity with strength g, and ion 2 with εg, one can derive that $\varepsilon = \min\left[1/\sqrt{1/r_1^2 - 1}, \sqrt{1/r_1^2 - 1}\right]$. The two arguments in the minimum function correspond to the two cases of $g_1 \geq g_2$ and $g_1 \leq g_2$, and we take the minimum of both because we assume $g_1 \geq g_2$.

Figure 6.2 displays the populations of the two ions, initially in states $|0\rangle = |4^2\mathrm{S}_{1/2}, m_J = 1/2\rangle$ and $|1\rangle = |3^2\mathrm{D}_{5/2}, m_J = 5/2\rangle$ as a function of time, and including technical noise in the simulation. As an example, both ions' coupling strengths to the cavity are chosen to be equal in the shown simulation run. While the Raman transition eventually transfers ion 1 (Figure 6.2a) from $|0\rangle$ to $|1\rangle$, ion 2 starts in state $|1\rangle$ and also ends in that state (Figure 6.2b). At intermediate times, the coherent cavity-mediated exchange of the excitation between the two ions is visible as ion 2 starts undergoing the reverse Raman transition from $|1\rangle$ to $|0\rangle$ while ion 1 is generating a photon in the cavity field. Entanglement exists in the system while both ions share the photonic excitation. The Rabi oscillation is, however, strongly damped because of the photon lifetime of only 1.6 µs.

These simulation results indicate that the experiment is feasible in our setup, even though the amount of entanglement generated would not be very large. Still, the experiment is interesting as a demonstration of the fundamental effect of coherent exchange of excitations between two ions in a cavity. In first measurements, the signature to look for would be the decrease and subsequent increase of the probability to find ion 2 in state $|3^2\mathrm{D}_{5/2}, m_J = 5/2\rangle$ as a function of evolution time. For the full demonstration of the effect, full state tomography would be necessary in order to quantify the entanglement generated.

Initial test measurements for this experiment were started in spring 2015 but were interrupted by the vacuum leak (cf. Appendix B). During the rebuilding of the setup, the simulations were refined and the idea of the experiment was discussed with the theorists F. Reiter, C. Muschik and A. S. Sørensen. From the theorists' point of view, the states that could be generated in our system might be interesting per se but due to their low concurrence would not be interesting in the context of dissipative state engineering and quantum computation schemes. An effort together with theorist F. Reiter at finding a dissipative scheme similar to References [211, 223] yielding higher concurrence, did not result in a feasible scheme for our system parameters. Furthermore, during the rebuilding of the setup after the vacuum accident, a new project for building a three-node quantum network in Innsbruck had been started, which shifted the focus to other experiments. As a consequence, the implementation of environment-induced generation of entanglement was discontinued. It should be noted however, that even if the entangled states cannot be used for quantum computing, exploring the excitation exchange in our ion-cavity system is interesting in its own right.

6.2 Entanglement between the electronic state of an ion and the time bin of a photon

In the most recent experiments performed in our setup [72–75], photonic qubits were encoded in the photons' polarisation. Such an encoding has the advantage of being directly compatible with atomic transitions, and by exploiting the atomic selection rules makes it possible to couple certain polarisations only to certain atomic transitions. Furthermore, qubits in polarisation encoding can be easily analysed using waveplates and polarising beam splitters. However, for systems that do not preserve polarisation well, such an encoding leads to decoherence. For example, a cavity exhibiting birefringence or long optical fibres with polarisation mode dispersion [224, 225] would prevent the use of polarisation-encoded qubits. Birefringence would make a polarisation encoding such as in References [72–75] useless, because the

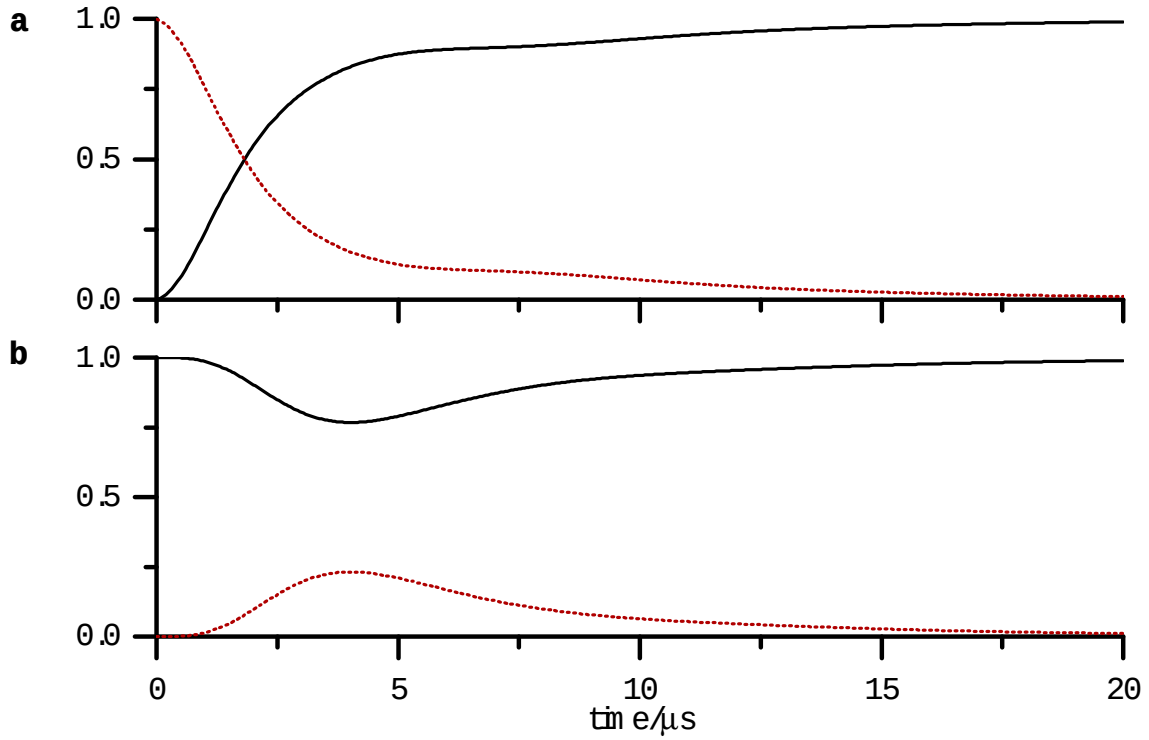

Figure 6.2: Populations of **a** ion 1 and **b** ion 2 as a function of time for $\Omega = 2\pi \cdot 50$ MHz, $\Delta = 2\pi \cdot 400$ MHz, $g = 2\pi \cdot 1.51$ MHz, $\kappa = 2\pi \cdot 50$ kHz, and equal coupling of both ions to the cavity ($r_1 = 1/\sqrt{2}$). The initial state is $|0,1\rangle = |4^2\mathrm{S}_{1/2}, m_J = 1/2\rangle \otimes |3^2\mathrm{D}_{5/2}, m_J = 5/2\rangle$. Red dotted lines show the population in $|0\rangle = |4^2\mathrm{S}_{1/2}, m_J = 1/2\rangle$, and black solid lines the population in $|1\rangle = |3^2\mathrm{D}_{5/2}, m_J = 5/2\rangle$. The populations indicate strongly damped coherent exchange of the photonic excitation between the two ions. The highest concurrence is reached after 1.6 μs.

polarisations of cavity photons would rotate during, e.g., a Raman transition, such that the final polarisation state is not well-defined. In particular, in fibre-cavity setups, birefringence can be a problem [226, 227], which has also instigated further improvements in fibre-mirror fabrication [228, 229]. The latest version of the fibre-cavity setup will use a cavity with an expected birefringence of 10% of the full width of the cavity resonance [230].

In such systems, for which polarisation encodings do not work, an encoding of the qubits in the time-bin degree of freedom can be used instead. Using time-bin encoding also relaxes the technical requirements for frequency conversion of photons to telecom wavelengths in quantum networks, as only one polarisation has to be converted. In this section, the experimental scheme and technical challenges for an implementation of time-bin encoding in our setup will be investigated.

6.2.1 Concept of the experiment

Time-bin encoding defines a qubit in terms of the time at which an event happens. In the case of photons, the time of a photon wave packet can be used: The qubit is in state $|0\rangle$ if the photon arrives during an earlier but well-defined time window (or time bin), and in state $|1\rangle$ if the photon

arrives during a later time bin. Typically, the qubit states are instead denoted by $|E\rangle$ for "early" and $|L\rangle$ for "late". This encoding originated from Bell-type experiments using energy-time entanglement [231] and was first developed in N. Gisin's group [232]. Further development of the concept has led to the generation of time-bin encoded qubits in nonlinear crystals as well as quantum dots [233–236], the distribution of time-bin-entangled photons over long distances [237–240], the interaction of time-bin-entangled photons with quantum memories [241], and even the use of time-bin-encoded qubits for quantum computation [242–244].

In our setup, entanglement would be generated between the electronic state of a trapped ion (or ions) and the time-bin degree of freedom of photons generated in the cavity via a Raman transition. The scheme for generating the entanglement assumes a single trapped ion coupled to the cavity and makes use of the $4^2\mathrm{S}_{1/2}$, $3^2\mathrm{D}_{5/2}$, and $4^2\mathrm{P}_{3/2}$ manifolds of the ion, with the specific states denoted by $|S_i\rangle$, $|D_i\rangle$, and $|P_i\rangle$.

For generating entanglement between the electronic state of the ion and the time-bin degree of freedom of a single photon, the ion is prepared in a superposition of ground states $|S_1\rangle$ and $|S_2\rangle$ (step 1). In this way, the two Raman pulses (steps 2 and 3) can occur directly one after another, thus reducing the time delay between the time bins. After the Raman pulses, the residual populations of the ground states are shelved ("hidden") (step 4), and the population from $|D_2\rangle$ is transferred to $|S_1\rangle$ (step 5), to enable rotations in the qubit basis $|S_1\rangle - |D_6\rangle$. These steps would be followed by state tomography. Note that in this case two different Raman transitions are used, but if the quantisation axis is orthogonal to the cavity axis, the photons generated via the two transitions will be projected onto the same polarisation mode of the cavity, such that the photons are indistinguishable in polarisation.

However, in order to drive the two transitions with a single laser beam, the Raman beam at 393 nm with a propagation direction orthogonal to the quantisation axis, will need to have a polarisation perpendicular to the quantisation axis, so as to drive with a superposition of σ_+- and σ_--polarised light. In this case, off-resonant driving of the "wrong" transition is possible during each time bin. An estimate of the spectral overlap of the two transitions shows that this effect would happen in about 5% of the attempts. The off-resonant excitation could be avoided by driving with a beam propagation parallel to the quantisation axis and using a fast switch for the polarisation of the Raman beam, such that between the two Raman pulses the polarisation can be switched between right-circular and left-circular polarisation. Alternatively, two Raman beams could be used.

For this scheme, the lower limit on the time separation between the time bins is given by the photon lifetime in the cavity: The first component of the photon has to have decayed from the cavity before generation of the second component starts in order to avoid temporal overlap between the two time bins. Control of amplitude and frequency of the Raman laser pulses during the Raman transition can be used improve the performance of the scheme: Pulse shaping allows us to reduce the time separation between the time bins to the minimum (given by the photon lifetime) and thus the required length of the interferometer for tomography. In addition, the efficiency of the Raman transition can be increased compared to a square pulse by shaping the laser pulse. Thus, even though the transition is driven only for a few microseconds, the photon component can be generated with higher efficiency. Finally, pulse shaping enables the generation of photon wave packets with arbitrary shape, which is not necessary for a proof-of-principle experiment, but becomes important for networking applications if the generated photons have to be reabsorbed in another ion-cavity system.

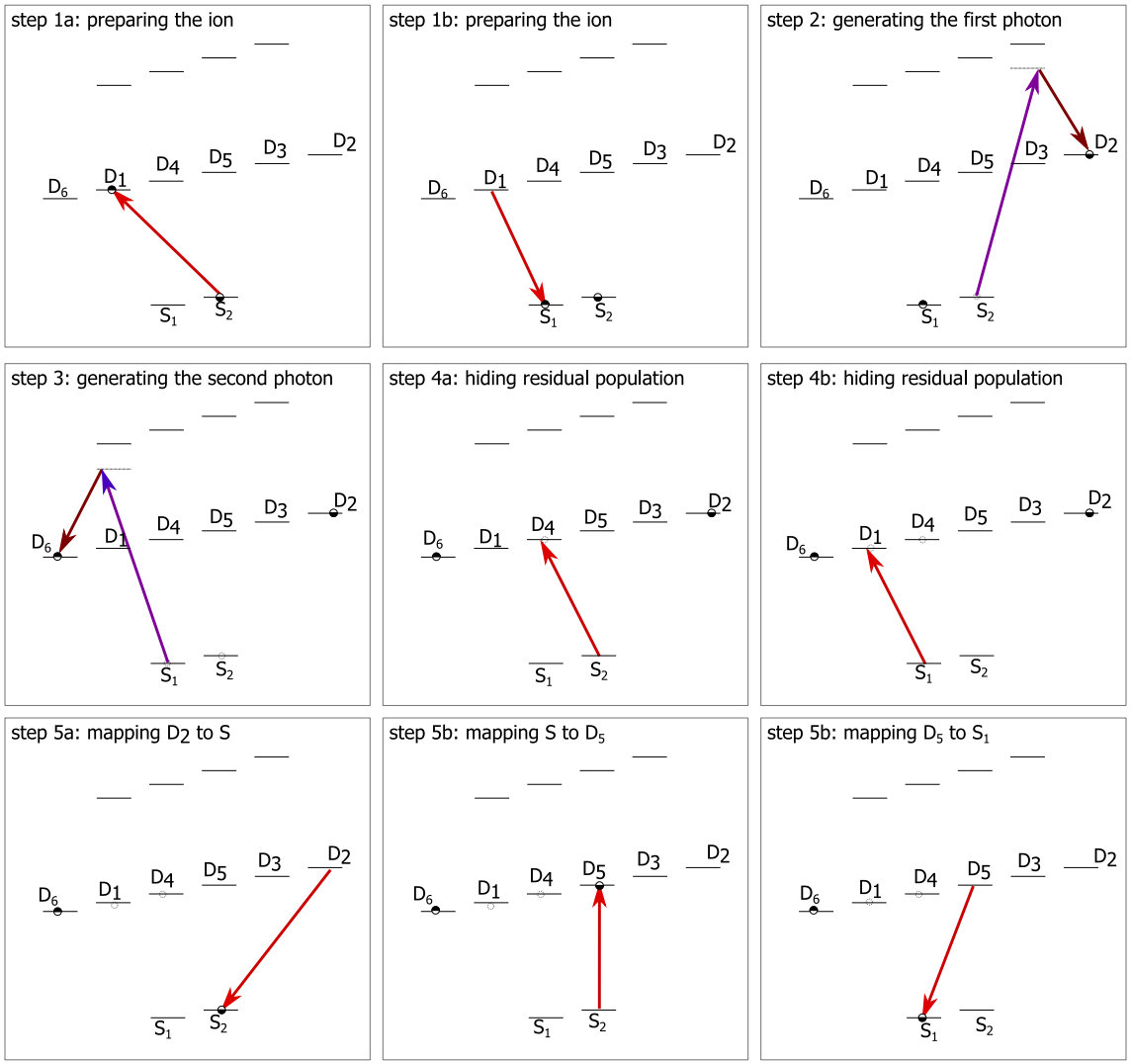

Figure 6.3: Scheme for the generation of entanglement between the electronic state of a single trapped $^{40}Ca^{+}$-ion and the time-bin degree of freedom of a photon generated in the cavity. The steps are explained in the main text. The quantisation axis is assumed to lie orthogonal to the cavity axis such that the generated photon components have the same polarisation.

Note also, that time-bin and polarisation encodings can be transformed into each other via polarising beam splitters and delay paths. This makes it possible to build a network in which both encodings are used, which is useful if some elements in the network are better suited for one encoding and others for another encoding.

6.2.2 Photon tomography

For the ion, the usual techniques for quantum state tomography can be used in order to analyse the entangled state [245]. For the analysis of the photonic component, an interferometric measurement is required [246, 247]: The three measurement bases for the reconstruction of the photonic component correspond to (1) measuring the populations of the photon in the time bin states $|E\rangle$ and $|L\rangle$, (2) measuring the interference of $|E\rangle$ and $|L\rangle$ with relative phase 0, and (3)

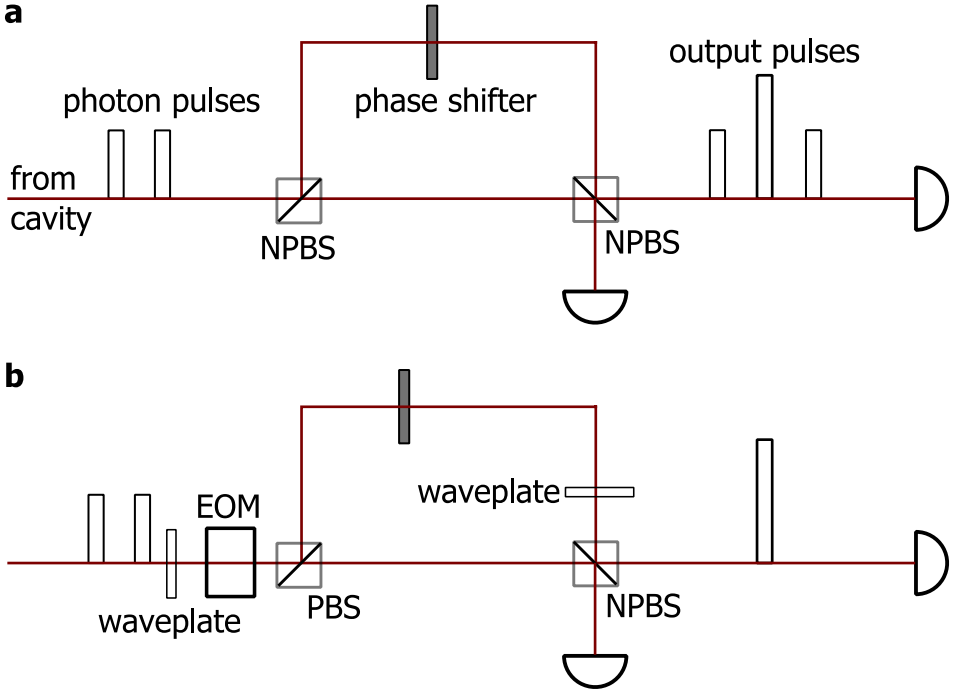

Figure 6.4: Schematic of an interferometer for tomography of time-bin entanglement. **a** Tomography of the photon component: three measurements are necessary with an interferometer. The central interference peak at the interferometer output needs to be measured with two different interferometer phases, controlled by the phase shifter. By splitting and recombining the photon pulses with two non-polarising beam splitter (NPBS), three output pulses are detected. **b** If an EOM together with a polarising beam splitter (PBS) is used to send the early photon along the long path and the late photon along the short path, there will only be one pulse in the output and the efficiency of the interference measurement will be increased, as the first and last detection peaks do not occur. The waveplate in the long path is necessary in order to align the polarisations for interference.

measuring the interference with relative phase $\pi/2$. The arms of the interferometer therefore have to be long enough such that the states $|E\rangle$ and $|L\rangle$ can be overlapped temporally. For full state tomography, the entangled state has to be measured in all combinations of the ion measurement bases and the photon measurement bases.

The two photon components exit the cavity at different times, so the generated photon is in a superposition of two wave packets in the output channel of the cavity, corresponding to $|E\rangle$ and $|L\rangle$. In order to interfere the two states, an interferometer is necessary whose length exactly matches the time separation of the two time bins. If the interferometer consists of just two non-polarising beam splitters, the two components can be detected at three different times at the output of the second beam splitter:

1. State $|E\rangle$ travelled through the short branch of the interferometer: detection at the earliest time.

2. State $|E\rangle$ travelled through the long branch and state $|L\rangle$ through the short branch: detection at an intermediate time. For this detection time, interference between $|E\rangle$ and $|L\rangle$

occurs as the two components overlap temporally on the second beam splitter.

3. State $|L\rangle$ travelled through long branch: detection at the latest time.

Only the events detected at the intermediate time are important for the interference part of the tomography, while the early- and late-time contributions can be used for measuring the populations of the two components Figure 6.4a shows a schematic of the measurement setup.

The detectors will only measure a single output pulse by using a Pockels cell together with a polarising beam splitter to send the state $|E\rangle$ along the long path and the state $|L\rangle$ along the short path. Accordingly, the efficiency for measuring the interference events is increased by a factor of two (cf. Figure 6.4). In this approach, it is necessary to rotate the polarisation of one of the interferometer arms such that the two photon components have the same polarisation at the second beam splitter/combiner and thus interfere. Note that this interferometric scheme is very similar to a setup that can be used for converting photonic time-bin qubits into polarisation qubits (cf. Section 5.1.4 in Reference [248]).

Finding the optimal timing

In this section, we try to understand what the optimal length of the first Raman pulse and the optimal length of the interferometer should be in our setup. The time between the two photon generation events is given by the length of the first Raman pulse plus some additional time $> \tau_c$ to make sure that the first photon component has left the cavity before the second Raman pulse starts. We assume a first Raman pulse of length t_1, a time delay between the two Raman pulses of duration t_2, and a second Raman pulse of length t_3, as shown in Figure 6.5a. During the time t_1, only a fraction $p(t_1)$ of the first photon is generated during the first Raman pulse, given by the normalised integral of the photon wave packet $w(t)$:

$$p(t_1) = \frac{1}{N}\int_0^{t_1} w(t)\mathrm{d}t, \quad N = \int_0^{\infty} w(t)\mathrm{d}t.$$

Here, $w(t)\mathrm{d}t$ is the probability of detecting the generated photon in the time interval $(t, t+\mathrm{d}t)$. Note that ideally $N = 1$, but due to imperfections in the Raman process, e.g., spontaneous emission, $N < 1$.

The delay line in the interferometer has a length L which compensates for the time delay $\tau = t_1 + t_2$ between the two time bins:

$$L(\tau) = \frac{c}{n}\tau,$$

where c is the speed of light and $n = 1.5$ the refractive index of the delay fibre. This delay corresponds to a fibre transmission probability $T(L)$, which depends on the losses of the fibre assumed to be 3 dB per kilometre. Our goal consists in finding a configuration that (1) maximises the fraction of the generated photon $p(t_1)$, (2) minimises the overlap of the two time bins by keeping t_2 as long as possible, and (3) minimises the photon losses by keeping the delay fibre as short as possible. In the following considerations, the waiting time t_2 between the time bins is kept fixed to $t_2 = 3\ \mu\mathrm{s} \approx 2\tau_c$, and we try to find a combination of values for t_1 and L, for which the overlap of the two time bins is below 1% while the overall efficiency including the transmission through the delay fibre is still above 1%. The value $t_2 = 2\tau_c$ was chosen because

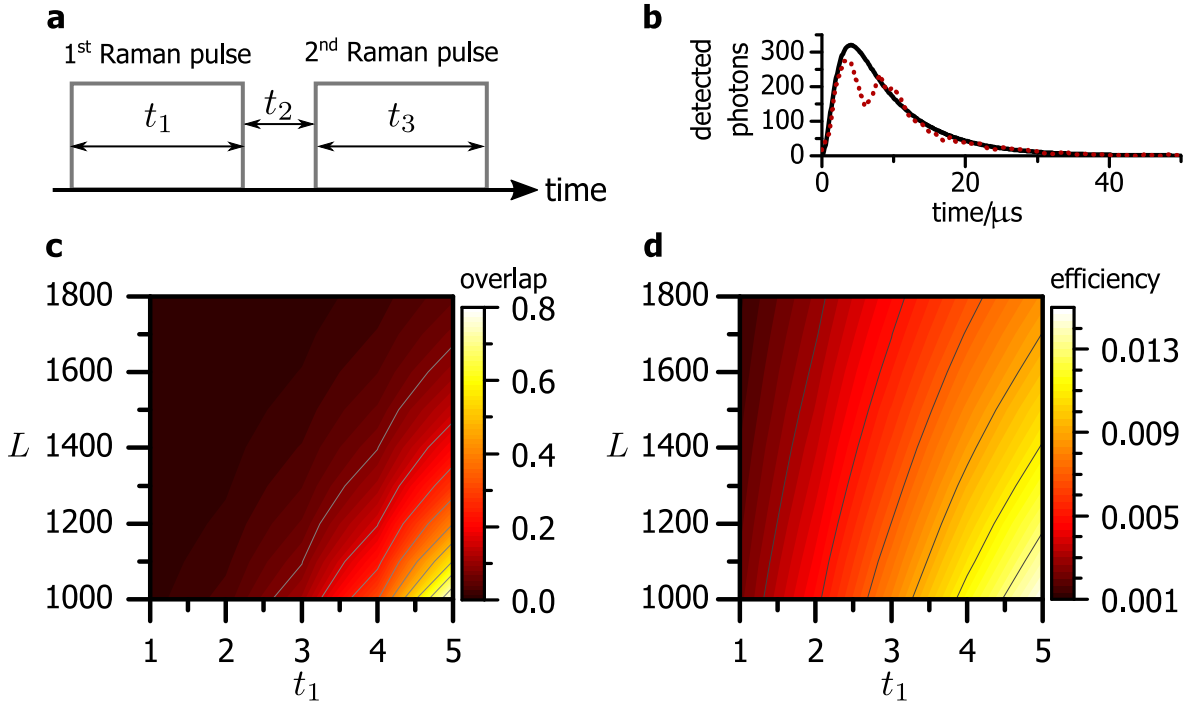

Figure 6.5: Efficiency of time-bin entanglement as a function of the time delay between the time bins. **a** Schematic of the relevant times for the time-bin entanglement experiment. In order to avoid temporal overlap of the photon components generated during the two Raman pulses, the delay t_2 should be longer than the photon lifetime in the cavity τ_c. **b** Photon wave packet with measured data (red dotted line) and simulation (black solid line), on which the calculations of overlap and efficiency are based [Data16a]. **c** Overlap of the two photon components as a function of the length t_1 of the first Raman pulse and the delay length L, while keeping $t_2 \approx 2\tau_c$ constant. **d** Efficiency for detecting the photon component of the first time bin at the output of the delay fibre as a function of the length t_1 of the first Raman pulse and the delay length L, while keeping $t_2 \approx 2\tau_c$ constant.

increasing t_2 to larger values would increase the required value for L and hence decrease the overall efficiency below 1%.

The overlap between the time bins is defined as the fraction of the photon component $p(t_1)$ generated in the first time bin that survives into the second time bin, given by the generated fraction in the first time bin multiplied by the exponential cavity decay factor $\exp(-t_1/\tau_c)$. Figure 6.5 shows surface plots of both overlap between the time bins (b) and the overall probability (efficiency) to detect a photon at the output of the delay fibre (c) as a function of t_1 and L, with $t_2 = 3\ \mu s \approx 2\tau_c$ fixed. The efficiency is given by the product of the generation probability of the first photon component $p(t_1)$, the optical path losses in the delay fibre, and the detector efficiency of 0.6. Note that the plotted values correspond to the efficiency for the long arm of the interferometer, while for the photon component in state $|E\rangle$, which travels through the short arm, the path efficiency is higher. The results show that in order to keep the overlap between the time bins low ($< 1\%$) and the efficiency high ($> 1\%$), a delay length of around 1500 m is required for $t_1 = 4\ \mu s$. Note that the coherence length of photons coming from the cavity is not a limiting factor. For a spectral width on the order of $\Delta\nu = 100$ kHz, the coherence length

$c/(n\Delta\nu)$ is about 2 km – longer than the required interferometer length.

The challenge of this experiment is therefore of technical nature, namely, how to build an interferometer with 1.5 km of fibre length and keep its relative phase stable. One consideration concerns the thermal drift in the long branch. With a thermal expansion coefficient for silica of $\alpha = 5.5 \cdot 10^{-6}$ K^{-1}, a temperature change of $\Delta T = 350$ µK amounts to a change of the fibre's optical path length of

$$\Delta L = L \cdot \alpha \cdot \Delta T = 570 \text{ nm}.$$

At a wavelength of λ =854 nm $= 2\pi/k$, such a length change corresponds to a phase shift of

$$\Delta\phi = n \cdot k \cdot \Delta L = \pi.$$

Accordingly, a strategy for passive stability and active stabilisation of the interferometer temperature would be required to guarantee that during the course of the experiment the relative phase either does not shift too much or can be compensated for via regular calibration measurements. The implementation would also depend on whether a fully fibre-coupled setup is used or a free-space setup, in which only the delay line is fibre-coupled. In general, the use of interferometers with arms of kilometre-scale length is possible, though challenging, e.g., by using a laser at a different wavelength for stabilising the interferometer. For example, Reference [249] proposes a 200 km interferometer based on optical fibres under vacuum. In other approaches, a piezo ring is used to control the length of a fibre coiled around the ring [250]. Note also that, e.g., References [237–240] report distribution of time-bin entanglement over long distances, but the interferometers used for analysing the entanglement are much shorter than in our case, since these experiments are done on faster time scales with time-bin separations on the order of nanoseconds.

Influence of photon losses on the interference visibility

Even though there are asymmetric losses in the interferometer arms, the visibility of the interferometric signal can still be close to one, as shown in this section. If the long path for state $|E\rangle$ is denoted as path 1 and the short path for state $|L\rangle$ as path 2 (cf. Figure 6.4), the photon state at the input of the non-polarising beam splitter is given by

$$|\Psi_{\text{in}}\rangle = c_1 e^{i\phi} |0_1\, 1_2\rangle + c_2 |1_1\, 0_2\rangle + c_3 |0\, 0\rangle, \quad |c_1|^2 + |c_2|^2 + |c_3|^2 = 1,$$

where the subscript indicates the spatial mode (path), $|0\, 0\rangle$ denotes the vacuum, and the phase ϕ is given by path length differences and the phase of the phase shifter in the long arm. This state can also be written as

$$|\Psi_{\text{in}}\rangle = \left[c_1 e^{i\phi} a_1^\dagger + c_2 a_2^\dagger + c_3\right] |0\, 0\rangle,$$

where $a_i^\dagger$ is the creation operator for mode i, and $i = 1, 2$ corresponds to the input modes of the beam splitter. At the non-polarising beam splitter, the relations between the input and output channels are given by

$$a_1^\dagger = \left(a_3^\dagger + a_4^\dagger\right)/\sqrt{2},$$
$$a_2^\dagger = \left(a_3^\dagger - a_4^\dagger\right)/\sqrt{2},$$

where $i = 3, 4$ refers to the two output modes of the beam splitter.

With these relations, the input state can be transformed into the output state $|\Psi_{\text{out}}\rangle$ of the beam splitter:

$$\begin{aligned}
|\Psi_{\text{out}}\rangle &= \left[\frac{c_1}{\sqrt{2}}e^{i\phi}\left(a_3^\dagger + a_4^\dagger\right) + \frac{c_2}{\sqrt{2}}\left(a_3^\dagger - a_4^\dagger\right) + c_3\right]|0\,0\rangle \\
&= \frac{1}{\sqrt{2}}\left[c_1 e^{i\phi}a_3^\dagger + c_1 e^{i\phi}a_4^\dagger + c_2 a_3^\dagger - c_2 a_4^\dagger + \sqrt{2}c_3\right]|0\,0\rangle \\
&= \frac{1}{\sqrt{2}}\left[c_1 e^{i\phi}|1_3\,0_4\rangle + c_1 e^{i\phi}|0_3\,1_4\rangle + c_2|1_3\,0_4\rangle - c_2|0_3\,1_4\rangle\right] + c_3|0\,0\rangle \\
&= \left[\frac{c_2 + c_1 e^{i\phi}}{\sqrt{2}}\right]|1_3\,0_4\rangle + \left[\frac{-c_2 + c_1 e^{i\phi}}{\sqrt{2}}\right]|0_3\,1_4\rangle + c_3|0\,0\rangle
\end{aligned}$$

Therefore, the probabilities p_3 and p_4 for detecting a photon in modes 3 and 4 are (assuming $c_1, c_2 \in \mathbb{R}$)

$$p_3 = \frac{1}{2}\left[c_1^2 + c_2^2\right] + c_1 c_2 \cos\phi$$

$$p_4 = \frac{1}{2}\left[c_1^2 + c_2^2\right] - c_1 c_2 \cos\phi$$

The visibility of the interference fringes can then be calculated as the ratio of the amplitude $a = c_1 c_2$ and the offset $b = (c_1^2 + c_2^2)/2$ of the interference fringe:

$$V = \frac{a}{b} = \frac{2c_1 c_2}{c_1^2 + c_2^2} = \frac{2c_1\sqrt{1 - c_1^2 - c_3^2}}{1 - c_3^2}$$

For a realistic scenario in our setup[3] with a probability of $c_2^2 = 8.2 \cdot 10^{-3}$ for the short arm and $c_1^2 = 4.3 \cdot 10^{-3}$, one finds that a visibility of 0.95 can still be reached, even though the vacuum component given by $c_3^2 = 1 - c_1^2 - c_2^2 = 0.9875$ is dominating and the efficiencies c_1^2 and c_2^2 in the two interferometer arms are different by a factor of 2.

Note, that although bounding the fidelity via the measured visibility is in principle possible through parity flops (see, e.g., References [251, 252]), the implementation of these in the hybrid ion-photon system is challenging, as it requires simultaneous $\pi/2$-pulses on both the photonic time bin qubit and the ion qubit. Although unitary operations on time-bin qubits are possible [242], it unclear how to implement global rotations of both the photonic time-bin qubit and the ion qubit without significant technical overhead. For this reason, it is expected that an analysis of the generated state via full state tomography would be less complicated than using parity flops.

Implementing time-bin entanglement in our setup is feasible but requires the solution of several technical problems, the most important of which is the stable operation of a kilometre-long interferometer. This interferometer would not be necessary in future networking protocols but is required for quantifying the performance of the protocol with a single node. One of the advantages of the scheme lies in avoiding the bichromatic Raman transition, which has been used for polarisation encoded experiments, relaxing the requirements on the control and calibration

[3] These values are based on the optical transmission of the elements in the interferometer as shown in Figure 6.4, and also include the photon generation efficiency (cf. p.113).

of the Raman laser frequency. Due to the expected technical challenges this project will not be implemented in our setup in the near future. If, however, issues will arise from birefringence in the fibre-cavity setup, we can come back to the considerations detailed in this section. For the fibre-cavity setup, for which a cavity decay rate on the order of a few megahertz is expected, the requirements on the interferometer can be relaxed, as the photons will be produced faster than in our setup, and therefore the time bin separation may be shorter.

6.3 Heralded photon absorption of an ion coupled to a cavity

In contrast to the previous projects in this chapter, the project under consideration in this section is a continuation of a previous project, i.e., quantum state mapping [73]. In the state mapping experiment, the quantum state of a single ion was mapped onto the polarisation state of a single photon. The experiment proposed here would implement the inverse process, i.e., a heralded quantum memory protocol in our ion-cavity system: A quantum state encoded in the polarisation state of a single photon (or a weak coherent pulse) would be mapped onto the electronic state of an ion via a cavity-mediated Raman transition. The successful absorption would be heralded by detection of the ion's state. After a variable storage time, the process could be reversed via a state-mapping protocol, such as the one presented in Reference [73]. This experiment is part of the efforts towards building a three-node network in Innsbruck and is similar to experiments executed or proposed in other systems, e.g., the ones reported in References [253–256]. While References [253, 254] describe the CQED-implementation of such a protocol with Rubidium atoms, without and with heralding, Reference [255] describes the absorption of photons in $^{40}Ca^{+}$ ions, but using high-numerical-aperture lenses and heralding via a second photon and the emission of a photon at 393 nm. Reference [256] on the other hand, deals with the absorption of photons in a quantum dot, which is heralded by emission of a photon. Our scheme aims at heralding the absorption via detection of the ion, which can be done with higher efficiency than the detection of photons.

6.3.1 Sequence of the experiment

The ion is cooled, optically pumped to one ground state, and prepared in the state $|D_{\text{initial}}\rangle = |3^2\text{D}_{5/2}, m_j = -1/2\rangle$ via a π-pulse on the quadrupole transition. In the next step, a photon in a superposition of polarisations H and V is sent into the cavity through the more transmissive mirror while a bichromatic Raman field illuminates the ion. Each of the two polarisation states of the photon is mapped to a different ground state in the ion via the Raman transition (step 1 in Figure 6.6).

The ion populations in the ground states – corresponding to the absorbed photon qubit – are mapped to two states $|D_1\rangle$ and $|D_2\rangle$ in the $3^2\text{D}_{5/2}$ manifold (step 2) in order to be able to herald the success of this absorption. Any residual population of the ion in the initial state $|D_{\text{initial}}\rangle$ is mapped to the ground state $|S\rangle$ (step 3 in Figure 6.6). If the photon has been absorbed by the ion, at this point in the sequence, the ion population would be distributed between $|D_1\rangle$ and $|D_2\rangle$, and no population would reside in $|S\rangle$. Sending light at 397 nm and 866 nm to the ion and detecting the ion's fluorescence will reveal if any population was in state $|S\rangle$ (step 4 in Figure 6.6): a "bright" ion signals that no photon has been absorbed, while a "dark" ion heralds

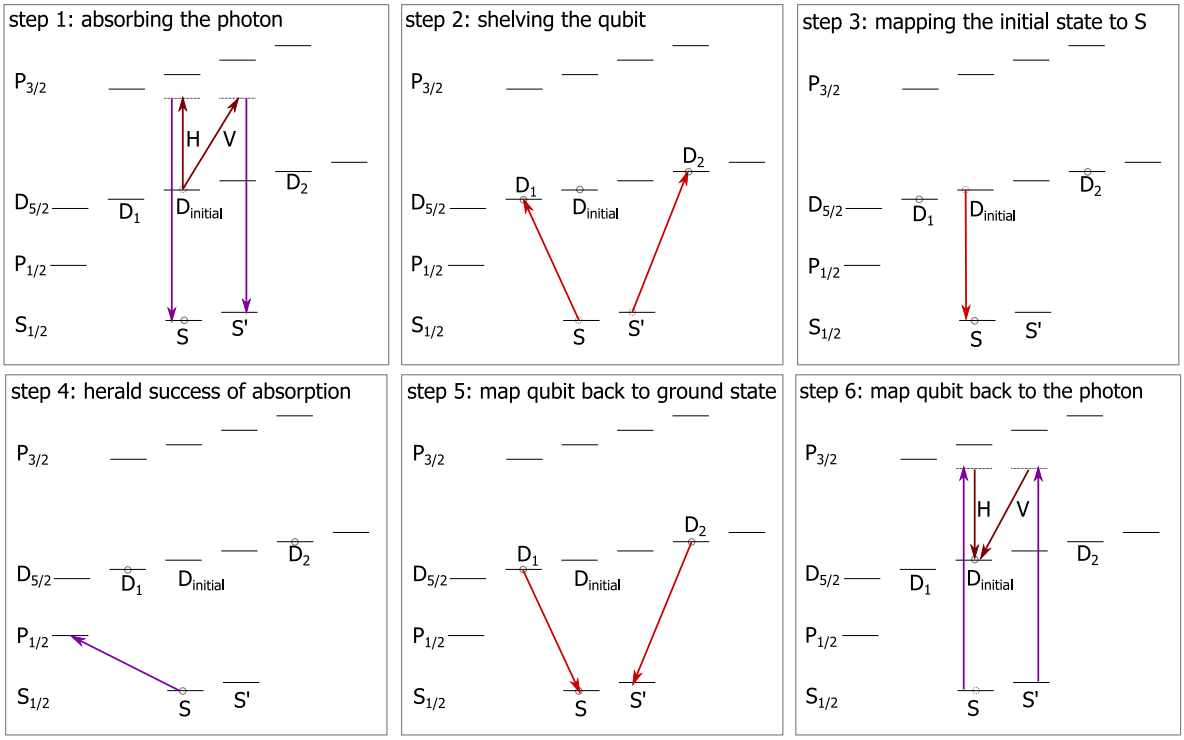

Figure 6.6: Sequence for heralded photon absorption. Note that step 6 is optional.

the successful absorption of the photon. Note that information in the qubit is not affected by this fluorescence measurement since it is stored in the states $|D_1\rangle$ and $|D_2\rangle$.

If the photonic qubit has been absorbed successfully, the qubit is mapped back into the ground states (step 5 in Figure 6.6). At this point, state tomography of the ion can follow to ascertain how well the mapping from the photon to the ion worked. Depending on the network application, the qubit could be mapped back onto a photon after optional manipulation of the quantum information in the ion (step 6 in Figure 6.6) instead of state tomography. In this case, the overall performance of the protocol would be quantified through process tomography [257].

6.3.2 Technical challenges of the scheme

Several technical challenges need to be addressed before the implementation of this protocol in our system. First, the efficiency of the photon absorption in the ion-cavity system has to be optimised. Efficient absorption requires careful mode-matching between the free-space photon and the cavity mode as well as correct timing of the photon arrival with respect to the Raman laser pulse. The cavity output path has already been modified such that injecting light into the cavity through the mirror with higher transmission (East mirror) is possible (cf. Section 4.6.1), thus avoiding the lower transmission of the West mirror, previously used for driving the cavity.

Moreover, the photon absorption process can be further optimised by changing amplitude and frequency of the Raman laser pulse during the absorption. This technique will also be necessary for future quantum network experiments with photons from different network nodes,

as the temporal shape of generated photons has to be controlled to guarantee indistinguishability between photons from different network node in interference for Bell measurements, or for absorption of the photon in another ion-cavity system [258]. The shaping of photon wave packets is currently investigated in our setup by D. A. Fioretto and M. Teller.

There are several other issues that affect the protocol performance and therefore need to be taken into account: Since the photons to be absorbed in initial test measurements will be weak coherent states and not single-photon Fock states, contributions from higher photon numbers have to be taken into account (see Reference [259] and references therein). Additionally, the fidelity of the state transfer from photon to ion will be affected not only by the quality of the Raman transition (e.g., off-resonant scattering, cf. Reference [73]), but also by the fidelity of pulses on the quadrupole transition, required for the ion-qubit manipulation, which contributes to overall protocol performance. The storage time of the quantum memory will be limited by the coherence time of the ion qubit. In view of future quantum network experiments, an effort towards increasing the coherence time may become necessary at some point in the future. It is necessary to detect the ion state on timescales much shorter than the ion's coherence time in order to perform the heralded absorption within the coherence time and to have the possibility for feedback into the sequence based on the result. This is technically feasible, as reported in References [193, 194].

Possible extensions of the scheme include using multiple ions in analogy to Reference [75] with the purpose of of increasing both the fidelity and the efficiency of the process. The excellent properties of trapped ions for quantum information processing could be used in another extension of the protocol in the following steps: (1) Write the photonic qubit into the ion, (2) store the information in the ion, (3) process the information (i.e,. rotate the qubit) in the ion.

In conclusion, the protocol for heralded photon absorption is not new, but in view of a future three-node quantum network, it should be implemented in Innsbruck. The challenges are of technical nature, but there are no fundamental limitations to an implementation in our setup. The current investigation of photon shaping via amplitude-modulated Raman pulses is a first step towards the full implementation.

6.4 Fast routing of photons in a quantum network

The proposal in this section is also closely related to the the envisioned three-node quantum network in Innsbruck, similar to the previous section. In this network, the necessity arises to route photons from a central node B to two peripheral nodes A and C, i.e., to be able to switch the photonic channels between the nodes. For example, one protocol for generating remote entanglement between peripheral nodes A and C uses a single trapped ion in node A, a single trapped ion in node C, and two trapped ions in a central node B. The protocol consists of the following steps:

1. Entangle one ion in node B with one photon and the ion in node A with one photon.

2. Interfere the two photons in a Bell measurement to generate entanglement between the ion in node A and one of the ions in node B.

3. Repeat the two steps above for the second ion of node B and the ion in node C.

4. Swap the entanglement to nodes A and B via projective measurements in node B and feedforward. Alternatively, entanglement between all three nodes could be generated by entangling the two ions in node B.

For the Bell measurements, the photons have to be matched in waveform (i.e., temporally), polarisation and frequency and in order to be able to interfere the photons from node B with both photons from node A and C, the cavity output channel has to be rerouted by a photonic switch before the second photon is generated. Such a switch should fulfil the following requirements:

- **Speed:** The switching has to happen fast: The duration of switching operations should be much shorter than the coherence time of the three nodes. Presumably, a switching of not more than a few microseconds should be sufficiently short.
- **High efficiency:** The device should have very low losses so as to keep the losses in the quantum network as low as possible and thus to keep the entanglement rate as high as possible. Higher losses mean that more trials are necessary to generate remote entanglement.
- **High extinction:** The photons should be sent to the intended node all of the time, i.e., the switch's extinction ratio between the two output modes should be very high.
- **Polarisation independence and fidelity:** The switch should be able to switch photons with arbitrary polarisation and should not alter the polarisation of photons. The latter requirement is not as demanding as the others since for a known polarisation rotation, the effect can be compensated for by polarisation optics behind the switch and before the Bell measurement setup.
- **Photon shape fidelity:** The switch should not modify the waveform of the switched photons in a way that compromises the temporal overlap with other photons in the Bell measurement. A modification of the shape might be compensated by reshaping upstream (by tailoring the Raman pulses) or downstream (e.g., with an AOM), but this would further complicate the protocol.

In the following subsection, various options for such a switch and its implementation in our setup are discussed with the goal of finding the option best suited to the requirements in the above list.

6.4.1 Options for switching

Nonlinear Sagnac interferometers

Nonlinear Sagnac interferometers rely on cross phase modulation (XPM) of the signal by pump light via the the Kerr-nonlinear Sagnac effect [260–264]. Such devices rely on the Kerr effect [265–268], i.e., the dependence of the refractive index on the intensity of pump light. This effect can be used to control the phase of signal light pulses in an interferometer, typically in a Sagnac configuration [269–271]: Depending on the presence of the pump light, the signal will interfere with itself in such a way that it is either transmitted through the interferometer or reflected. Both $\chi^{(3)}$ materials (silicon, silica) or cascaded $\chi^{(2)}$ materials (lithium niobate) can be

used for such devices, which makes it easy to integrate them with standard single-mode optical fibres.

Because of their all-optical functionality, such devices can operate in a pulsed regime and and can be very fast (below nanoseconds timescales). Polarisation independence can be achieved by having perpendicularly polarised pump pulses of slightly different wavelength than the signal. These devices have insertion loss values as low as 2.1 dB and a switching contrast of up to $150:1$ [260]. Their use for the switching of polarisation-entangled photons without significant loss in fidelity with respect to the unswitched state [262] proves their suitability in maintaining polarisation and photon shape.

However, the application of such a device in our setup is not straightforward: in published experiments [260], photon pulses with time durations on the order of 100 ps were switched, while the photons produced by an ion coupled to our cavity are typically tens of microseconds long. The switching window, i.e., the maximum time duration during which a signal pulse can be switched – which corresponds to the maximum length of a signal pulse – is given by the length of the interferometer. It can be controlled via the length of the fibre, and the group velocity of pump pulse in the interferometer: the longer the fibre and the lower the group velocity, the longer the switching window. In the experiment presented in reference [262], the fibre length was $100 - 500$ m for switching windows of 190 ps and 900 ps. In order to scale this up to the pulse length of photons in our setup, the fibre would need to be a factor of $10,000$ longer. This is unrealistic due to the corresponding losses in the fibre.

In a discussion with Professor P. Kumar, several other options emerged, but none of them is straightforward to implement or guarantees a successful solution. By choosing an optical fibre with specific dispersion characteristics, it is possible to lower the group velocity of the pump light, which would increase the duration of the switching window, but not enough for photons with the temporal shape in our setup. Instead of standard optical fibres, a microstructured fibre with a smaller mode diameter (see, e.g., Reference [272]) could be used to increase the XPM induced by the pump light. Instead of using an optical fibre as a nonlinear medium, the nonlinearity of noble gases could be used. Experiments on this topic have been done in several research groups (see Reference [273] for a review), especially in the context of attosecond physics. Instead of the Sagnac interferometer with an optical fibre, one might think of employing a Mach-Zehnder interferometer with the pump light only in one of the two arms, which might help in avoiding the losses in a long fibre. One might also consider using continuous-wave light instead of pulses so as to be able to switch with longer time windows. However, in that case, the power of the pump laser would have to be increased significantly for reaching the necessary cross-phase modulation.

It should also be noted that the device employed in References [260–264] was designed for telecom wavelengths (signal at 1310 nm, pump at 1545 nm and 1555 nm), not for our wavelength of 854 nm. This would not be an obstacle in itself for using it as switch, since B. Lanyon's team in Innsbruck is working on converting photons at 854 nm to the telecom C-band around 1550 nm.

In conclusion, this approach to switching is not suited to our setup because of its technical difficulties, which forbid an implementation in our laboratory. Additionally, the switching speed achieved in such devices is much faster than required in our case.

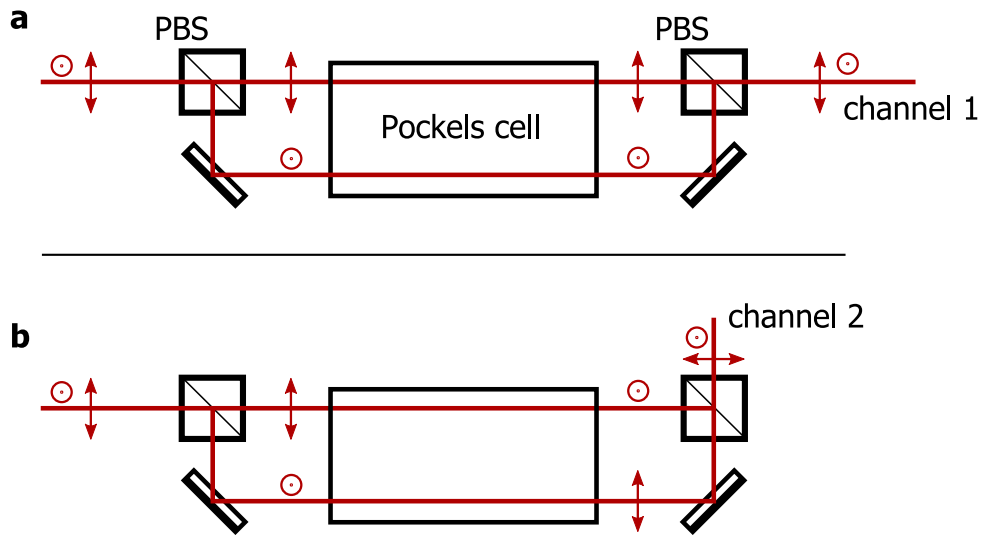

Figure 6.7: Setup for fast switching of photons between two channels, using a Pockels cell. The input light polarisation is split on the first PBS, and then sent through the same Pockels cell. The symbols $\odot$ and $\updownarrow$ denote vertical and horizontal polarisation, respectively. **a** When the Pockels cell does not rotate the polarisation, both polarisations (horizontal and vertical) are transmitted into channel 1. **b** If the EOM rotates the polarisations by $90°$, both polarisations are switched to output channel 2. Note that instead of a PBS, a beam displacer with displacement of a few millimetres can be used in order to facilitate sending both branches through the same Pockels cell.

MEMS technology

Microelectromechanical systems (MEMS) employ microscopic structures based on semiconductor technology, which can be used as actuators. For example, small mirrors can be controlled in such systems. However, this technology is not suitable for our purpose, since the switches involve mechanical parts and hence the speed of such devices is limited to the 100-kHz-range – too slow for the requirements in our setup.

Acousto-optic modulators

Acousto-optic modulators would provide a sufficiently fast switching speed, but their diffraction efficiency is typically around 80%, which is low compared to other solutions. Additionally, although there are polarisation independent devices, which use acoustic waves in the crystal along the direction of the light propagation, such devices have an even lower diffraction efficiency. Accordingly, AOMs are not best suited to our requirements.

Pockels cells

A free-space Pockels cell in the configuration shown in Figure 6.7, suggested by B. Lanyon, should fulfil all our requirements: Pockels cells can be switched within nanoseconds, their efficiency can be very close to unity, and their extinction ratio exceed $1000 : 1$. In addition, by decomposing the input polarisation into the two axes of the Pockels cell crystal, the scheme depicted in Figure 6.7 should work for arbitrary input polarisations. Also, the photon shape should not be affected, as the crystals are quite short (few centimetres) and their dispersion should therefore play a minor role.

One possible issue is piezo-electric ringing that translates into the transmission signal and is especially relevant for the long pulses required in our setup: The polarisation of the transmitted light drifts after the Pockels cell is switched on. After it is switched off, the polarisation oscillates. The oscillations are damped with time constants on the order of 100 µs. However, by shifting the switching to parts of the sequence outside the time window during which the photon is transmitted through the Pockels cell, we expect to mitigate or eliminate this problem.

In order to test such a setup, the following measurements, suitable for a summer student's project, are suggested. Weak coherent pulses at 854 nm with pulse lengths on the order of 10 µs and a similar pulse separation should be sent to the test setup. The pulses may be produced with an AOM. At the two outputs of the setup, fast photodiodes should be used for detecting the transmission of the pulses. The signal controlling the state of the AOM should be synchronised with the signal for switching the Pockels cell on or off. One should test that single pulses can be switched with arbitrary input polarisation, and that the polarisations at the output and the input are the same. Additionally, the extinction ratio and the efficiency of the setup should be tested. In a final measurement, it should be checked that the switch preserves the temporal shape of the light pulses. Out of several options, a switch based on a Pockels cell seems to be the most suitable for our setup. A test setup[4] has been built and this solution is currently being tested in the lab.

[4]The components are: Calcite beam-displacer (Thorlabs, BD40); KD*P Pockels cell (Leysop, EM510M-HHT-AR854); Pockels cell driver (Bergmann Meßgeräte Entwicklung, no part number); splitter box for controlling how the driver is triggered (Bergmann Meßgeräte Entwicklung, BME_GS01).

Conclusion

In this thesis, I described the oldest cavity-QED setup in Innsbruck. The description includes the theoretical basics for ion trapping and cavity quantum electrodynamic as well as the experimental setup with a characterisation of the ion trap, the cavity, and the combined system.

The setup was used for the following experiment: We explored the effect of the cavity field onto an ion qubit, which was dispersively coupled to the cavity mode. In Ramsey experiments, the phase shift and dephasing caused by coherent states with different mean photon numbers in the cavity mode were measured. In addition, these measurements were used to reconstruct the photon number distribution in the cavity field for coherent states as well as for a state with mixed thermal and coherent statistics. These measurements and reconstruction used methods developed in microwave cavities to implement a photon statistics analyser for optical photons, using the ion as a probe for the cavity field.

Several extensions of the experiments were proposed: The sensitivity of the setup can be enhanced, and the full density matrix of the cavity field can in principle be accessed. In addition, the scenario can be reversed and the cavity output field can be used to infer the state of the ion qubit, which would make it possible to apply feedback to the qubit state based on the information extracted via the cavity photon. Furthermore, it is possible to prepare non-classical cavity field states in the optical domain by reaching the strong-pull regime of dispersive cavity-QED.

In addition to the experiment executed during my thesis work, the feasibility of several smaller projects in our experimental setup was investigated. Topics reach from the fundamental exploration of the interaction between ion qubits and their environment via the cavity decay to quantum networking applications. For example, the feasibilty of a protocol for entanglement between the electronic state of an ion and the time-bin of a single photon was analysed. In further networking-related topics, I presented a proposal for the implementation of heralded absorption of a photon in an ion coupled to our cavity as well as an analysis of different options for implementing a photon switch in quantum networks.

In summary, the topics covered in this thesis demonstrate that our cavity-QED setup is well-suited for both experiments in fundamental quantum optics as well as for application-driven projects in the context of quantum networking. Innsbruck is a thriving environment for the latter kind of research, with two more cavity-QED setups being built. Research in this direction in our setup will be continued by my fellow PhD students D. A. Fioretto and M. Teller as well as new PhD students and Postdocs.

Appendix A

Miscellaneous

A.1 Clebsch-Gordan coefficients

Table A.1: Clebsch-Gordan coefficients for the transitions between the $4^2S_{1/2}$ (column) and $4^2P_{3/2}$ (row) manifolds.

	$m_J = -3/2$	$m_J = -1/2$	$m_J = 1/2$	$m_J = 3/2$
$m_J = -1/2$	1	$\sqrt{2/3}$	$\sqrt{1/3}$	0
$m_J = 1/2$	0	$\sqrt{1/3}$	$\sqrt{2/3}$	1

Table A.2: Clebsch-Gordan coefficients for the transitions between the $3^2D_{5/2}$ (column) and $4^2P_{3/2}$ (row) manifolds.

	$m_J = -3/2$	$m_J = -1/2$	$m_J = 1/2$	$m_J = 3/2$
$m_J = -5/2$	$\sqrt{2/3}$	0	0	0
$m_J = -3/2$	$-\sqrt{4/15}$	$\sqrt{2/5}$	0	0
$m_J = -1/2$	$\sqrt{1/15}$	$-\sqrt{2/5}$	$-\sqrt{1/5}$	0
$m_J = 1/2$	0	$\sqrt{1/5}$	$\sqrt{2/5}$	$-\sqrt{1/15}$
$m_J = 3/2$	0	0	$-\sqrt{2/5}$	$\sqrt{4/15}$
$m_J = 5/2$	0	0	0	$-\sqrt{2/3}$

A.2 Derivation of the ion-cavity coupling strength

In order to derive the formula for the ion-cavity coupling strength given in Equation 3.9, we use the following formula for the atomic decay constant (cf., e.g., chapter 6.3 in Reference [94]):

$$\Gamma = \frac{\omega^3 \boldsymbol{d}^2}{3\pi\hbar\varepsilon_0 c^3},$$

where $\boldsymbol{d}$ is the electric dipole moment associated with the transition, $\omega = 2\pi\nu = 2\pi c/\lambda$ is the transition frequency, ε_0 is the vacuum permittivity, and c the speed of light. Note, that $\Gamma = 2\gamma$

is the full width of the transition. This formula can be derived in the Weisskopf-Wigner theory of spontaneous emission. For the TEM_{00} mode, the strength of the electric field in the cavity is given by (cf., e.g., chapter 12.2 in Reference [274])

$$E_0 = \sqrt{\frac{\hbar\omega}{2\varepsilon_0 V_0}} = \sqrt{\frac{2\hbar\omega}{\pi\varepsilon_0 L w_0^2}},$$

where $V_0 = \pi L w_0^2/4$ is the mode volume, L is the cavity length, and w_0 the cavity waist. Combining these formulae and replacing the frequency with the wavelength, we find for the maximum coupling strength with the atomic dipole located at an antinode of the cavity field and dipole and electric field aligned:

$$g = \frac{|\boldsymbol{d}|E_0}{\hbar} = \sqrt{\frac{3\varepsilon_0 c\Gamma\lambda^2}{2\pi^2 L w_0^2}} = \sqrt{\frac{3\varepsilon_0 c\gamma\lambda^2}{\pi^2 L w_0^2}}$$

For calculating the coupling strength on a specific transition, this number needs to be multiplied with the corresponding Clebsch-Gordan coefficient (cf. Appendix A.1).

A.3 Lamb-Dicke parameters for beams in the experiment

This section contains the calculated Lamb-Dicke parameters for the different motional modes of the trap and the laser beams available in the experiment. The Lamb-Dicke factor describes how large the ground state wave function of an oscillating particle is with respect to the wavelength of the laser with which the particle is interacting. It is given by

$$\eta = k\cos(\varphi)\sqrt{\frac{\hbar}{2m\omega}},$$

where $k = 2\pi/\lambda$ is the wave number of the laser light, φ is the angle between the laser beam and the mode under consideration, and $x_0 = \sqrt{\frac{\hbar}{2m\omega}}$ is the ground-state extent of the particle of mass m in a motional mode of the trap with frequency ω. In order to be able to control the motional state of the particle well, the condition $\eta^2(2n+1) \ll 1$ has to be fulfilled, where n is the number of phonons in the mode to be cooled [82]. If this condition is fulfilled, the system is in the Lamb-Dicke regime, and internal transitions of the particle which change the number of motional quanta are suppressed, enabling sideband cooling. The condition $\eta \ll 1$ is a necessary but not sufficient condition for reaching the Lamb-Dicke regime.

In the following Table A.3, the Lamb-Dicke parameters are listed for our setup for the north-east beam at 729 nm and the north-front beam at 393 nm, assuming angles of $45°$ of the beams with respect to the trap axis[1]. See Section 4.2.1 for a definition of the angles of the radial modes. Note, that the relatively large Lamb-Dicke factors for the laser beam at 393 nm imply that during Raman transitions, coupling to the sidebands is non-negligible, as the Rabi frequency on the carrier is reduced by a factor of $(1-\eta^2 n)$ (cf. Section 3.2.2), corresponding to a factor of 0.82 for 11 phonons in the axial mode.

[1] A MATLAB script for calculating these numbers available on our directory of the university git server under `git/simulations/qfp_utils/common/lamb_dicke_parameters_cqed.m`.

Table A.3: Lamb-Dicke factors for beams in our setup. Radial frequencies of 1.7 MHz (3.0 MHz) correspond to an RF power of 2 W (5 W). The same frequency is used for both radial modes (split by 57.3(7) kHz at 2 W RF power; cf. Section 4.2.1) since it is not clear which of the two modes has the higher frequency. The expression $\eta^2\,(2n+1)$ is evaluated for phonon occupations corresponding to the Doppler limit of $n = 11$ for the axial mode and $n = 6$ for $\omega_{\text{radial}} = 1.7$ MHz and $n = 4$ for $\omega_{\text{radial}} = 3.0$ MHz.

wavelength	beam direction	mode, $\omega/(2\pi)$	$\varphi/^\circ$	η	$\eta^2\,(2n+1)$
729 nm	north-east	axial, 1.0 MHz	45.0	0.069	0.110
	north-east	radial1, 1.7 MHz	49.2	0.037	0.018
	north-east	radial2, 1.7 MHz	74.3	0.020	0.005
	north-east	radial1, 3.0 MHz	49.2	0.049	0.022
	north-east	radial2, 3.0 MHz	74.3	0.015	0.002
393 nm	north-front	axial, 1.0 MHz	45.0	0.127	0.371
	north-front	radial1, 1.7 MHz	74.3	0.037	0.018
	north-front	radial2, 1.7 MHz	49.2	0.090	0.105
	north-front	radial1, 3.0 MHz	74.3	0.028	0.007
	north-front	radial2, 3.0 MHz	49.2	0.068	0.042

A.4 Dimensions of the temperature stabilisation box

The temperature stabilisation box for the reference cavity for the lasers at 393 nm and 783 nm was built to fit around the vacuum chamber in which the cavity is set up. The following table gives the dimensions of the box for future reference.

Table A.4: Dimensions of the walls of the temperature stabilisation box.

material	number of pieces	dimensions/cm^3
wood	2	$46 \times 67 \times 2$
	2	$29 \times 67 \times 2$
	1	$46 \times 31 \times 2$
polystyrol	2	$44 \times 67 \times 3$
	2	$23 \times 67 \times 3$
	1	$37.8 \times 22.8 \times 3$
aluminium	2	$38 \times 65 \times 0.15$
	2	$23 \times 65 \times 0.15$
	1	$38 \times 23 \times 0.15$

A.5 Estimation of the AC-Stark shift of the ion caused by the cavity locking laser

In this section, we estimate how much the energy levels of the ion are AC-Stark shifted by the cavity locking laser. Due to the fact that no values for the cavity mirror transmissions at 783 nm

are available, a symmetric cavity is assumed in the estimation with an estimated incoupling efficiency of $\varepsilon = 15\%$. This number is based on the amplitude of the reflection dip of the 783 nm laser off the cavity West mirror during the rebuild of the cavity. The laser has an input power of typically 12.5 µW, and a waist of $w = 11.7$ µm in the cavity at 783 nm. The finesse of the cavity at 783 nm was measured as $19.7(3) \cdot 10^3$ (see Section 4.4.2).

For these parameters the intra-cavity power in the TEM_{00} mode can be calculated as $I_{\mathrm{cav}} \approx 45\ \mathrm{mW} \cdot 2/(\pi w^2)$, where $\pi w^2/2$ is the mode area[2]. The AC-Stark shift caused by this intensity, assuming a pointlike particle, can then be calculated using the unshifted frequency ω_0, the width Γ of the transition and the detuning Δ of the light field from the transition as [275]

$$\Delta\omega_{00} = \frac{1}{\hbar}\frac{3\pi c^2}{2\omega_0^3}\frac{\Gamma}{\Delta},$$

yielding a frequency shift of $2\pi \cdot 87$ kHz on the transition between $|4^2\mathrm{P}_{3/2}, m_J = 1/2\rangle$ and $|3^2\mathrm{D}_{5/2}, m_J = 1/2\rangle$. The contribution from the transition $3^2\mathrm{D}_{5/2} - 4^2\mathrm{S}_{1/2}$ is neglected due to the small width of that transition.

Considering only the direction $\hat{x}$ perpendicular to the cavity axis, we can then calculate the frequency shift caused by the light at 783 nm in the TEM_{01} mode in the ion. Assuming a Gaussian wave packet $S(x)$ of the ion perpendicular to the cavity axis and the spatial intensity profile of the TEM_{lm}-mode $I_{lm}(x)$, the corresponding shift is calculated as

$$\Delta\omega_{01} = \frac{\int I_{01}(x-d)S(x)\mathrm{d}x}{\int I_{00}(x)\delta(x)\mathrm{d}x}\Delta\omega_{00}.$$

Here, d is the displacement of the ion position from the centre of the cavity antinode due to imperfect alignment. Assuming an upper bound on the spatial extent of the ion along the cavity axis of 62 nm (corresponding to the standard deviation of the Gaussian probability distribution of the ion $S(x)$) (see Section 4.2.1), and using a displacement $d = 0.95$ µm, the corresponding frequency shift is $\Delta\omega_{01} = 2\pi \cdot 1.22$ kHz. The phase shift of $-0.12 \cdot \pi$ measured with the ion coupled to an antinode in the waist of the cavity mode at 854 nm (cf. p.88), corresponds to a frequency shift of 1.2 kHz. The measured phase offset can therefore be explained by an AC-Stark shift caused by the cavity locking laser and an imperfectly coupled ion, which is displaced by $d = 0.95$ µm from the cavity centre. Note, that a displacement of the ion by 0.95 µm from the antinode in a direction orthogonal to the cavity axis still corresponds to 99% of the full ion-cavity coupling strength.

A.6 Sensitivity of the squared statistical overlap for distinguishing distributions

In order to understand if the values of the squared statistical overlap (SSO) extracted in Section 5.4 are reasonable, the sensitivity of this measure was investigated. Figure A.1 displays

[2] This follows from $I_{\mathrm{cav}} = 4\frac{\mathcal{F}}{\pi}\varepsilon^2 I_{\mathrm{in}}$, which can be derived from interference of intra-cavity field and drive field (neglecting absorption and scattering losses), cf., e.g., [104, 105].

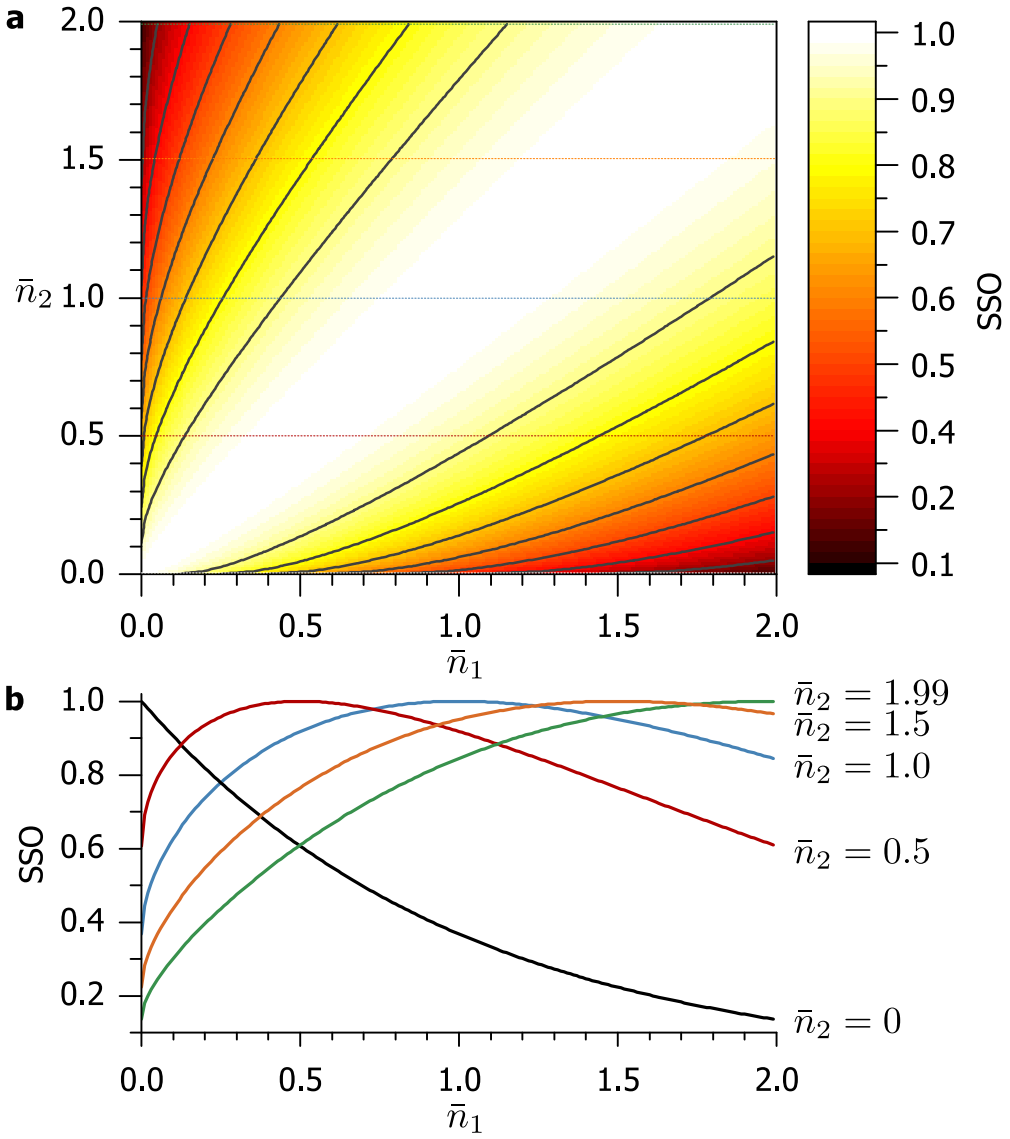

Figure A.1: Sensitivity of the squared statistical overlap (SSO) for comparing two Poisson distributions with mean $\bar{n}_1$ and $\bar{n}_2$. **a** SSO as a function of $\bar{n}_1$ and $\bar{n}_2$. **b** Cuts through **a** for different constant values of $\bar{n}_2$. The higher $\bar{n}_2$, the less sensitive is the SSO for distinguishing between the distributions since the SSO yields values close to one even if $|\bar{n}_1 - \bar{n}_2| \approx 0.5$ for $\bar{n}_2 > 0.5$.

a plot of the SSO for two Poisson distributions $p_1(n)$ and $p_2(n)$ with means $\bar{n}_1$ and $\bar{n}_2$:

$$\mathrm{SSO} = \left[\sum_{n=0}^{9} \sqrt{p_1(n) \cdot p_2(n)}\right]^2$$
$$p_i(n) = \frac{\bar{n}_i^n}{n!} e^{-}\bar{n}_i.$$

The basis is cut at $n = 9$, as in the reconstruction algorithm (cf. Section 5.4). As visible from the plot, there is a plateau of high SSO values, which grows wider for higher mean photon numbers. Accordingly, the SSO is a better measure for distinguishing between two Poisson distributions

if at least one of the distributions has a small mean photon number. The larger the mean photon numbers get, the less sensitive the SSO: As visible in Figure A.1b, the SSO between two Poisson distributions is close to one even if the mean photon numbers of the distributions are different by 0.5. We conclude that for the low mean photon numbers of up to 1.6 used in the experiment, the SSO is an appropriate measure of overlap.

A.7 Comparing the bandwidths of photodiode and cavity for the calibration of thermal cavity drive

The bandwidths of the photodiode[3] and the cavity have to be taken into account for calibrating the mean photon number for the noise drive measurement (Section 5.4.3). In order to infer how much of the thermal light actually enters the cavity, we assume exponential gain profiles for both cavity and photodiode of the form $g(\nu) = \exp(-\nu/B)$ with bandwidth B. Integrating the gain, yields the area under the gain curve, which is proportional to B. By dividing the areas, i.e., the bandwidths, we can infer the amount of light that enters the cavity. Since the cavity width is a full width at half maximum, we need to define the photodiode bandwidth BW for the comparison as the frequency for which the gain is half, which corresponds to BW ≈ 2.1 MHz. The ratio of the cavity bandwidth 2κ and this derived photodiode bandwidth is used as scaling factor with a value of $2\kappa/\mathrm{BW} = 0.41$. The parameter V_{AC} in the calibration of the noise drive is multiplied by this number.

A.8 Derivation of formulae for uncertainties

Uncertainty of the calibration of the intra-cavity mean photon number

The expected photon rate is given by

$$R_{\mathrm{APD}} = p_{\mathrm{out}} \cdot 2\kappa \cdot \eta = \underbrace{\frac{\mathcal{T}_2}{\mathcal{T}_1 + \mathcal{T}_2 + \mathcal{L}}}_{p_{\mathrm{out}}} \cdot \underbrace{2\pi \frac{\mathrm{FSR}}{\mathcal{F}}}_{2\kappa} \cdot \eta = \frac{\mathcal{T}_2 \mathcal{F}}{2\pi} \cdot 2\pi \frac{\mathrm{FSR}}{\mathcal{F}} \cdot \eta = \mathcal{T}_2 \cdot \mathrm{FSR} \cdot \eta,$$

where p_{out} is the probability for a photon to leave the cavity through the output mirror, given by

$$p_{\mathrm{out}} = \frac{T_2}{T_1 + T_2 + \mathcal{L}_{\mathrm{tot}}} \approx \frac{T_2}{T_1 + T_2 + \frac{2\pi}{\mathcal{F}} - (T_1 + T_2)} = \frac{\mathcal{F} T_2}{2\pi},$$

η is the path efficiency, and $2\kappa = \mathcal{F}L/(\pi c)$ is the full width of the cavity mode with L the cavity length, $\mathcal{F}$ the finesse, and c the speed of light. The uncertainty for the rate is therefore given by

$$\Delta R_{\mathrm{APD}} = R_{\mathrm{APD}} \sqrt{\left(\frac{\Delta \mathcal{T}_2}{\mathcal{T}_2}\right)^2 + \left(\frac{\Delta \mathrm{FSR}}{\mathrm{FSR}}\right)^2 + \left(\frac{\Delta \eta}{\eta}\right)^2}.$$

[3] Thorlabs, PDA36A with a bandwidth of 5.5 MHz at 10 dB gain.

The uncertainty for the expected number of counts $C_0 = R_{\mathrm{APD}}\tau/c$ is then given by

$$\Delta C_0 = \frac{\Delta R_{\mathrm{APD}} \cdot \tau}{c},$$

and the uncertainty for the calibrated intracavity mean photon number follows as

$$\Delta\bar{n} = \bar{n}\sqrt{\left(\frac{\Delta C}{C}\right)^2 + \left(\frac{\Delta C_0}{C_0}\right)^2}.$$

For the data [Data17f], including the correction factor ξ, it is

$$\Delta\bar{n} = \bar{n}\sqrt{\left(\frac{\Delta C}{C}\right)^2 + \left(\frac{\Delta C_0}{C_0}\right)^2 + \left(\frac{\Delta \xi}{\xi}\right)^2}.$$

Note that the Poissonian statistics of the detection process enter via the uncertainty of the measured counts C, given by $\Delta C = \sqrt{C}$.

Uncertainty of the contrast of the measured Ramsey fringes

Since the contrast C of the Ramsey fringes is calculated as $C = B/A$ with offset B and amplitude A (see Section 5.3.2), the uncertainty of the contrast is given by

$$\Delta C = C\sqrt{\left(\frac{\Delta B}{B}\right)^2 + \left(\frac{\Delta A}{A}\right)^2 - 2\frac{\mathrm{cov}(A,B)}{AB}},$$

where ΔA and ΔB are given by the standard uncertainties from the fit to the Ramsey fringe data and $\mathrm{cov}(A,B)$ is the covariance from the fit.

Uncertainty of the coupling strength from the linear fit to the Ramsey fringe shift as a function of $\bar{n}$

The uncertainty of the coupling strength δg is determined from the uncertainty of the slope δs extracted from a linear fit to the data of the fringe shift vs. $\bar{n}$ and from the uncertainty of the detuning $\delta\Delta$ (see Section 5.3.2). The coupling strength is given via

$$s = \frac{g^2}{\Delta} \cdot 2\tau \Leftrightarrow g = \sqrt{\frac{s\Delta}{2\tau}}.$$

The derivatives of g with respect to s and Δ are

$$\frac{\partial g}{\partial s} = \frac{1}{2s}\sqrt{\frac{s\Delta}{2\tau}} = \frac{g}{2s}, \quad \frac{\partial g}{\partial \Delta} = \frac{1}{2\Delta}\sqrt{\frac{s\Delta}{2\tau}} = \frac{g}{2\Delta}.$$

Combining these and using Gaussian propagation of uncertainty, the uncertainty of the coupling strength, δg, is

$$\delta g = \delta g = \sqrt{\left(\frac{\partial g}{\partial s} \cdot \delta s\right)^2 + \left(\frac{\partial g}{\partial \Delta} \cdot \delta\Delta\right)^2} = \sqrt{\frac{\Delta \cdot (\delta s)^2}{8s\tau} + \frac{s \cdot (\delta\Delta)^2}{8\Delta\tau}}$$

As Δ and s are determined independently, there is no covariance term in the propagation of uncertainty.

Uncertainty for the photon number resolution of the Ramsey measurement

The uncertainty for the photon number resolution $\delta\bar{n} = \delta\phi\frac{\Delta}{g^2\tau}$ (see Section 5.3.4) is given as

$$\delta(\delta\bar{n}) = \sqrt{\left(\frac{\delta\phi}{g^2\tau}\delta\Delta\right)^2 + \left(\frac{2\Delta\,\delta\phi}{g^3\tau}\delta g\right)^2},$$

with the uncertainties of the detuning $\delta\Delta$ and the coupling strength δg. $\delta\phi$ is the phase resolution.

Uncertainty analysis for the reconstructed photon number distributions

This section contains a description of how the uncertainties for the reconstructed photon distributions (see Section 5.4) were estimated in a way similar to the estimation of the phase resolution (Section 5.3.4). For this purpose of estimating uncertainties for the reconstructed distributions (and derived quantities such as the reconstructed mean photon number $\bar{n}_{\text{rec}}$ or the Mandel Q-parameter), the following steps were followed:

1. From the reconstruction algorithm, a parameter pair $(\eta_{\text{opt}}, \delta n_{\text{opt}})$ is extracted which best describes the data.

2. These values are used to simulate an ideal Ramsey fringe, by integrating the master equation with $(\eta_{\text{opt}}, \delta n_{\text{opt}})$ as input. The simulated fringe consists of $N = 51$ points, each consisting of a phase value ϕ_k of the second Ramsey pulse and a calculated ion excitation probability Q_k ($k = 1, ..., N$), such that the ideal fringe mimics a measured fringe.

3. A Ramsey fringe with noise is simulated, based on the ideal fringe generated in the previous step: Taking into account the quantum projection noise from the $M = 250$ cycles in the measurement, for each point k in the ideal fringe, noise is added by calculating the ion excitation as $p_k = m_k/M$, where m_k is the number of times the ion is found in the excited state when measuring M times. The probability Π_k for finding m_k is given by the binomial distribution

   $$\Pi_k(m_k) = \binom{M}{m_k} Q_k^M \; (1 - Q_k)^{M - m_k}.$$

   This is repeated for all phase points ϕ_k, such that a noisy Ramsey fringe is simulated. Due to this construction, the excitation probabilities of this fringe are subject to quantum projection noise.

4. A sinusoidal function is fitted to the noisy Ramsey fringe, and the values $(\eta_i, \delta n_i)$ are found which best explain this fringe by maximising the likelihood function (Equation 5.4).

5. Steps 3 and 4 are repeated until the standard deviations σ_η and $\sigma_{\delta n}$ of the extracted $\{(\eta_i, \delta n_i)\}$ have converged. The following convergence criterion is used: The standard deviations as a function of the index i should vary less than 5% over a range of ten runs before the process is stopped. The uncertainties η and δn are then defined as: $\Delta\eta = \sigma_\eta$ and $\Delta\delta n = \sigma_{\delta n}$.

6. The corresponding values $(\eta \pm \Delta\eta, \delta n \pm \Delta\delta n)$ can now be used to calculate uncertainties of the derived quantities such as the reconstructed mean photon number $\bar{n}_{\mathrm{rec}}$ or the Mandel Q-parameter by calculating the photon distributions for the parameter pairs $(\eta + \Delta\eta, \delta n + \Delta n)$ and $(\eta - \Delta\eta, \delta n - \Delta n)$.

A.9 Code for the digital filter in the cavity lock

This Python code is based on the filter implementation in Reference [159]. It was provided to us by the first author of that reference and adapted to our purposes. Running the file in Python will upload the filter function, defined in lines 32-49, to the RedPitaya.

```
"""
Written by Albert Ryou.
Last modified 20170401 by Konstantin Friebe.

Send to RP
"""

from rpyc import connect
from PyRedPitaya.pc import RedPitaya
from struct import pack, unpack
from math import *
import cmath
import parser
import sys
import os
import numpy as np
import scipy.signal
from collections import deque


def convert_2c(val, bits):
    """Take a signed integer and return it in 2c form"""
    if (val>=0):
        return val
    return ((1 << bits)+val)
numbits=32
def convertsimple(val):
    return convert_2c(val,numbits)
def sendpitaya (addr, val):
    redpitaya.write(addr,convert_2c(val,numbits))

Resonance1 = 6600  #centre frequency of the stop band for the notch
    filter
Resonance2 = 12000  # resonance frequency at which to put a notch
ManualCutoff = 4800  # cut-off frequency of the low-pass filter

# elliptic filter
StopbandHalfWidth1 = 3200
StopbandHalfWidth2 = 4000
b1, a1 = scipy.signal.ellip(2,0.01,120,[Resonance1-StopbandHalfWidth1,
    Resonance1+StopbandHalfWidth1],btype='bandstop',analog=True,output='
```

```
    ba')
b3, a3 = scipy.signal.ellip(2,0.01,120,ManualCutoff,btype='lowpass',
    analog=True,output='ba')
b2, a2 = scipy.signal.ellip(2,0.01,120,[Resonance2-StopbandHalfWidth2,
    Resonance2+StopbandHalfWidth2], btype='bandstop', analog=True, output
    ='ba')
# maximum frequency should be sampling frequency of the RedPitaya, i.e.,
     243 kHz
# maximum number of points should be 30720
w1, h1 = scipy.signal.freqs(b1, a1, worN=np.linspace(1, 243e3, 30720))
w2, h2 = scipy.signal.freqs(b2, a2, worN=np.linspace(1, 243e3, 30720))
w3, h3 = scipy.signal.freqs(b3, a3, worN=np.linspace(1, 243e3, 30720))
# transfer function:
Zfilter = 20*h1*h2*h3

# additional scaling factor multiplied to filter function:
multiplierFilter = 100
filterMultiplied = [item*multiplierFilter for item in Zfilter]
filterMultiplied = np.asarray(filterMultiplied)
Z = filterMultiplied

# calculate coefficients used in the filter:
coeff = np.fft.ifft(Z)
coefficients = coeff * 0.10

REDPITAYA_IP = "192.168.0.33"  # IP address of the RedPitaya board.

theshift = 12
theprefactor = 1e2

LEDADDRESS = 0x40000030
OUTPUTBITSHIFTADDRESS = 0x40300000
FIRCOEFFSADDRESS = 1076887552+4*(32)
FIRCOEFFSADDRESSOFFSET = 1076887552+4*(4)
maxsendlen = 31*512

def sendpitayaarray (addr, dats):
    """Send array to RedPitaya."""
    thelen=len(dats)
    startind=0
    endind=min(thelen,startind+maxsendlen-1)
    while(startind<thelen):
        redpitaya.write (FIRCOEFFSADDRESSOFFSET,startind*4)
        redpitaya.writes(addr,dats[startind:endind])
        startind=endind+1
        endind=min(thelen-1,startind+maxsendlen)

conn = connect(REDPITAYA_IP, port=18861)
redpitaya = RedPitaya(conn)
redpitaya.write(LEDADDRESS, 0)  # DAC/ADC behaves better with LEDS off.
sendpitaya(OUTPUTBITSHIFTADDRESS,theshift)  # Right-shift by 15 bits
    before outputting result!
nels=512
nrams=60
```

```
thearray=[];
maxval=0.
numarray=[]

for x in range (nrams*nels): #first we build up the array
    theval=int(round(theprefactor*coefficients[x]))
    maxval=max(maxval,abs(theval))
    thearray.append(convertsimple(theval))
    numarray.append(theval)
sendpitayaarray(FIRCOEFFSADDRESS,thearray)

# file ends here.
```

A.10 Battery box for cavity length control

This section contains a circuit diagram of the battery box used for controlling the length of the cavity as well as a description of how to use the box. The circuit is displayed in Figure A.2. It consists of two battery packs (labelled "BATTERY1" and "BATTERY2" in the diagram. Each of the packs contains 30 individual batteries of 9 V each. This is due to the fact that the 300 V batteries used previously are no longer produced. The batteries are in parallel with diodes (INA148) as depolarisation protection. The battery stack for the fast piezo is stored in a second container, which is connected to the battery box proper via banana cables. Black cables correspond to the minus pole and red cables to the plus pole of the battery stacks. Additionally, in the battery box the cables pertaining to the slow piezo are marked with green tape and the ones to the fast piezo with red tape.

The maximum possible output voltage to the piezos can be controlled with two potentiometers labelled "LIMIT SLOW BATTERY" and "LIMIT FAST BATTERY". The output voltages are controlled via the potentiometers "TUNE SLOW" and "TUNE BOTH", while their sign is controlled by switches "SIGN SLOW PIEZO" and "SIGN FAST PIEZO". If the potentiometer "TUNE BOTH" is used, a fraction of $33\ \mathrm{k\Omega}/(33\ \mathrm{k\Omega} + 68\ \mathrm{k\Omega}) = 0.327 \approx 1/3$ of the voltage applied to the fast piezo is also applied to the slow piezo with a sign determined by the switch "SIGN FAST FORWARD", but only if the cavity is locked, i.e., if the switch "LOCK/SCAN" is in the "LOCK" position. This feature is useful for experiments during which the locked cavity is translated along its axis, i.e., for precise relative alignment of the cavity standing wave and the trapped ion. The ratio $1:3$, determined by resistors R7 and R8, stems from the fact that the ratio of piezo layers in fast and slow piezo is also $1:3$. Using this feedforward, both piezo stacks move by the same amount.

A scan generator can be connected to "SCAN IN" and a PID controller to "PID IN". The scan voltage is applied to the slow piezo, but only if the switch "LOCK/SCAN" is in "SCAN" position, while the PID feedback signal is sent to the fast piezo, independent of the "LOCK/SCAN" switch. The output voltages to the piezos are connected to "SLOW PIEZO OUT" and "FAST PIEZO OUT". Since the polarity of the signals can be changed, and BNC connectors are used, the cables carrying the voltages are isolated for safety. The cables are additionally shielded, and the shield is electrically connected to ground.

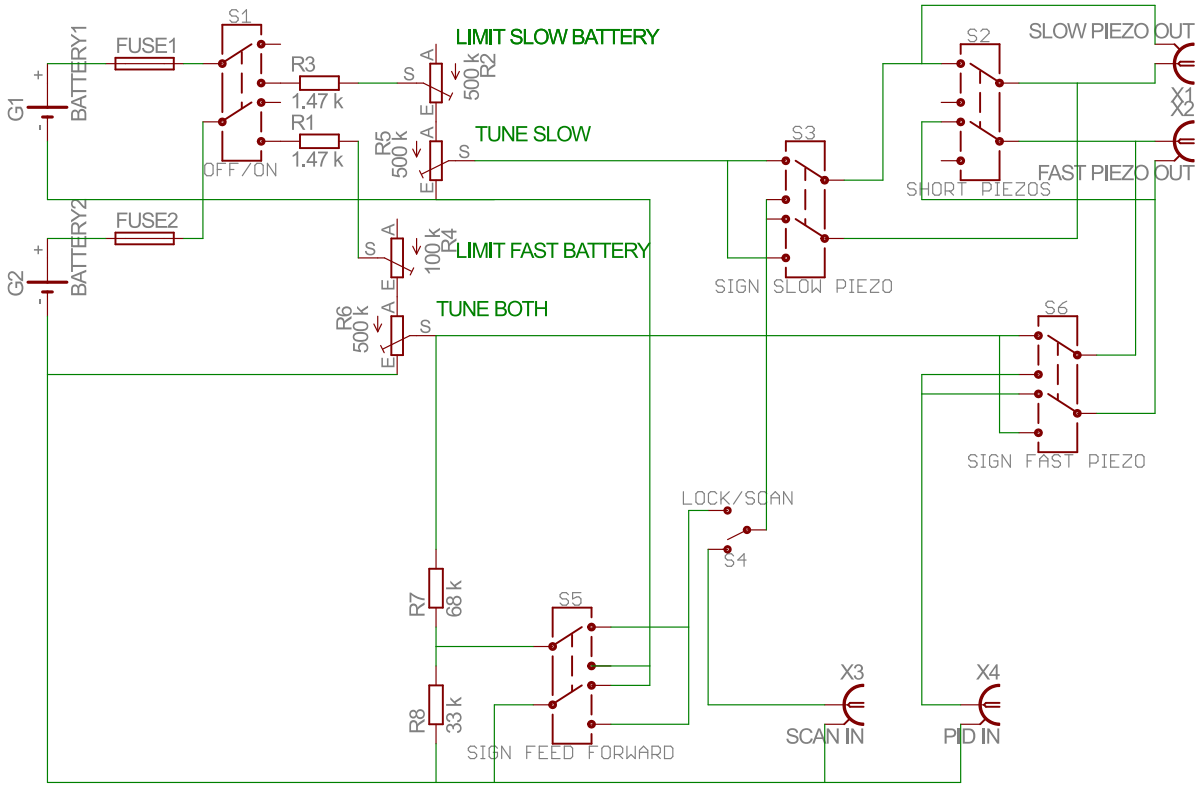

Figure A.2: Circuit diagram for the battery box used in the experiment for controlling the length of the cavity. See main text for details.

Appendix B

Rebuilding the experiment

This appendix gives an overview of the vacuum leak and the subsequent rebuilding of both the cavity and the experimental setup.

B.1 Reason for the rebuilding

During a routine firing of the TiSub pump on 1 April 2015, a leak opened up in the flange on which the TiSub pump was mounted. This caused a pressure spike of at least 10^{-4} mbar, giving rise to a plasma that formed at the high-voltage trap feedthrough of the vacuum chamber. The following steps were then taken: A scroll-pump and a turbo-pump were connected to the angle valve (west-back-bottom side of the setup), the screws on the TiSub pump flange were tightened further, and liquid resin[1] was applied to the TiSub flange to close the leak. At this point, it was noticed that the finesse of the cavity had dropped to about $1,000$, which was ascribed to contamination of the mirrors due to the sudden rise in pressure. Next, the chamber was heated using strong flash lamps through the front and back windows and heating tape.

After five days of pumping and heating, the pressure had been reduced to around $5{\cdot}10^{-9}$ mbar, but switching on the oven in an attempt to load ions in the trap increased the pressure to $2 \cdot 10^{-5}$ mbar. By degassing the oven and firing the TiSub pump, we were able to reduce the pressure further to around $5 \cdot 10^{-10}$ mbar, but it was not possible to load ions or to detect atomic fluorescence. In addition, no cavity transmission signal was found. Analysing microscope picture of the cavity, it was finally found that the mirrors had become misaligned, presumably due to the glue changing its properties during the heating process with flash lamps and heating tape. Accordingly, the decision was made to open the vacuum chamber, rebuild the cavity, and replace the oven. The trap was to be tested during the work to rebuild the cavity, so as to be certain that in the end all in-vacuum elements were functional.

The leak in the TiSub flange probably opened because the current source for the pump had been improperly connected to the pump in recent years. Instead of using the dedicated feedthrough pins for the ground connection, one of the screws of the flange had been used. Presumably, the high current flowing through the pump had caused thermal stress in the flange and gasket, leading to a leak. The new pump has a connector which requires a special cable, making such a wrong connection impossible.

[1] VacSeal.

B.2 Timeline

B.2.1 Opening the vacuum chamber

The chamber was opened on 30 April, 2015. On this occasion, the following steps were taken:

- The wires for the cavity piezos were cut, so that we could to remove the cavity on its mount from the chamber.
- The connectors of the calcium oven were cut. The oven had been mounted between the cavity and the west collimating lens in such a way that removing the cavity without removing the oven was not possible.
- The cavity and lens mount were unscrewed from the slip-stick piezo translation stages and removed from the chamber together with the screws. These elements were stored in a test vacuum chamber at pressures around 10^{-6} mbar to avoid further contamination.
- The insulation at the ends of the piezo wires was removed with sandpaper.
- An angled aluminium piece was inserted and screwed to the translation stages to shield the trap from the test oven.
- A test oven (commercial, by Alvatec) was inserted to test the trap functionality while the cavity was being rebuilt. The oven was connected to the old oven's connectors with barrel connectors.
- The TiSub pump was replaced.

During this operation, the vacuum chamber was back-filled with dry nitrogen to minimise contamination of the chamber.

The chamber was then pumped out with a mobile pump station and baked on the optical table at about $110°$C for five days using heating tape and aluminium foil to distribute heat evenly. Before cooling down, the test oven was degassed. Its indium seal was removed by sending a current through the oven and watching for pressure spikes due to the emission of the protective argon gas in the oven and outgassing of the calcium alloy.

Attempts at observing atomic fluorescence from the oven failed. Moreover, sending currents up to 5 A through the oven increased the pressure in the vacuum chamber up to 10^{-5} mbar. For that reason, the chamber was reopened on 13 May, and the stainless steel wire between the new oven and the old oven's connectors was replaced with oxygen-free copper wire in order to reduce the wire resistance. During this operation, a barrel connector fell into the south-west flange. This connector was recovered in the flange of the angle valve, and the oven was replaced. Next, the bottom flange was temporarily removed to fasten the connection between the copper wires of the feedthrough and the stainless steel rod of the old oven's connectors, since this connection had been observed to limit the stability of the oven mounting. During the same time as the operations described in this paragraph, a setup for testing cavity mirrors was built. This setup included adapters for mounting the cavity mirrors in their stainless steel rings glued to the piezo holders, and three-dimensional translation stages for precise alignment.

B.2.2 Loading ions and rebuilding the the cavity

After degassing the TiSub pump and the new oven, including breaking the indium seal, and baking the chamber again for about three days, atomic fluorescence was finally observed on 28 May. While these works were carried out, the cavity and its mount had been removed from the storage vacuum chamber and moved to the test station. It was found that the glue between both piezo stacks and their holders was damaged. For the slow stack, there were also damaged glue layers between the piezo layers. The insulation from the piezo wires was removed, and the capacitances of the piezo stacks were measured to be 4 nF for the slow stack and 2 nF for the fast stack.

The piezo holders were then removed from the U-shaped cavity mount, and the piezo stacks were reglued using epoxy glue[2], which was thermally cured on a hot plate. The temperature was increased from room temperature over 20 minutes to $90°$C, held there for 90 minutes, and then slowly decreased back to room temperature. By 1 June, a cavity mode had been recovered with a measured finesse of about $63,000$ at 844 nm. This laser wavelength was used as it was readily available at the cavity test station. The residual glue[3] on the U-shaped cavity mount with a thickness of around 300 µm was removed.

After the PMT was aligned to the ion trap, on 3 June, ions were loaded and observed in the trap for the first time after the vacuum leak. At this point in time, the length of the cavity in the test setup had been increased towards the concentric regime, while maintaining the cavity mode. The cutout in the west lens mount was extended slightly at the lower side so that aiming the new commercial oven at the trap through the lens holder and the cavity mount would be possible. The lens holder was then baked at $400°$C for 24 hours.

The cavity was rebuilt and measured to have a finesse of about $70,000$ at a length of 19.92 mm at 844 nm. After cleaning the mirrors from possible contaminations, the piezo mounts with the mirrors were reglued to the U-shaped mount. The glue[4] for the cavity and the lenses was first pre-cured, using ultraviolet (UV) light, and then heat-cured at about $70°$C for four hours, with the temperature ramped up and down slowly. After the heat cure, the cavity mode was found to be misaligned. This was probably caused by the temperature having been above the glass transition temperature, which was specified to occur at $86 \pm 40°$C, with the exact value depending on how the glue is cured.

Therefore, in the next trial, the output mirror was first glued to the U-shaped mount using epoxy glue[5], which was thermally cured at $90°$C for about 1.5 hours. After gluing the output mirror, we found that for the aligned cavity, there was a gap of around 560 µm between the input mirror and the corresponding part of the U-shaped mount. We thus decided to include a non-magnetic stainless steel spacer. In this way, the amount of glue used was minimised in order to avoid large mirror displacements due the glue shrinking while being cured. The spacer had a small cutout so as not to obscure the hole for the atom beam from the oven, which is drilled through the mirror mount. It was wedge-shaped with a thickness of 500 µm on the cavity input side (west) and 420 µm on the cavity output side (east).

We decided at this point to change the glue being used, as UV-curing for the very small gaps

[2]Epotek, 353ND.
[3]Dymax, OP-66-LS.
[4]Dymax, OP-67.
[5]Epotek, 353ND.

with the new spacer was not feasible, since the UV light would not access the whole volume of the glue. Instead, Epotek 301 was used in the corners of the mount for room-temperature pre-curing and Epotek 353ND in the centre of the mount for thermal curing. During the room-temperature pre-curing, the cavity mode was realigned to compensate for the glue shrinkage. After about 24 hours of pre-curing, the cavity assembly was heat-cured on a heat plate. The challenge consisted in heating the fresh glue to as high a temperature as possible so as to move its glass-transition temperature as high as possible, while at the same time keeping the temperature low at the top of the assembly such that the old glue in the piezo stacks and mirror mounts would not be heated above its glass-transition temperature. Unfortunately, it is not known at which exact temperature the old glue was cured, such that it was not clear at which temperature the fresh glue could be glued. We therefore heated the heat-plate to $152°$C for one hour, corresponding to a temperature of $88°$C at the U-shaped mount, as measured by a thermocouple fixed with Kapton tape[6]. This time, the cavity mode survived the baking process with a finesse of about $70,000$.

B.2.3 Re-installing the cavity in the chamber

On 29 June, we opened the vacuum chamber again to re-install the realigned cavity assembly. During this operation, the following steps were taken:

- The shield of the trap from the oven was removed.
- A new commercial oven from Alvatec was installed. The oven connections to the feed-through were tested.
- The collimating lenses on their mount and the cavity assembly were fixed to the translation stages.
- The piezo wires on the trap assembly were connected to the piezo wires going to the feed-through. Barrel connectors were used for this purpose, with ceramic washers between the two screws to prevent the connectors from touching the cavity assembly, which would cause electrical shorts. The connections of the wires were tested with a multimeter.
- The path of the atomic beam from the oven to the trap centre was cleared by sticking a clean wire through the alignment hole in the cavity mount.
- The oven was aligned to the trap. This was difficult due to the instability of the oven mounting. It later turned out that the oven was still flexible enough to shift on its own in the vacuum chamber.
- During the operation, we sent light through the cavity to see if the alignment had survived. Although we did not observe the cavity modes immediately, we closed the chamber. The modes were observed on the same day after closing the chamber, with a finesse around $70,000$.

[6] DuPont, Kapton.

- The TiSub pump adapter flange was replaced. The pump is mounted on a CF40 flange, which is connected to the CF63 flange of the vacuum chamber with an adapter. This adapter was exchanged.

After we closed the chamber, heating tape for baking the chamber in situ was installed together with thermocouples for temperature monitoring. The temperature was increased slowly at a rate of about $2°$C per hour. While the temperature was still increasing, the TiSub filaments were degassed, and the oven seal was melted. The maximum measured temperature was $75°$C, while the average of the four thermocouples was around $60°$. Baking continued for about 14 days until 16 July. After reducing the temperature back to room temperature, the pressure went down to $1 \cdot 10^{-9}$ mbar and reached the mid-10^{-11} mbar range over the following two months. The cavity had survived the baking without too large loss of finesse (cf. Section 4.4).

Atomic fluorescence was observed on 23of June. However, it was found that the oven position had shifted in the vacuum chamber, and had sprayed calcium on the inside of both the back and front windows. Due to this contamination of the vacuum windows, the beam layout for the repumping beams and one of the Doppler cooling beams was changed (cf. Section 4.3.1). Loading ions was finally achieved on 5 August, and on 21 August, the coupling of a single ion to the cavity mode was observed for the first time after the vacuum leak.

The remaining work consisted of rearranging the optics around the vacuum chamber, installing the magnetic field coils, and recovering the qubit spectroscopy. Additionally, the trap and cavity were characterised and the cavity lock rebuilt. These issues had been solved by the end of 2015. However, ion lifetimes were still quite short (mostly < 1 hour) which only improved by early 2016.

Appendix C

Publications

This appendix contains a list of papers and proceedings articles published during the course of this thesis.

In preparation:

- M. Lee, K. Friebe, D. A. Fioretto, K. Schüppert, F. R. Ong, D. Plankensteiner, V. Torggler, H. Ritsch, R. Blatt, T. E. Northup, *An ion-based nondestructive sensor for cavity photon numbers*, submitted to Phys. Rev. Lett., preprint arXiv:1810.13340

Published:

- M. Lee, K. Friebe, F. R. Ong, D. A. Fioretto, K. Schüppert, R. Blatt, T. E. Northup, *Quantum decoherence of a single ion qubit induced by photon-number fluctuations*, Proc. SPIE 9980, Quantum Communications and Quantum Imaging XIV, 99800D (2016)

- B. Casabone, K. Friebe, B. Brandstätter, K. Schüppert, R. Blatt, T. E. Northup, *Enhanced quantum interface with collective ion-cavity coupling*, Phys. Rev. Lett. 114, 023602 (2015)

- T. E. Northup, B. Casabone, K. Friebe, K. Schüppert, F. R. Ong, M. Lee, D. Fioretto, K. Ott, S. Garcia, J. Reichel, R. Blatt, *An ion-cavity interface for quantum networks*, Proc. SPIE 9615: Quantum Communications and Quantum Imaging XIII, 961506 (2015)

- B. Brandstätter, A. McClung, K. Schüppert, B. Casabone, K. Friebe, A. Stute, P. O. Schmidt, C. Deutsch, J. Reichel, R. Blatt, T. E. Northup, *Integrated fiber-mirror ion trap for strong ion-cavity coupling*, Rev. Sci. Instrum. 84, 123104 (2013)

- B. Casabone, A. Stute, K. Friebe, B. Brandstätter, K. Schüppert, R. Blatt, T. E. Northup, *Heralded entanglement of two ions in an optical cavity*, Phys. Rev. Lett. 111, 100505 (2013)

- A. Stute, B. Casabone, B. Brandstätter, K. Friebe, T. E. Northup, R. Blatt, *Quantum-state transfer from an ion to a photon*, Nat. Photonics **7**, 219 (2013)

List of data sets

This appendix lists all data sets described in this thesis, i.e., the acquisition date and time. Each data set is uniquely identified by the date of acquisition and the time in hours and minutes of the start of the scan. If two scans are started in the same minute, e.g., 1728, their file names are set as 1728_01 and 1728_02 and so on.

The files are stored either on the old group server "anna" in `cqed\data`, e.g., `\anna\cqed\data\20170323`, or in the equivalent directory on the more recent zidshare server. Additionally, analysis files of the data are stored on `anna\cqed\analysis\` under the respective date, or in the equivalent directory on the zidshare server.

In the following list, I additionally include the reference to the page in the paper lab book of the corresponding scan. If no time is given for a data set, it was measured without the automatic saving of the control software, e.g., by reading an oscilloscope or multimeter. Please also always check corresponding entries in the electronic lab notebook (ELN)[1], since some quick small-scale measurements are only recorded there, and sometimes the entries contain additional helpful information on the measurements.

Data sets in this thesis

[Data12] Measurement of the linewidth of the locked Raman laser at 786 nm. *Time:* -, pages –, Date: 9 March (see ELN), 2012.

[Data14] Measurement of the linewidth of the reference cavity at 783.5 nm. *Time:* -, pages 0027–15, Date: 22 October, 2014.

[Data15a] Characterisation of the lock of the repumping laser at 854 nm. *Time:* -, pages 0027–186, Date: 24 March (see ELN 27 March 2015), 2015.

[Data15b] Measurement of a polarisation dependence of the finesse (not reproducible). *Time:* -, pages 0034–135, Date: 4 November, 2015.

[Data15c] Measurement of the relative drift rate between the repumper cavity and the reference cavity of the 786 laser. *Time:* -, pages 0034–161, Date: 13 November, 2015.

[Data15d] Two measurements of the heating rate of the axial motional mode. *Time: 1607, 1610; 1615, 1621, 1626*, pages 0034–125, Date: 28 October, 2015.

[1] `https://lxqo.uibk.ac.at/labblogs/cqed`; not accessible from outside the group.

[Data16a] Measurement of a photon wave packet, used for estimating the efficiency for ion-photon time-bin entanglement. *Time: 1319.02*, pages 0041–127, Date: 23 September, 2016.

[Data16b] Measurement of the background gas collision rate with trapped ions. *Time:* -, pages 0036–87, Date: 10 February, 2016.

[Data16c] Measurement of the frequency difference between the the TEM_{01}- and TEM_{10}-modes and the TEM_{00}-mode. *Time:* -, pages 0036–155, Date: 8 May, 2016.

[Data16d] Measurement of the FSR of the experiment cavity. *Time:* -, pages 0036–155, Date: 8 May, 2016.

[Data16e] Measurement of the resonance of the EOM used in the transfer lock. *Time:* -, pages : 0041–8, Date: 17 June, 2016.

[Data16f] Measurement of the transmission of the North-Front beam at 393 nm through the whole vacuum chamber to estimate influence of calcium coating of the Back viewport. *Time:* -, page : no reference in paper lab book. See electronic lab notebook entry of the following day, Date: 3 June, 2016.

[Data16g] Measurement of the visibility of the cavity standing wave. *Time: 1825*, pages 0045–65, Date: 14 December, 2016.

[Data17a] FFT of the cavity lock error signal. *Time:* -, pages 0045–106, Date: 23 March, 2017.

[Data17b] Measurement of a Ramsey fringe when driving the dispersively coupled cavity with additional noise. *Time: 2243*, pages 0054–130, Date: 8 October, 2017.

[Data17c] Measurement of mechanical resonances of the experiment cavity and its mount via acoustic excitation. *Time:* -, pages 0045–107, Date: 27 March, 2017.

[Data17d] Measurement of mechanical resonances of the experiment cavity and its mount via piezo excitation. *Time:* -, pages 0045–105, Date: 23 March, 2017.

[Data17e] Measurement of phase shift and dephasing induced by the cavity field of the mode at finesse $32.2(2) \cdot 10^3$ to the $|4^2\mathrm{P}_{3/2}, m_j = +1/2\rangle \rightarrow |3^2\mathrm{D}_{5/2}, m_j = +1/2\rangle$-transition of a single trapped ion. Data taken with 250 cycles per point, Doppler cooling and a detuning of $125(1)$ MHz. *Time: 2309, 2301, 2248, 2245, 2252, 2257.02, 2306.02*, pages 0054–122, Date: 3 October, 2017.

[Data17f] Measurement of phase shift and dephasing induced by the cavity field of the mode at finesse $54.8(4) \cdot 10^3$ to the $|4^2\mathrm{P}_{3/2}, m_j = +1/2\rangle \rightarrow |3^2\mathrm{D}_{5/2}, m_j = +1/2\rangle$-transition of a single trapped ion. Data taken with 250 cycles per point, Doppler cooling and a detuning of $125(1)$ MHz. *Time: 2129, 2227, 2219, 2221, 2126, 2224, 2135, 2236, 2123.02*, pages 0054–127 to 0054–131, Date: 8 October, 2017.

[Data17g] Measurement of phase shift and dephasing induced by the cavity field of the mode at finesse $54.8(4) \cdot 10^3$ to the $|4^2\mathrm{P}_{3/2}, m_j = +3/2\rangle \rightarrow |3^2\mathrm{D}_{3/2}, m_j = +1/2\rangle$-transition of a single trapped ion. Data taken with 250 cycles per point, Doppler cooling and a detuning of $125(1)$ MHz. *Time: 1430.03, 2125, 2216.02, 2307.02, 2058, 2220, 2302, 2227*, pages 0057–, Date: 20 December, 2017.

[Data17h] Measurement of the carrier frequency and the axial and radial sideband frequencies of the $|4^2\mathrm{S}_{1/2}, m_j = +1/2\rangle \rightarrow |3^2\mathrm{D}_{5/2}, m_j = +5/2\rangle$-transition of a single trapped ion at an endcap voltage of 770 V and an RF power of 3.0 W. *Time: 1509, 1520*, pages 0057–10, Date: 4 December, 2017.

[Data17i] Measurement of the carrier frequency and the red axial and radial sideband frequencies of the $|4^2\mathrm{S}_{1/2}, m_j = +1/2\rangle \rightarrow |3^2\mathrm{D}_{5/2}, m_j = +5/2\rangle$-transition of a single trapped ion at an endcap voltage of 770 V and an RF power of 2.0 W. *Time: 1602*, pages 0054–101, Date: 20 September, 2017.

[Data17j] Measurement of the dark counts of apdA, apdD, and apdE. *Time:* -, pages : 0045–185, Date: 30 May, 2017.

[Data17k] Measurement of the dark counts of apdH. *Time:* -, pages : 0052–121, Date: 29 June, 2017.

[Data17l] Measurement of the decoherence caused by off-resonant excitation and spontaneous emission. *Time: 2205, 2215, 2229, 2247, 2303, 2316*, pages 0054–115, Date: 28 September, 2017.

[Data17m] Measurement of the decoherence caused by off-resonant excitation and spontaneous emission (second measurement). *Time: 1946, 2002, 1959, 1957, 1954, 1952, 1949*, pages 0054–129, Date: 8 October, 2017.

[Data17n] Measurement of the finesse of the accessible TEM_{00} cavity modes. *Time:* -, pages 0045–80, Date: 8 February, 2017.

[Data17o] Measurement of the frequency stability of the locked cavity. *Time:* -, page : no reference in paper lab book. See electronic lab notebook entry of the following day, Date: 25 April, 2017.

[Data17p] Measurement of the mean phonon number in the axial mode after sideband cooling. *Time: 1546, 1548*, pages 0054–102, Date: 21 September, 2017.

[Data17q] Measurement of the mean phonon number in the radial mode 1 after sideband cooling. *Time: 1829, 1852*, pages 0054–104, Date: 21 September, 2017.

[Data17r] Measurement of the mean phonon number in the radial mode 2 after sideband cooling. *Time: 1827, 1849*, pages 0054–104, Date: 21 September, 2017.

[Data17s] Measurement of the mean phonon number when cooling only the radial mode 1. *Time: 1419, 1417*, pages 0054–100, Date: 20 September, 2017.

[Data17t] Measurement of the radial sideband splitting. *Time: 1640*, pages 0054–97, Date: 19 September, 2017.

[Data17u] Measurement of the transfer function of the cavity. *Time:* -, pages 0045–110, Date: 28 March, 2017.

[Data17v] Measurement of the transmission of the South-Front beam at 397 nm through the whole vacuum chamber to estimate influence of calcium coating of the Front viewport. *Time:* -, page : no reference in paper lab book. See electronic lab notebook entry of the following day, Date: 13 November, 2017.

[Data18] Analysis of recorded single-ion trapping times from 2016-2018. *Time:* -, pages –, Date: 20 February, 2018.

List of Figures

List of Tables

Bibliography

[1] M. Planck, *Wege zur physikalischen Erkenntnis: Reden und Vorträge* (Hirzel, Leipzig, 1944).

[2] T. H. Maiman, Nature **187**, 493 (1960).

[3] I. M. Ross, Proc. IEEE **86**, 7 (1998).

[4] C. L. Degen, F. Reinhard, and P. Cappellaro, Rev. Mod. Phys. **89**, 035002 (2017).

[5] M. Krenn, M. Malik, T. Scheidl, R. Ursin, and A. Zeilinger, "Quantum communication with photons," in *Optics in Our Time* (Springer International Publishing, Cham, 2016) pp. 455–482.

[6] M. A. Nielsen and I. L. Chuang, *Quantum Computation and Quantum Information* (Cambridge University Press, Cambridge, 2010).

[7] J. Preskill, arXiv:1801.00862v2 (2018).

[8] S. Haroche and J. M. Raimond, *Exploring the Quantum: Atoms, Cavities and Photons* (Oxford University Press, New York, 2006).

[9] M. Brune, F. Schmidt-Kaler, A. Maali, J. Dreyer, E. Hagley, J. M. Raimond, and S. Haroche, Phys. Rev. Lett. **76**, 1800 (1996).

[10] C. Guerlin, J. Bernu, S. Deléglise, C. Sayrin, S. Gleyzes, S. Kuhr, M. Brune, J.-M. Raimond, and S. Haroche, Nature **448**, 889 (2007).

[11] C. Sayrin, I. Dotsenko, X. Zhou, B. Peaudecerf, T. Rybarczyk, S. Gleyzes, P. Rouchon, M. Mirrahimi, H. Amini, M. Brune, J.-M. Raimond, and S. Haroche, Nature **477**, 73 (2011).

[12] J. Gambetta, A. Blais, D. I. Schuster, A. Wallraff, L. Frunzio, J. Majer, M. H. Devoret, S. M. Girvin, and R. J. Schoelkopf, Phys. Rev. A **74**, 042318 (2006).

[13] D. I. Schuster, A. A. Houck, J. A. Schreier, A. Wallraff, J. M. Gambetta, A. Blais, L. Frunzio, J. Majer, B. Johnson, M. H. Devoret, S. M. Girvin, and R. J. Schoelkopf, Nature **445**, 515 (2007).

[14] H. Walther, B. T. H. Varcoe, B.-G. Englert, and T. Becker, Rep. Prog. Phys. **69**, 1325 (2006).

[15] I. M. Georgescu, S. Ashhab, and F. Nori, Rev. Mod. Phys. **86**, 153 (2014).

[16] T. E. Northup and R. Blatt, Nat. Photonics **8**, 356 (2014).

[17] A. Reiserer and G. Rempe, Rev. Mod. Phys. **87**, 1379 (2015).

[18] E. M. Purcell, Phys. Rev. **69**, 681 (1946).

[19] P. Goy, J. M. Raimond, M. Gross, and S. Haroche, Phys. Rev. Lett. **50**, 1903 (1983).

[20] R. G. Hulet, E. S. Hilfer, and Klepp, Phys. Rev. Lett. **55**, 2137 (1985).

[21] W. Jhe, A. Anderson, E. A. Hinds, D. Meschede, L. Moi, and S. Haroche, Phys. Rev. Lett. **58**, 666 (1987).

[22] W. Jhe, A. Anderson, E. Hinds, D. Meschede, L. Moi, and S. Haroche, Phys. Rev. Lett. **58**, 1497 (1987).

[23] D. J. Heinzen, J. J. Childs, J. E. Thomas, and M. S. Feld, Phys. Rev. Lett. **58**, 1320 (1987).

[24] M. G. Raizen, R. J. Thompson, R. J. Brecha, H. J. Kimble, and H. J. Carmichael, Phys. Rev. Lett. **63**, 240 (1989).

[25] F. Bernardot, P. Nussenzveig, M. Brune, J. M. Raimond, and S. Haroche, EPL **17**, 33 (1992).

[26] Y. Kaluzny, P. Goy, M. Gross, J.-M. Raimond, and S. Haroche, Phys. Rev. Lett. **51**, 1175 (1983).

[27] R. J. Brecha, L. Orozco, M. G. Raizen, M. Xiao, and H. J. Kimble, J. Opt. Soc. Am. B **12**, 2329 (1995).

[28] W. D. Phillips, Rev. Mod. Phys. **70**, 721 (1998).

[29] R. J. Thompson, G. Rempe, and H. J. Kimble, Phys. Rev. Lett. **68**, 1132 (1992).

[30] J. J. Childs, K. An, M. S. Otteson, R. R. Dasari, and M. S. Feld, Phys. Rev. Lett. **77**, 2901 (1996).

[31] C. J. Hood, M. S. Chapman, T. W. Lynn, and H. J. Kimble, Phys. Rev. Lett. **80**, 4157 (1998).

[32] A. Boca, R. Miller, K. M. Birnbaum, A. D. Boozer, J. McKeever, and H. J. Kimble, Phys. Rev. Lett. **93**, 233603 (2004).

[33] P. Maunz, T. Puppe, I. Schuster, N. Syassen, P. W. H. Pinkse, and G. Rempe, Phys. Rev. Lett. **94**, 033002 (2005).

[34] G. Rempe, F. Schmidt-Kaler, and H. Walther, Phys. Rev. Lett. **64**, 2783 (1990).

[35] B. T. H. Varcoe, S. Brattke, M. Weidinger, and H. Walther, Nature **403**, 743 (2000).

[36] S. Brattke, B. T. H. Varcoe, and H. Walther, Phys. Rev. Lett. **86**, 3534 (2001).

[37] M. Hennrich, T. Legero, A. Kuhn, and G. Rempe, Phys. Rev. Lett. **85**, 4872 (2000).

[38] A. Kuhn, M. Hennrich, and G. Rempe, Phys. Rev. Lett. **89**, 067901 (2002).

[39] J. McKeever, A. Boca, A. D. Boozer, R. Miller, J. R. Buck, A. Kuzmich, and H. J. Kimble, Science **303**, 1992 (2004).

[40] T. Legero, T. Wilk, M. Hennrich, G. Rempe, and A. Kuhn, Phys. Rev. Lett. **93**, 070503 (2004).

[41] W. Paul, Rev. Mod. Phys. **62**, 531 (1990).

[42] A. D. Ludlow, M. M. Boyd, J. Ye, E. Peik, and P. O. Schmidt, Rev. Mod. Phys. **87**, 637 (2015).

[43] G. R. Guthöhrlein, M. Keller, K. Hayasaka, W. Lange, and H. Walther, Nature **414**, 49 (2001).

[44] M. Keller, B. Lange, K. Hayasaka, W. Lange, and H. Walther, Nature **431**, 1075 (2004).

[45] D. R. Leibrandt, J. Labaziewicz, V. Vuletić, and I. L. Chuang, Phys. Rev. Lett. **103**, 103001 (2009).

[46] J. D. Sterk, L. Luo, T. A. Manning, P. Maunz, and C. Monroe, Phys. Rev. A **85**, 062308 (2012).

[47] P. Herskind, A. Dantan, J. Marler, M. Albert, and M. Drewsen, Nat. Phys. **5**, 494 (2009).

[48] T. Steinmetz, Y. Colombe, D. Hunger, T. W. Hänsch, A. Balocchi, R. J. Warburton, and J. Reichel, Appl. Phys. Lett. **89**, 111110 (2006).

[49] M. Steiner, H. M. Meyer, C. Deutsch, J. Reichel, and M. Köhl, Phys. Rev. Lett. **110**, 043003 (2013).

[50] M. Cetina, A. Bylinskii, L. Karpa, D. Gangloff, K. M. Beck, Y. Ge, M. Scholz, A. T. Grier, I. Chuang, and V. Vuletić, New J. Phys. **15**, 053001 (2013).

[51] S. Begley, M. Vogt, G. K. Gulati, H. Takahashi, and M. Keller, Phys. Rev. Lett. **116**, 223001 (2016).

[52] M. H. Devoret and R. J. Schoelkopf, Science **339**, 1169 (2013).

[53] G. Wendin, Rep. Prog. Phys. **80**, 106001 (2017).

[54] A. Wallraff, D. I. Schuster, A. Blais, L. Frunzio, R. S. Huang, J. Majer, S. Kumar, S. M. Girvin, and R. J. Schoelkopf, Nature **431**, 162 (2004).

[55] C. J. Axline, L. D. Burkhart, W. Pfaff, M. Zhang, K. Chou, P. Campagne-Ibarcq, P. Reinhold, L. Frunzio, S. M. Girvin, L. Jiang, M. H. Devoret, and R. J. Schoelkopf, Nat. Phys. **14**, 705 (2018).

[56] H. J. Kimble, Nature **453**, 1023 (2008).

[57] C. Hamsen, K. N. Tolazzi, T. Wilk, and G. Rempe, Phys. Rev. Lett. **118**, 133604 (2017).

[58] C. Hamsen, K. N. Tolazzi, T. Wilk, and G. Rempe, Nat. Phys. (2018).

[59] C. F. Roos, *Controlling the Quantum State of Trapped Ions*, Ph.D. thesis, Leopold-Franzens-Universität Innsbruck (2000).

[60] A. B. Mundt, *Cavity QED with Single Trapped Ca^+-Ions*, Ph.D. thesis, Leopold-Franzens-Universität Innsbruck (2003).

[61] A. B. Mundt, A. Kreuter, C. Becher, D. Leibfried, J. Eschner, F. Schmidt-Kaler, and R. Blatt, Phys. Rev. Lett. **89**, 103001 (2002).

[62] A. Kreuter, *Spontaneous emission of a single trapped Ca+ ion*, Ph.D. thesis, Leopold-Franzens-Universität Innsbruck (2004).

[63] A. Kreuter, C. Becher, G. P. T. Lancaster, A. B. Mundt, C. Russo, H. Häffner, C. Roos, J. Eschner, F. Schmidt-Kaler, and R. Blatt, Phys. Rev. Lett. **92**, 203002 (2004).

[64] C. M. Russo, *Photon Statistics of a Single Ion Coupled to a High-Finesse Cavity*, Ph.D. thesis, Leopold-Franzens-Universität Innsbruck (2008).

[65] C. Russo, H. G. Barros, A. Stute, F. Dubin, E. S. Phillips, T. Monz, T. E. Northup, C. Becher, T. Salzburger, H. Ritsch, P. O. Schmidt, and R. Blatt, Appl. Phys. B **95**, 205 (2009).

[66] H. G. Barros, A. Stute, T. E. Northup, C. Russo, P. O. Schmidt, and R. Blatt, New J. Phys. **11**, 103004 (2009).

[67] H. G. de Barros, *Raman Spectroscopy and Single-Photon Source in an Ion-Cavity System*, Ph.D. thesis, Leopold-Franzens-Universität Innsbruck (2010).

[68] F. Dubin, C. Russo, H. Barros, A. Stute, C. Becher, P. Schmidt, and R. Blatt, Nat. Phys. **6**, 350 (2010).

[69] A. Stute, *A Light-Matter Quantum Interface: Ion-Photon Entanglement and State Mapping*, Ph.D. thesis, Leopold-Franzens-Universität Innsbruck (2012).

[70] A. Stute, B. Casabone, B. Brandstätter, D. Habicher, P. O. Schmidt, T. E. Northup, and R. Blatt, Appl. Phys. B **107**, 1145 (2012).

[71] B. Casabone, *Two Ions Coupled to a Cavity: From an Enhanced Quantum Computer Interface Towards Distributed Quantum Computing*, Ph.D. thesis, Leopold-Franzens-Universität Innsbruck (2015).

[72] A. Stute, B. Casabone, P. Schindler, T. Monz, P. O. Schmidt, B. Brandstätter, T. E. Northup, and R. Blatt, Nature **485**, 482 (2012).

[73] A. Stute, B. Casabone, B. Brandstätter, K. Friebe, T. E. Northup, and R. Blatt, Nat. Photonics **7**, 219 (2013).

[74] B. Casabone, A. Stute, K. Friebe, B. Brandstätter, K. Schüppert, R. Blatt, and T. E. Northup, Phys. Rev. Lett. **111**, 100505 (2013).

[75] B. Casabone, K. Friebe, B. Brandstätter, K. Schüppert, R. Blatt, and T. E. Northup, Phys. Rev. Lett. **114**, 023602 (2015).

[76] M. Brune, P. Nussenzveig, F. Schmidt-Kaler, F. Bernardot, A. Maali, J. M. Raimond, and S. Haroche, Phys. Rev. Lett. **72**, 3339 (1994).

[77] P. Bertet, A. Auffeves, P. Maioli, S. Osnaghi, T. Meunier, M. Brune, J. M. Raimond, and S. Haroche, Phys. Rev. Lett. **89**, 200402 (2002).

[78] D. I. Schuster, A. Wallraff, A. Blais, L. Frunzio, R.-S. Huang, J. Majer, S. M. Girvin, and R. J. Schoelkopf, Phys. Rev. Lett. **94**, 123602 (2005).

[79] D. I. Schuster, *Circuit Quantum Electrodynamics*, Ph.D. thesis, Yale University (2007).

[80] B. R. Johnson, M. D. Reed, A. A. Houck, D. I. Schuster, L. S. Bishop, E. Ginossar, J. M. Gambetta, L. DiCarlo, L. Frunzio, S. M. Girvin, and R. J. Schoelkopf, Nat. Phys. **6**, 663 (2010).

[81] P. K. Ghosh, *Ion traps* (Clarendon Press, 1995).

[82] D. J. Wineland, C. Monroe, W. M. Itano, D. Leibfried, B. E. King, and D. M. Meekhof, J. Res. Natl. Inst. Stand. Technol. **103**, 259 (1998).

[83] D. Leibfried, R. Blatt, C. Monroe, and D. Wineland, Rev. Mod. Phys. **75**, 281 (2003).

[84] F. G. Major, V. N. Gheorghe, and G. Werth, *Charged Particle Traps* (Springer, Berlin, Heidelberg, 2005).

[85] G. Werth, V. N. Gheorghe, and F. G. Major, *Charged particle traps II* (Springer, Berlin, Heidelberg, 2009).

[86] C. Hempel, *Digital Quantum Simulation, Schrödinger Cat State Spectroscopy and Setting Up a Linear Ion Trap*, Ph.D. thesis, Leopold-Franzens-Universität Innsbruck (2014).

[87] M. Kumph, *2D Arrays of Ion Traps for Large Scale Integration of Quantum Information Processors*, Ph.D. thesis, Leopold-Franzens-Universität Innsbruck (2015).

[88] M. Niedermayr, *Cryogenic surface ion traps*, Ph.D. thesis, Leopold-Franzens-Universität Innsbruck (2015).

[89] E. Mathieu, J. Math. Pures Appl. **13**, 137 (1868).

[90] D. J. Berkeland, J. D. Miller, J. C. Bergquist, W. M. Itano, and D. J. Wineland, J. Appl. Phys. **83**, 5025 (1998).

[91] H. G. Dehmelt (Academic Press, 1968) pp. 53–72.

[92] N. F. Ramsey, Phys. Rev. **78**, 695 (1950).

[93] N. F. Ramsey, Rev. Mod. Phys. **62**, 541 (1990).

[94] M. O. Scully and M. S. Zubairy, *Quantum Optics* (Cambridge University Press, 1997).

[95] W. Heisenberg, Z. Phys. **43**, 172 (1927).

[96] C. Gardiner and P. Zoller, *Quantum Noise: A Handbook of Markovian and Non-Markovian Quantum Stochastic Methods with Applications to Quantum Optics* (Springer, Berlin, Heidelberg, Berlin, 2004).

[97] A. Sørensen and K. Mølmer, Phys. Rev. Lett. **82**, 1971 (1999).

[98] E. Solano, R. L. de Matos Filho, and N. Zagury, Phys. Rev. A **59**, R2539 (1999).

[99] A. Sørensen and K. Mølmer, Phys. Rev. A **62**, 022311 (2000).

[100] S. Hill and W. K. Wootters, Phys. Rev. Lett. **78**, 5022 (1997).

[101] W. K. Wootters, Phys. Rev. Lett. **80**, 2245 (1998).

[102] R. J. Glauber, Phys. Rev. **131**, 2766 (1963).

[103] C. A. Blockley, D. F. Walls, and H. Risken, EPL **17**, 509 (1992).

[104] A. E. Siegman, *Lasers* (University Science Books, 1986).

[105] B. E. A. Saleh and M. C. Teich, *Fundamentals of Photonics* (John Wiley & Sons, Inc., 2001).

[106] C. Fabry and A. Perot, Ann. Chim. Phys. **16**, 7 (1899).

[107] A. Perot and C. Fabry, Astrophys. J. **9**, 87 (1899).

[108] B. Brandstätter, A. McClung, K. Schüppert, B. Casabone, K. Friebe, A. Stute, P. O. Schmidt, C. Deutsch, J. Reichel, R. Blatt, and T. E. Northup, Rev. Sci. Instrum. **84**, 123104 (2013).

[109] B. Brandstätter, *Integration of Fiber Mirrors and Ion Traps for a High-Fidelity Quantum Interface*, Ph.D. thesis, Leopold-Franzens-Universität Innsbruck (2013).

[110] E. T. Jaynes and F. W. Cummings, Proc. IEEE **51**, 89 (1963).

[111] A. Blais, R.-S. Huang, A. Wallraff, S. M. Girvin, and R. J. Schoelkopf, Phys. Rev. A **69**, 062320 (2004).

[112] A. A. Clerk, M. H. Devoret, S. M. Girvin, F. Marquardt, and R. J. Schoelkopf, Rev. Mod. Phys. **82**, 1155 (2010).

[113] S. T. Gulde, *Experimental Realization of Quantum Gates and the Deutsch-Jozsa Algorithm with Trapped $^{40}Ca^{+}$ Ions*, Ph.D. thesis, Leopold-Franzens-Universität Innsbruck (2003).

[114] M. Guggemos, *Precision spectroscopy with trapped $^{40}Ca^{+}$ and $^{27}Al^{+}$ ions*, Ph.D. thesis, Leopold-Franzens-Universität Innsbruck (2017).

[115] W. W. Macalpine and R. O. Schildknecht, Proceedings of the IRE **47**, 2099 (1959).

[116] J. D. Siverns, L. R. Simkins, S. Weidt, and W. K. Hensinger, Appl. Phys. B **107**, 921 (2012).

[117] M. Brownnutt, M. Kumph, P. Rabl, and R. Blatt, Rev. Mod. Phys. **87**, 1419 (2015).

[118] R. Hendricks, D. Grant, P. Herskind, A. Dantan, and M. Drewsen, Appl. Phys. B **88**, 507 (2007).

[119] D. R. Leibrandt, R. J. Clark, J. Labaziewicz, P. Antohi, W. Bakr, K. R. Brown, and I. L. Chuang, Phys. Rev. A **76**, 055403 (2007).

[120] K. Sheridan, W. Lange, and M. Keller, Appl. Phys. B **104**, 755 (2011).

[121] F. Zähringer, *Quantum walks and relativistic quantum simulations with trapped ions*, Ph.D. thesis, Leopold-Franzens-Universität Innsbruck (2012).

[122] D. James, Appl. Phys. B **66**, 181 (1998).

[123] M. Hettrich, T. Ruster, H. Kaufmann, C. F. Roos, C. T. Schmiegelow, F. Schmidt-Kaler, and U. G. Poschinger, Phys. Rev. Lett. **115**, 143003 (2015).

[124] J. Jin and D. A. Church, Phys. Rev. Lett. **70**, 3213 (1993).

[125] R. Gerritsma, G. Kirchmair, F. Zähringer, J. Benhelm, R. Blatt, and C. Roos, Eur. Phys. J. D **50**, 13 (2008).

[126] A. Kreuter, C. Becher, G. P. T. Lancaster, A. B. Mundt, C. Russo, H. Häffner, C. Roos, W. Hänsel, F. Schmidt-Kaler, R. Blatt, and M. S. Safronova, Phys. Rev. A **71**, 032504 (2005).

[127] J. Eschner, G. Morigi, F. Schmidt-Kaler, R. Blatt, *et al.*, J. Opt. Soc. Am. B **20**, 1003 (2003).

[128] P. Jurcevic, *Quantum Computation and Many-Body Physics with Trapped Ions*, Ph.D. thesis, Leopold-Franzens-Universität Innsbruck (2017).

[129] G. Morigi, J. Eschner, and C. H. Keitel, Phys. Rev. Lett. **85**, 4458 (2000).

[130] C. F. Roos, D. Leibfried, A. Mundt, F. Schmidt-Kaler, J. Eschner, and R. Blatt, Phys. Rev. Lett. **85**, 5547 (2000).

[131] R. Lechner, C. Maier, C. Hempel, P. Jurcevic, B. P. Lanyon, T. Monz, M. Brownnutt, R. Blatt, and C. F. Roos, Phys. Rev. A **93**, 053401 (2016).

[132] R. Lechner, *Multimode cooling techniques for trapped ions*, Ph.D. thesis, Leopold-Franzens-Universität Innsbruck (2016).

[133] P. D. Lett, R. N. Watts, C. I. Westbrook, W. D. Phillips, P. L. Gould, and H. J. Metcalf, Phys. Rev. Lett. **61**, 169 (1988).

[134] J. Dalibard and C. Cohen-Tannoudji, J. Opt. Soc. Am. B **6**, 2023 (1989).

[135] G. Birkl, J. A. Yeazell, R. Rückerl, and H. Walther, EPL **27**, 197 (1994).

[136] S. Ejtemaee and P. C. Haljan, Phys. Rev. Lett. **119**, 043001 (2017).

[137] G. Hechenblaikner, M. Gangl, P. Horak, and H. Ritsch, Phys. Rev. A **58**, 3030 (1998).

[138] D. Wineland and W. Itano, Phys. Rev. A **20**, 1521 (1979).

[139] H. J. Metcalf and P. van der Straten, *Laser Cooling and Trapping* (Springer, Berlin, Heidelberg, 2001).

[140] R. Loudon, *The quantum theory of light* (Oxford University Press Inc., New York, 1973).

[141] D. Habicher, *Abbildung, Adressierung und Zustandsdetektion Zweier Ionen in einem Optischen Resonator*, Master's thesis, Leopold-Franzens-Universität Innsbruck (2011).

[142] M. Teller, *Single-ion addressing for the high-fidelity implementation of quantum network protocols*, Master's thesis, Universität Innsbruck (2017).

[143] P. Schindler, D. Nigg, T. Monz, J. T. Barreiro, E. Martinez, S. X. Wang, S. Quint, M. F. Brandl, V. Nebendahl, C. F. Roos, *et al.*, New J. Phys. **15**, 123012 (2013).

[144] E. J. Salumbides, V. Maslinskas, I. M. Dildar, A. L. Wolf, E.-J. van Duijn, K. S. E. Eikema, and W. Ubachs, Phys. Rev. A **83**, 012502 (2011).

[145] J. R. De Laeter, J. K. Böehlke, P. De Bièvre, H. Hidaka, H. S. Peiser, K. J. R. Rosman, and P. D. P. Taylor, Pure Appl. Chem. **75**, 683 (2003).

[146] J. Benhelm, *Precision spectroscopy and quantum information processing with trapped Calcium ions*, Ph.D. thesis, Universität Innsbruck (2008).

[147] R. W. P. Drever, J. L. Hall, F. V. Kowalski, J. Hough, G. M. Ford, A. J. Munley, and H. Ward, Appl. Phys. B **31**, 97 (1983).

[148] E. Black, Am. J. Phys. **69**, 79 (2001).

[149] R. Stricker, *Gatteroperationen hoher Güte in einem optischen Quantenbit*, Master's thesis, Universität Innsbruck (2017).

[150] L.-S. Ma, P. Jungner, J. Ye, and J. L. Hall, Opt. Lett. **19**, 1777 (1994).

[151] H. Rohde, *Experimente zur Quanteninformationsverarbeitung in einer Linearen Ionenfalle*, Ph.D. thesis, University of Innsbruck (2001).

[152] T. Monz, private communication (2016).

[153] T. W. Lynn, *Measurement and Control of Individual Quanta in Cavity QED*, Ph.D. thesis, California Institute of Technology (2003).

[154] F. Bielsa, A. Dupays, M. Fouché, R. Battesti, C. Robilliard, and C. Rizzo, Appl. Phys. B **97**, 457 (2009).

[155] P. Dupré, Phys. Rev. A **92**, 053817 (2015).

[156] F. Kranzl, *Charakterisierung optischer faserbasierter Fabry-Perot-Resonatoren*, Master's thesis, Universität Innsbruck (2018).

[157] J. Schupp, private communication (2018).

[158] N. C. Pisenti, A. Restelli, B. J. Reschovsky, D. S. Barker, and G. K. Campbell, Rev. Sci. Instrum. **87**, 124702 (2016).

[159] A. Ryou and J. Simon, Rev. Sci. Instrum. **88**, 013101 (2017).

[160] J. Eschner, Eur. Phys. J. D **22**, 341 (2003).

[161] P. Pham, *A general-purpose pulse sequencer for quantum computing*, Master's thesis, Massachusetts Institute of Technology (2005).

[162] P. Schindler, *Frequency synthesis and pulse shaping for quantum information processing with trapped ions*, Master's thesis, Leopold-Franzens-Universität Innsbruck (2008).

[163] M. Brune, S. Haroche, V. Lefevre, J. M. Raimond, and N. Zagury, Phys. Rev. Lett. **65**, 976 (1990).

[164] M. Brune, S. Haroche, J. M. Raimond, L. Davidovich, and N. Zagury, Phys. Rev. A **45**, 5193 (1992).

[165] G. Nogues, A. Rauschenbeutel, S. Osnagi, M. Brune, J. M. Raimond, and S. Haroche, Nature **400**, 239 (1999).

[166] S. Deléglise, I. Dotsenko, C. Sayrin, J. Bernu, M. Brune, J.-M. Raimond, and S. Haroche, Nature **455**, 510 (2008).

[167] B. Vlastakis, G. Kirchmair, Z. Leghtas, S. E. Nigg, L. Frunzio, S. M. Girvin, M. Mirrahimi, M. H. Devoret, and R. J. Schoelkopf, Science **342**, 607 (2013).

[168] R. W. Heeres, B. Vlastakis, E. Holland, S. Krastanov, V. V. Albert, L. Frunzio, L. Jiang, and R. J. Schoelkopf, Phys. Rev. Lett. **115**, 137002 (2015).

[169] E. T. Holland, B. Vlastakis, R. W. Heeres, M. J. Reagor, U. Vool, Z. Leghtas, L. Frunzio, G. Kirchmair, M. H. Devoret, M. Mirrahimi, and R. J. Schoelkopf, Phys. Rev. Lett. **115**, 180501 (2015).

[170] C. Wang, Y. Y. Gao, P. Reinhold, R. W. Heeres, N. Ofek, K. Chou, C. Axline, M. Reagor, J. Blumoff, K. M. Sliwa, L. Frunzio, S. M. Girvin, L. Jiang, M. Mirrahimi, M. H. Devoret, and R. J. Schoelkopf, Science **352**, 1087 (2016).

[171] A. S. Parkins, P. Marte, P. Zoller, O. Carnal, and H. J. Kimble, Phys. Rev. A **51**, 1578 (1995).

[172] R. Walser, J. I. Cirac, and P. Zoller, Phys. Rev. Lett. **77**, 2658 (1996).

[173] D. M. Meekhof, C. Monroe, B. E. King, W. M. Itano, and D. J. Wineland, Phys. Rev. Lett. **76**, 1796 (1996).

[174] C. Monroe, D. M. Meekhof, B. E. King, and D. J. Wineland, Science **272**, 1131 (1996).

[175] D. Kienzler, H.-Y. Lo, B. Keitch, L. de Clercq, F. Leupold, F. Lindenfelser, M. Marinelli, V. Negnevitsky, and J. P. Home, Science **347**, 56 (2015).

[176] H. Häffner, C. Roos, and R. Blatt, Phys. Rep. **469**, 155 (2008).

[177] F. Schmidt-Kaler, H. Häffner, S. Gulde, M. Riebe, G. Lancaster, J. Eschner, C. Becher, and R. Blatt, EPL **65**, 587 (2004).

[178] A. Reiserer, S. Ritter, and G. Rempe, Science **342**, 1349 (2013).

[179] M. Hosseini, K. M. Beck, Y. Duan, W. Chen, and V. Vuletić, Phys. Rev. Lett. **116**, 033602 (2016).

[180] H. Carmichael, *An Open Systems Approach to Quantum Optics* (Springer, Berlin, Heidelberg, Berlin, 1993).

[181] C. W. Gardiner and A. S. Parkins, Phys. Rev. A **50**, 1792 (1994).

[182] H. J. Carmichael, *Statistical Methods in Quantum Optics 1: Master Equations and Fokker-Planck Equations* (Springer, Berlin, Heidelberg, 1999).

[183] J. R. Johansson, P. D. Nation, and F. Nori, Comp. Phys. Comm. **183**, 1760 (2012).

[184] J. R. Johansson, P. D. Nation, and F. Nori, Comp. Phys. Comm. **184**, 1234 (2013).

[185] V. B. Braginsky and F. Y. Khalili, Rev. Mod. Phys. **68**, 1 (1996).

[186] D. York, Can. J. Phys. **44**, 1079 (1966).

[187] M. Brune, E. Hagley, J. Dreyer, X. Maître, A. Maali, C. Wunderlich, J. M. Raimond, and S. Haroche, Phys. Rev. Lett. **77**, 4887 (1996).

[188] J. A. Nelder and R. Mead, Comput. J. **7**, 308 (1965).

[189] C. A. Fuchs, *Distinguishability and Accessible Information in Quantum Theory*, Ph.D. thesis, University of New Mexico (1995).

[190] L. Mandel, Opt. Lett. **4**, 205 (1979).

[191] J. Goetz, S. Pogorzalek, F. Deppe, K. G. Fedorov, P. Eder, M. Fischer, F. Wulschner, E. Xie, A. Marx, and R. Gross, Phys. Rev. Lett. **118**, 103602 (2017).

[192] G. Rempe, R. J. Thompson, H. J. Kimble, and R. Lalezari, Opt. Lett. **17**, 363 (1992).

[193] A. H. Myerson, D. J. Szwer, S. C. Webster, D. T. C. Allcock, M. J. Curtis, G. Imreh, J. A. Sherman, D. N. Stacey, A. M. Steane, and D. M. Lucas, Phys. Rev. Lett. **100**, 200502 (2008).

[194] R. Noek, G. Vrijsen, D. Gaultney, E. Mount, T. Kim, P. Maunz, and J. Kim, Opt. Lett. **38**, 4735 (2013).

[195] H. Ritsch, G. J. Milburn, and T. C. Ralph, Phys. Rev. A **70**, 033804 (2004).

[196] M. Khanbekyan, L. Knöll, A. A. Semenov, W. Vogel, and D.-G. Welsch, Phys. Rev. A **69**, 043807 (2004).

[197] D. Fukuda, G. Fujii, T. Numata, K. Amemiya, A. Yoshizawa, H. Tsuchida, H. Fujino, H. Ishii, T. Itatani, S. Inoue, and T. Zama, Opt. Express **19**, 870 (2011).

[198] C. W. Gardiner and M. J. Collett, Phys. Rev. A **31**, 3761 (1985).

[199] C. Noh and D. G. Angelakis, Rep. Prog. Phys. **80**, 016401 (2017).

[200] I. de Vega and D. Alonso, Rev. Mod. Phys. **89**, 015001 (2017).

[201] H.-J. Briegel, W. Dür, J. I. Cirac, and P. Zoller, Phys. Rev. Lett. **81**, 5932 (1998).

[202] K. Härkönen, F. Plastina, and S. Maniscalco, Phys. Rev. A **80**, 033841 (2009).

[203] M. Tavis and F. W. Cummings, Phys. Rev. **170**, 379 (1968).

[204] P. Domokos, J. M. Raimond, M. Brune, and S. Haroche, Phys. Rev. A **52**, 3554 (1995).

[205] S.-B. Zheng and G.-C. Guo, Phys. Rev. Lett. **85**, 2392 (2000).

[206] J. Pachos and H. Walther, Phys. Rev. Lett. **89**, 187903 (2002).

[207] A. S. Sørensen and K. Mølmer, Phys. Rev. Lett. **91**, 097905 (2003).

[208] F. Reiter, D. Reeb, and A. Sørensen, Phys. Rev. Lett. **117**, 040501 (2016).

[209] M. B. Plenio, S. F. Huelga, A. Beige, and P. L. Knight, Phys. Rev. A **59**, 2468 (1999).

[210] A. Beige, D. Braun, B. Tregenna, and P. L. Knight, Phys. Rev. Lett. **85**, 1762 (2000).

[211] M. J. Kastoryano, F. Reiter, and A. S. Sørensen, Phys. Rev. Lett. **106**, 090502 (2011).

[212] B. Kraus, H. P. Büchler, S. Diehl, A. Kantian, A. Micheli, and P. Zoller, Phys. Rev. A **78**, 042307 (2008).

[213] S. Diehl, A. Micheli, A. Kantian, B. Kraus, H. P. Büchler, and P. Zoller, Nat. Phys. **4**, 878 (2008).

[214] F. Verstraete, M. M. Wolf, and J. I. Cirac, Nat. Phys. **5**, 633 (2009).

[215] G. Vacanti and A. Beige, New J. Phys. **11**, 083008 (2009).

[216] J. T. Barreiro, P. Schindler, O. Gühne, T. Monz, M. Chwalla, C. F. Roos, M. Hennrich, and R. Blatt, Nat. Phys. **6**, 943 (2010).

[217] J. Cohen and M. Mirrahimi, Phys. Rev. A **90**, 062344 (2014).

[218] E. Kapit, J. T. Chalker, and S. H. Simon, Phys. Rev. A **91**, 062324 (2015).

[219] E. Kapit, Phys. Rev. Lett. **116**, 150501 (2016).

[220] C. D. Freeman, C. M. Herdman, and K. B. Whaley, Phys. Rev. A **96**, 012311 (2017).

[221] F. Reiter, A. S. Sørensen, P. Zoller, and C. A. Muschik, Nat. Commun. **8**, 1822 (2017).

[222] S. M. Tan, J. Opt. B **1**, 424 (1999).

[223] Y. Lin, J. P. Gaebler, F. Reiter, T. R. Tan, R. Bowler, A. Sørensen, D. Leibfried, and D. J. Wineland, Nature **504**, 415 (2013).

[224] C. Antonelli, M. Shtaif, and M. Brodsky, Phys. Rev. Lett. **106**, 080404 (2011).

[225] M. Brodsky, E. C. George, C. Antonelli, and M. Shtaif, Opt. Lett. **36**, 43 (2011).

[226] K. Schüppert, *Doppelbrechung in Faserresonatoren*, Master's thesis, Leopold-Franzens-Universität Innsbruck (2012).

[227] M. Uphoff, M. Brekenfeld, G. Rempe, and S. Ritter, New J. Phys. **17**, 013053 (2015).

[228] H. Takahashi, J. Morphew, F. Oručević, A. Noguchi, E. Kassa, and M. Keller, Opt. Express **22**, 31317 (2014).

[229] K. Ott, S. Garcia, R. Kohlhaas, K. Schüppert, P. Rosenbusch, R. Long, and J. Reichel, Opt. Express **24**, 9839 (2016).

[230] K. Schüppert, Private communication (2018).

[231] J. D. Franson, Phys. Rev. Lett. **62**, 2205 (1989).

[232] J. Brendel, N. Gisin, W. Tittel, and H. Zbinden, Phys. Rev. Lett. **82**, 2594 (1999).

[233] I. Marcikic, H. de Riedmatten, W. Tittel, V. Scarani, H. Zbinden, and N. Gisin, Phys. Rev. A **66**, 062308 (2002).

[234] A. Martin, F. Kaiser, A. Vernier, A. Beveratos, V. Scarani, and S. Tanzilli, Phys. Rev. A **87**, 020301 (2013).

[235] H. Jayakumar, A. Predojević, T. Kauten, T. Huber, G. S. Solomon, and G. Weihs, Nat. Commun. **5**, 4251 (2014).

[236] L. Yu, C. M. Natarajan, T. Horikiri, C. Langrock, J. S. Pelc, M. G. Tanner, E. Abe, S. Maier, C. Schneider, S. Höfling, M. Kamp, R. H. Hadfield, and Y. Fejer, M. M.and Yamamoto, Nat. Commun. **6**, 8955 (2015).

[237] I. Marcikic, H. de Riedmatten, W. Tittel, H. Zbinden, M. Legré, and N. Gisin, Phys. Rev. Lett. **93**, 180502 (2004).

[238] T. Honjo, H. Takesue, H. Kamada, Y. Nishida, O. Tadanaga, M. Asobe, and K. Inoue, Opt. Express **15**, 13957 (2007).

[239] J. F. Dynes, H. Takesue, Z. L. Yuan, A. W. Sharpe, K. Harada, T. Honjo, H. Kamada, O. Tadanaga, Y. Nishida, M. Asobe, and A. J. Shields, Opt. Express **17**, 11440 (2009).

[240] T. Inagaki, N. Matsuda, O. Tadanaga, M. Asobe, and H. Takesue, Opt. Express **21**, 23241 (2013).

[241] M. Gündoğan, P. M. Ledingham, K. Kutluer, M. Mazzera, and H. de Riedmatten, Phys. Rev. Lett. **114**, 230501 (2015).

[242] P. C. Humphreys, B. J. Metcalf, J. B. Spring, M. Moore, X.-M. Jin, M. Barbieri, W. S. Kolthammer, and I. A. Walmsley, Phys. Rev. Lett. **111**, 150501 (2013).

[243] J. M. Donohue, M. Agnew, J. Lavoie, and K. J. Resch, Phys. Rev. Lett. **111**, 153602 (2013).

[244] Y. He, X. Ding, Z.-E. Su, H.-L. Huang, J. Qin, C. Wang, S. Unsleber, C. Chen, H. Wang, Y.-M. He, X.-L. Wang, W.-J. Zhang, S.-J. Chen, C. Schneider, M. Kamp, L.-X. You, Z. Wang, S. Höfling, C.-Y. Lu, and J.-W. Pan, Phys. Rev. Lett. **118**, 190501 (2017).

[245] T. Monz, *Quantum information processing beyond ten-ion qubits*, Ph.D. thesis, Leopold-Franzens-Universität Innsbruck (2011).

[246] H. Takesue and Y. Noguchi, Opt. Express **17**, 10976 (2009).

[247] H. Jayakumar, *Coherent Creation of Photon Pairs and Generation of Time-Bin Entangled Photons from a Quantum Dot*, Ph.D. thesis, Leopold-Franzens-Universität Innsbruck (2013).

[248] P. Kok and B. W. Lovett, *Introduction to Optical Quantum Iinformation Processing* (Cambridge University Press, 2010).

[249] C. Hilweg, F. Massa, D. Martynov, N. Mavalvala, P. T. Chruściel, and P. Walther, New J. Phys. **19**, 033028 (2017).

[250] M. Leifgen, *Protocols and Components for Quantum Key Distribution*, Ph.D. thesis, Humboldt-Universität zu Berlin (2016).

[251] J. Benhelm, G. Kirchmair, C. F. Roos, and R. Blatt, Nat. Phys. **4**, 463 (2008).

[252] L. Slodička, G. Hétet, N. Röck, P. Schindler, M. Hennrich, and R. Blatt, Phys. Rev. Lett. **110**, 083603 (2013).

[253] H. P. Specht, C. Nölleke, A. Reiserer, M. Uphoff, E. Figueroa, S. Ritter, and G. Rempe, Nature **473**, 190 (2011).

[254] N. Kalb, A. Reiserer, S. Ritter, and G. Rempe, Phys. Rev. Lett. **114**, 220501 (2015).

[255] N. Piro, F. Rohde, C. Schuck, M. Almendros, J. Huwer, J. Ghosh, A. Haase, M. Hennrich, F. Dubin, and J. Eschner, Nat. Phys. **7**, 17 (2011).

[256] A. Delteil, Z. Sun, S. Fält, and A. Imamoğlu, Phys. Rev. Lett. **118**, 177401 (2017).

[257] M. Ježek, J. Fiurášek, and Z. Hradil, Phys. Rev. A **68**, 012305 (2003).

[258] J. Dilley, P. Nisbet-Jones, B. W. Shore, and A. Kuhn, Phys. Rev. A **85**, 023834 (2012).

[259] L. Giannelli, T. Schmit, and G. Morigi, arXiv:1807.01535 (2018).

[260] M. A. Hall, J. B. Altepeter, and P. Kumar, New J. Phys. **13**, 105004 (2011).

[261] M. A. Hall, J. B. Altepeter, and P. Kumar, New J. Phys. **14**, 039501 (2011).

[262] M. A. Hall, J. B. Altepeter, and P. Kumar, Phys. Rev. Lett. **106**, 053901 (2011).

[263] Y.-P. Huang and P. Kumar, New J. Phys. **14**, 053038 (2012).

[264] N. N. Oza, Y.-P. Huang, and P. Kumar, IEEE Photonics Technol. Lett. **26**, 356 (2014).

[265] J. Kerr, Philos. Mag. **50**, 337 (1875).

[266] J. Kerr, Philos. Mag. **50**, 446 (1875).

[267] M. Bass, J. M. Enoch, E. W. Van Stryland, and W. L. Wolfe, *Handbook of Optics, Volume IV* (McGraw-Hill, 2001).

[268] R. D. Guenther, *Modern Optics* (John Wiley & Sons, Inc., 1990).

[269] G. Sagnac, Comptes Rendues Acad. Sci. **157**, 708 (1913).

[270] G. Sagnac, Comptes Rendues Acad. Sci. **157**, 1410 (1913).

[271] B. Culshaw, Meas. Sci. Technol. **17**, R1 (2006).

[272] M. A. Foster, A. C. Turner, M. Lipson, and A. L. Gaeta, Opt. Express **16**, 1300 (2008).

[273] P. S. J. Russell, P. Hölzer, W. Chang, A. Abdolvand, and J. C. Travers, Nat. Photonics **8**, 278 (2014).

[274] D. Meschede, *Optik, Licht und Laser* (Vieweg + Teubner Verlag, Wiesbaden, 2005).

[275] R. Grimm, M. Weidemüller, and Y. B. Ovchinnikov (Academic Press, 2000) pp. 95 – 170

Index

Acknowledgements

Experimentelle Quantenoptik ist Teamarbeit. Aus diesem Grund bedanke ich mich an erster Stelle bei Rainer Blatt: Dank Deiner unermüdlichen Bemühungen um die Arbeitsgruppe kann man in Innsbruck in internationalem Umfeld und bestens ausgestattet in einer offenen wissenschaftlichen Umgebung arbeiten. Ebenso vielen Dank, Tracy Northup, für die Leitung des CQED Teams, kritisches Nachhaken, das Abschirmen der Studenten von Verwaltungsaufgaben, sowie fürs Formulierungsfeilen beim Paperschreiben. Auf der administrativen Ebene waren Patricia Moser, Renate Rupprechter, Karin Köhle, Michaela Palz, sowie im konstruktiven Bereich die elektronischen und mechanischen Werkstätten unersetzlich und hilfreich.

Dank geht auch an eine lange Reihe von teils ehemaligen Mitgliedern der Arbeitsgruppe für die gute Atmosphäre. In alphabetischer Reihenfolge: Ben Ames (Zeichentrickfilm, unterhaltsamste Obergurgl-Vorträge, American DIY), Virgile Andreani (Slow Food), Gabriel Araneda Machuca (Musik und gute Laune), Matthias Brandl, Michael Brownnutt (epistemologisches Madagaskar), Yves Colombe (Politik im TechCafe), Guillaume Coppola (Strela), Lorenzo Dania (how many pages?), Alexander Erhard (Karteln im Zug nach Wien), Michael Guggemos (willst Du schlägern?), Johannes Haag (unerschütterlich gelassen, Musiksession in Obergurgl), Max Harlander (Watten, watten, watten), Daniel Heinrich (Wiesbaden-Mainz), Gabriel Hétet (WM 2014 am Marktplatz), Cornelius Hempel (IQOQI Concierge), Markus Hennrich (der gutmütigste Prüfer), Óscar Andrey Herrera (Thomas Bernhard und Whiplash), Daniel Higginbottom (easy going), Gerard Higgins (die charmantesten Beleidigungen), Philip Holz (Dvořák und russisch), Pierre Jobez (Apéro!), Petar Jurcevic, Florian Kranzl (korrekt), Vojtěch Krčmarský (Pitztal), Florian Kress (französisches Essen), Muir Kumph (Elektronik), Kirill Lakhmanskiy (Bürogenosse, Politik und Bier), Kirsten Langer (Blutwurst), Ben Lanyon (Fragen... und Antworten), Regina Lechner (lab cleanup!), Bryan Luu (Wissbegier), Christine Maier, Tyler Malloy (Mittagessen), Esteban Martinez (der Schwan wartet noch...), Martin Meraner (BigBand), Thomas Monz (verstörend, aber wichtig), Martin van Mourik, Daniel Nigg (Garant für beste Laboratmosphäre), Anton Nolf, Fabian Pokorny (KGB), Lukas Postler, Nadia Roeck, Christian Roos, Rafael Rothganger de Paiva (TV, McDonalds, Flugzeuge...), Dominic Schärtl, Philipp Schindler, Josef Schupp (Once upon a time in the West), Heng Shen, Lukaš Slodička (Patscherkofel bei Nacht), Tetsu Takekoshi, Slava Uryumtsev, ...

Aus dem CQED-Team danke ich besonders Birgit Brandstätter (Nonkonformismus), Bernardo Casabone (ansteckend enthusiastisch), Dario Alessandro Fioretto (Ge-schäfte witternd und swing-fanatisch), Moonjoo Lee (koreanische Arbeitsmoral und absurder Humor), Andreas Stute (der Altmeister), Florian Ong (Käse und Mahler), Klemens Schüppert (der grüne Kollege aus der Mühle), Markus Teller (ansteckend optimistisch).

Schließlich danke ich Hansjörg Rabanser für die Kunstintervention, meinen Eltern fürs Ermöglichen des Studiums und meiner Frau, dass sie mich auch ohne Doktortitel geheiratet hat.